Order Number 9116324

Vectorized algorithms for Monte Carlo simulation of kilovolt electron and photon transport

Wilderman, Scott James, Ph.D.

The University of Michigan, 1990

U·M·I
300 N. Zeeb Rd.
Ann Arbor, MI 48106

VECTORIZED ALGORITHMS FOR MONTE CARLO SIMULATION OF KILOVOLT ELECTRON AND PHOTON TRANSPORT

by

Scott James Wilderman

A dissertation submitted in partial fulfillment
of the requirements for the degree of
Doctor of Philosophy
(Nuclear Engineering)
in The University of Michigan
1990

Doctoral Committee:

Adjunct Associate Professor Michael Flynn, Co-Chairman
Professor William Martin, Co-Chairman
Professor Charles Cowley
Professor Glenn Knoll
James Rathkopf, Physicist, Lawrence Livermore National Laboratory

RULES REGARDING THE USE OF

MICROFILMED DISSERTATIONS

Microfilmed or bound copies of doctoral dissertations submitted to The University of Michigan and made available through University Microfilms International or The University of Michigan are open for inspection, but they are to be used only with due regard for the rights of the author. Extensive copying of the dissertation or publication of material in excess of standard copyright limits, whether or not the dissertation has been copyrighted, must have been approved by the author as well as by the Dean of the Graduate School. Proper credit must be given to the author if any material from the dissertation is used in subsequent written or published work.

ACKNOWLEDGEMENTS

I would like to thank everyone on my committee for their patience during the final stages of this project, and specifically Professor Charles Cowley for examining the summaries of the theoretical cross sections on short notice and Dr. James Rathkopf for going out of his way to accomodate my perpetually changing plans. I would also like to acknowledge Professor Glenn Knoll for initiating this project by way of introducing me to Dr. Flynn and for arranging financial support for me during the project's initial stages.

I would like to express my most sincere thanks and my deepest respect and admiration to Dr. Michael J. Flynn for a multitude of reasons, especially for allowing me the latitude to pursue the directions I felt most interesting, for pushing me in exposing the results of this work in various academic circles, and for guiding me through the nuances involved in conducting an research project.

Lastly, I wish to thank Professor Bill Martin for his invaluable assistance with the numerical aspects of this work and for his support, encouragement, friendship, and understanding, and mostimportantly, for the timely swift kick(s) in the behind, which, I am certain, are solely responsible for ultimately bringing this effort to an end.

This research was funded by Henry Ford Hospital, Detroit, Michigan.

Supercomputing resources were provided by the San Diego Supercomputing Consortium at the University of California at San Diego.

TABLE OF CONTENTS

LIST OF FIGURES

Figure

LIST OF TABLES

Table

CHAPTER I

INTRODUCTION

1.1 Initial Motivation for this Work

This work originated as an investigation of the effect of the transport of secondary radiation away from primary interaction sites on the inherent spatial resolution of radiation detectors used in medical imaging. It had previously been presumed that spatial resolution is limited only by the finite size of the detector elements, and not by secondary radiation transport. Although investigations of the effects of photon transport on detection efficiency and energy resolution had been performed for various detectors, [Ch76, Ch80, Ru83], systematic determinations of inherent spatial resolutions over the range of available detector materials for kilovolt energy photons have not been attempted.

Knowing the range of photons to be substantially greater than that of electrons of comparable energy in the same media, preliminary calculations were made assuming that the transport of electrons could be ignored, and that incident x-ray photon energy could be considered deposited at the exact site of transformation through any of the various photon collision processes into electron energy. Efforts to quantify detector resolution degradation concentrated on the investigation of the transport of secondary photons, which consist primarily of characteristic x-rays emitted follow-

ing photo-absorptions and incoherently scattered photons. Elementary calculations using a Monte Carlo technique and the stated approximations indicated that photon energy is deposited in a sharp, narrow peak (less than 10 microns wide) at the point of incidence, with a long low level tail of energy deposition at greater distances [Fl83]. Thus it was concluded that while secondary photon transport is involved in spreading energy deposition throughout a detector, it is not the primary factor responsible for the degradation of spatial resolution of point images.

At this point the approximation of ignoring the transport of electrons was re-examined. As implied above, most photon interactions generate secondary electrons. Often, these electrons are energetic enough to liberate additional electrons through collisions with atomic electrons, or to produce photons either through bremsstrahlung interactions or through the de-excitation of the target atoms subsequent to inner shell electron ionization collisions (in high energy physics, this process of electrons and photons being continually produced from a single incident radiation is often called a cascade or shower). Since it had been shown that photon transport alone was not responsible for the lateral spread of energy deposition, examination of the coupled transport of photons and secondary electrons in the cascade process presented itself as the next phase in the investigation. As it was soon discovered that scattering and transport theory for electrons is much less well understood than for photons, especially in energy ranges typically expected for electrons produced in diagnostic radiographic procedures, the focus of the work shifted from the specific problem of detector spatial resolution prediction to a general investigation of kilovolt energy electron transport.

1.2 Basic Electron Transport Processes

As they traverse media, electrons interact with atomic nuclei, tightly bound atomic electrons, loosely bound electrons, and, in condensed media, the weak plasma formed by the conduction electrons of the material. These interaction processes may result in the loss of energy, change of direction and/or the creation directly or indirectly of secondary particles. Generally, the processes are grouped in two categories, with nuclear scattering considered an elastic event, and all electron-electron scattering processes as well as large energy loss nuclear events (nuclear bremsstrahlung) considered inelastic events. For illustrative purposes, elastic nuclear scattering can be described as the billiard ball type scattering of a point charge electron as it passes near a point charge nucleus. The inelastic processes have no such simple classical analog, and in general are greatly dependent on the structure of the target atom. The most prevalent inelastic interactions are those involving the loosely bound electrons, and these may result in the ejection of the target electron with substantial energy transfer (as the incident and atomic electron are of equal mass, all of the incident energy may be transferred); the excitation of the atom to a higher energy atomic electron configurations, with little energy transfer; production of a bremsstrahlung photon in the field of the target electrons, with potentially large energy transfer; and, in condensed media, the excitation of resonant vibrations of the conduction electron plasma. The most common inelastic process involving the inner, tightly bound atomic electrons is the ionization of the target atom, resulting in the ejection of the target electron and the creation of an inner shell vacancy which must somehow be filled by an electron from a lower energy shell, resulting in either Auger electron or characteristic x-ray emission. The final inelastic process, nuclear bremsstrahlung,

is actually a form of the same process as nuclear 'elastic' scattering. In all scattering processes involving the acceleration of an electron, a photon is emitted. In almost all situations, the energy of this photon is in the very low or infrared region and the collision approaches the idealized process [Mo64]. However, the emitted photon may sometimes carry a great deal of energy, in which case the collision is considered to be inelastic. Rather general and informative reviews of the interactions of electrons with media and some of the attempts to describe the interactions are found in the articles by Bethe and Ashkin [Be58], Birkhoff [Bi59] and Zerby and Keller [Ze68].

Efforts to determine differential interaction cross sections for the individual interactions have been extensive but remain incomplete. Theoretical investigations of individual atomic events are complicated by the fact that an electron may interact with one or more atomic electrons from one or more atoms simultaneously, and treatments of individual nuclear collisions are hampered by incomplete descriptions of the varied effects of the screening of the nuclear charge by the atomic electrons, of the spin of both the incident electron and the target nucleus, and of the structure and finite size of the nucleus.

In addition, treatments of the cumulative effects of many collisions over a given tracklength, through solution of the transport equation, have produced several energy loss and multiple elastic scattering descriptions. In modeling angular deflections, this involves the determination of the distribution of electrons traversing a given distance s, which emerge at an angle θ within $d\theta$, given by $f(s,\theta)d\theta$. Methods for determining the aggregate effects of inelastic collisions take two tacks, the first analogous to the angular deflection case in that a distribution function for the losses ΔE, namely, $f(s,\Delta E)d\Delta E$, is determined, and the second involving the prediction of the instantaneous energy loss due to all possible processes per unit pathlength for

a particle of a given energy, $\frac{dE}{dx}(E)$. Mathematical descriptions of these cumulative effects generally require that energy loss and angular deflection be separable events over the given tracklength, leading to the contradictory assumptions that the effect of nuclear scattering can be ignored in determining energy loss and that energy loss can be neglected in determining aggregate deflection.

1.3 Application of the Monte Carlo Technique to Electron Transport Problems

All electron transport problems essentially reduce to the need to solve the transport equation,

$$\frac{\partial n(\mathbf{v},\mathbf{r},t)}{\partial t} + \mathbf{v}\cdot\nabla_{\mathbf{r}} n + \frac{\partial \mathbf{v}}{\partial t}\cdot\nabla_{\mathbf{v}} n = \int d\mathbf{v}'\, v'\, \Sigma(\mathbf{v}'\rightarrow\mathbf{v})\, n(\mathbf{v}',\mathbf{r},t) - v\,\Sigma(\mathbf{v})\, n(\mathbf{v},\mathbf{r},t) + S(\mathbf{v},\mathbf{r},t), \qquad (1.1)$$

where $n(\mathbf{v},\mathbf{r},t)$ is the phase space density of the particles, $\mathbf{v}$ their velocity, $\mathbf{r}$ their position, $\Sigma(\mathbf{v}'\rightarrow\mathbf{v})$ the probability per pathlength that a particle with initial velocity $\mathbf{v}'$ will have final velocity $\mathbf{v}$ consequent to a collision, $\Sigma(\mathbf{v})$ the probability per unit path of a particle with velocity $\mathbf{v}$ undergoing any collision and $S(\mathbf{v},\mathbf{r},t)$ an external source term.

Because of the inherent mathematical difficulties in analytically solving this equation except under severe approximation, the Monte Carlo method has been used extensively for modeling the behavior of electrons in condensed media. In the Monte Carlo method, the particle phase space density at all velocities, positions and times is not calculated, but rather only estimated integral forms of the density at given velocities and positions of interest, such as the distribution in energy of particles leaving a volume through a given surface. In an analog Monte Carlo simulation, a large number of individual particles are 'tracked' by comparing known or approxi-

mated probability distribution functions for all possible events which the particles might undergo with random numbers so as to determine each particle's phase space parameters after each event (inelastic or elastic scattering collision, bremsstrahlung collision, escape from the volume, etc.). Particles are tracked until they are absorbed, slow sufficiently so as to no longer be of interest, or escape the volume. The results of these individual 'histories' are tabulated, under the assumption that as the number of histories collected becomes large, the normalized tabulation of the results will approach the actual normalized solution for n, if the distribution functions are derived from cross sections which accurately model the physical processes.

Many authors have written Monte Carlo electron transport codes, all of which can generally be classed into three types: pure single scattering algorithms; elastic single scattering algorithms; and condensed history methods. In the single scattering model, collisions are treated as distinct events giving rise to angular deflection, to energy loss, and possibly to secondary radiations. Every collision which an electron undergoes is examined, as in a conventional Monte Carlo particle transport algorithm, based on the relevant cross sections differential in scattering angle and energy loss. Theoretically, if the cross sections for the individual events are well defined, the accuracy of the calculation will be determined by the statistics of the Monte Carlo technique. This type of calculation is advantageous in situations when the number of collisions is small (low initial energy or thin targets), when the single scattering cross sections are well known (high initial energy), and when the cumulative scattering distributions are not well known (low initial energy, very thin or very thick targets). The disadvantages of single scattering calculations lie in excessive run times in cases when a great number of individual events occur for each particle tracked (high initial energy), and in uncertainty introduced when the descriptions of the single scattering

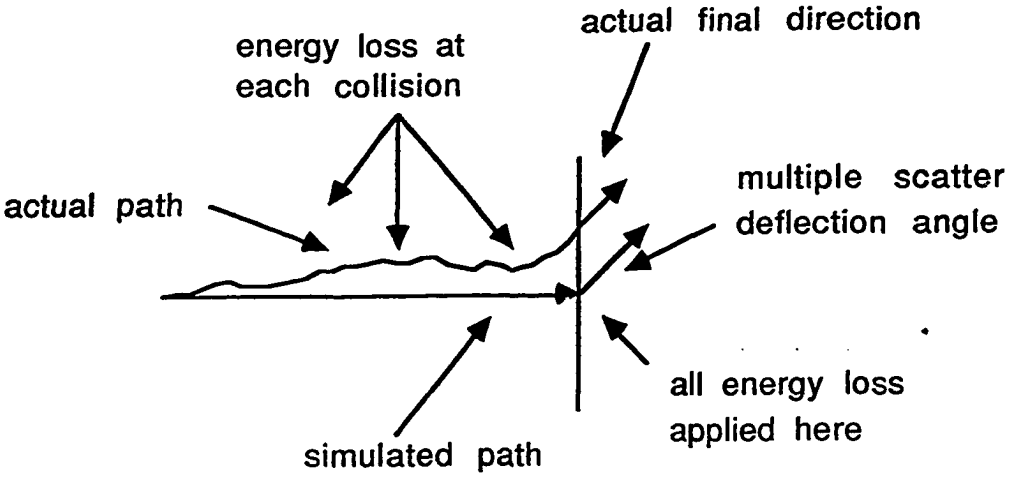

Figure 1.1: Condensed Electron Path

cross sections are incomplete (low initial energy).

In the single elastic scattering model, energy loss is considered to occur continuously between individual elastic collisions. This has the advantages over the pure single scattering model of reducing the total number of collisions which must be modeled (and hence the computation time) and alleviating the need for exact models of inelastic collision processes, but at the expense of knowingly subverting the perfect physical analogy and of introducing some computational problems.

The condensed history algorithm treats both energy loss and angular deflection over a specific pathlength as amalgamations of the effects of the many individual events over the given path, but usually treats secondary radiation production as discrete events. A particle is assumed to begin a short segment of its history traveling in a known direction with a known energy. A suitable distance is assumed to be traversed, after which the electron is modeled as moving in a different direction and with a lower energy, as shown in figure 1.1. The deflection is determined from an appropriate multiple elastic scattering distribution, and the energy loss from any of

a number of energy loss models. A general requirement for the validity of such an algorithm is that the amount of scattering should be small enough that the difference between the step size and the actual tracklength is small. At low energies this requirement becomes difficult to fulfill, since single nuclear scattering is much less preferentially forward at low energies than at high energies and the total deflection in an interval long enough to be accurately modeled by multiple scattering theories can become quite large. An advantage of the condensed history method is that less computing time is required in tracking very high energy electrons, which suffer tens of thousands of individual collisions as they slow. The disadvantage is that errors and validity restrictions are introduced into the model through inaccuracies of the aggregate energy loss and scattering models, which are sometimes derived based on incompatible assumptions. Thus, at both low and high energies, all three methods have advantages and disadvantages.

Initial investigations for the present work centered on condensed history type calculations. It was found that the existing generation of "production" codes [Be68, Fo78, Ne85], written in efforts to describe transport of relatively high energy radiation, do not address all of the problems encountered in modeling the transport of kilovolt electrons. It has been generally assumed that the applicability of the first generation of high energy condensed history transport codes to a given problem is related to the difference between the energies of the electrons in the problem being considered and the atomic shell binding energies of the given media [Ha85]. Binding energies increase rapidly with increasing atomic number (K shell binding energies for a few elements are given in table 1.1). Obviously, approximations which are valid for energies much larger than the binding energies of the atomic electrons will not be valid for all shells for all elements. It can be seen from table 1.1 that in the low

Element	Atomic Number	K Edge Energy (keV)
Helium	2	.0246
Neon	10	.8669
Aluminum	13	1.560
Argon	18	3.203
Copper	29	8.979
Krypton	36	14.33
Silver	47	25.51
Xenon	54	34.56
Gold	79	80.72
Uranium	92	110.0

Table 1.1: K edge Energies of Various Elements

kilovolt energy range this applicability criteria is not met for heavier elements.

Given these problems, an examination was undertaken of single scattering methods (encompassing both the direct analog and single elastic algorithms) proposed originally by workers investigating the effects of low energy electron transport on electron probe microanalysis measurements, and later extended to scanning electron microscopy, Mössbauer spectroscopy, and microlithography simulations. A gradual progression in the literature from calculations using simple cross sections of rather dubious validity to those using extremely complex modeling with computationally cumbersome cross sections was observed. Despite use of less approximate models, it is not obvious whether the inelastic cross sections employed even in some of the later efforts sufficiently describe the processes being modeled. Thus, two potential problems are found with single scattering models, the first pertaining to the uncertain accuracy and the numerical difficulty in evaluation of expressions for single scatter-

ing cross sections at low energies, and the second to the prohibitive computational effort, due to the large number of collisions, required at high energies.

Attempts to skirt problems associated with using one type of transport algorithm by employing one of the others are not always practical because the choice of technique is often limited by the output information desired. For example, integrated dose calculations in tissue for kilovolt range x-ray beams do not require the type of energy resolution afforded by single scattering codes which treat individual plasma losses, which will be in the range of tens of electron volts. Conversely, microlithography energy deposition calculations using hundreds of angstrom cells in plastics can not use the hundreds of micron step sizes typical of condensed history techniques. Difficulties might also arise if detailed spatial resolution is required for relatively high energy electrons in a high Z material. Condensed history codes might lack accuracy, and single scattering models would involve too many collisions per history.

1.4 Scope of this Work

The following observations and conclusions were reached concerning the status of Monte Carlo coupled photon and electron transport calculations in the kilovolt energy range:

1. The cumulative distributions used in condensed history codes do not always accurately model the phenomena to which they are applied at low energy. Further, few systematic efforts at determining the range of validity of the various models as a function of energy and atomic number have been undertaken.

2. The effects of inaccuracy in the basic multiple scattering models on overall kilovolt electron Monte Carlo calculations, although reported for various models for certain problems, is not clearly understood.

3. The increased probability of large angle scattering at low energy jeopordizes the validity of the condensed history approach itself. Published work delineating the range of suitable application of this type of model is incomplete.

4. Simple cross section models used in some single scattering codes break down at low energies. Although the accuracy of individual cross sections with respect to experiment as a function of energy has been much more extensively documented than the accuracy of the various scattering distributions, especially for more commonly used elastic scattering cross sections, the region of valid application of various widely used single scattering cross sections has not completely defined.

5. Because of the lack of complete evaluations of single scattering cross sections, optimal schemes for modeling physics processes for single scattering computations have not been systematically identified.

6. Accurate single scattering calculations may not be computationally viable at moderately high initial energies owing to the great number of collisions. Systematic determinations of computing speed (and hence applicability) versus atomic number and energy have not been reported.

7. It appears that there is an energy region near the atomic binding levels of the various atoms for which condensed history codes (because of the limitations of the algorithm) and single scattering codes (because of inordinate run times) may be equally suitable or equally inappropriate. A systematic investigation of the best suited model in this energy region has not been reported.

In summary, for both condensed history and single scattering Monte Carlo calculations, the accuracy of the basic physics models, the effect of individual model

inaccuracy on overall calculations, and the inherent restrictions on the global algorithms have been examined in only a piecemeal fashion. Thus the optimal scheme for modeling electron transport in the kilovolt energy range is not known.

Based on these observations, a fourfold focus of effort has developed for this work. First, a thorough examination of the applicability of the available single scattering cross sections based on accuracy in comparison to experiment (where possible) and on computational efficiency, with particular emphasis placed on their applicability in the kilovolt energy range, has been undertaken. Second, a similar evaluation of the utility of various cumulative energy loss and angular deflection distributions has been performed. Where possible, modifications have been made to existing theories in efforts to extend the range of validity to lower energies. Third, a determination of the effects of the accuracy of individual models on overall calculations has been included and on this basis an optimal Monte Carlo scheme has been developed which balances accuracy in comparison to experiment with computational efficiency. This third facet of this work encompasses the effort to define the effective validity range of the three types of Monte Carlo algorithms. Lastly, because of the large number of collisions expected for single scattering simulations and the recent availability of pipeline vector supercomputers, the implementation of vectorized versions of the various transport algorithms has been performed.

It should be noted that some effects necessary for the description of electron transport in the range of energies near the atomic binding energies, such as the transport of photons and atomic de-excitation, have been included and so have been discussed for the sake of completeness in the description of the model, although in a cursory fashion, with the implied assumption that existing theories are reliable at the energies in question. Other potentially significant effects have been glossed over or

even ignored altogether. Among these are crystalline effects such as channeling and diffraction, surface effects, some chemical binding effects in compounds, and post collisional interaction effects.

It is realized, on final note, that the theory sections contain a great deal of simple review which might be considered superfluous by anyone familiar with electron scattering theory. It is included for two reasons. First, as it is desired to compare predicted and experimentally determined ranges of validity, cursory review of the approximations made in the derivations of the various cross sections is instructive in determining the source of the predicted validity limits. Second, it is felt that most people interested in these results would come from engineering and not physics backgrounds, and so might find these brief reviews and explanations of principles most helpful.

References

[Be58] H.A. Bethe and J. Ashkin, "Passage of Radiations Through Matter," *Experimental Nuclear Physics,* **II**, E. Segré, ed., Wiley and Sons, New York, (1958).

[Be68] M.J. Berger and S.M. Seltzer, *Monte Carlo Code System for Electron and Photon Transport through Extended Media*, Oak Ridge National Laboratory Radiation Shielding Information Center document CCC-107, (1968).

[Bi59] R.D. Birkhoff, "The Passage of Fast Electrons through Matter," *Corpuscles and Radiation in Matter II, Encyclopedia of Physics***34**, S. Flügge, ed., Springer–Verlag, Berlin, (1958).

[Ch76] C. Chen, J.A. Lockwood, L. Hsieh, *Nucl. Instrum. & Methods* **138**, (1976) 363.

[Ch80] C.S. Chen,K. Doi,C. Vyborny, H.-P. Chu and G. Holje, *Med. Phys.* **7**, (1980) 627.

[Fl83] M.J. Flynn, S.J. Wilderman, and J. Mulvaney, *SPIE Trans.* **419**, (1983) 184.

[Fo78] R.L. Ford and W.R. Nelson, *The EGS Code System: Computer Programs for the Monte Carlo Simulation of Electromagnetic Cascade Showers (Version 3)*, Stanford Linear Accelerator Center document SLAC-210, (1978).

[Ha85] J.A. Halbleib, private communication (1985).

[Mo64] J.W. Motz, H. Olsen, and H.W.Koch, *Rev. Mod. Phys.* **36**, (1964) 881.

[Ne85] W.R. Nelson, H. Hirayama and D.W.O. Rogers *The EGS4 Code System*, Stanford Linear Accelerator Center Report SLAC-265 (1985)

[Ru83] B. Rutt, *Ph.D. Thesis*, Universtiy of Toronto, (1983).

[Ze68] C.D. Zerby and F.L. Keller, *Nucl. Sci. Eng.* **27**, (1967) 190.

CHAPTER II

EVALUATION OF SINGLE SCATTERING CROSS SECTIONS

This chapter evaluates previous calculations of electron scattering cross sections, based on comparison to experiment and facility of implementation, in hopes of identifying those most suitable for use in Monte Carlo electron transport simulations. Clearly, it would be impractical to identify and examine all known cross section formulations, devise numerical schemes to evaluate them, and then compare the results against all reported experimental results. Therefore, emphasis is placed on those formulations that have previously been used in Monte Carlo calculations and on others which have been derived under less severe approximation than those commonly used and which are expressed in an easily evaluated form for all atomic numbers and all energies between one and roughly several hundred kilovolts.

First, the single framework common to the derivations of most scattering cross sections is described. Then, cross sections describing three physical phenomena, elastic nuclear scattering, inelastic atomic scattering (including ionization, excitation, collective conduction electron excitation) and nuclear bremsstrahlung are investigated. Each of these examination sections begins with a cursory description of the process being modeled followed by an overview of basic analytical methods used in

the derivation of differential cross sections for the given phenomenon, the premise being that some *a priori* information about the validity of given calculations can be culled from knowing the approximations employed in the derivations. The framework suitable for the evaluation of the various cross section versus relevant experiments for each particular phenomenon is briefly described, and the actual mathematical form of all cross sections tested is presented. Following a summary of cross sections used in previous Monte Carlo calculations and a review of experiments relevant to the evaluation of the particular physical process, a comparison of the results of the computations for each model with the experimental data is presented, thus defining ranges of validity. Results and computational aspects of obtaining numerical results for the various formulations are also discussed.

2.1 Basic Electron Scattering Calculation Formalisms

With the exception of a few special cases in inelastic scattering, almost all widely used electron scattering cross section are derived employing one of two formalisms (either that of Schrödinger or that of Dirac) to describe the quantum mechanics of the interaction and use one of two calculation techniques (either the Born approximation or the method of partial waves) to determine the interaction probabilities that define particular cross sections. It is instructive to summarize these two formalisms and two methods, since the applicability of cross sections derived under the various scenarios depends greatly upon both the formalism and solution method selected. The very rough outline of the highlights of the techniques presented here is based on the books by Mott and Massey [Mo49] and Reimer [Re85], although quantum mechanical scattering calculations are described in nearly every basic quantum mechanics text.

2.1.1 Formalisms

Schrödinger's description of electron quantum mechanics gives for the time dependent electron wave function $\Psi(\mathbf{r},t)$,

$$\frac{\hbar^2}{2m}\nabla^2\Psi - V(\mathbf{r})\Psi = -i\hbar\frac{\partial}{\partial t}\Psi, \tag{2.1}$$

in which V is the interaction potential. This expression is not invariant under a Lorentz transformation and is thus non-relativistic, and so calculations based on Schrödinger's equation are often described as non-relativistic treatments. Knowing the wave function provides pertinent information in scattering calculations in that the probability that an electron which is described by Ψ can be found at time t in a volume element $d\mathbf{r}$ is given by $|\Psi(\mathbf{r},t)|^2 d\mathbf{r}$.

Solutions for $\Psi(\mathbf{r},t)$ are usually sought in a separable form

$$\Psi(\mathbf{r},t) = \psi(\mathbf{r})e^{-iEt/\hbar}$$

which can be substituted into 2.1, leading to a time independent equation

$$\nabla^2\psi + \frac{2m}{\hbar^2}[E - V(\mathbf{r})]\psi = 0. \tag{2.2}$$

in which E is the electron energy.

Dirac's formalism requires that the electron be described by four wave functions $\Psi_\lambda(\mathbf{r},t)$ which simultaneously satisfy

$$\begin{aligned}
(p_0 + mc)\Psi_1 + (p_1 - ip_2)\Psi_4 + p_3\Psi_3 &= 0 \\
(p_0 + mc)\Psi_2 + (p_1 + ip_2)\Psi_3 - p_3\Psi_4 &= 0 \\
(p_0 - mc)\Psi_3 + (p_1 - ip_2)\Psi_2 + p_3\Psi_1 &= 0 \\
(p_0 - mc)\Psi_4 + (p_1 + ip_2)\Psi_1 - p_3\Psi_2 &= 0
\end{aligned} \tag{2.3}$$

in which

$$p_0 = -\frac{\hbar}{ic}\frac{\partial}{\partial t} + \frac{V(\mathbf{r})}{c}$$

and

$$p_1 = \frac{\hbar}{i}\frac{\partial}{\partial x} + \frac{eA_1(\mathbf{r})}{c}, \qquad \text{etc,}$$

and in which $\mathbf{A}(\mathbf{r})$ is the magnetic vector potential and the subscripts 1, 2, and 3 on p and A refer to x, y, and z components. The probability of finding the electron in $d\mathbf{r}$ at t is now given by

$$\sum_{\lambda=1}^{4} |\Psi_\lambda(\mathbf{r},t)|^2 d\mathbf{r}.$$

It can easily be seen that a time independent expression in analogy to Schrödinger's can be derived and the expression for p_0 replaced by

$$p_0 = \frac{E + V(\mathbf{r})}{c}.$$

Dirac's equations, by taking into account the electron spin, were derived so as to be invariant under a Lorentz transformation and so his treatment is often referred to as a relativistic treatment. 'Relativistic' is a rather loose term, usually taken to mean that the particle velocity is on the same order as the speed of light. As the mass of an electron is small and the relation between kinetic energy E and velocity v of any particle is given by

$$\beta = \frac{v}{c} = \frac{\sqrt{E(E+2mc^2)}}{E+mc^2},$$

it can be seen that as low as 10 keV, the electron velocity is 20% of the speed of light, and at 1 keV, it is still 6% of c, and so despite the success of some non-relativistic treatments of electron scattering at these energies, even in a crude sense all kilovolt energy electrons are relativistic.

The techniques used in determining cross sections in either description are similar for similar problems. In general, the wave function (or functions in the Dirac case) describing the incident electron is assumed to represented by a plane wave, and by the sum of a plane wave and a scattered wave after the collision. If the z direction is taken as the incident direction, and the wave number k is given by $mv/\hbar$ then the amplitude of the incident plane wave is proportional to e^{ikz}. If we assume that the scattering potential $V(r)$ falls off faster than $1/r$, the amplitude of the scattered wave at some point (r, θ, ϕ) will be given by $r^{-1}f(\theta)e^{ikr}$. Thus we are searching for solutions of either Schrödinger's equation or Dirac's equations which take the form

$$\psi \sim e^{ikz} + r^{-1}e^{ikr}f(\Omega) \tag{2.4}$$

for large r. The scattered portion of the wave is given by the second term and so the number of electrons scattered through an area element $r^2 d\Omega$ is given by

$$\left[\frac{e^{ikr}f(\theta)}{r}\right]\left[\frac{e^{ikr}f(\theta)}{r}\right]^* r^2 d\Omega$$

In the Schrödinger's formalism this yields a probability of scattering into solid angle $d\Omega$ (i. e., the differential cross section) of

$$\sigma(\Omega)d\Omega = |f(\Omega)|^2 d\Omega. \tag{2.5}$$

In the Dirac case, four wave functions of the form of 2.4 must be sought,

$$\psi_\lambda \sim a_\lambda e^{ikz} + r^{-1}e^{ikr}f_\lambda(\Omega) \tag{2.6}$$

and the number of scattered particles per solid angle per incident particle is given by

$$\sigma(\Omega)d\Omega = \frac{\sum_{\lambda=1}^{4} |f_\lambda(\Omega)|^2}{\sum_{\lambda=1}^{4} |a_\lambda|^2} d\Omega. \tag{2.7}$$

For the case of a plane wave, it can be shown that a_λ's are not independent, and it can be argued that since a scattered wave can be thought of as consisting of a superposition of plane waves, the f_λ's are not independent either. The expression for σ can be written

$$\sigma(\Omega)d\Omega = \frac{|f_3(\Omega)|^2 + |f_4(\Omega)|^2}{|a_3|^2 + |a_4|^2} d\Omega. \tag{2.8}$$

The determination of the cross section involves solving for the wave function and comparing this with the asymptotic solution to get the f_λ's. The explicit procedure which is followed is determined by assumptions about the potential, in other words, how the atom is to be described. The above expressions of the Schrödinger and Dirac formalisms can be used to determine wave functions describing a free electron, and so are strictly valid only when the motion of the atomic electrons is ignored. If the potential is assumed to be spherically symmetric, as, for example, unscreened and exponentially screened coulomb fields are, direct substitution of expressions for $V(\mathbf{r})$ are allowed. For more explicit treatments of the atom, the wave function ψ must be a function of the positions of all of the electrons in the problem, i. e., $\psi(\mathbf{r}, \mathbf{r}_1, \mathbf{r}_2, \ldots, \mathbf{r}_Z)$ if the atom in question contains Z electrons. The forms of the equations which define ψ and include descriptions of the atomic electrons are somewhat different from those given above for the case of ignoring the electrons, but the differences are typically removed by substitution in the solution procedure. Further, ψ can usually be expressed as the product of a wave function describing the incident electron (ψ') and one describing the atomic electrons (ψ''), as

$$\psi(\mathbf{r}, \mathbf{r}_1, \mathbf{r}_2, \ldots, \mathbf{r}_Z) \sim \psi'(\mathbf{r})\psi''(\mathbf{r}, \mathbf{r}_1, \mathbf{r}_2, \ldots, \mathbf{r}_Z).$$

This often leads to expressions in which the potential is a function of the wave

function describing the atom,

$$V(\mathbf{r}) = V(\psi''(\mathbf{r}_1, \mathbf{r}_2, \ldots, \mathbf{r}_Z)),$$

and f_λ a function of such a potential and the scattered electron wave function. Only rarely are the equations solvable in closed analytical form, even for atoms with few electrons, such as hydrogen and helium.

2.1.2 Interaction Potentials

Two basic models for describing the Coulomb potentials in many electron atoms have gained widespread acceptance. One is due to Thomas and Fermi in which the atom is modeled statistically as a collection of electrons which can be localized within a volume in which the potential is roughly uniform and so obey Fermi-Dirac statistics. In this case the electron density $n(r)$ is related to the potential by

$$n(r) = \frac{[-2mV(r)]^{3/2}}{3\pi^2\hbar^3}.$$

Since in this model the potential must also satisfy Poisson's equation, subject to the boundary conditions that $V(r) \to -Ze^2/r$ as $r \to 0$ and $rV(r) \to 0$ as $r \to \infty$, a differential equation for $V(r)$ can be derived. Using the common transformations

$$V(r) = -\frac{Ze^2}{r}\chi(x),$$

and

$$r = bx$$

with

$$b = \frac{1}{2}\left(\frac{3\pi}{4}\right)^{2/3}\frac{\hbar^2}{me^2Z^{1/3}}$$

an expression is obtained

$$x^{1/2}\frac{d^2\chi}{dx^2} = \chi^{3/2} \tag{2.9}$$

subject to $\chi = 1$ at $x = 0$ and $\chi = 0$ as $x \rightarrow \infty$. Both the approximation of small local perturbations and the use of a statistical model can be shown to be more appropriate at high Z.

Hartree [Ha28] devised a scheme for determining wave functions using Schrödinger's equation to describe each electron. Assuming that the potential seen by a given electron can be described as a central field constituting the nuclear field and the field of each other electron, as complete set of simultaneous integro-differential equations for the electron wave functions can be obtained. The wave function ψ_i for the ith electron will be described by

$$\nabla_i^2 \psi_i + \frac{2m}{\hbar^2}\left[-\frac{Ze^2}{r_i} + e^2 \sum_{i \neq j} |\psi_j(\mathbf{r}_j)| \frac{d\mathbf{r}}{|\mathbf{r}_j - \mathbf{r}_i|}\right] \psi_i = E_i \psi_i. \tag{2.10}$$

Potentials determined by this method are often described as being self-consistent, because the equations for the individual ψ_i functions depend upon the resultant potential.

2.1.3 Solution Procedures

The two jumping off methods used in either formalism to solve for ψ are the first Born approximation, in which the scattered electron wave in the expression for f_λ is assumed to be unperturbed and given by e^{ikr}, and the partial wave expansion method, in which ψ is expanded in spherical harmonics. This leads to solutions for f_λ in terms of infinte series of 'partial waves' dependent on the potential and the shift in phase of the partial waves of the expansion. Only for an unscreened coulomb field can the phase shifts be determined analytically, and approximation or numerical evaluation is necessary.

In summary, deriving cross sections generally involves solving for ψ based on the scattering center potential using various approximations, and finally comparing the

result with the sought after asymptotic expression of equation 2.4 to determine the $f_\lambda(\theta)$'s. Although general comments can be made about how the approximations effect the form of the cross sections, it is more convenient to discuss the inherent approximations when examining the specific cases of elastic and inelastic scattering.

2.2 Elastic Electron Nuclear Scattering

In elastic nuclear scattering, an incident electron interacts with an atom, resulting in the deflection of the electron through some angle. Since the atomic electron configuration is unchanged by the collision, the interaction is sometimes referred to as involving only the nucleus, although the atomic electrons actually play a large role in the elastic scattering of kilovolt electrons. Because the center of mass energy is small owing to the large mass difference between the nucleus and the electron, the resultant energy transfer from such a collision can usually be considered to be negligible. Although this may not be strictly true for extremely relativistic electrons and large scattering angles, such cases are not considered here. Additionally, it has been pointed out that all electron nuclear collisions result in the emission of photons as the electron is accelerated. Most emitted photons, however, have energies in the infrared range and so the electron energy loss can be ignored ([Sc49] as cited by [Mo64]). The effect on the the shape of the differential cross section at low velocities is also small, as seen in figure 2.1 (taken from [Mo64]), which shows the effect of photon emission on the experimentally determined elastic scattering cross sections.

The case of elastic nuclear scattering is unique in that commonly used cross sections exist which have been *exactly* derived (for suitable forms of the potential) under both Schrödinger's and Dirac's descriptions, using the method of partial waves. In addition, many approximate models based on the first Born approximation are

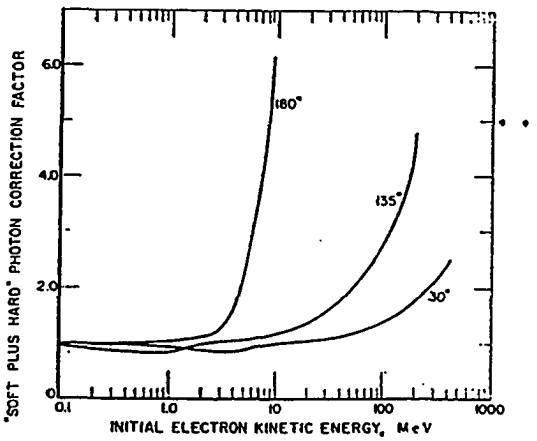

FIG. 7. Dependence of the "soft plus hard" photon correction on the initial electron kinetic energy for electron scattering angles of 30, 135, and 180 deg. This correction is evaluated from Eq. (4.14) where the first term (soft) is given by Eq. (4.05) and the second term (hard) is given by the Racah formula (4.02) for $d^2\sigma_H/d\Omega dT_2$ and by the Mott-Born formula (1A-101) for $d\sigma/d\Omega$. For the energies larger than 10 MeV, these curves were evaluated from Eq. (4.16).

Figure 2.1: Photon Emission Correction Factor

available. A thorough review of analytical techniques is given by Motz *et al* [Mo64]. This review is supplemented at lower energies by that of Walker [Wa70]. Walker's conclusion that relativistic (Dirac) treatments of scattering are necessary at energies in the tens of eV range (re-iterated by Sin Fai Lam and Baylis [Si81]) is especially noteworthy. A brief summary of the theory is presented here, encompassing both relativistic and non-relativistic treatments and emphasizing the validity conditions for the various cross sections.

2.2.1 First Born Approximation in Schrödinger's Equation

As shown in the previous section, solutions for the electron wave function after the collision derived under Schrödinger's equation take the form $\psi \sim e^{ikz} + r^{-1}e^{ikr}f(\theta)$ and the differential scattering cross section is given by

$$\sigma(\Omega)d\Omega = |f(\Omega)|^2 d\Omega. \tag{2.11}$$

In almost all instances the scattering is isotropic in the azimuthal angle and

$$\sigma(\Omega)d\Omega = \sigma(\theta)2\pi \sin\theta d\theta, \tag{2.12}$$

but it should be stressed that most of the calculations discussed here derive $\sigma(\Omega)d\Omega$.

We start by rewriting Schrödinger's equation, assuming that the energy E can be expressed as $\frac{1}{2}mv^2$ so that $2mE/\hbar^2$ can be taken as k^2. We then have for Schrödinger's equation for the electron wave function

$$\nabla^2\psi + [k^2 - \frac{2m}{\hbar^2}V(r)]\psi = 0. \tag{2.13}$$

If we assume that $V(r)$ is spherically symmetric, it can be shown that ψ must have the form

$$\psi \sim e^{ikz} - \frac{e^{ikr}}{4\pi r}\frac{2m}{\hbar^2}\int e^{-ik\mathbf{n}\cdot\mathbf{r}'}V(r')\psi(\mathbf{r}')\,d\mathbf{r}' \tag{2.14}$$

where $\mathbf{n}$ is a unit vector in the direction of $\mathbf{r}$. The assumption of spherical symmetry of $V(\mathbf{r})$ is usually valid, especially for many electron atoms since the nuclear Coulomb field, which is constant, is Z times the potential due to any electron and since these fluctuating electron induced potentials vary slowly with distance [Sc68]. In the Born approximation, we assume that the outgoing wave is not much perturbed, so that we may replace $\psi(\mathbf{r}')$ in the integral of 2.14 by $e^{ikz'}$. If we then compare 2.14 with 2.4, drop the primes, convert to spherical co-ordinates, perform the integrals over the angles and use the identity

$$\int_0^\pi \exp[iKr\cos\phi]\sin\phi\,d\phi = \frac{2\sin Kr}{Kr},$$

the scattering amplitude can be expressed as

$$f(\theta) = -\frac{2m}{\hbar^2}\int_0^\infty V(r)\frac{\sin Kr}{Kr}r^2\,dr, \tag{2.15}$$

in which $K = 2k\sin\frac{\theta}{2} = 2mv\sin\frac{\theta}{2}/\hbar$. It is obvious then that, under the First Born approximation using Schrödinger's equation, every postulated atomic potential which

is a function of r alone can be used to generate a cross section, and a great many exist in the literature.

Additionally, since V(r) is an atomic field, it is often convenient to express 2.15 as an integral involving the charge density of the atom. If $e\rho(r)$ denotes the charge density everywhere in the atom and the nucleus is considered to be a point charge, the interaction potential can be expressed as

$$V(r) = -\frac{Ze^2}{r} + e^2 \int \frac{\rho(r')}{|\mathbf{r} - \mathbf{r}'|}\, d\mathbf{r}'. \tag{2.16}$$

Assuming that the charge density can be determined exclusively from the position probabilities (i.e., the wave functions) of the atomic electrons,

$$e\rho(r) = e \sum_{i=1}^{Z} |\psi_i(\mathbf{r})|^2 \tag{2.17}$$

Once the charge density is known, the following expression can be derived for the scattering amplitude in the Born approximation,

$$f(\theta) = \frac{2m}{\hbar^2} e^2 \frac{Z - F(\theta)}{K^2} \tag{2.18}$$

where $F(\theta)$, the atomic form factor is given by

$$F(\theta) = 4\pi \int_0^\infty \rho(r) \frac{\sin Kr}{Kr} r^2\, dr. \tag{2.19}$$

The cross section in this case is given by

$$\sigma(\Omega)d\Omega = \frac{4m^2e^4Z^2}{\hbar^4K^4} \left(1 - \frac{F(\theta)}{Z}\right)^2 d\Omega. \tag{2.20}$$

This method of using the charge density ρ has the advantage that its accuracy is limited by the confidence in the wave function determination. Thus numerous authors have devised schemes to model potentials and calculate form factors. Therefore, the remainder of this subsection is thus devoted to descriptions of the commonly used potentials and charge distributions and their evaluation in 2.15 or 2.19, whether numerical or analytical, and is restricted to the more commonly used models.

Unscreened Point Nucleus

In the simplest case, the atom is represented as an unscreened point nucleus of charge Ze, giving an interaction potential between the atom and the electron of $V(r) = Ze^2/r$. Substituting this into 2.15 and using 2.11 we obtain the classical result of Rutherford,

$$\sigma(\theta)d\Omega = \frac{e^4Z^2}{p^2v^2}\frac{d\Omega}{(1-\cos\theta)^2} \tag{2.21}$$

in which p is the relativistic momentum, $mv/\sqrt{1-\beta^2}$. This is identical to the classical derived coulomb scattering cross section of Rutherford [Ru11], and so it and most cross sections of similar form, despite their quantum mechanical derivations, are usually referred to as Rutherford cross sections. Note that this cross section for an unscreened potential has the rather unwieldy property of being infinite at $\theta = 0$.

In essence, models using an unscreened potential ignore the presence of the atomic electrons, an approximation which is valid for the close collisions (small impact parameters) which lead to large angle scattering events, and for collisions involving very fast electrons, in which the interaction time is small. The approximation works poorly for small angle collisions and for slow electrons. A general condition of validity is $\alpha Z^{1/3} \ll \hbar K$ [Mo64] where α is the fine structure constant.

Exponentially Screened Point Nucleus

In a slightly more complex model of the nucleus which does take into account the presence of the atomic electrons, the potential is given as

$$V(r) = \frac{Ze^2e^{-r/\theta_s}}{r},$$

in which θ_s is variable quantifying the decay of the potential with distance. In this model of $V(r)$, the nucleus is seen as a point charge which is "screened" by the

atomic electrons at large distances, with the magnitude of screening assumed to be described by an exponential. Equation 2.15 can be solved analytically using this potential, resulting in a cross section with form quite similar to 2.21 and generally referred to as the screened Rutherford cross section,

$$\sigma(\theta)d\Omega = \frac{e^4 Z^2}{p^2 v^2} \frac{d\Omega}{(1 - \cos\theta + 2\eta_s)^2} \tag{2.22}$$

in which η_s is the screening parameter given by

$$\eta_s = \frac{1}{4} \frac{1}{p^2 \theta_s^2}. \tag{2.23}$$

A correction based on calculations employing the second Born approximation and involving the division of θ_s by a constant has been given by Nigam *et al.* [Ni59]. Since Nigam's constant must be determined for each element (either by detailed second Born calculations or empirically), since tabulated values are not available, and since the values are typically around unity, this correction is not employed here.

The first reported use of this cross section is by Wentzel [We27], who used for θ_s the Thomas-Fermi radius, r_{TF}, given by

$$r_{TF} = .885\, a_0\, Z^{-1/3} \tag{2.24}$$

in which a_0 is the Bohr radius, $\hbar^2/me^2$. This yields for the Wentzel screening parameter

$$\begin{aligned} \eta_{sw} &\equiv \eta_0 \\ &= \frac{1}{4} \frac{1}{p^2 r_{TF}^2} \\ &= \frac{1}{4} \frac{1-\beta^2}{\beta^2} \frac{Z^{2/3}}{\hbar^2} \left(\frac{\alpha}{.885}\right)^2 \end{aligned} \tag{2.25}$$

where α is the fine structure constant.

i	a_i	b_i
1	0.10	6.0
2	0.55	1.2
3	0.35	0.3

Table 2.1: Parameters for Molière's fit to Thomas-Fermi Potential

Thomas-Fermi Potentials

Molière has approximated a Thomas-Fermi potential in the form

$$V(r) = -\frac{Ze^2}{r}\sum_{i=1}^{3} a_i e^{-b_i r/r_{TF}} \tag{2.26}$$

with the values of the constants given in table 2.1. This form of the potential can be shown to lead to a cross section given by

$$\sigma(\theta)d\Omega = \frac{e^4 Z^2}{p^2 v^2}\left[\sum_{i=1}^{3}\frac{a_i}{(1-\cos\theta+2\eta_0 b_i^2)}\right]^2 d\Omega \tag{2.27}$$

Molière has devised an expression for interpolating a single value of η_s to conform with the cross sections as expressed in equation 2.22,

$$\eta_s = \eta_0\left[1.13 + 3.76\left(\frac{Z\alpha}{\beta}\right)^2\right] \tag{2.28}$$

with η_0 the Wentzel parameter given by equation 2.26. This model is subject to the general restrictions applying to the Thomas-Fermi model of the atoms, and hence is of suspect validity for low Z materials and for very high and very small momentum transfers [Mo64].

In conjunction with a multiple elastic scattering theory (as discussed in Chapter III), Ford and Nelson [Fo78] have used Molière's expression for the screening parameter with $\beta = 1$ in the right hand factor of 2.28 at all energies.

Hartree Potentials

Salvat and co-workers [Sa84b, Sa86] report parameterizations of atomic electron densities derived from relativistic Hartree potentials in the form

$$\rho(r) = \frac{Z}{4\pi r}\left[A\alpha_1^2 e^{-\alpha_1 r} + (1-A)\alpha_2^2 e^{-\alpha_2 r}\right] \tag{2.29}$$

in which A, α_1 and α_2 are Z dependent constants. Such a formalism, when applied to equation 2.19, yields an expression for the term containing the form factors in 2.20 of the form

$$\frac{1}{K^4}\left(1 - \frac{F(\theta)}{Z}\right)^2 = \left(\frac{A}{\alpha_1^2 + K^2} + \frac{A-1}{\alpha_2^2 + K^2}\right)^2. \tag{2.30}$$

Tables of forms factors evaluated in the first Born approximation formula of equation 2.19 have been published by Hubbell *et al.* [Hu75]. They use a charge density $\rho(r)$ given by a Hartree potential, in their description of coherent photon scattering processes. Despite the ease of application of the tabulated values in conjunction with equation 2.20, no application of this data in Monte Carlo electron transport work has been reported.

Cross sections of these types are subject to the limitations of the Born approximation, but should accurately describe the screening.

2.2.2 Partial Wave Expansion Technique in Schrödinger's Equation

In this method the solution for ψ is expanded as the sum of an infinite series of terms consisting of radially dependent factors $f_l(r)$, expansion coefficients A_l, and Legendre polynomials $P_l(\cos\theta)$, and given by

$$\psi = \sum_{l=0}^{\infty} A_l P_l(\cos\theta) f_l(r), \tag{2.31}$$

with each term of the expansion (labeled ψ_l), being considered a 'partial wave'. In solving Schrödinger's equation under such an expansion by use of separation of variables, it can be shown that the radial factors must be solutions to

$$\frac{d^2(rf_l(r))}{dr^2} + \left(k^2 - \frac{2mv}{\hbar}V(r) - \frac{l(l+1)}{r^2}\right)(rf_l(r)) = 0. \tag{2.32}$$

Noting that we must have ψ asymptotically approaching the expression 2.4, defining

$$rf_l(r) \equiv G_l(r),$$

and noting that the last two terms of the previous expression vanish for large r, we expect solutions for the G_l's to be of the form

$$G_l \sim C_l \sin(kr - \tfrac{1}{2}l\pi + \delta_l). \tag{2.33}$$

Here δ_l, the phase shifts, are constants dependent on k and $V(r)$ and are in fact defined by the expression for G_l and the equation 2.32. The constants A_l (and hence the C_l's) are determined by requiring that ψ approach the expression 2.4, leading to the result

$$A_l = (2l+1)i^l e^{i\delta_l}.$$

Thus we have

$$\psi = \sum_{l=0}^{\infty}(2l+1)i^l e^{i\delta_l}(kr)^{-1}\sin(kr - \tfrac{1}{2}l\pi + \delta_l)P_l(\cos\theta). \tag{2.34}$$

If we subtract from this expression for the final wave (initial plane wave plus scattered wave), the expanded form of an incident plane wave, we are left with an expression for the asymptotic scattered wave $r^{-1}e^{ikr}f(\theta)$ which leaves for the scattering amplitude

$$f(\theta) = \frac{1}{2ik}\sum_{l=0}^{\infty}(2l+1)(e^{2i\delta_l} - 1)P_l(\cos\theta). \tag{2.35}$$

Again, it is obvious then that every postulated atomic potential can be used to generate a cross section, if phase shifts satisfying equation 2.32 can be determined.

Normally, this must be done numerically. An approximate expression valid for small values of the phase shifts can be derived [Mo49],

$$\delta_l \sim -\frac{2mk}{\hbar^2}\int_0^\infty V(r)\left[\left(\frac{\pi}{2kr}\right)^{1/2} J_{n+\frac{1}{2}}(kr)\right]^2 r^2 dr, \tag{2.36}$$

but this can be shown to yield results equivalent to those determined under the Born approximation.

Salvat, Mayol and co-workers [Sa85, Sa87] have parameterized Z dependent Hartree potentials of the form

$$V(Z,r) = \sum_{i=1}^{3} a_i(z)e^{-c_i(Z)r} \tag{2.37}$$

so as to be applied in determining approximate phase shifts from equation 2.36 through numerical integration. However, no widely used cross sections are derived based on the partial wave expansion method in Schrödinger's formalism, most likely because the extensive numerical work involved in th solution procedure can be performed in Dirac's technique with greater faithfulness to the physics and at little additional cost in computational effort.

2.2.3 First Born Approximation in the Dirac formalism

It was shown in the previous section that in Dirac's formalism the cross section is dependent upon 4 wave functions of the form

$$\psi_\lambda \sim a_\lambda e^{ikz} + r^{-1}e^{ikr} f_\lambda(\Omega)$$

The Dirac equation 2.4 for the four wave functions can be written in second order by applying an operator of the form

$$(E + V(r)) + \beta - i\alpha \cdot \nabla$$

(where α and β represent appropriate 4 x 4 matrices operating on ψ), by making use of commutation relations on α and β, and by assuming that the vector potential $\mathbf{A}(\mathbf{r})$ is zero. In the Born approximation, V^2 is assumed to be negligible and any wave functions in terms which involve the potential are assumed to be given by their unscattered component, $a_\lambda e^{ikz}$, leading to

$$\nabla^2\psi_\lambda + k^2\psi_\lambda = \left[\frac{2EV(\mathbf{r})}{\hbar^2}\right]\psi_\lambda + \left[\frac{i}{\hbar c}\sigma\cdot\nabla V(\mathbf{r})\right]a_{\lambda'}e^{ikz} \tag{2.38}$$

in which σ is a 4 x 4 matrix, determined from 2.4, which relates the λ's to the λ''s. Using the typical method of comparing the calculated ψ's with the asymptotic solution, it can be shown that

$$\begin{aligned} f_3 &= \left\{\left[\gamma - \frac{1}{2}(\gamma-1)(1-\cos\theta)\right]a_3 + \frac{1}{2}(1-\gamma)\sin\theta a_4\right\}f(\theta) \\ f_4 &= \left\{\left[\gamma - \frac{1}{2}(\gamma-1)(1-\cos\theta)\right]a_4 - \frac{1}{2}(1-\gamma)\sin\theta a_3\right\}f(\theta) \end{aligned} \tag{2.39}$$

in which

$$f(\theta) = \frac{m}{2\pi\hbar^2}\int V(r')e^{ik(\mathbf{n}_0-\mathbf{n})\cdot\mathbf{r}'}d\mathbf{r}',$$

where $\mathbf{n}_0\cdot\mathbf{n}=\cos\theta$ and $\gamma = \sqrt{1-\beta^2}$. This yields for the cross section

$$\sigma(\Omega)d\Omega = \frac{1-\beta^2\sin^2\frac{1}{2}\theta}{1-\beta^2}|f(\theta)|^2. \tag{2.40}$$

Since $\mathbf{n}_0$ is a unit vector in the direction of $\mathbf{r}$ and so $\mathbf{n}_0\cdot\mathbf{r} = z$, it is seen that the expression defining $f(\theta)$ is equivalent to that for the scattering amplitude as determined from Schrödinger's equation in the Born approximation (equation 2.15) and we so essentially have

$$\sigma_{DB}(\Omega)d\Omega = \frac{1-\beta^2\sin^2\frac{1}{2}\theta}{1-\beta^2}\sigma_{SB}(\Omega)d\Omega, \tag{2.41}$$

in which the subscripts refer to the Dirac-Born and Schrödinger-Born cross sections. The two factors representing the differences both tend to unity as the velocity decreases (and also for small angles), which is expected since the Schrödinger treatment

is non-relativistic. Mott refers to the factor in the numerator as the spin correction and that in the denominator as a relativistic correction, but the usefulness and accuracy of his designations are somewhat in dispute (see [Re85]). Applications of this cross section in Monte Carlo electron transport methods have not been observed.

2.2.4 Partial Wave Formulations using Dirac's Formalism

In solving Dirac's equation by the method of partial waves, we again need solutions only for ψ_3 and ψ_4, and we again assume that the scattering potential is spherically symmetric and that the magnetic vector potential is zero. Now two solutions must be sought, one representing electrons with spin parallel and one with spin antiparallel to the direction of propagation. It can be shown that in order to satisfy the set of solutions that the wave functions must have the form

$$\begin{aligned} \psi_3(\Omega) &= \sum_{l=0}^{\infty} \left[(l+1)e^{i\delta_l} G_l + l e^{i\delta_{-l-1}} G_{-l-1}\right] i^l P_l(\cos\theta) \\ \psi_4(\Omega) &= \sum_{l=1}^{\infty} \left[-e^{i\delta_l} G_l + e^{i\delta_{-l-1}} G_{-l-1}\right] i^l P_l^1(\cos\theta) e^{\subset}\phi \end{aligned} \tag{2.42}$$

in which $P_l^1(\cos\theta)$ is the associated Legendre polynomial of the first kind, δ_l and δ_{-l-1} are the phase shifts which are present in the asymptotic forms of G_l and G_{-l-1} respectively,

$$G_l \sim r^{-1}\sin(kr - \tfrac{1}{2}l\pi + \delta_l),$$

$$G_{-l-1} \sim r^{-1}\sin(kr - \tfrac{1}{2}l\pi + \delta_{-l-1}),$$

The G's are solutions to

$$\frac{d^2G_n}{dr^2} + \left(\frac{2}{r} - \frac{\alpha'}{\alpha}\right) G_n + \left[\alpha\beta - \frac{n(n+1)}{r^2} + \frac{n}{r}\frac{\alpha'}{\alpha}\right] G_n = 0 \tag{2.43}$$

where n refers to either l or $-l-1$ and

$$\alpha = \frac{E - V(r) + mc^2}{\hbar c}, \qquad \beta = \frac{E - V(r) - mc^2}{\hbar c},$$

and the primes on α refer to the first derivative with respect to r. For arbitrary initial spin directions, $\psi_3 = Ae^{ikz}, \psi_4 = Be^{ikz}$, it can be shown that

$$\begin{aligned} f_3(\Omega) &= Af(\theta) - Bg(\theta)e^{-i\phi} \\ f_4(\Omega) &= Bf(\theta) + Ag(\theta)e^{i\phi} \end{aligned} \tag{2.44}$$

where

$$\begin{aligned} f(\theta) &= \frac{1}{2ik}\sum\left[(l+1)(e^{2i\delta_l}-1) + l(e^{2i\delta_{-l-1}}-1)\right]P_l(\cos\theta) \\ g(\theta) &= \frac{1}{2ik}\sum\left[-e^{2i\delta_l} + e^{2i\delta_{-l-1}}\right]P_l^1(\cos\theta). \end{aligned} \tag{2.45}$$

This gives for the differential cross section

$$\sigma(\Omega)d\Omega = \left\{|f|^2 + |g|^2 + (fg^* - gf^*)\frac{-AB^*e^{i\phi} + A^*Be^{-i\phi}}{|A|^2 + |B|^2}\right\}d\Omega. \tag{2.46}$$

For unpolarized beams, which is always the case in this work, the cross terms are zero and

$$\sigma(\Omega)d\Omega = \left(|f|^2 + |g|^2\right)d\Omega. \tag{2.47}$$

At this point we again turn our attention to calculations which employ various models of the atomic potential.

Unscreened Coulomb Potential

In general the phase shifts can not be analytically determined, although Mott [Mo49] derived them for the case of an unscreened point Coulomb potential for both nuclear elastic and free electron inelastic scattering. In his calculation, the cross section takes the form of

$$\sigma(\Omega)d\Omega = \lambda\!\!\!^{-2}\left[q^2(1-\beta^2)|F|^2\csc^2(\theta/2) + |G|^2\sec^2(\theta/2)\right]d\Omega. \tag{2.48}$$

in which $F=F_0+F_1$ and $G=G_0+G_1$ with

$$\begin{aligned} F_0 &= \frac{i}{2}\exp\left\{iq\ln[\sin^2(\theta/2)]\right\}\frac{\Gamma(1-iq)}{\Gamma(1+iq)} \\ F_1 &= \frac{i}{2}\sum_{k=0}^{\infty}(-1)^k[kD_k+(k+1)D_{k+1}]P_k(\cos\theta) \\ G_0 &= -iq\cot^2(\theta/2)F_0 \\ G_1 &= \frac{i}{2}\sum_{k=0}^{\infty}(-1)^k[k^2D_k-(k+1)^2D_{k+1}]P_k(\cos\theta) \end{aligned} \tag{2.49}$$

where Γ is the well known Gamma function and

$$D_k=\frac{e^{-i\pi k}}{k+iq}\frac{\Gamma(k-iq)}{\Gamma(k+iq)}-\frac{e^{-i\pi\rho_k}}{\rho_k+iq}\frac{\Gamma(\rho_k-iq)}{\Gamma(\rho_k+iq)},$$

with $\rho_k=\sqrt{k^2-(Z\alpha)^2}$, $\alpha=e^2/\hbar c$ and $q=Z\alpha/\beta$.

This has been evaluated numerically by numerous authors [McK48, Fe52, Do56, Sh56] some of whom [Fe69, Va74b] give detailed prescriptions for the evaluation. The series of 2.49 are very slowly converging for small angles, and a transformation due to Yennie *et al.* [Ye54] is often employed. This transformation, which can be applied to any Legendre series, $f(\theta)$, which is given by

$$f(\theta)=\sum_{l=0}^{\infty}A_lP_l(\cos\theta),$$

is derived from recursion relations for Legendre polynomials and yields for the transformed series

$$(1-\cos\theta)^m f(\theta)=\sum_{l=0}^{\infty}A_l^{(m)}P_l(\cos\theta),$$

in which the "reduced" coefficients are given by

$$A_l^{(m)}=A_l^{(m-1)}-\frac{l+1}{2l+3}A_{l+1}^{(m-1)}-\frac{l}{2l-1}A_{l-1}^{(m-1)}.$$

Vande Putte [Va74b] has evaluated the series of 2.49 for numerous elements with atomic numbers between 6 and 92 and for energies as low as 50 keV for angles from 10° to 179° and reports that only transformations employing $m=2$ and $m=3$ in

E (keV)	Z = 4	Z = 13	Z = 29	Z = 47	Z = 79
1	6.0	17.0	> 30.0	> 30	> 30
2	5.0	13.0	> 30.0	> 30	> 30
5	4.0	13.0	25.0	> 30	> 30
10	5.0	6.0	14.0	> 30	> 30
20	5.0	5.0	9.0	> 30	27.0
50	4.0	4.0	4.0	15.0	21.0

Table 2.2: Smallest Angle for Convergence of Mott Series for Transformation Order $m = 1$

double precision assure convergence in all instances. Felder reports similar results, but suggests that $m = 3$ be used for elements with $Z \leq 50$ and $m = 4$ for $Z > 50$. Results for the present work are somewhat different. Tables 2.2 through 2.4 show the smallest angle for which both the F_1 and G_1 series converge (to .01% using less than 500 terms) as a function of energy for different elements and for different values of m, the reduction transformation order. There was no convergence at angle less than 50° without transformation, and best convergence occurs using a second order transformation. It should be noted however that at small angles, where convergence is least likely, the constant terms are much greater than the series term, and so the error in the cross section due to the error in the series term is often small at very small angles. However, in some of the tests run in this work, at high Z materials and angles around 20°, the 500th term in the unconverged series was as large as 1% of the cross section, and so such unconverged results must be considered unreliable.

Because of the exact nature of the the above derivation (in the context of the use of unscreened potential, of course), this cross section is often used in electron

E (keV)	Z = 4	Z = 13	Z = 29	Z = 47	Z = 79
1	7.0	6.0	5.0	11.0	16.0
2	6.0	5.0	4.0	4.0	12.0
5	5.0	5.0	6.0	7.0	8.0
10	5.0	7.0	5.0	5.0	5.0
20	5.0	5.0	5.0	5.0	5.0
50	5.0	5.0	5.0	5.0	5.0

Table 2.3: Smallest Angle for Convergence of Mott Series for Transformation Order $m = 2$

E (keV)	Z = 4	Z = 13	Z = 29	Z = 47	Z = 79
1	17.0	16.0	19.0	26.0	> 30
2	15.0	16.0	13.0	20.0	> 30
5	18.0	16.0	16.0	17.0	28.0
10	22.0	17.0	15.0	15.0	14.0
20	15.0	15.0	17.0	18.0	16.0
50	20.0	18.0	16.0	16.0	16.0

Table 2.4: Smallest Angle for Convergence of Mott Series for Transformation Order $m = 3$

transport calculations. At large angles, when the screening effect is small, this cross section is expected to be quite accurate. At small angles, Berger has proposed a refinement to take screening into account. He multiples the unscreened exact Mott cross by a screening factor, $F_{scr}(\theta)$, given by the ratio of the screened to unscreened Rutherford cross section,

$$F_{scr}(\theta) = \frac{(1-\cos\theta)^2}{(1-\cos\theta+2\eta_s)^2} \tag{2.50}$$

To take into account the infinite value of unscreened cross sections at $\theta = 0$, Berger uses just the screened Rutherford cross section.

Several useful approximations may be employed in instances in which the unscreened exact cross section does not easily converge. Bartlett and Watson [Ba39] have devised an approximated expression for the solution for σ, applicable at small angles,

$$\sigma(\Omega)d\Omega = \frac{e^4Z^2}{p^2v^2}\frac{1+\frac{\pi\beta\alpha Z}{\sqrt{2}}\cos\gamma(1-\cos\theta)^{1/2}}{1-\cos\theta)^2}d\Omega. \tag{2.51}$$

The ratios between the value of this expression and results of the evaluation of 2.48 (using unconverged results as needed) were calculated and found to be within 1% of unity for all elements tested for angles as high as 30°, for energies less than 20 keV. At higher energies (in the 50 keV range), the deviations from unity of these ratios reach a few percent for all elements at angles greater than 20 degrees. In using this approximate cross section, the correction of 2.50 may be applied to account for screening.

Methods Employing Realistic Potentials

The obvious numerical difficulties in evaluating the Dirac exact cross section using realistic potentials are going to lie in determining the phase shifts. Many methods

have been tried, and they are summarized in early work of Mott and Massey [Mo49] supplemented by the excellent review of Walker [Wa70]. None of the techniques lead to closed form expressions for the cross section however, and typically only numerical results for particular elements at energies of interest to the various authors are presented in the literature, as in [Ya76] (using Thomas-Fermi potentials) and [Ak78a, Ko81a, Ko81b, Gu76, Ga79] (using Hartree potentials).

There does exist one accurate calculation of the elastic scattering cross section using a partial wave technique (performed by Riley *et al.*, [Ri75, Ri83]) which is universally applicable. They used a numerical integration scheme employing static potentials determined from Hartree-Fock wave functions reported in the literature. Fitted data is presented in the form

$$\sigma(Z,E,\theta) = \left(\frac{Z\alpha^2}{\gamma\beta^2}\right)^2 \sum_{m=1}^{4} A_m(Z,E)[1-\cos\theta+2B(Z,E)]^{-m} + \sum_{l=0}^{6} C_l(Z,E)P_l(\cos\theta) \tag{2.52}$$

in which α is the fine structure constant, γ is the dimensionless total energy $(1+E/mc^2)$, and the P_l's are Legendre polynomials. The coefficients A_m, C_l and B are tabulated at 9 energies between 1 and 256 keV for all elements with Z from 1–100.

Approximations inherent in the use of the static potential include the neglect of exchange effects (estimated to be negligible below 1 keV) and the assumption of an unpolarized atom. The error introduced by this second approximation has been estimated to be as high as a factor of 3 or 4 for high Z atoms at 1 keV and 0° scattering angle, but diminishing to a few percent at angles of around 10° [Be89].

2.2.5 Cross Sections Used by Previous Investigators

Many investigators have treated elastic scattering on an event by event basis. Table 2.5 summarizes the elastic scattering models used by various investigators.

Elastic Scattering Treatment	Monte Carlo Authors
σ_{Ruth}, Wentzel screening	Newbury *et al.* [Ne80] Bishop [Bi67] Špalek [Sp82] McDonald *et al.* [McD71] Proykova [Pr79] Shimizu *et al.* [Sh75] Newbury and Myklebust [Ne79a] Felsteiner [Fe83] Shimizu *et al.* [Sh76]
σ_{Ruth}, Wentzel/Nigam screening	Murata *et al.* [Mu79, Mu80] Murata, Kyser and Ting [Mu81] Murata *et al.* [Mu71] Sheldon and Ogilvie [She80] Matsukawa *et al.* [Ma73] Hawryluk *et al.* [Ha74]
σ_{Ruth}, Empirical Screening after Wen/Nig	Hamm *et al.* [Ha79] Shimizu [Shi80] Valkealahti and Nieminen [Va83] Adesida *et al.* [Ad78, Ad80]
First Born, Int. of Approx. $\rho(r)$, from DHFS potentials	Salvat *et al.* [Sa84b, Sa86]
σ_{Mott} [McK48], Moliére screening	Mæhlum and Stadsnes [Mæ67]
$\sigma_{Mott}/\sigma_{Ruth}\times$ Moliére screened σ_{Ruth} [Be63]	Terrisol and Patau [Ter78] Berger, Seltzer and Maeda [Be70]
PWEM, TFD Potentials [Ya76]	Shimizu *et al.* [Sh77] Ichimura *et al.* [Ic80] Shimizu *et al.* [Sh79]
PWEM from Akkerman *et al.* [Ak78a], Potentials from Green [Gr69]	Akkerman and Chernov [Ak80]
PWEM with fitted Hartree potentials	Kotera *et al.* [Ko81a]
PWEM with HF potentials, including crystalline effects, after Green [Gr76]	Kotera *et al.* [Ko81b]
PWEM, after Gunnarson [Gu76]	Valkealahti and Nieminen [Va84]
PWEM, Potentials from Smrčkra [Sm70]	Ganachaud and Cailler [Ga79]

Table 2.5: Single Elastic Scattering Treatments in Monte Carlo Electron Transport Codes

2.2.6 Summary of Available Experiments

A listing ordered alphabetically by author of the experiments suitable for the present evaluation process is given in table 2.6. It can not be assumed that every reported measurement has been surveyed. However, the recent paper by Herbák [He85] claims that very little work has been done recently (from 1975 – 1985) above 1 keV, Gupta and Rees [Gu75] claim to have a complete list of experiments employing energies from 100 – 625 eV for Ne, and Bromberg [Br74] purports to have completely summarized all noble gas experiments around 1 keV up to 1974, so it may be assumed with a fair degree of confidence that no major studies have been missed.

Most experiments employ either very thin foils, vaporized metals or volumes of noble gases. In general, data is scarce for lower energy electron incident on metal foils and higher energy electrons incident on gas samples.

2.2.7 Evaluations and Conclusions

Approximation for the various cross sections and there anticipated ranges of validity have been discussed in the course of explaining their source. The logical conclusion is that the partial wave cross sections developed through Dirac's formalism are the most accurate in *every* situation. Thus, even though it suffers from inaccuracies in its inherent assumptions, because of its inclusiveness with respect to elements and energies covered, the parameterization of Riley appears to be the best available source of accurate theoretical data. However, because screened Rutherford cross sections and First Born cross sections using Hartree potentials are used as well in standard kilovolt energy Monte Carlo electron transport calculations, both are evaluated here and compared to the screened partial wave results of Riley. The experiments of Kessler and Lindner and of Herbák *et al.* were selected for compar-

Authors	Element Z	Angles	Energies (keV)
Bienlein *et al.* [Bi59a]	79	40–150	155
Bienlein *et al.* [Bi59b]	29,47,58,79	120	120,155,209
	79	120	80–300
Chase and Cox [Ch40]	13	0–6, 30–120	50
Dougal [Do65]	79	20,30,45, 65	100–400
Herbák *et al.* [He85]	2,10,18	50–130	1, 2, 3
Hughes *et al.* [Hu32]	2	15–150	.025–.70
Hughes and McMillian [Hu33]	10	7–150	.010–.80
Jansen and de Heer [Ja76a]	36,54	5–55	.1–1
Jansen *et al.* [Ja76b]	2,7,10,18	5–55	.1–1
Keck [Ke62]	82	30–135	70
Kessler and Lindner [Ke65]	80	0–150	.2–4
Kessler and Weichert [Ke68]	80	45–135	46,79,100,204
Kinzinger [Ki53]	13,79	25–150	245
	13,79	120	150–400
Langstroth [La33]	13	70–160	8–20
Motz *et al.* [Mo63]	29,50,79	20–110	50,100,200,400
Pettus *et al.* [Pe56]	79	70–150	200
Rester and Rainwater [Re65]	13	30–150	100–3000
Saegusa and Kikuchi [Sa37]	28,47,78,79	30–110	10,20,30
Saunderson *et al.* [Sa41]	13,29,47,79	0–45	230

Table 2.6: Single Elastic Scattering Experiments

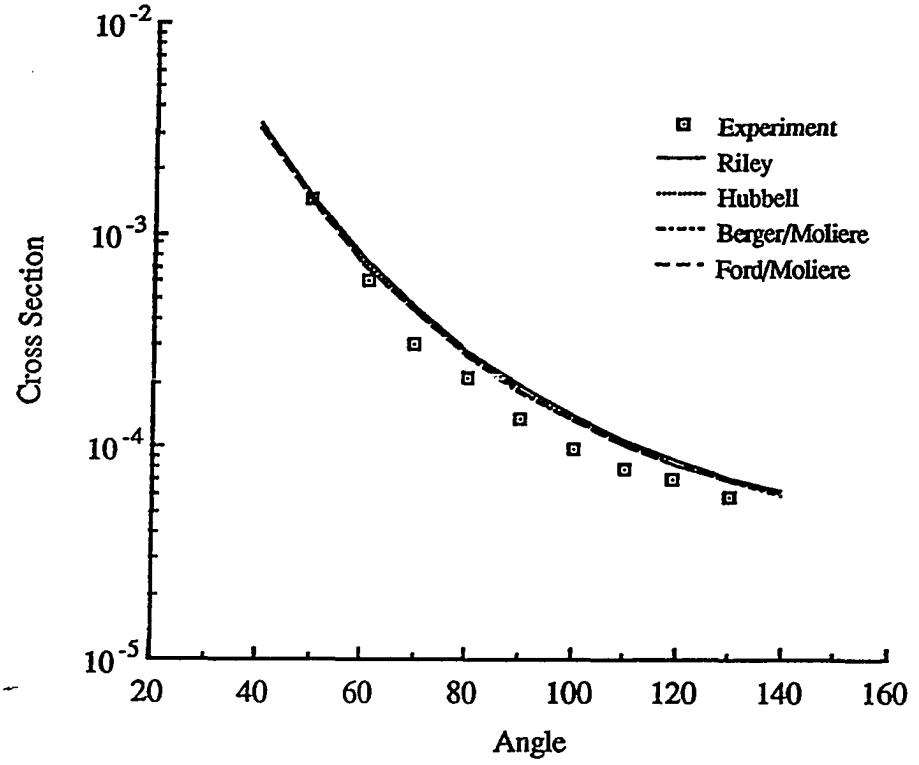

Figure 2.2: Elastic Scattering Cross Section Evaluation for Helium at 2 keV

ison with the calculations of Riley (screened Dirac partial wave), Berger (factored unscreened Dirac partial wave and Schrödinger first Born screening with Molière's Thomas-Fermi potentials), Hubbell (Schrödinger first Born screening with Hartree potentials), and Ford and Nelson (Schrödinger first Born screening with modified Molière Thomas-Fermi potentials). The results are shown in figures 2.2 through 2.4.

It is clear from the figures that for higher Z materials, only the partial wave results of Riley are adequate for all energies and angles. The problems in the Born approximation cross sections are exacerbated (by the use of the Born approximation for the Hubbell data and by inadequacies in the screening parameter determination

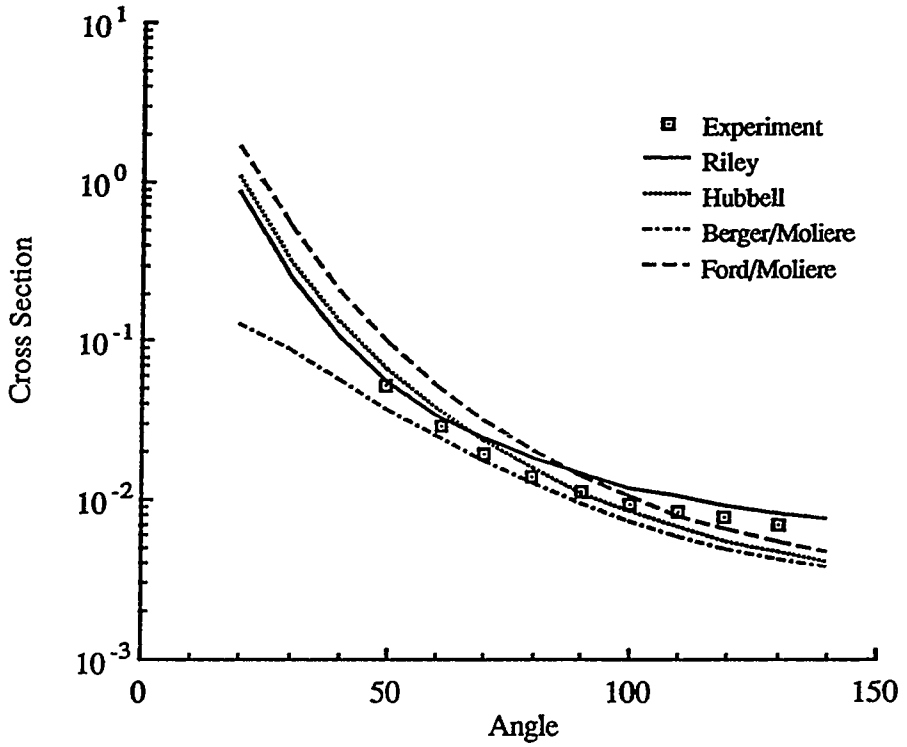

Figure 2.3: Elastic Scattering Cross Section Evaluation for Argon at 2 keV

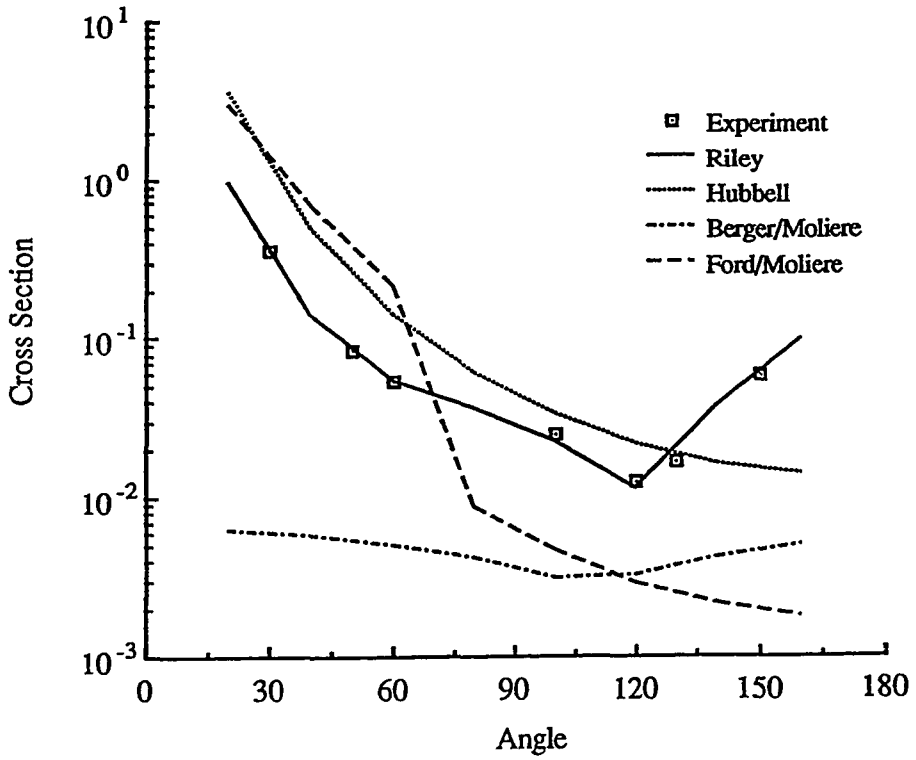

Figure 2.4: Elastic Scattering Cross Section Evaluation for Mercury at 4 keV

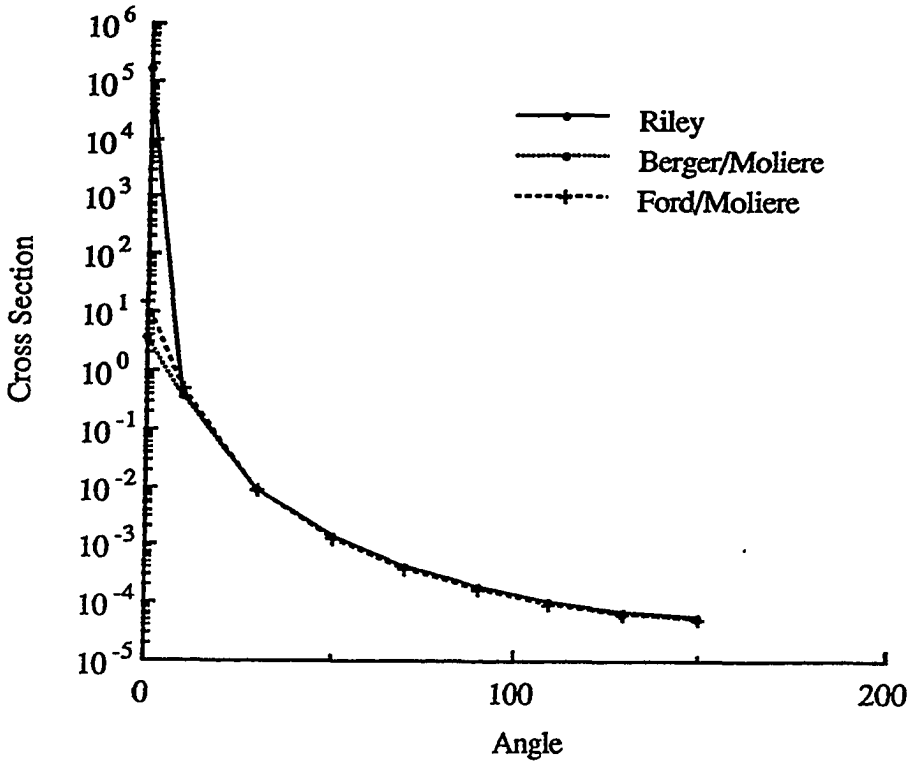

Figure 2.5: Elastic Scattering Cross Sections for Nickel at 30 keV

for the other cross sections) at small angles, and low energies, and high atomic numbers, as can be seen in figures 2.5 through 2.7.

The shape of the cross section (except at small angles) seems to be adequately modeled by all four of the formalisms over most of the energy and atomic number range of interest, so that as long as small angle partial wave data is available, more approximate cross sections can be used. Figure 2.8 shows the rough line dividing energy and atomic number into regions in which approximate cross sections adequately (to about 5%) determine the large angle scattering shape. The area below the curve represents regions requiring a relativistic partial wave cross section at all angles, and that above represents the regime in which approximate methods will suffice at large

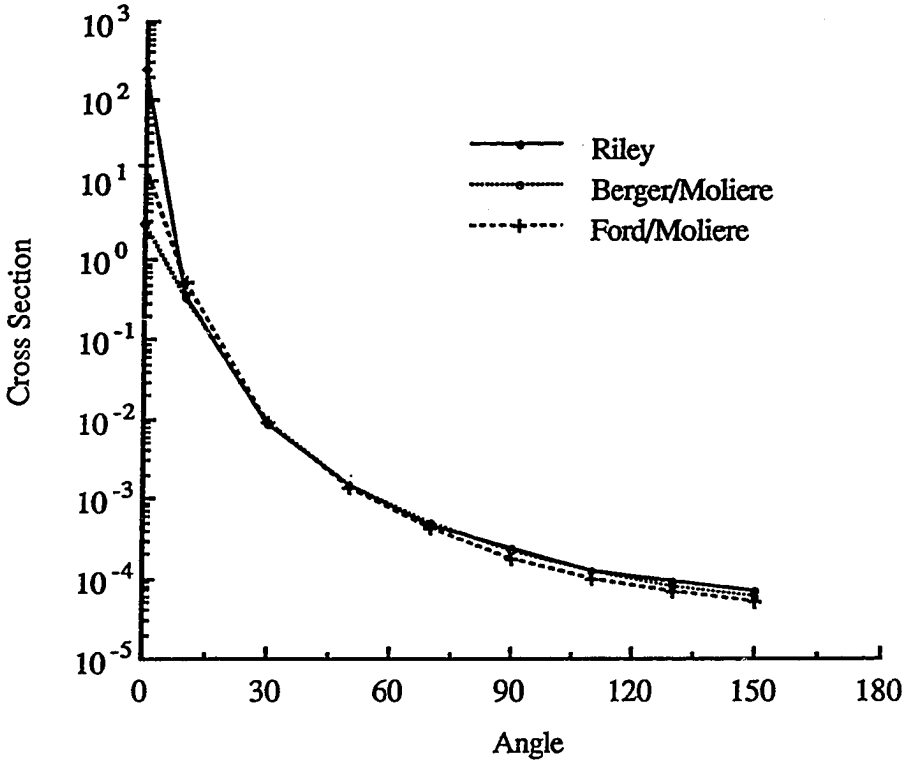

Figure 2.6: Elastic Scattering Cross Sections for Silver at 50 keV

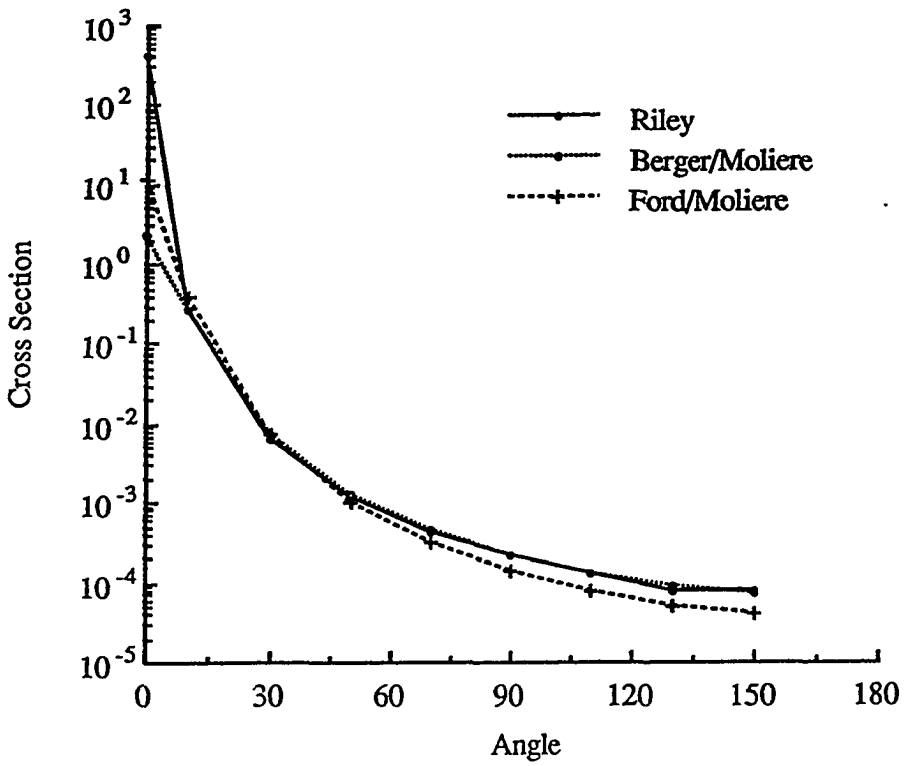

Figure 2.7: Elastic Scattering Cross Sections for Gold at 100 keV

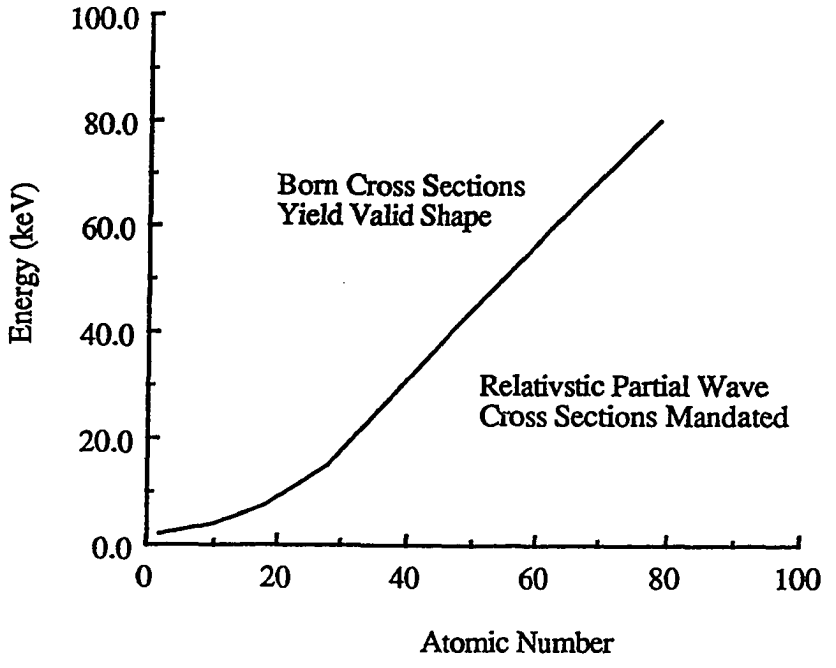

Figure 2.8: Region of Applicability of Approximate Cross Sections

angles.

2.3 Inelastic Scattering Cross Sections

The discussions in this section of this chapter concern inelastic collision processes, which have been grouped here as atomic excitations and ionizations, fast collisions with free electrons, and collective excitations of the conduction electron plasma. Because of the complexity of the problem (the collisions involve interactions with an ensemble of bound electrons), quantum mechanical cross sections for inelastic scattering for multiple electron atoms can generally be derived only in Schrödinger's formalism using the Born approximation. Thus a wide range of alternative descriptions have been employed, including classical scattering theory, the use of the Maxwell's equations (the Complex Dielectric Constant Method, CDCM) and even wholly empirical formulations. Often, distinct descriptions of the various inelastic processes are taken from different sources and then somehow combined in attempts to develop

models which provide complete representations of inelastic scattering. This last set of methods, which has found some degree of success, will be reviewed here also. Formulations describing interactions with bound (inner) electrons are presented first, followed by methods for describing collisions with free electrons.

2.3.1 Bound Electron Ionization and Excitation Cross Sections

In the excitation process, energy from an incident electron is transfer to the electrons of an atom permitting atomic electron rearrangement into one of numerous possible higher energy excited states. A perfect description of the process, suitable for a true analog Monte Carlo calculation, which would employ doubly differential cross sections for all final states, and so would be computationally cumbersome in transport simulations. Fortunately, in almost all Monte Carlo simulations, the exact state of the atom after the excitation does not need to be known, but rather only a weighted distribution of emergent energy (E') and angle (Ω') of the scattered electron averaged over all excitation collisions needs to be determined, as in

$$\sigma(E,E',\Omega')dE'd\Omega' = \sum_{all\ states\ n} \sigma_n^{ex}(E,E',\Omega')dE'd\Omega' \tag{2.53}$$

This it sufficient because the de-excitation which occurs subsequent to a typical excitation collision, and which is extremely dependent on the atomic electron configuration (this is discussed in chapter IV), does not usually give rise to secondary particles with energy of any consequence, and so can be ignored.

In ionization collisions, it happens that enough energy is transferred during the collision to liberate completely one of the target atomic electrons. Often, the ejected atomic electron can carry enough energy that its progress needs to be tracked in a Monte Carlo simulation. Also, if the transport problem requires that high energy de-excitation process be modeled, it is also important to know the subshell from

which the electron has been ejected, as vacancies in the inner shells of high Z atoms contain enough energy to emit energetic particles. Thus our ideal model of ionization is a cross section differential in scattering angle and energy loss for both the incident and ejected electrons for each subshell nl as a function of incident electron energy,

$$\sigma_{nl}^{ion}(E_1, E_1', E_2', \Omega_1', \Omega_2')dE_1'dE_2'd\Omega_1'd\Omega_2'.$$

It is clear that ionization collisions are a subset of excitation collisions, those in which in its final state, the atom contains a vacancy in one of its shells. We now examine the various attempts which have been made at describing this process.

Bethe-Born Theory

The only framework in which successful calculations of cross sections for inelastic scattering from multiple electron atoms have been made is given by Bethe [Be30] in his general theory of inelastic collisions. A fine review, the relevant highlights of which are presented here, was given by Inokuti [In68] and by Fano [Fa64]. The discussion begins by considering a general inelastic collision as the perturbation of the ground state of an atom, whose wave function is given by

$$\psi_0(\mathbf{r}_1, \mathbf{r}_2, \ldots, \mathbf{r}_Z)$$

where the r's refer to the positions of the atomic electrons, leading to some quantifiable final state labeled n, described by

$$\psi_n(\mathbf{r}_1, \mathbf{r}_2, \ldots, \mathbf{r}_Z).$$

In Schrödinger's formalism, the description of the inelastic scattering of an electron by an atom is given by

$$\sigma_n d\Omega = \frac{m^2c^4}{4\pi^2\hbar^4}\frac{k'}{k}\left|\int e^{i\mathbf{K}\cdot\mathbf{r}}\psi_n^* V \psi_0 d\mathbf{r} d\mathbf{r}_1 \ldots d\mathbf{r}_Z\right|^2 d\Omega \qquad (2.54)$$

in which

$$V = -\sum_{j=1}^{Z} \frac{e^2}{|\mathbf{r} - \mathbf{r}_j|} + \frac{Ze^2}{r}.$$

Performing all the integrals over $\mathbf{r}$ using

$$\int \frac{e^{i\mathbf{K}\cdot\mathbf{r}}}{|\mathbf{r} - \mathbf{r}_j|} = \frac{4\pi}{K^2} e^{i\mathbf{K}\cdot\mathbf{r}_j}$$

yields

$$\sigma_n d\Omega = \frac{4m^2c^4e^4}{\hbar^4 K^4} \frac{k'}{k} |\epsilon_n(\mathbf{K})|^2 \, d\Omega \tag{2.55}$$

in which $|\epsilon_n(\mathbf{K})|^2$ is defined as

$$|\epsilon_n(\mathbf{K})|^2 = \int \psi_n^* \sum_{j=1}^{Z} e^{i\mathbf{K}\cdot\mathbf{r}_j} \psi_0 d\mathbf{r}_1 \ldots d\mathbf{r}_Z$$

and is called the inelastic scattering form factor, directly analogous to the elastic form factor. Inokuti notes that under the usual assumptions often made at this point regarding spherical symmetry, degenerate states and others that ϵ_n becomes a function of scalar K, and that $d\Omega = 2\pi \sin\theta d\theta = \pi/kk' \, d(K^2)$, so that if the variable $Q = (\hbar K)^2/2m$ is introduced, the expression for σ_n reduces to

$$\sigma_n dQ = \frac{2\pi e^4}{mv^2} |\epsilon_n(K)|^2 \frac{dQ}{Q^2}. \tag{2.56}$$

Often, the contribution from all states n are summed to yield

$$\sigma dQ = \frac{2\pi e^4}{mv^2} S(K) \frac{dQ}{Q^2}, \tag{2.57}$$

which contains the common substitution

$$S(K) = \sum_n |\epsilon_n(K)|^2, \tag{2.58}$$

where S is referred to as the inelastic scattering function. Thus it is seen that as in the case of elastic scattering, devising inelastic cross sections becomes a problem of evaluating a factor determined by the dynamics of the atom.

One simple approach is to assume that the scattering function S is simply related to the form factor F, by

$$S(K) = Z - \frac{F^2(K)}{Z}. \tag{2.59}$$

Schnatterly [Sc79] has proposed using the results derived for F with a Wentzel exponential screened potential to yield an expression for the total cross section. Salvat and Parallada [Sa84a, Sa84b] have also used the above approximation.

Bethe introduced the concept of the generalized oscillator strength, $f_n(K)$, given by

$$f_n = \frac{E_n}{Q} |\epsilon_n(K)|^2, \tag{2.60}$$

where E_n is the energy above the ground state energy of the n^{th} state. We eventually arrive at

$$\sigma_n dQ = \frac{2\pi e^4}{mv^2} f_n \frac{dQ}{QE_n} \tag{2.61}$$

where f_n is the generalized oscillator strength for the state n, and these oscillator strengths are constrained by the rule that their sum over all possible states is given by Z. In principle, if all states can be specified and all oscillator strengths determined, Bethe's first Born theory would completely describe inelastic collisions. Tables of such quantities have recently been compiled for certain well studied atoms, but general tables are not yet available. Programs for calculating the oscillator are also available, but require substantial *a priori* knowledge of the most probable final state electron configurations. This definition of the cross section finds its greatest utility in serving as the basis for integrals for the total cross section and average energy loss, as will be seen it chapter III. One last note, Fano [Fa64] has has shown that the relativistic version of this formalism leads to as expression for σ_n of

$$\sigma_n dQ = \frac{2\pi e^4 Z}{mv^2} \left\{ \frac{|\epsilon_n(K)|^2}{Q^2(1+Q/2mc^2)^2} + \frac{|\beta_t G_n(K)|^2}{[Q(1+Q/2mc^2)-(E_n-E_0)^2/2mc^2]^2} \right\} \left(1 + \frac{Q}{mc^2}\right) dQ. \tag{2.62}$$

in which the second term described the contribution to the cross section due to virtual photon exchange. Like $|\epsilon_n(K)|^2$, $|\beta_t G_n(K)|^2$ can be expressed as a function of the generalized oscillator strength, and formalisms using this expression almost always involve the integration over Q, as discussed in the next chapter.

Ionization Cross Sections in the Born Approximation Many authors have investigated the scaling of the total ionization cross section with Z and E, first examined analytically by Mott and Massey [Mo49] who integrated the Bethe-Born cross section over all ionization energy transfers. Most of the later works, which have been summarized by Powell [Po76a, Po76b], yield semi-empirical expressions following the general form of the Mott and Massey result,

$$\sigma_s \sim A_s \frac{Z_s B_s \ln(C_s E)}{I_s^2 E}, \tag{2.63}$$

in which the subscript s implies a given subshell, I is the binding energy of the shell, A, B, and C are constants, Z_s is the number of electrons in the subshell and E the incident energy. Some of these formulations have been used in Monte Carlo calculations, with the most detailed study being that of Newbury and Myklebust [Ne79b].

Arthurs and Moiseiwitsch [Ar58] have used relativistic Born approximation wave functions to describe the incident and target electrons in their determination of total cross sections for the ionization of K shells. They expect their results to be applicable at low atomic numbers, since they use the approximation of Møller (valid for outer, unbound electrons, as discussed later in this chapter), which assumes that the effective screened nuclear charge is small. They arrive at

$$\sigma_K = \pi a_0^2 \frac{S(E/E_K)(\gamma\alpha)^2}{Z_e^2(\gamma^2 - 1)} \tag{2.64}$$

E/E_K	2.5	5.0	7.5	10.0	15.0	20.0
$S(E/E_K)$	5.4	10.1	12.1	13.2	14.8	15.6

Table 2.7: Arthur and Moiseiwitsch S Function Data

in which a_0 is the Bohr radius; α the fine structure constant; $\gamma^2 = 1/(1-\beta^2)$; Z_e the effective nuclear charge, given by $Z-0.3$ for K shells; and $S(E/E_K)$ is interpolated from the data given in table 2.7.

Kolbenstvedt [Ko67] treats ionizations by dividing the cross section into large and small impact parameter sections, using a slight modification of Møller's theory for the close collisions and for distant collisions a method suggested by Williams [Wi35] in which large impact parameter electron ionizations are assumed to emanate from virtual photon photo-ionizations, and so

$$\sigma_i = \int_{E_i}^{k_0} \sigma_{pe}(k) N(k) dk, \tag{2.65}$$

in which $\sigma_{pe}(k)$ is the photo-ionization cross section for a photon of energy k, $N(k)$ is the virtual photon spectrum for the passing electron and k_0 the maximum virtual photon energy. Using an expression for $N(k)dk$ from Jackson [Ja62], Kolbenstvedt obtains for the distant collision K shell cross section

$$\sigma_K = \frac{0.275}{\tau_1} \frac{(\tau_2+1)^2}{\tau_2(\tau_2+2)} \left[\ln \frac{1.19\tau_2(\tau_2+2)}{\tau_1} - \frac{\tau_2(\tau_2+2)}{(\tau_2+1)^2} \right], \tag{2.66}$$

with σ in barns and τ_1 and τ_2 as before. In this work, Kolbenstvedt's results are applied to shells outside the K shell by using the appropriate binding energy and scaling by the number electrons in the outer shells.

Seltzer [Se89] determines a differential ionization cross section (given by the integrand in equation 2.65) for distant collisions using this same technique, taking for

$N(K)$ an expression from [Ja75] which is integrated over all impact parameters and given in terms of Bessel functions of the first kind of order 0 and 1 and the minimum and maximum impact parameters. He uses calculated values of the subshell orbital radii for the minimum impact distances and semi-classical expression for the maximum impact parameters values. Like Kolbenstvedt, he uses a modified version of Møller's free electron cross section to describe close collisions.

Parameterizations of Born Approximation Ionization Cross Section Data

Scofield [Sc78] has published a parameterized fit for the total cross sections for the K and L-I through L-III subshells for several elements, using Hartree wave functions to describe the atomic electrons. His data is of the form

$$\sigma = \frac{A}{\beta^2}\left(B + b_1 + \frac{b_2}{W'} + \frac{b_3}{(p')^2} + \frac{Bb_4}{p'} + \frac{b_5}{(p')^4}\right) \tag{2.67}$$

where W is the electron total energy and the primes imply that the quantities are normalized by either mc^2 or mc, as appropriate. A and $b_1 \ldots b_5$ are the subshell and element dependent parameters, and B is taken from

$$B = \ln(p')^2 - \beta^2.$$

This parameterization can be used in conjunction with interpolation and extrapolation to provide a set of total cross section values for the inner shells of atoms.

Lotz [Lo70] has devised a parameterization for the ionization cross section of the i^{th} subshells of the form

$$\sigma_i = a_i q_i \frac{\ln(E/E_i)}{EE_i}\{1 - b_i \exp[-c_i(E/E_i - 1)]\} \tag{2.68}$$

in which q_i is the number of equivalent electrons in the subshell, E_i the binding energy, and a_i, b_i and c_i subshell dependent constants.

Pressa and Newell [Pr70] have re-evaluated Lotz's constants and applied a relativistic correction factor of the form

$$F_{rel} = F(v)/f(v) \tag{2.69}$$

in which $F(v)$ and $f(v)$ represent relativistic and non-relativistic Coulomb velocity distributions describing the dynamics of the electron-electron collision and can be given by

$$F(v) = \frac{\tau_1}{\tau_2}\left(\frac{2+\tau_1}{2+\tau_2}\right)\left(\frac{1+\tau_2}{1+\tau_1}\right)^2\left[\frac{(1+\tau_2)^2}{(1+\tau_2)^2+\frac{\tau_1}{\tau_2}\frac{2+\tau_1}{2+\tau 2}\left(\frac{1+\tau_2}{1+\tau_1}\right)^2}\right]^{3/2} \tag{2.70}$$

and

$$f(v) = \frac{\tau_1}{\tau_2}\left(\frac{\tau_2}{\tau_1+\tau_2}\right)^{3/2} \tag{2.71}$$

in which τ_1 is the shell binding energy divided by the electron rest mass and τ_2 the incident electron energy divided by mc^2. For the values of the constants in 2.68, Pressa and Newell give the values shown here in table 2.8.

Excitation Cross Sections in the Born Approximation Streitwolf [St59] has derived an expression for excitation energy losses in the first Born formalism. He arrives at

$$\begin{aligned} \sigma(\Delta E = E_F)d(\Delta E) &= \frac{.34\pi e^4}{EE_F^2} \\ \sigma(\Delta E \neq E_F)d(\Delta E) &= \frac{\pi e^4}{E(\Delta E - E_F)^2,} \end{aligned} \tag{2.72}$$

in which E_F is the Fermi level energy. It is obvious that a discontinuity exists in this cross section at energy transfers near the Fermi level. Shimizu [Sh76] has proposed a method to remove this anomaly. He assumes that the maximum is the cross section is found at energy transfers equal to the Fermi level energy, and notes that at an

Subshell	a_i	b_i	c_i
	(10^{-14} cm^2 eV^2)		
K	4.0	0.75	0.50
L_1	4.0	0.50	0.60
$L_{2,3}$	2.6	0.92	0.19
M_1	4.0	0.30	0.60
$M_{2,3}$	4.0	0.60	0.40
N_1	4.0	0.00	0.00
$M_{4,5}$	1.4	0.96	0.13
$N_{2,3}$	4.0	0.50	0.50
$N_{4,5}$	2.0	0.94	0.15
$N_{6,7}$	1.0	0.97	0.11

Table 2.8: Pressa and Newell Parameters

energy transfer of $2.715E_F$, the lower expression in 2.72 yields the same value for the differential cross section as the upper expression maximum, $.34\pi e^4/EE_F^2$. He therefore proposes that the cross section be assumed to be constant over the energy transfer range $E_F \leq \Delta E \leq 2.75E_F$, yielding a total cross section for this distribution given by

$$\sigma_t = \frac{\pi e^4}{E}\left(\frac{1.1662}{E_F} - \frac{1}{\Delta E_{max} - E_F}\right). \tag{2.73}$$

Several authors have used this expression in Monte Carlo calculations, despite the fact that functionally it is little different from other, simpler expressions (as seen later) and that it has one major disadvantage in that the cross section for energy transfers near the Fermi energy is quite high, so that a lot of Monte Carlo time is spent processing low loss events [Sh76].

Classical Binary Encounter Theories

The treatment of excitations as a classical two body collision between an incident electron and an atomic electron has been extremely successful. In a series of articles subsequent to his initial broaching of the subject, Gryzinski [Gr65a, Gr65b, Gr65c] first derived general, exact expressions for differential cross sections in two body collisions, exact expressions for cross sections in two body Coulomb interactions, and finally approximate expressions for the application of inelastic scattering. Approximations are made in considering that other atomic electrons and nuclei have no effect on the collision, and that the exact distribution of atomic velocities are unknown. Starting with a 'field' particle (target) with initial velocity $\mathbf{v}_1$ and a 'test' particle (projectile) with velocity $\mathbf{v}_2$, Gryzinski defines geometry variables θ, Θ, φ and D which describe the orientation of the initial trajectories and the line segment representing the distance of closest approach had there been no collision. Using the

appropriate conservation laws he then derives expressions for the state change variables of the projectile $(\Delta E, \vartheta, \phi)$ and the target $(\widetilde{\Delta E}, \tilde{\vartheta}, \tilde{\phi})$ in terms of the geometric variables and the center of mass system scattering angle, which contains all of the dependence on the scattering field. He then shows that the cross section for interaction can be expressed in terms of the geometric variables

$$\sigma(\theta, \Theta, \varphi, D) = \frac{|\mathbf{v}_2 - \mathbf{v}_1|}{|\mathbf{v}_2|} f(\theta, \varphi)\, d\theta d\varphi \frac{d\Theta}{2\pi} 2\pi D dD \tag{2.74}$$

where $f(\theta, \varphi)d\theta d\varphi$ represents the probability that the components of the target particle velocity will be described by θ and φ. If we let u and $f_u(\theta, \Theta, \varphi, D)$ represent a state change variable and the function describing it, the expressions for the cross sections differential in u will be given the integral over the geometric variable space in those regions for which $u = f_u(\theta, \Theta, \varphi, D)$. Defining $h_u(\theta, \Theta, \varphi, D) = u - f_u(\theta, \Theta, \varphi, D)$, Gryzinski arrives at the exact (for a strictly two body collision), general expression

$$\sigma(u) = \int\int\int\int \frac{|\mathbf{v}_2 - \mathbf{v}_1|}{|\mathbf{v}_2|} f(\theta, \varphi)\delta[h_u(\theta, \Theta, \varphi, D)] d\theta d\varphi \frac{d\Theta}{2\pi} 2\pi D dD \tag{2.75}$$

where u represents any of the dynamical variables. Although cross sections differential in energy and angle can be derived form this expression, the quantity of most interest is the cross section differential in energy exchange. Gryzinski integrates 2.75 over φ, Θ and D (after a change of variables to the c.m. scattering angle) to obtain for the case of electron - electron scattering

$$\sigma(\Delta E) = \frac{\pi e^4}{\Delta E^2 E_1} \int_{\theta_{min}(\Delta E)}^{\theta_{max}(\Delta E)} f_V \left[1 - 2\frac{E_1}{\Delta E}\sin^2\theta\right] f(\theta) d\theta \tag{2.76}$$

where

$$f_V = \left(\frac{v_1}{v_2}\right)^2 \left(\frac{v_2^2}{v_1^2 + v_2^2 + 2v_1 v_2 \cos\theta}\right)^{3/2}$$

and the integration limits are determined from the kinematic relation between the orientation angle θ and the energy transfer ΔE. Note that E_1 represents the average kinetic energy of the target electron.

Approximations concerning the velocity distribution (both the speed and orientation) of the atomic electron must now be introduced, and Gryzinski presents results for several cases. The simplest case is obviously the situation of targets at rest. For this Gryzinski derives

$$\sigma(\Delta E) = \frac{2\pi e^4}{m_e v_2^2} \frac{1}{(\Delta E)^2}. \tag{2.77}$$

For the case of isotropically oriented field particles Gryzinski derives

$$\begin{aligned} \sigma(\Delta E) &= \frac{\pi e^4}{(\Delta E)^2} \left(\frac{v_1}{v_2}\right)^2 \left(\frac{4}{3} + \frac{|\Delta E|}{E_1}\right) && \text{if } 0 \leq -\Delta E \leq E_2 - E_1 \\ &= \frac{\pi e^4}{(\Delta E)^2} \left(\frac{v_2}{v_1}\right)^2 \left(\frac{4}{3} - \frac{1}{3}\frac{|\Delta E|}{E_2}\right) \sqrt{1 - \frac{|\Delta E|}{E_2}} && \text{if } E_2 - E_1 \leq -\Delta E \leq E_2 \end{aligned} \tag{2.78}$$

Both of these results are commonly used in Monte Carlo calculations and are of the same rough $1/(\Delta E^2)$ form encountered in many scattering theories. At this point Gryzinski departs from analytically evaluating the exact expression 2.76 with unrealistic velocity distributions and instead reduces 2.76 using approximations for the dependencies of f_V on θ and θ_{min} and θ_{max} on ΔE. This yields the result

$$\sigma(\Delta E) = \frac{\pi e^4}{(\Delta E)^3} \left(\frac{v_1}{v_2}\right)^2 \left(\frac{v_2^2}{v_2^2 + v_1^2}\right) \left[\frac{\Delta E}{E_1}\left(1 - \frac{E_1}{E_2}\right) + \frac{4}{3}\right] \left(1 - \frac{\Delta E}{E_2}\right)^{E_1/(E_1+\Delta E)} \tag{2.79}$$

The final stage in Gryzinski's development of the classical theory toward realistic situations involves applying the above formulation to the case of field particles distributed in velocity by noting that

$$(\sigma(\Delta E))_{AVE} = \int_0^\infty \sigma(\Delta E, v_1) f(v_1) dv_1.$$

He derives

$$(\sigma(\Delta E))_{AVE} = \frac{\pi e^4}{(\Delta E)^3}\left(\frac{v_1}{v_2}\right)^2\left(\frac{v_2^2}{v_2^2+v_1^2}\right)\left[\frac{\Delta E}{E_1}\left(1-\frac{E_1}{E_2}\right)+\frac{4}{3}\ln\left(2.7+\left(\frac{E_2-\Delta E}{E_1}\right)^{1/2}\right)\right]\left(1-\frac{\Delta E}{E_2}\right)^{E_1/(E_1+\Delta E)} \quad (2.80)$$

which is the most widely used (in Monte Carlo calculations) form of his theory.

Gryzinski now determines the total cross section and stopping power, or average energy loss per unit path, given by

$$\sigma_{tot} \equiv \int_{-\Delta E_{min}}^{-\Delta E_{max}} \sigma(\Delta E)\, d(\Delta E)$$

and

$$\frac{dE}{dx} \equiv n_e \int_{-\Delta E_{min}}^{-\Delta E_{max}} \sigma(\Delta E)\Delta E\, d(\Delta E)$$

respectively, were n_e is the number density of atomic electrons, for each of the cross sections expressions which he has derived. For the case of target electrons at rest but bound in some configuration so that there is a minimum excitation energy U he finds

$$\sigma_{tot} = \frac{2\pi e^4}{m_e v_2^2}\frac{1}{U}\left(1-\frac{U}{E_2}\right), \quad (2.81)$$

and

$$\frac{dE}{dx} = n_e \frac{2\pi e^4}{m_e v_2^2}\ln\frac{E_2}{U}. \quad (2.82)$$

For the case of isotropically distributed field particle velocities, he derives

$$\begin{aligned} \sigma_{tot} &= \frac{\pi e^4}{U^2}\frac{2}{3}\frac{v_2}{v_1}\left(1-\frac{U}{E_2}\right)^{3/2} && \text{if } E_2 \le E_1+U \\ &= \frac{\pi e^4}{U^2}\left(\frac{v_1}{v_2}\right)^2\left[\frac{2}{3}+\frac{U}{E_1}\left(1-\frac{U}{E_2-E_1}\right)\right] && \text{if } E_2 \ge E_1+U \end{aligned} \quad (2.83)$$

and

$$\frac{dE}{dx} = n_e \frac{\pi e^4}{U}\left(\frac{v_2}{v_1}\right)^2 \left[\frac{4}{3}\left(1+\frac{U}{2E_2}\right)\left(1-\frac{U}{E_2}\right)^{1/2} - \frac{U}{E_2}\ln\frac{1+(1-U/E_2)^{1/2}}{1-(1-U/E_2)^{1/2}}\right] \quad \text{if } E_2 \le U+E_1$$

$$= n_e \frac{\pi e^4}{U}\left(\frac{v_1}{v_2}\right)^2 \left[\frac{4}{3}\left(1-\frac{U}{E_2-E_1}\right)+\frac{U}{E_1}\ln\frac{E2-E_1}{U} + \frac{U}{E_1}\left(\frac{E_2}{E_1}\right)^{1/2}\left(\frac{4}{3}\frac{E_2}{E_2-E_1}+\frac{2}{3}-\left(\frac{E_2}{E_1}\right)^{1/2}\ln\frac{1+(E_1/E_2)^{1/2}}{1-(E_1/E_2)^{1/2}}\right)\right] \quad \text{if } E_2 \ge U+E_1 \tag{2.84}$$

For the case of distributed velocity field particles he derives

$$\sigma_{tot} = \frac{\pi e^4}{U^2}\left(\frac{v_1}{v_2}\right)^2\left(\frac{v_2^2}{v_2^2+v_1^2}\right)\left[\frac{U}{E_1}+\frac{2}{3}\left(1-\frac{U}{2E_2}\right)\times \ln\left(2.7+\left(\frac{E_2-U}{E_1}\right)^{1/2}\right)\right]\left(1-\frac{U}{E_2}\right)^{1+E_1/(E_1+U)} \tag{2.85}$$

and

$$\frac{dE}{dx} = n_e \frac{\pi e^4}{U^2}\left(\frac{v_1}{v_2}\right)^2\left(\frac{v_2^2}{v_2^2+v_1^2}\right)\left[\frac{U}{E_1}\left(1-\frac{E_1}{E_2}\right)\ln\frac{E_2}{U} + \frac{4}{3}\left(1-\frac{U}{E_2}\right)\ln\left(2.7+\left(\frac{E_2-U}{E_1}\right)^{1/2}\right)\right]\left(1-\frac{U}{E_2}\right)^{E_1/(E_1+U)} \tag{2.86}$$

Usually, Monte Carlo authors assume that the minimum excitation energy U and the average kinetic energy of the orbital electrons can be taken to be equivalent and given by the shell binding energy, E_b. This, however, leads to numerically incorrect results at E_2 near E_b, in that the value of the total cross section section derived for 2.85 does not equal the value of a numerical integration from E_b to E_2 of the differential cross section of 2.80. Differences between a numerical integration and 2.85, which are dependent only upon the ratio of E_2/E_b, are shown in figure 2.9.

Physically, the approximation of $U = E_b$ is equivalent to limiting the cross section to ionization collisions, and assuming $E_1 = E_b$ is valid for large E_2, so the cross section should be good for ionizations at high incident energies. When this cross

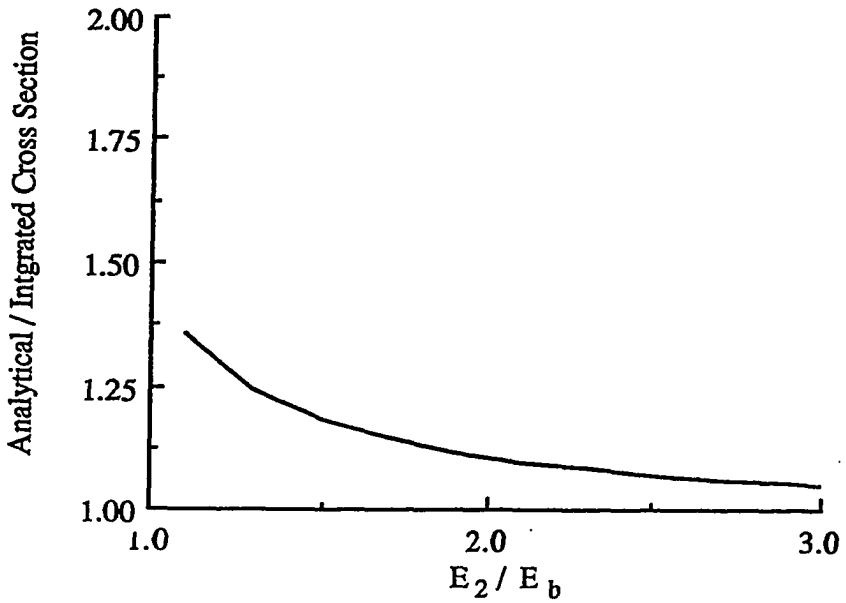

Figure 2.9: Error in Gryzinski's Total Cross Section near E_b

section is used as an excitation cross section, U, the minimum loss is set equal to roughly the Fermi energy, regardless of the subshell [Ter78]. It appears as though this cross section has been often misapplied, either by the author assuming the ionization cross section suffices to describe all inelastic collisions [Ad80], or by the author using the minimum energy loss as the orbital electron average [Sh76].

Pressa and Newell have suggested that their relativistic correction (equation 2.69) be applied to Gryzinski's results, and along similar lines, Gryzinski has amended his own work by employing a 'free fall' model of the atom [Gr86], with which he derives a total cross section of the form

$$\sigma_i = \frac{\pi e^4}{U^2} \frac{1}{(\sqrt{\lambda^2+k}+1)^2} \left[1+\frac{2}{\sqrt{\lambda^2+k}}+\frac{2}{3}\left(1+\frac{1}{\lambda^2}\right)\right]\left(1-\frac{1}{\lambda^2}\right) \qquad (2.87)$$

in which $\lambda \sim E/E_b$ and $k = W/I_{min}$ in which I_{min} is the minimum ionization potential and W the average binding energy for a given shell, with a 'shell' defined

as all occupancy levels with the same angular momentum quantum number. This result is not examined here, because of the lack of data for spin dependent subshell binding energies.

Angular deflections from collisions described by the classical model are almost always modeled in the binary collision approximation, and the distribution is taken from

$$\sin^2\theta = \frac{\Delta E}{E_2}. \tag{2.88}$$

Differential Inverse Mean Free Path from Complex Dielectric Constant Method

If a condensed material can be considered as a gas of electrons with a spatially dependent charge distribution, the differential inverse mean free path (DIMFP) can be deduced from Maxwell's equations as a function of the complex dielectric constant. This technique is commonly called the complex dielectric constant method (CDCM). The DIMFP differs from a cross section conceptually in that it is derived for the medium as a whole and only in approximation is it reduced to a cross section per atom, whereas a microscopic cross section is derived per atom, and only in the approximation of ignoring the effects of surrounding atoms can it be applied as an inverse mean free path for a condensed media. This technique was pioneered by Ritchie, Tung, Ashley and co-workers [Ri59, As79, Tu79], who show that the differential mean free path $\tau(\hbar\omega, E)$, which is a function of the electron $\hbar\omega$ is given in the first Born approximation by

$$\tau(E,\hbar\omega) = \frac{2e^2}{\pi\hbar^2 v^2}\int_{k_-}^{k_+}\frac{dk}{k}\mathrm{Im}\left[\frac{-1}{\epsilon(k,\omega)}\right] \tag{2.89}$$

in which $\hbar k$ is the momentum transfer and $\hbar\omega$ the energy transfer, $\epsilon(k,\omega)$ the dielectric response of the media and the integration limits are given by

$$k_{\pm} = \sqrt{2m}(\sqrt{E} \pm \sqrt{E - \hbar\omega}).$$

The main problem with this method arises in the selection of the proper form of the dielectric response function. The only extant calculations are those made for particular solids for particular applications, and require that atomic electron wave functions be determined. No simple, closed form expressions universally applicable are available in the literature, and so despite the success of this technique in predicting average energy losses for low energy electrons in certain media, its application was not pursued in this work.

Empirical Methods for Total Excitation Distributions

Several empirical models have been employed in attempts to model single collision energy losses. The most obvious candidate model is one which is based on the leading $1/(\Delta E)^2$ term in the free electron scattering and the classical binary encounter, in which the energy loss is proportional to $1/\Delta^2$, as in

$$f(\Delta E) = \frac{K}{(\Delta E)^2}. \tag{2.90}$$

The constant K can be determined from the need to normalize $f(\Delta E)$, and is given by

$$K = \frac{\Delta E_{max} \cdot \Delta E_{min}}{\Delta E_{max} - \Delta E_{min}}. \tag{2.91}$$

The total mean free path for collisions described by such an energy loss density function is usually taken as

$$\lambda_t = \overline{\Delta E} \cdot \left|\frac{dE}{dx}\right|^{-1} \tag{2.92}$$

in which $\overline{\Delta E}$ is the average energy loss per collision, easily seen to be given by

$$\overline{\Delta E} = \frac{\Delta E_{max} \cdot \Delta E_{min}}{\Delta E_{max} - \Delta E_{min}} \ln \frac{\Delta E_{max}}{\Delta E_{min}}$$

and $\left|\frac{dE}{dx}\right|$ is energy loss per pathlength, discussed in the next chapter. Note that this model retains some consistency with the physics, in that the stopping power, given by

$$-\frac{dE}{dx} = \int_{\Delta E_{min}}^{\Delta E_{max}} \Sigma(\Delta E)\, \Delta E\, d(\Delta E) \tag{2.93}$$

is preserved.

Another often used expression assumes an exponential distribution of losses, $K_1 e^{-\Delta/K_2}$. Again, the total cross section and the normalization constants are taken so that the mean energy loss per unit pathlength is consistent with experimental values. If I is the average ionization potential (discussed in the next chapter) then the normalized density function is given by

$$f(\Delta E) = \frac{1}{I} \frac{e^{-\Delta E/I}}{e^{-\Delta E_{min}/I} - e^{-\Delta E_{max}/I}} \tag{2.94}$$

and the average energy loss is given by

$$\overline{\Delta E} = \frac{(\Delta E_{min} + I)e^{-\Delta E_{min}/I} - (\Delta E_{max} + I)e^{-\Delta E_{max}/I}}{e^{-\Delta E_{min}/I} - e^{-\Delta E_{max}/I}} \tag{2.95}$$

The upper energy loss limit is usually taken to be $\Delta E_{max} = E$, and the lower limit some energy near the Fermi level. Liljequist [Li78a, Li78b] suggests 7 eV. These expressions have the drawback that they provide no information about the shell with which the collision took place, and so can not be used to predict vacancies in inner shells or the energy of ejected electrons.

2.3.2 Cross Sections for Free and Valence Electron Scattering

In many electron atoms, the outer electrons can be so loosely bound that they are considered isolated for their parent atom. Several types of scattering descriptions

can be applied in such a case.

Scattering from Free Electrons

If an electron scattering interaction occurs primarily with a loosely bound outer shell electron (such that the initial energy of the incident electron is much greater than the binding energy of the target electron), the target electron-atom system can be consider to be comprised of just a free electron. The process can then be described by the quantum mechanics of the electron-electron system. This is an important process because interactions with the outer electrons are likely to give rise to high energy secondary electrons, usually called delta-rays or knock-on electrons.

Mott [Mo30] first explored the scattering of electrons from free electrons at rest, and Møller [Mø32] derived under Dirac's formulation in the first Born approximation an expression for the cross section per electron describing such an interaction as

$$\sigma(\Delta E)d(\Delta E) = \frac{2\pi e^4}{mv^2}\left[\frac{1}{\Delta E^2} + \frac{1}{(E-\Delta E)^2} + \left(\frac{E'}{E'+1}\right)^2 - \frac{2E'+1}{(E'+1)^2}\frac{1}{\Delta E(E-\Delta E)}\right]d(\Delta E) \tag{2.96}$$

in which the primes imply quantities normalized by the electron rest mass. In this description, the incident and target electrons are indistinguishable subsequent to the collision, the cross section is derived assuming a maximum transfer of $1/2E$ and so the incident particle is arbitrarily assumed to have the higher energy.

The primary restriction on the use this cross section arises from the assumption of a free, unbound target, but it has been used in Monte Carlo calculations to describe *all* inelastic processes [Pr79]. As noted earlier, it has also been used to describe the ionization of inner shells due to close collisions by introducing the electron binding energies into the expression [Ko67, Se89]. Modifying 2.96 to take into account binding effects by applying a classical binary encounter correction has also proposed [Se89].

Together, these two modifications necessitate three numerical corrections. First, the two $1/(E-\Delta E)$ terms in 2.96 are replaced by $1/(E-\Delta E+E_b)$, where E_b is the binding energy. Next, a term G is added inside the brackets given by

$$G=\frac{8E_2}{3\pi}\left[\frac{1}{(\Delta E)^3}+\frac{1}{(E-\Delta E+E_b)^3}\right]\left[\arctan\sqrt{y}+\frac{\sqrt{y}(y-1)}{(y+1)^2}\right] \tag{2.97}$$

in which $y=(\Delta E+E_b)/E_1$ and E_1 is the average kinetic energy of the electron in the subshell, Lastly a multiplicative factor, P, given by

$$P=\frac{E}{E+E_b+E_1} \tag{2.98}$$

is applied.

Plasmon Excitation Cross Sections

A mode of energy loss not modeled by the Bethe theory or classical theory is the excitation of collective electron gas formed by the atomic conduction electrons. If the conduction electrons are assumes to form a weak plasma in the media, vibrations at a classically determined frequency may be excited. Although interest and effort in this area was initiated by Pines and Bohm [Pi52] most of the detailed investigation into this phenomenon has been carried out by Ritchie and co-workers at Oak Ridge National Laboratory. Ritchie [Ri57] essentially restricted the work on the Complex Dielectric Constant Method (in which all electron scattering collisions are treated as the response of the media to perturbations in the electric field caused by the impinging electron) to only those collisions resulting the excitation of the conduction electron plasma. The basics of the techniques are essentially equivalent, and so will not be presented here. All plasmon excitations result in the incident electron losing energy equivalent to a characteristic plasmon energy, which is usually approximated

(somewhat crudely) by $\hbar\omega_p$ where ω_p is the medium's plasma frequency given by

$$\omega_p = \left(\frac{n_e e^2}{\pi m}\right)^{1/2} \tag{2.99}$$

in which n_e is the number density of the conduction electrons. The most widely used expression for the mean free path for such an interaction is that given by Quinn [Qu62],

$$\lambda_p = \frac{2a_0 E}{\hbar\omega_p}\left(\ln\frac{\sqrt{E_F+\hbar\omega_p}-\sqrt{E_F}}{\sqrt{E}-\sqrt{E-\hbar\omega_p}}\right)^{-1}, \tag{2.100}$$

where a_0 is the Bohr radius. A simpler expression due to Ashley and Ritchie [As70]

$$\lambda_p = \frac{v^2\hbar^2}{e^2\omega_p}\left(\ln\frac{v}{1.13v_f}\right)^{-1}, \tag{2.101}$$

has also been used [Ter78].

The angular deflections resulting from plasmon excitations, because they are small (Shimizu [Sh76] states that they are less that 6 mrad) are sometimes ignored, but are most often taken from

$$f_p(\theta)d\theta = \frac{1}{2\pi n_e a_0}\frac{\theta_E}{\theta^2+\theta_E^2} \tag{2.102}$$

in which $\theta_E = \hbar\omega_p/2E$.

2.3.3 Transport Models Used by Previous Investigators

The use of specific inelastic scattering cross sections in Monte Carlo transport simulations has been briefly reported above. More complete summaries of previous Monte Carlo treatments of inner ionization are given in table 2.9, of previous excitation processes (including plasmon excitation) are given in table 2.10, and of delta ray production cross sections in table 2.11.

In the remainder of this section, some common complete descriptions of inelastic scattering, comprised of a combination of components drawn from the available pool of single scattering cross sections for the various processes, are summarized.

Ionization Treatment	Monte Carlo Authors
Gryzinski Binary Encounter [Gr59]	Reimer and Krefting [Re76] ETRAN (SANDYL) [Co74] Terrisol and Patau [Ter78] Akkerman and Chernov [Ak80] Adesida *et al.* [Ad78, Ad80] Ichimura *et al.* [Ic80] Shimizu *et al.* [Sh79] Shimizu [Shi80] Valkealahti *et al.* [Va83, Va84] Ganachaud and Cailler [Ga79] Sheldon and Ogilvie [She80]
Bethe–Mott–Massey (total)	Heńoc and Maurice [He76] Myklebust *et al.* [My76] Green [Gr63] Murata *et al.* [Mu71] Newbury *et al.* [Ne79a, Ne79b]
Kolbenstvedt Total Cross Section [Ko67]	ETRAN [Be68]
First-Born, Num. Int over f_n after [Ma72]	Green and Leckey [Gr76]
First-Born by Tung *et al.* [Tu76]	Hamm *et al.* [Ha79]
Adjusted σ_{Moller}, each shell	Seltzer [Se89]
First-Born Inner Shell Ion. (Ar only) [Eg75]	Unnikrishnan and Prasad [Un79]

Table 2.9: Single Scattering Ionization Treatments in Monte Carlo Electron Transport Codes

Excitation Treatment	Monte Carlo Authors
Streitwolf Total Outer Shell Ex. [St59]	Sheldon and Ogilvie [She80] Shimizu [Shi80] Shimizu *et al.* [Sh76]
Classical Total Inner Shell Ex. [Gr65c] Modified Classical for Excitations	Shimizu *et al.* [Sh76] Valkealahti *et al.* [Va83, Va84] Adesida *et al.* [Ad78, Ad80] Terrisol and Patau [Ter78]
Classical Inner Ionization [Ga69]	Akkerman and Chernov [Ak78b]
Eggarter Total Excite. [Eg75] (Ar only)	Unnikrishnan and Prasad [Un79]
σ_{Moller}, each shell	Proykova [Pr79]
Schnatterly First Born for $\sigma_{in,tot}$ [Sc79]	Felsteiner [Fe83] Salvat and Parallada [Sa84a, Sa84b]
CDCM [Tu76]	Hamm *et al.* [Ha79]
Outer Shell Excitations by CDCM	Ganachaud and Cailler [Ga79]
Outer Shell Excitations by CDCM [Ak78a]	Akkerman and Chernov [Ak80]
CDCM, with Glick and Ferrell [Gl60] pair-distribution function correction	Green and Leckey [Gr76]
Semi-empirical Outer Shell Ex. [Re76]	Shimizu *et al.* [Sh79]
Semi-empirical Outer Shell Ex. [Sh78]	Shimizu [Sh78] Adesida *et al.* [Ad78, Ad80]
Empirical: $f_{ex}(\Delta E) = e^{-\Delta E/I_p}$	Newbury *et al.* [Ne80] Murata, Kotera and Nagami [Mu80] Špalek [Sp82] Shimizu *et al.* [Sh75]
Empirical: $f_{ex}(\Delta E) = C/(\Delta E)^2$	Salvat and Parallada [Sa84a, Sa84b] Liljequist [Li78a] Liljequist *et al.* [Li78b] Špalek [Sp82]
Ashley and Ritchie Plasmon Ex. [As70]	Terrisol and Patau [Ter78] Hamm *et al.* [Ha79]
Ritchie Plasmon Excitation [Ri59]	Green and Leckey [Gr76]
Aiyama Plasmon Excitation [Ai74]	Sheldon and Ogilvie [She80]
Quinn Plasmon Excitation [Qu62]	Shimizu *et al.* [Sh76] Shimizu [Shi80]
Plasmon Excitation by CDCM	Ganachaud and Cailler [Ga79]
Pines Surface Plasmon Excitation [Pi63]	Sheldon and Ogilvie [She80]

Table 2.10: Treatments of Atomic Excitation in Monte Carlo Electron Transport Codes

Free Electron Cross Section	Monte Carlo Authors
Møller cross section	Terrisol and Patau [Ter78] Murata, Kyser and Ting [Mu81] Berger [Be63] ETRAN [Be68] ETRAN (SANDYL) [Co74] Vande Putte [Va74a] EGS [Fo78, Ne85] Mæhlum and Stadsnes [Mæ67]

Table 2.11: Free Electron Collision Cross Sections Used in Monte Carlo Electron Transport Codes

One common technique uses accurate cross sections for different components of the atomic structure (such as inner shell ionization) which are important to the calculation (primarily this would include inner shell ionizations if the decay products are of interest and delta-ray production if knock-on secondaries are important) and switches to empirical or approximated models for other, less important components within the same model. The overall result is then adjusted to agree with experiment in some way, most commonly by forcing agreement of the model's stopping power with the semi-empirical Bethe stopping power. For instance, Gryzinski's cross section may be used to model inner shell ionizations, Møller's cross section for scattering from the free electrons, and one of the empirical models, with the stopping power term reduced so as to reflect the losses due to the explicitly treated scattering types, as in

$$\left|\frac{dE}{dx}\right|_{red} = \left|\frac{dE}{dx}\right|_{exp} - \int \Delta E\,[\sigma_G(\Delta E) + \sigma_M(\Delta E)]\,d(\Delta E) \qquad (2.103)$$

Several such adjustments have previously been reported. The first involves using the Gryzinski excitation model for the inner shells and then lumping of all outer collisions into a single subshell with an empirical binding energy E_b' [Sh76, Ad78,

Ad80] which is determined so that

$$n_e^{outer}\int_{E_b'}^{E}\sigma_G(\Delta E)\Delta E d(\Delta E)=\left|\frac{dE}{dx}\right|_{exp}-\sum_{inner\ shells}n_e^{in}\int\sigma_G(\Delta E)\Delta E d(\Delta E). \tag{2.104}$$

Other models use one of the empirical distributions discussed earlier to model excitations. Some models simply define a stopping power equal to the left side of equation 2.104, which they apply in a non-single scattering mode [Ic80, Re76], as explained in chapter V.

Models which do not rely on the experimental stopping power values range from the simple, modeling only ionization processes for all shells, to the complex, using one or another of the ionization models, DIMFP calculations for the valence excitation description, and including plasmon scattering [Ak80, Ga79, Gr76, Ha79], and have met with varying degrees of success. As stated earlier, because of the unavailability of a closed formed technique for determining differential inverse mean free paths from dielectric constant data, this more complex technique was not modeled in this work.

2.3.4 Experiments Used in Evaluating Single Inelastic Scattering Cross Sections

A great body of literature has arisen in attempts to define the cross sections for every conceivable transition for every atom. Thus, although it would theoretically be possible to collect all published experiments and compare results for each possible interaction, it would not in any sense be practical for a single investigator. The alternative of collecting all experimental data, summing over the losses due to all transitions and comparing this with excitation distribution functions also seems impractical. Thus, identifiable errors in the excitation loss distribution functions are be expected to show up only in macroscopic experiments, such as energy distributions

Authors	Element Z	Energies (keV)
Davis *et al.* [Da72]	47,79	20 – 140
Jessenberger and Hink [Je75]	28	E_K – 50
Platten *et al.* [Pl85]	14	4 – 10

Table 2.12: Single Ionization Experiments

of transmitted or backscattered electrons. And so for the case of excitations, what can actually be evaluated are not individual cross sections by comparison with single scattering experiments, but complete models of inelastic scattering, by comparison with macroscopic data. Therefore, the evaluation here is limited to ionization cross sections, for which a large volume of single scattering data is available, and complete inelastic scattering models, which are evaluated based on the conclusions about kilovolt energy range stopping power discussed in the next chapter.

Ionization experiments in the kilovolt energy range have been summarized recently (for K shells) by Casnati *et al.* [Ca82], and that summary is not repeated here. The experiments selected for the comparison in this section are given in table 2.12.

2.3.5 Evaluations and Conclusions

The modified Møller, Scofield, Pressa and Newell, Kolbenstvedt, Arthurs and Moiseiwitsch, Gryzinski and relativistically corrected Gryzinski cross sections were used for the ionization cross section comparison. Preliminary results showed that the Arthurs and Moiseiwitsch cross section, because of the limited data available for evaluating their S function, would not be applicable over a wide enough range of

energies to be useful. The Scofield formalism presents a similar problem, but only at energies very near the thresholds, and since the results are generally good at higher energies, they are included in the evaluation. The Møller cross section, because it describes only close collisions, was found inappropriate for modeling inner ionization cross sections in most applications, but was included for reference. Also, it was noted that as the theoretical cross sections typically underestimated experimental data, and since the relativistic correction to the Gryzinski cross section was found to increase that cross section in the range of 5 to 20%, this corrected form of the Gryzinski evaluation was applied throughout the analysis.

Thus, results of the evaluations of the Kolbenstvedt, Pressa and Newell, Møller, Scofield and relativity corrected Gryzinski cross sections are plotted in figures 2.10 through 2.13.

It is seen that at energies much greater than the binding energy, all of the four cross sections provide roughly equivalent and quite reasonable results, throughout the range of atomic numbers and into the L shell. At energies near the threshold, the Kolbenstvedt cross section over estimates the cross section for all Z, and the Gryzinski cross section, even with the relativistic correction, greatly underestimates the cross section. The parameterizations of Pressa and Newell and of Scofield provide similar data, except for the Gold L shell case, in which instance the Scofield data more closely models the experimental data. Results from other calculations not modeled against experiment suggest a general relation between the two parameterizations in which the Pressa and Newell data is slightly greater than Scofield's results near K shell thresholds (by roughly the same fraction for all elements), less than the Scofield data near L shell thresholds (more pronouncedly so for higher Z elements), and roughly equivalent to the Scofield numbers for all shells and elements at energies

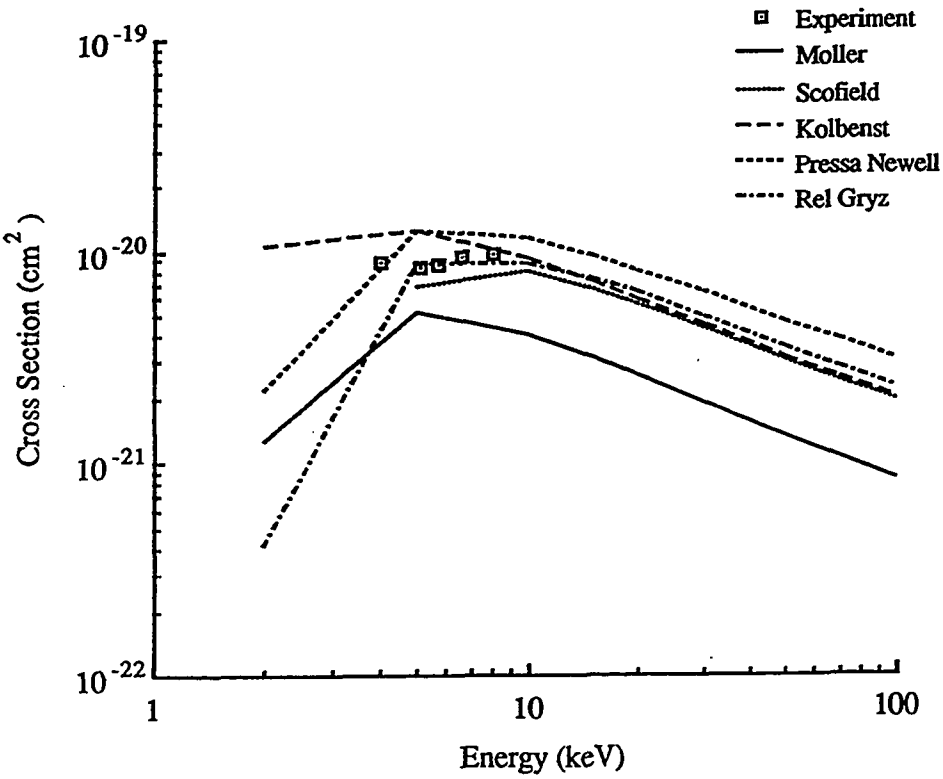

Figure 2.10: Comparison of K Ionization Cross Sections with Experiment for Silicon

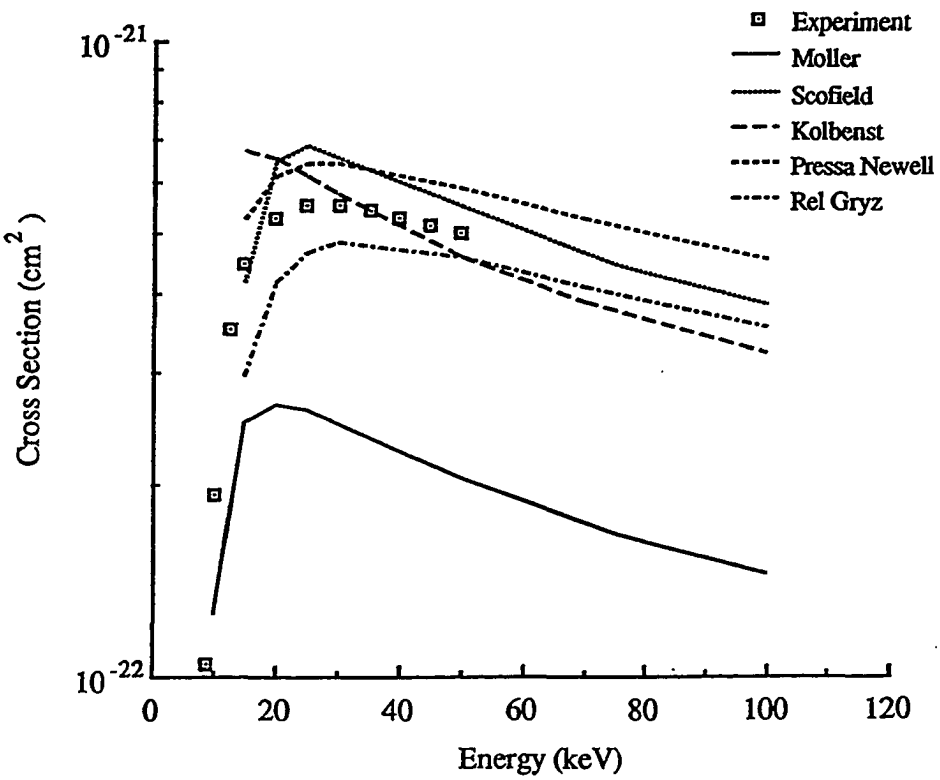

Figure 2.11: Comparison of K Ionization Cross Sections with Experiment for Nickel

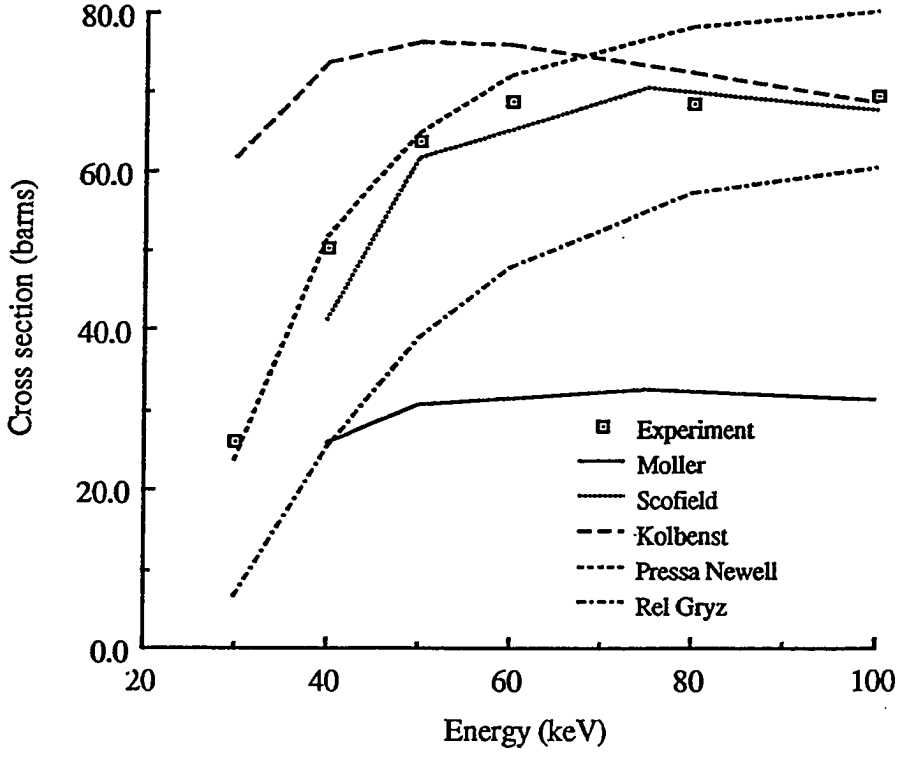

Figure 2.12: Comparison of K Ionization Cross Sections with Experiment for Silver

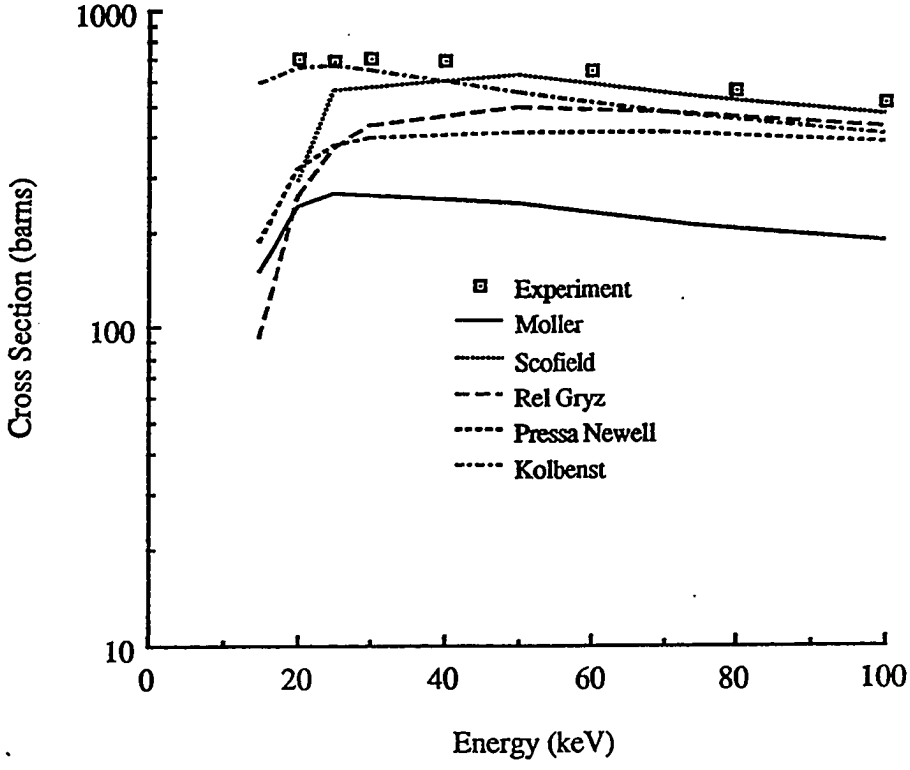

Figure 2.13: Comparison of $L-III$ Ionization Cross Sections with Experiment for Gold

much greater than the thresholds.

Since no discrete transition excitation cross sections are examined here, the excitation models employed in this work can be evaluated to a limited extent, and then only based on comparison of the energy loss per pathlength that they predict as (parts of complete models of inelastic scattering) with experimentally derived stopping power data. These evaluations are discussed in Chapter VI, in which complete single inelastic scattering models are constructed and evaluated.

2.4 Bremsstrahlung Cross Sections

According to classical electrodynamics, a charged particle which is somehow accelerated must emit radiation. As the deflections resulting from all electron scattering collisions constitute accelerations, a bremsstrahlung photon is emitted with unit probability in all electron collisions [Ja75]. What shall be used here to distinguish bremsstrahlung collisions from 'ordinary' collisions is the energy of the emitted photon. In most instances, the photon carries an experimentally undetectable amount of energy, and the effects of the bremsstrahlung process may be ignored. However, it is possible for a scattered electron to a generate photon with as much as the complete energy of the incident electron. These 'hard' collisions will be treated separately as bremsstrahlung interactions. Interactions with both nuclei and atomic electrons give rise to bremsstrahlung photons, although electron-electron interactions are far less likely to produce such energetic photons.

Recently, Seltzer and Berger summarized the available cross sections with an emphasis on their application in Monte Carlo electron transport calculations [Se85]. Therefore, a detailed comparison of theoretical and experimental results similar to that presented in the previous sections in this chapter will not be given here, but

instead the conclusions of Seltzer and Berger will be cited. A cursory review of the applicable cross section formulations will be presented, however, with emphasis on the analytically determined validity conditions and the computational aspects of evaluating those formulations typically used in Monte Carlo transport calculations. A list of pertinent experiments, most of which were used in the evaluation by Seltzer and Berger, is included for completeness.

2.4.1 Summary of Current Theories

Two review articles form the basis of this brief survey. The first is a general survey of early efforts in this area, categorized according to the approximations employed [Ko59], and the second, Seltzer and Berger's grouping based on applicability at various energies ranging from 1 keV to 10 GeV [Se85]. As with the case of elastic scattering, in the energy range of interest here, the two main classifications of electron bremsstrahlung cross section formulations are those employing the first Born approximation and those using partial wave expansion methods. A third, smaller, group of analytically ponderous derivations based on an unscreened, non-relativistic dipole approximation with Coulombic wave functions has been found useful in deriving non-relativistic corrections to the Born cross sections [So31, El39]. Other applications of the dipole approximation method are restricted to the extreme relativistic range, and are not cited here.

Unlike the other differential scattering cross sections examined in this chapter, the bremsstrahlung cross section is most easily calculated in the matrix formulation of quantum mechanics, in which cross section is given in terms of a particular matrix element which is dependent on the incoming and outgoing wave functions of the

electron and the direction of the photon polarization. This yields

$$\sigma(Z,E,k,\Omega_e,\Omega_p)dkd\Omega_e d\Omega_p = \frac{\alpha r_0^2}{(2\pi)^4}\frac{k^2 E_0 p_0 p_1}{E_1}|M|^2 \tag{2.105}$$

in which E is the electron energy and p its momentum with the subscripts 0 and 1 referring to before and after the collision, k is the photon energy, Ω_e the electron and Ω_p the photon final direction, and M the bremsstrahlung matrix element, given by

$$M = \int \psi_1^* \epsilon_\lambda e^{-ikz}\psi_0 d\mathbf{r}. \tag{2.106}$$

In 2.106, ψ is the standard 4 element Dirac electron wave function and ϵ_λ a unit vector in the direction of the photon polarization. Obviously, solving for the cross section consists of evaluating the matrix element, which, in turn, primarily involves solving for the initial and final wave functions describing the incident electron. As with all previously examined cross section derivations, two solution methods predominate. Indeed, Seltzer and Berger limit their discussion to first Born approximation calculations mainly attributable to Bethe and Heitler [Be34] and to recent partial wave calculations of Pratt and co-workers [Ts71].

Bethe and Heitler [Be34] solved 2.106 in the Born approximation to yield a solution for the triply differential cross section. Obviously then, their results will be limited by the same conditions as other Born cross sections, typically $\alpha Z/\beta \ll 1$. Their results (and the results of others using similar approximations) have been well summarized by Koch and Motz [Ko59], who use a system for classifying cross sections based on the degree of integration over the totally differential cross section, with the number 1 signifying triply differential, 2 meaning integrated over electron angle, 3 integrated over electron and photon angle and 4 integrated over all variables, the total cross section; the letter B to signify that the Born approximation has been employed; and a letter N or S denoting whether or not screening was included (S

for screening, N for no screening). The formulae most widely cited for use in Monte Carlo codes are those labeled 3BS and 3BN by Koch and Motz. The expression 3BS was derived in the extreme relativistic limit, and so should be of limited utility for the present application, although it have been widely used in Monte Carlo electron transport codes [Fo78, Co74] at low energies. Its form is given by

$$\sigma_{3BS}(k)dk = 4Z^2 r_0^2 \alpha \frac{dk}{k} \left\{ \left[1 + \left(\frac{W_0}{W_1} \right)^2 \right] \left(\frac{\phi_1(\delta)}{4} - \frac{1}{3} \ln Z \right) - \frac{2}{3} \frac{W_0}{W_1} \left(\frac{\phi_2(\delta)}{4} - \frac{1}{3} \ln Z \right) \right\} \tag{2.107}$$

in which W represents the total energy, $E + mc^2$,

$$\delta = \frac{k\, mc^2}{2W_0 W_1}, \tag{2.108}$$

$$\phi_1(\delta) = 4 \int_\delta^1 (q - \delta)^2 (1 - F(q))^2 \frac{dq}{q^3} + 4 + \frac{4}{3} \ln Z, \tag{2.109}$$

and

$$\phi_2(\delta) = 4 \int_\delta^1 \left(q^3 - 6\delta^2 q \ln \frac{q}{\delta} + 3\delta^2 q - 4\delta^3 \right) (1 - F(q))^2 \frac{dq}{q^4} + \frac{10}{3} + \frac{4}{3} \ln Z \tag{2.110}$$

in which $F(q)$ is the atomic form factor defined in equation 2.19 of section 2 of this chapter. Nelson *et al.* [Ne85] have used Thomas-Fermi form factors which lead to approximate forms of the functions ϕ_1 and ϕ_2, given by

$$\begin{aligned} \phi_1(\delta') &= 20.867 - 3.242\delta' + 0.625(\delta')^2 \quad \text{if } \delta' \leq 1, \\ &= 21.12 - 4.184 \ln(\delta' + 0.952) \quad \text{otherwise,} \end{aligned} \tag{2.111}$$

and

$$\begin{aligned} \phi_2(\delta') &= 20.029 - 1.930\delta' + 0.086(\delta')^2 \quad \text{if } \delta' \leq 1, \\ &= 21.12 - 4.184 \ln(\delta' + 0.952) \quad \text{otherwise,} \end{aligned} \tag{2.112}$$

in which $\delta' = 1.36\,\delta$. An empirical correction factor, based on interpolation of various plots from Koch and Motz of $\sigma_{exp}/\sigma_{Born}$, is included to enhance accuracy at energies below 50 MeV.

The other widely cited Born expression (Koch and Motz 3BN), which does not include a screening correction, is given by

$$\sigma_{3BN}(k')dk' = \frac{Z^2 r_0^2 \alpha dk'}{k'} \frac{p_1'}{p_0'} \left\{ \frac{4}{3} - 2W_0'W_1' \left(\frac{(p_1')^2 + (p_0')^2}{(p_1')^2(p_0')^2} \right) + \frac{\epsilon_0 W_1'}{(p_0')^3} + \frac{\epsilon_1 W_1'}{(p_1')^3} - \frac{\epsilon_1 \epsilon_0}{p_0' p_1'} + L \left[\frac{8}{3} \frac{W_0'W_1'}{p_0'p_1'} + \frac{(k')^2((W_0')^2(W_1')^2 + (p_0')^2(p')^2)}{(p_0')^3(p_1')^3} + \frac{k'}{2p_0'p_1'} \left(\frac{W_0'W_1' + (p_0')^2}{(p_0')^3} \epsilon_0 - \frac{W_0'W_1' + (p_1')^2}{(p_1')^3} \epsilon_1 + \frac{2k'W_0'W_1'}{(p_0')^2(p_1')^2} \right) \right] \right\} \quad (2.113)$$

where

$$L = 2 \ln \left[\frac{W_0'W_1' + p_0'p_1' - 1}{k'} \right]; \qquad \epsilon_n = \ln \left(\frac{W_n' + p_n'}{W_n' - p_n'} \right),$$

and the primes imply energy quantities in units of mc^2 and momentum variables in terms of mc. This cross section is used in all but the latest versions of ETRAN and its descendants in conjunction with several energy dependent empirical corrections to improve its accuracy. As in the case of elastic scattering, the lack of inclusion of screening restricts the validity (in theory) of this unscreened cross section to cases in which $(Z^{-1/3}/\alpha) \gg (W_0 W_1 / k mc^2)$ holds.

In practice, this cross section (3BN) must be corrected to account for screening, and both 3BN and 3BS must be corrected for low energy discrepancies caused by the lessening validity of the Born approximation at low energies. A screening correction derived by comparing results of the 3BS formula with and without form factors has been used previously at higher energies [Se89]. Corrections for the Born approximation are typically called 'Coulomb corrections', with the most widely cited being a multiplicative correction due to Elwert [El39], valid at non-relativistic energies. This factor is based on a comparison of non-relativistic Born approximation results with

non-relativistic Sommerfeld results [So31] derived for interactions in the Coulomb field of the nucleus and is given by

$$f_E = \frac{\beta_0 [1 - \exp(-2\pi Z\alpha/\beta_0)]}{\beta_1 [1 - \exp(-2\pi Z\alpha/\beta_1)]} \tag{2.114}$$

where again the subscripts 0 and 1 refer to the initial and final electron states and α is the fine structure constant. This correction is most applicable in the region of $k \rightarrow E_0$ (the 'tip' region). Even with screening and Coulomb correction terms, empirical correction factors are usually used with these cross sections at lower energies [Co74].

Tseng, Pratt and co-workers, in a series of papers (including particularly [Ts71, Ts74, Pr77, Ts79, Ki81, Pr81a, Pr81b, Ki83]) have reported the results of their investigation of the problem of nuclear bremsstrahlung using partial wave expansion series for the electron wave functions, which they obtain by numerical integration of the radial Dirac equation, using a relativistic Hartree potential. Errors are conservatively expected to be in the range of 5 to 10 %, but possibly higher at energies around 1 keV for very low Z materials [Se85].

The singly differential cross section data [Pr77, Pr81b] consists of tables of the scaled cross section,

$$\frac{\beta^2}{Z^2} k\, \sigma(Z, E, k) dk$$

as a function of the initial electron energy E at 20 points between 1 keV and 2 MeV, and the output photon fractional energy k/E at 12 points ranging between 0 and 1 for elements with atomic numbers $2 \leq Z \leq 92$. The actual calculations were performed only for elements of atomic number 2, 8, 13, 47, 79, and 92, and interpolative techniques then employed to fill the tables. For the current work, tables were constructed extending through all 12 k/E values employed by Pratt *et al.*, but only through 12 of their energy points (those lying between 1 and 500 keV) and at

atomic numbers 3, 13, 24, 47, 79 and 92. These were chosen to incorporate Pratt's data at a few materials of interest to certain medical physics applications. Cross sections for other materials are interpolated or extrapolated as needed. Pratt *et al.* have also published tabulated data of 'shape functions' $S(Z,E,k,\theta_k)$ [Ts79, Ki83], which they define as

$$S(Z,E,k,\theta_k)d\Omega_k = \frac{\sigma(Z,E,k,\theta_k)dkd\Omega_k}{\sigma(Z,E,k)dk}. \tag{2.115}$$

They have parameterized their results in the form

$$S(Z,E,k,\theta_k)d\Omega_k = \frac{A(Z,E,k)}{4\pi(1-\beta\cos\theta)^{9/2}}\sum_{l=0}^{5} B_l(Z,E,k)\,P_l(\cos\theta), \tag{2.116}$$

and they present data for the coefficients A and B_l for elements 2, 8, 13, 47, and 92 at electron energies of 1,5, 10, 50, 100 and 500 keV, and at fractional photon energies (k/E) values of 0.0, 0.6, 0.8, and 0.95. In the present work, cross sections for other elements are determined by interpolating or extrapolating the expanded shape function values (as opposed to the coefficients) as needed.

2.4.2 Cross Sections Used by Previous Investigators

At energies being considered here, bremsstrahlung scattering is a low probability occurence. Nevertheless, in certain applications it is of paramount importance, and so has been treated by several authors. A table summarizing the treatment of bremsstrahlung by previous Monte Carlo investigators is given in table 2.13.

The citations listed in table 2.13 use expressions only for the cross section which are differential only in photon energy, $\sigma(k)dk$. Models for the angular dependence of the photons are given in table 2.14. Only one model has gained widespread, and it assumes that all photons are emitted with a constant angle. This is a poor approximation in the kilovolt energy range, as seen from figure 2.14, taken from

Bremsstrahlung Cross Section	Monte Carlo Authors
Bethe-Heitler (Koch 3BN) [Ko59] w/ Elwert Correction	ETRAN *et al.* [Co74, Se89] Kulkarni and Supe [Ku84] Sundararaman *et al.* [Su73]
Bethe-Heitler (Koch 3BS) [Ko59] and Thomas-Fermi Form Factors	EGS [Fo78, Ne85] GEANT [Br87]
Pratt [Pr81b]	ETRAN [Se89]

Table 2.13: Bremsstrahlung Cross Sections Used in Monte Carlo Electron Transport Codes

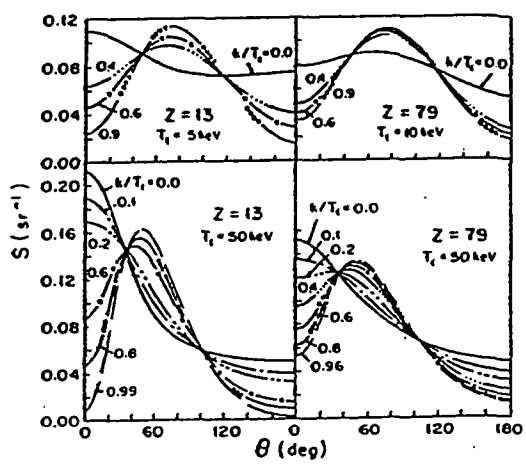

FIG. 7. Shape function for Al and Au at T_1=5, 10, and 50 keV for various k/T_1.

Figure 2.14: Angular Distribution of Emitted Bremsstrahlung Photons

[Ts79]. Typically, electrons are assumed to not be deflected, an assumption which is valid only at relativistic energies.

2.4.3 Electron-Electron Bremsstrahlung

Electrons scattering from atomic electrons may also give rise to bremsstrahlung photons. At very high energies, the singly differential cross section is of nearly the same shape as that for nuclear bremsstrahlung for unscreened point charges (and

Photon Angular Dependence	Monte Carlo Authors
$\theta = mc^2/(E_0 + mc^2)$	ETRAN *et al.* [Co74, Se89] GEANT [Br87] EGS [Fo78, Ne85]

Table 2.14: Models of Bremsstrahlung Photon Angular Dependence Used in Monte Carlo Electron Transport Codes

thus having a difference given by a ratio of $1/Z$ for $Z > 1$). At low energies, several effects combine to cause the electron-electron bremsstrahlung cross section to deviate significantly from the nuclear cross section. First, the maximum energy of the emitted photon, which is limited for electron scattering by kinematics, deviates significantly from its maximum value (E_0, for $\beta \rightarrow \infty$) and approaches its minimum value, $E_0/2$ for $\beta \rightarrow 0$. Second, the binding energy of the atomic electron becomes significant compared to the incident electron energy. Collisions with bound electrons have been examined by Haug and Keppler [Ha84] who have shown that for a given energy loss by the incident electron, collisions with the inner, more tightly bound electrons produce broader and less sharply peaked spectra than collisions with less tightly bound electrons. Their results are restricted to transfers to the target electron which are much greater than the binding energy, however. Third, the cross section vanishes at very low energy because of the lack of a dipole moment in the electron-electron system. Lastly, the effects of nuclear screening and electron screening differ more greater at lower energies.

The theory of Haug [Ha75] is almost universally used in Monte Carlo simulations to describe electron-electron bremsstrahlung. His first Born approximation calculation is derived to describe the scattering from free electrons, and thus ignores both binding and screening effects. Haug has analytically integrated over his Born

expression for the fully differential cross section

$$\sigma(k, p_1, p_1', \Omega_k, \Omega_{e_1}, \Omega_{e_1'}) dk dp_1 dp_1' d\Omega_k d\Omega_{e_1} d\Omega_{e_1'}$$

(here the primes refer to the target electron and momentum and energy variables are expressed in mc or mc^2 units, respectively), yielding for the doubly differential cross section

$$\sigma(k, \theta_k) dk d\theta_k = \frac{\alpha r_0^2}{\pi} \frac{k}{\omega \rho} \sqrt{\frac{\rho^2 - 4}{\omega^2 - 4}} \frac{1}{\pi} \int A \, d\Omega_{e_1} dk d\Omega. \tag{2.117}$$

In this expression, the term A is function of the momenta of the three particles [Ha75] and ρ and ω are defined by

$$\begin{aligned} \omega^2 &= 2(p_0 p_0' + 1) \\ \rho^2 &= 2(p_1 p_1' + 1) \\ &= 2[p_0 p_0' - k(p_0 + p_0') + 1]. \end{aligned} \tag{2.118}$$

Haug has evaluated $1/\pi \int A \, d\Omega_{e_1}$, but the expression he gives for this term is lengthy and is not repeated here (it can be found in the appendix of Haug's article). The singly differential cross section can be obtained by numerical integration of 2.117.

A non-relativistic cross section has been reported by Fedyushin [Fed52] and Garibyan [Ga53] in the form

$$\sigma(k) dk = \frac{4}{15} \frac{\alpha r_0^2}{k} F\left(\frac{4k}{p_0^2}\right) \tag{2.119}$$

in which the function F is defined by

$$F(x) = \left[17 - \frac{3x^2}{(2-x)^2}\right] \sqrt{1-x} + \frac{12(2-x)^4 - 7x^2(2-x)^2 - 3x^4}{(2-x)^3} \ln \frac{1 + \sqrt{1-x}}{x} \tag{2.120}$$

and in which energy and momentum quantities are given in terms of the mc^2 and mc respectively. Haug notes that evaluation of this expression yields results identical to his for electron energies up to 20 keV.

Seltzer [Se89] reports a method in which screening is taken into account by means similar to that used for the nuclear screening correction. In this case, incoherent scattering functions, $S(Z, v)$, are used to describe the electron screening, based on the theory of Wheeler and Lamb [Wh39]. These functions have the effect of decreasing the cross section except for high Z materials and high momentum transfers.

Ratios of the electron to nuclear bremsstrahlung cross sections are given in figures 2.15 through 2.17, in which electron bremsstrahlung is described by the theory of Haug (without the incoherent scattering functions, which would decrease the cross section anyway) and the nuclear process by the result of Tseng *et al.* The electron cross section results presented in the figure have been multiplied by Z to reflect the presence of the atomic electrons. It is seen that the bremsstrahlung cross section for the production of energetic photons is less than 1% of the nuclear cross section for almost all energies and atomic numbers below 100 keV. The only exception is for low atomic numbers, high projectile electron energies, and relatively low photon energies, in which case the ratio approaches 3% or so. On the basis of these results, electron-electron scattering is not treated in the present work.

2.4.4 Experimental Data Base

A list of relevant experiments (those conducted in the energy range from 1 to 100 keV) is presented in table 2.15.

2.4.5 Models Used in the Current Work

Clearly, the calculations and tabulations of Pratt and co-workers are the most appropriate for use in the current work for describing electron-nuclear bremsstrahlung, and so are exclusively employed here. Additionally, the angular distribution of

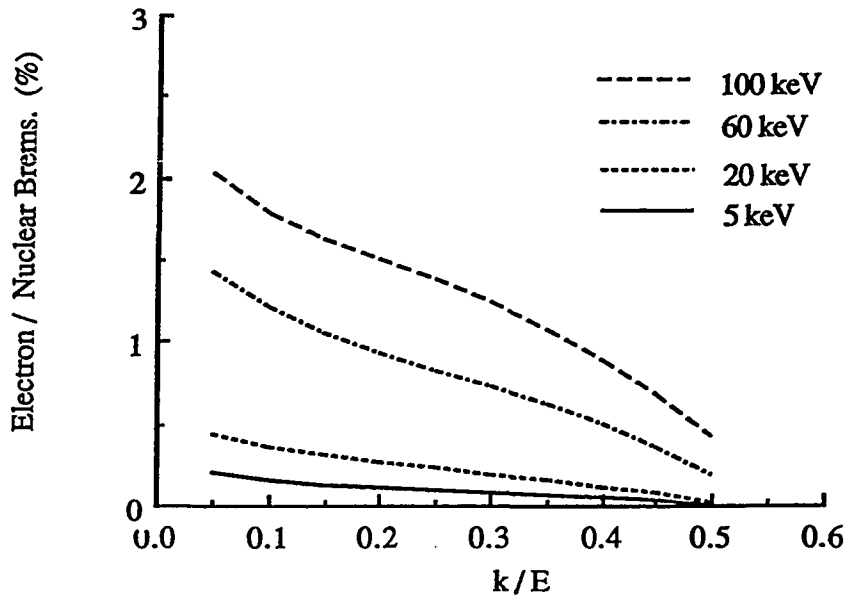

Figure 2.15: Ratio of Electron to Nuclear Bremsstrahlung for Aluminum

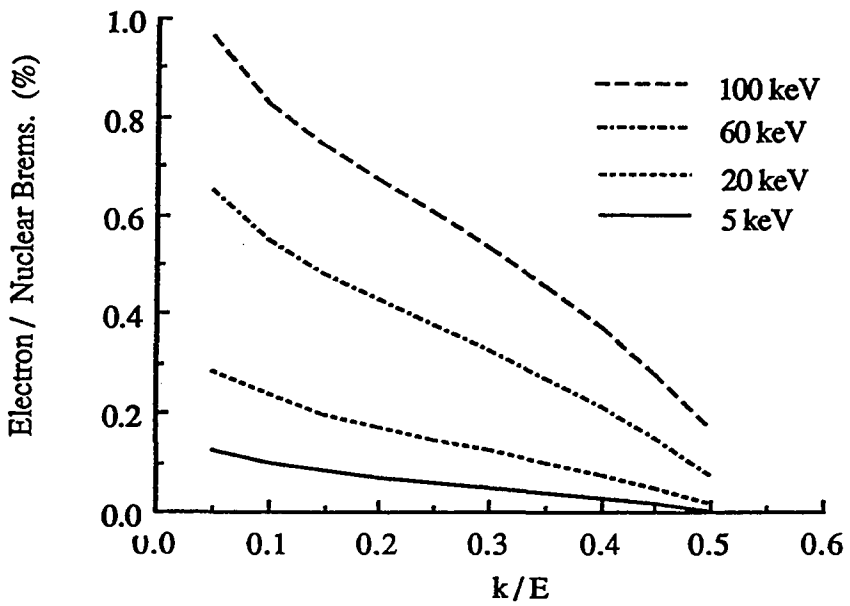

Figure 2.16: Ratio of Electron to Nuclear Bremsstrahlung for Copper

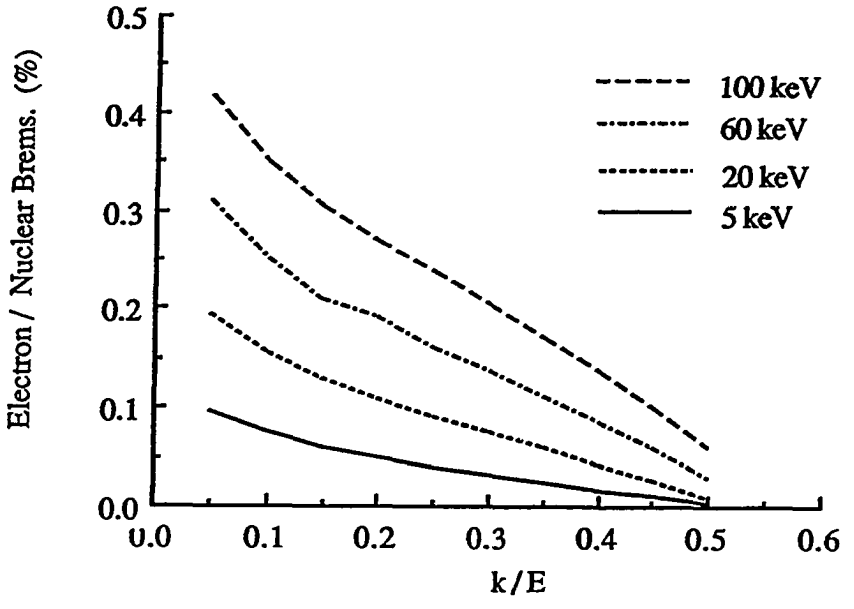

Figure 2.17: Ratio of Electron to Nuclear Bremsstrahlung for Tungsten

Elements	Energy (keV)	Author
6 - 79	25, 34	Amrehn [Am56]
6 - 92	50, 75, 100	Ambrose *et al.* [Am87]
36, 54	6, 8, 10	Aydinol *et al.* [Ay80]
2 - 92	2.5, 10	Hippler *et al.* [Hi81]
13	34	Kerscher *et al.* [Ke55]
13, 79	50	Motz and Placious [Mo58]
13, 29, 47, 79	50, 100	Quarles and Heroy [Qu81]
10, 18, 36, 54	6 - 10	Semaan and Quarles [Se81]
10 - 80	6, 6.5	Semaan and Quarles [Se82]

Table 2.15: Experiments used in Evaluating Bremsstrahlung Cross Sections

bremsstrahlung photons, which is clearly not a delta function in this energy regime, is modeled by employing the doubly differential cross section section, through use of the shape functions of Kissel. Finally, the angular distribution of the incident electrons is assumed to be given by the elastic scattering cross section, regardless of the energy of the emitted photon. This assumption is based on the fact that as the photon energy approaches zero, the shape of the electron angular scattering distribution does in fact equal the elastic scattering shape [Ts79].

References

[Ad78] I. Adesida, R. Shimizu and T.E. Everhart, *Appl. Phys. Lett.* **33**, (1978) 849.

[Ad80] I. Adesida, R. Shimizu and T.E. Everhart, *J. Appl. Phys.* **51**, (1980) 5962.

[Ai74] T. Aiyama and K. Yada, *J. Phys. Soc. Japan* **36**, (1974) 1554.

[Ak78a] A.F. Akkerman and G.Ya. Chernov, *Soviet Phys. Tech. Phys.* **48**, (1978) 48.

[Ak78b] A.F. Akkerman and G.Ya. Chernov, *Phys. Stat. Sol. B* **89**, (1978) 329.

[Ak80] A.F. Akkerman and G.Ya. Chernov, *Phys. Stat. Sol. B* **101**, (1980) 109.

[Am56] H. Amrehn, *Z. Physik* **144**, (1956) 529.

[Am87] R. Ambrose, J.C. Altman and C.A. Quarles, *Phys. Rev. A* **35**, (1987) 529.

[Ar58] A. M. Arthurs and B. L. Moiseiwitsch, *Proc. Phys. Soc. (Lond.)* **A247**, (1958) 550.

[As70] J.C. Ashley and R.H. Ritchie, *Phys. Stat. Sol.* **40**, (1970) 673.

[As79] J.C. Ashley, C.J. Tung and R.H. Ritchie, *Surface Science* **81**, (409) 1979.

[Ay80] M. Aydinol, R. Hipple, I. McGregor and H. Kleinpoppen, *J. Phys. B* **13**, (1980) 989.

[Ba39] J. Bartlett and R.E. Watson, *Phys. Rev.* **56**, (1939) 612.

[Be30] H. A. Bethe, *Ann. Physik* **5**, (1930) 325.

[Be34] H. A. Bethe and W. Heitler, *Proc. Phys. Soc. (Lond.)* **A146**, (1934) 83.

[Be63] M.J. Berger, "Monte Carlo Calculation of the Penetration and Diffusion of Fast Charged Particles," in *Methods in Computational Physics*, vol. 1, B. Adlu, S. Fernbach, M. Rotenberg, eds., Academic Press, New York, (1963) 135.

[Be68] M.J. Berger and S.M. Seltzer, *Monte Carlo Code System for Electron and Photon Transport through Extended Media*, Oak Ridge National Laboratory Radiation Shielding Information Center document CCC-107, (1968).

[Be70] M.J. Berger, S.M. Seltzer and K. Maeda, *J. Atmos. Terrestial Phys.* **32**, (1970) 1015.

[Be89] M. J. Berger and R.Q. Wang, *Monte Carlo Transport of Electrons and Photons*, T. M. Jenkins, W. R. Nelson and A. Rindi, Eds., Plenum Press, New York (1989)

[Bi59a] H. Bienlein, G. Felsner, K. Güthner, H. v. Issendorff and H. Wegener, *Z. Physik* **154**, (1959) 376.

[Bi59b] H. Bienlein, G. Felsner, R. Fleischmann, K. Güthner, H. v. Issendorff and H. Wegener, *Z. Physik* **155**, (1959) 101.

[Bi67] H.E. Bishop, *Brit. J. Appl. Phys.* **18**, (1967) 703.

[Br74] J.P. Bromberg, *J. Chem. Phys.* **61**, (1974) 963.

[Br87] R. Brun, F. Bruyant, M. Maire, A.C. McPherson and P. Zanarini, *GEANT3 User's Guide*, CERN Data Handling Division Document DD/EE/84-1 (1987).

[Ca82] E. Casnati, A. Tartari and C. Baraldi, *J. Phys. B* **15**, (1982) 155.

[Ch40] C.T. Chase and R.T. Cox, *Phys. Rev.* **58**, (1940) 243.

[Co74] H. M. Colbert, *SANDYL A Computer Program for Calculating Combined Photon-Electron Transport in Complex Systems*, Sandia Report SLL-74-0012 (1974).

[Da72] D.V. Davis, V. D. Mistry and C.A. Quarles, *Physics Letters* **38A**, (1972) 169.

[Do56] J. A. Doggett and L. V. Spencer, *Phys. Rev.* **103**, (1956) 1597.

[Do65] R.C. Dougal, *Proc. Phys. Soc. (Lond.)* **85**, (1965) 851.

[Eg75] E. Eggarter, *J. Chem. Phys.* **62**, (1975) 833.

[El39] G. Elwert, *Ann. Phys.* **34**, (1939) 178.

[Fa64] U. Fano, *Ann. Rev. Nucl. Sci.* **13**, (1964) 1.

[Fe52] H. Feshbach, *Phys. Rev.* **88**, (1952) 295.

[Fed52] B.K. Fedyushin, *Zhur. Eksp. Teor. Fiz.* **22**, (1952) 140.

[Fe69] R.M. Felder, *MOGUS - A Code for Evaluating the Mott Scattering Cross Section and the Goudsmit-Saunderson Angular Multiple-Scattering Distribution for Use in Electron Transport Calculations*, Brookhaven National Laboratory Report BNL 50199 (T-549), 1969.

[Fe83] J. Felsteiner, *J. Phys. D* **14**, (1983) 2229.

[Fo78] R.L. Ford and W.A. Nelson, *The EGS Code System: Computer Programs for the Monte Carlo Simulation of Electromagnetic Cascade Showers (Version 3)*, Stanford Linear Accelerator Center Report SLAC-210 (1978)

[Ga53] G.M. Garibyan, *Zhur. Eksp. Teor. Fiz.* **24**, (1953) 617.

[Ga69] J.D.Garcia, *Phys. Rev.* **177**, (1969) 223.

[Ga79] J.P. Ganachaud and M. Cailler, *Sur. Sci.* **83**, (1979) 498.

[Gl60] M. Glick and R.A. Ferrell, *Ann. Phys.* **11**, (1960) 359.

[Gr59] M. Gryzinski, *Phys. Rev.* **115**, (1959) 374.

[Gr63] M. Green, *Proc. Phys. Soc.* **82**, (1963) 204.

[Gr65a] M. Gryzinski, *Phys. Rev.* **138**, (1965) A305.

[Gr65b] M. Gryzinski, *Phys. Rev.* **138**, (1965) A322.

[Gr65c] M. Gryzinski, *Phys. Rev.* **138**, (1965) A336.

[Gr86] M. Gryzinski and J. A. Kunc, *J. Phys. B* **19**, (1986) 2479.

[Gr69] A.E.S. Green, D.L. Sellin and A.S. Zachor, *Phys. Rev.* **184**, (1969) 1.

[Gr76] A.J. Green and R.C.G. Leckey, *J. Phys. D* **9**, (1976) 2123.

[Gu75] S.C. Gupta and J.A. Rees, *J. Phys. B* **8**, (1975) 417.

[Gu76] O. Gunnarsson and B.I. Lundqvist, *Phys. Rev. B* **13**, (1976) 4274.

[Ha28] D.R. Hartree, *Proc. Cambridge Phil. Soc.* **24**, (1928) 111.

[Ha74] R.J. Hawryluk, A.M. Hawryluk, and H.I. Smith, *J. Appl. Phys.* **45**, (1974) 2551.

[Ha75] E. Haug, *Z. Physik* **30a**, (1975) 1099.

[Ha79] R.N. Hamm, J.E. Turner, H.A. Wright, R.H. Ritchie, *IEEE Trans. Nucl. Sci.* **NS–26**, (1979) 4892.

[Ha84] E. Haug and M. Keppler, *J. Phys. B* **17**, (1984) 2075.

[He76] J. Heńoc and F. Maurice, National Bureau of Standards Special Publication 460, (1976) 61.

[He85] J. Herbák, Á. Köver, E. Szmola, D. Berényi and I.Cserny, *Acta. Phys. Hung.* **58**, (1985) 63.

[Hi81] R. Hippler, K. Saeed, I. McGregor and H. Kleinpoppen, *Phys. Rev. Lett.* **46**, (1981) 1622.

[Hu32] A.L. Hughes, J.H. McMillian and G.M. Webb, *Phys. Rev.* **41**, (1932) 154.

[Hu33] A.L. Hughes, J.H. McMillian, *Phys. Rev.* **43**, (1933) 875.

[Hu75] J. H. Hubbell, W. J. Veigle, E. A. Briggs, R. T. Brown, D. T. Cromer and R. J. Howerton, *J. Phys. Chem. Ref. Data* **4**, (1975) 471.

[Ic80] S. Ichimura, M. Aratama and R. Shimizu, *J. Appl. Phys.* **51**, (1980) 2853.

[In68] M. Inokuti, *Rev. Mod. Phys.* **43**, (1971) 297.

[Ja62] J. D. Jackson, *Classical Electrodynamics,*, John Wiley and Sons, Inc. New York (1962).

[Ja75] J. D. Jackson, *Classical Electrodynamics, 2nd Ed.*, John Wiley and Sons, Inc. New York (1975).

[Ja76a] R.H.J. Jansen and F.J. de Heer, *J. Phys. B* **9**, (1976) 213.

[Ja76b] R.H.J. Jansen, F.J. de Heer, H.J. Luyken, B. van Wingerden and H.J. Blaauw, *J. Phys. B* **9**, (1976) 185.

[Je75] J. Jessenberger and W. Hink, *Z. Physik* **A275**, (1975) 331.

[Ke55] R. Kerscher and H. Kulenkampff, *Z. Physik* **140**, (1955) 632.

[Ke62] K. Keck, *Z. Physik* **167**, (1962) 468.

[Ke65] J. Kessler and H. Lindner, *Z. Physik* **183**, (1965) 1.

[Ke68] J. Kessler and N. Weichert, *Z. Physik* **212**, (1968) 48.

[Ki53] E. Kinzinger, *Z. Naturforsch.* 8a, (1953) 312.

[Ki81] L. Kissel, C. MacCallum and R.H. Pratt, *Bremsstrahlung Energy Spectra from Electrons of Kinetic Energy 1 keV* $\leq T \leq$ *2000 keV Incident on Neutral Atoms 1* $\leq Z \leq$ 92, Sandia Laboratory Report SAND81-1377 (1981).

[Ki83] L. Kissel, C.A. Quarles and R.H. Pratt, *At. Data Nuc. Data Tables* **28**, (1983) 381.

[Ko59] H.W. Koch and J.W. Motz, *Rev. Mod. Phys.* **31**, (1959) 920.

[Ko67] H. Kolbenstvedt, *J. Appl. Phys.* **38**, (1967) 4785.

[Ko81a] M. Kotera, K. Murata and K. Nagami, *J. Appl. Phys.* **52**, (1981) 997.

[Ko81b] M. Kotera, K. Murata and K. Nagami, *J. Appl. Phys.* **52**, (1981) 7403.

[Ku84] R.N. Kulkarni and S.J. Supe, *Phys. Med. Biol.* **29**, (1984) 185.

[La33] G.O. Langstroth, *Proc. Roy. Soc.* **A140**, (1933) 159.

[Li54] J. Lindhard, *Kgl. Danske Videnskab. Selskab. Mat.Fys. Medd.* **28**, (1954) No. 8.

[Li70] D.A. Liberman, D.T. Cromer and J.T. Waber, *Comput. Phys. Commun.* **2**, (1970) 107.

[Li78a] D. Liljequist, *J. Phys. D* **11**, (1978) 839.

[Li78b] D. Liljequist, T. Ekdahl and U. Bäverstam, *Nucl. Instrum. & Methods* **155**, (1978) 529.

[Lo70] W. Z. Lotz, *Z. Physik* **232**, (1970) 101.

[Mæ67] B. Mæhlum and J. Stadsnes, *Phys. Norv.* **2**, (1967) 111.

[Ma72] S.T. Manson, *Phys. Rev. A* **6**, (1972) 1013.

[Ma73] T. Matsukawa, K. Murata and R. Shimuzu, *Phys. Stat. Sol. B* **55**, (1973) 371.

[McD71] I.R. McDonald, A.M. Lamki and G.F.G. Delaney, *J. Phys. D* **4**, (1971) 1210.

[McK48] W. McKinley and H. Feshbach, *Phys. Rev.* **74**, (1948) 12.

[Mø32] C. Møller, *Ann. Physik* **14**, (1932) 568.

[Mo30] N.F. Mott, *Proc. Roy. Soc.* **A126**, (1930) 259.

[Mo49] N. F. Mott and H. S. W. Massey, *The Theory of Atomic Collision, 2nd Ed.*, Clarendon Press, Oxford, (1949).

[Mo58] J. W. Motz and R. C. Placious, *Phys. Rev.* **109**, (1958) 235.

[Mo63] J.W. Motz, R.C. Placious and C.E. Dick, *Phys. Rev.* **132**, (1963) 2558.

[Mo64] J.W. Motz, H. Olsen, and H.W.Koch, *Rev. Mod. Phys.* **36**, (1964) 881.

[Mu71] K. Murata, T. Matsukawa and R. Shimizu, *Jap. J. Appl. Phys.* **10**, (1971) 678.

[Mu79] K. Murata, M. Kotera and K. Nagami, *Microbeam Analysis–1979*, D.E. Newbury, ed., San Fransicso Press, San Fransisco (1979) 35.

[Mu80] K. Murata, M. Kotera, K. Nagami, *Proceedings of the Eighth International Conference on X-Ray Optics and Microanalysis*, D. Beaman, R. Ogilvie, D. Wittry, eds., Pendell Publishing Co., Midland, MI, (1980) 434.

[Mu81] K. Murata, D.F. Kyser and C.H. Ting, *J. Appl. Phys.* **52**, (1981) 4396.

[My76] R.L. Myklebust, D.E. Newbury and H. Yakowitz, National Bureau of Standards Special Publication 460, (1976) 105.

[Ne79a] D.E. Newbury and R.L. Myklebust, *Ultramicrosopy* **3**, (1979) 391.

[Ne79b] D.E. Newbury and R.L. Myklebust, *Microbeam Analysis – 1979*, San Fransisco Press, Inc., San Fransisco, (1979) 51.

[Ne80] D.E. Newbury, R.L. Myklebust and K.F.J.Heinrich, *Proceedings of the Eighth International Conference on X-Ray Optics and Microanalysis*, D. Beaman, R. Ogilvie, D. Wittry, eds., Pendell Publishing Co., Midland, MI, (1980) 57.

[Ne85] W.R. Nelson, H. Hirayama and D.W.O. Rogers *The EGS4 Code System*, Stanford Linear Accelerator Center Report SLAC-265 (1985)

[Ni59] B.P. Nigam, M.K. Sundararaman and T.-Y.-Wu, *Phys. Rev.* **115**, (1959) 491.

[Pe56] W.G. Pettus, H.G. Blosser, and F.L. Hereford, *Phys. Rev.* **101**, (1956) 17.

[Pi52] D. Pines and D. Bohm, *Phys. Rev.* **85**, (1952) 338.

[Pi63] D. Pines *Elementary Excitations in Solids*, W.A. Benjamin, Inc., New York, 1963.

[Pl85] H. Platten, G Schiwietz and G. Nolte, *Physics Letters* **107A**, (1985) 83.

[Po47] L.T. Pockman, D.L. Webster, P. Kirkpatrick and K. Harworth, *Phys. Rev.* **71**, (1947) 330.

[Po76a] C. J. Powell, National Bureau of Standards Special Publication 460, (1976) 97.

[Po76b] C. J. Powell, *Rev. Mod. Phys.* **48**, (1976) 33.

[Pr70] V. M. Pressa and W. R. Newell, *Phys. Scr.* **3**, (1971) 165.

[Pr77] R.H. Pratt, H.K.Tseng, C.M. Lee, L. Kissel, C. MacCallum and M. Riley, *At. Data Nuc. Data Tables* **20**, (1977) 175.

[Pr79] A. Proykova, *Nucl. Instrum. & Methods* **160**, (1979) 321.

[Pr81a] R.H. Pratt, *Comments Atom. Mol. Phys.* **10**, (1981) 121.

[Pr81b] R.H. Pratt, H.K.Tseng, C.M. Lee, L. Kissel, C. MacCallum and M. Riley, *At. Data Nuc. Data Tables* **26**, (1981) 477.

[Qu81] C.A. Quarles and D.B. Heroy, *Phys. Rev. A* **24**, (1981) 48.

[Qu62] J.J. Quinn, *Phys. Rev.* **126**, (1962) 1453.

[Re65] D.H. Rester and J. Rainwater, *Phys. Rev.* **140**, (1965) A165.

[Re68] L. Reimer, *Optik* **27**, (1968) 86.

[Re76] L. Reimer and E.R. Krefting, National Bureau of Standards Special Publication 460, (1976) 45.

[Re85] L. Reimer, *Scanning Electron Microscopy*, Springer-Verlag, Berlin, (1985).

[Ri57] R.H. Ritchie, *Phys. Rev.* **106**, (1957) 874.

[Ri59] R.H. Ritchie, *Phys. Rev.* **114**, (1959) 644.

[Ri75] M.E. Riley, C.J. MacCallum, and F. Biggs, *At. Data Nuc. Data Tables* **15**, (1975) 443.

[Ri83] M.E. Riley, C.J. MacCallum, and F. Biggs, *At. Data Nuc. Data Tables* **28**, (1983) 379.

[Ru11] E. Rutherford, *Phil. Mag.* **21**, (1911) 669.

[Sa37] H. Saegusa and K. Kikuchi, *Tohoku Univ. Sci. Reports* **25**, (1937) 817.

[Sa41] J.L. Saunderson and O.S. Duffendack, *Phys. Rev.* **60**, (1941) 190.

[Sa84a] F. Salvat and J. Parellada, *J. Phys. D* **17**, (1984) 185.

[Sa84b] F. Salvat and J. Parellada, *J. Phys. D* **17**, (1984) 1545.

[Sa85] F. Salvat, R. Mayol, E. Mollins and J. Parellada, *J. Phys. D* **18**, (1985) 1401.

[Sa86] F. Salvat, J.D. Martinez, R. Mayol, and J. Parellada, *Comp. Phys. Comm.* **42**, (1986) 93.

[Sa87] F. Salvat, R. Mayol and J. D. Martinez, *J. Phys. B* **20**, (1987) 6597.

[Sc49] J. Schwinger, *Phys. Rev.* **75**, (898) 1949.

[Sc68] L. I. Schiff, *Quantum Mechanics, 3rd Edition*, McGraw-Hill Book Company, New York, (1968).

[Sc78] J.H. Scofield, *Phys. Rev. A* **18**, (1978) 963.

[Sc79] S.E. Schnatterly, *Solid State Physics* **34**, (1979) 275.

[Se81] M. Semaan and C. Quarles, *Phys. Rev. A* **24**, (1981) 2280.

[Se82] M. Semaan and C. Quarles, *Phys. Rev. A* **26**, (1982) 3152.

[Se85] S.M. Seltzer and M.J. Berger, *Nucl. Instrum. & Methods Phys. Research* **B12**, (1985) 95.

[Se89] S. M. Seltzer, *Monte Carlo Transport of Electrons and Photons*, T. M. Jenkins, W. R. Nelson and A. Rindi, Eds., Plenum Press, New York (1989) 81.

[Sh56] N. Sherman, *Phys. Rev.* **103**, (1956) 1601.

[Sh75] R. Shimizu, Y. Kataoka, T. Matsukawa, T. Ikuta, K. Murata, and H. Hashimoto, *J. Phys. D* **8**, (1975) 820.

[Sh76] R. Shimizu, Y. Kataoka, T. Ikuta, T. Koshikawa, and H. Hashimoto, *J. Phys. D* **9**, (1976) 101.

[Sh77] R. Shimizu, M. Aratama, S. Ichimura, Y. Yamazaki, T. Ikuta, *Appl. Phys. Lett.* **31**, (1977) 692.

[Sh78] R. Shimizu and T.E. Everhart, *Appl. Phys. Lett.* **33**, (1978) 784.

[Sh79] R. Shimizu, S. Ichimura and M. Aratama, *Microbeam Analysis - 1979*, San Fransisco Press, Inc., San Fransisco, (1979) 30.

[She80] G.L. Sheldon and R.E. Ogilvie, *Proceedings of the Eighth International Conference on X-Ray Optics and Microanalysis*, D. Beaman, R. Ogilvie, D. Wittry, eds., Pendell Publishing Co., Midland, MI, (1980) 63.

[Shi80] R. Shimizu, *Proceedings of the Eighth International Conference on X-Ray Optics and Microanalysis*, D. Beaman, R. Ogilvie, D. Wittry, eds., Pendell Publishing Co., Midland, MI, (1980) 13.

[Si81] L. T. Sin Fai Lam and W. E. Baylis, *J. Phys. B* **14**, (1981) 559.

[Sm70] L. Smrčka, *Czech. J. Phys.* **B20**, (1970) 291.

[So31] A. Sommerfeld, *Ann. Phys.* **11**, (1931) 257.

[Sp82] A. Špelek, *Nucl. Instrum. & Methods* **198**, (1982) 399.

[St59] H.W. Streitwolf, *Ann. Phys. Leipzig* **3**, (1959) 183.

[Su73] V. Sundararaman, M.A. Prasad, and R.B. Vora, *Phys. Med. Biol.* **18**, (1973) 208.

[Ter78] M. Terrisol and J.-P. Patau, *J. Phys* **39**, (1978) 189.

[Ts71] H.K. Tseng and R. H. Pratt, *Phys. Rev. A* **3**, (1971) 100.

[Ts74] H.K. Tseng and R. H. Pratt, *Phys. Rev. Lett.* **33**, (1974) 516.

[Ts79] H.K. Tseng, R. H. Pratt and C.M. Lee, *Phys. Rev. A* **19**, (1979) 187.

[Tu76] C.J. Tung, *et al.*, RADC-TR-76-125, (1976).

[Tu79] C.J. Tung, J.C. Ashley and R.H. Ritchie, *Surface Science* **81**, (427) 1979.

[Un79] K. Unnikrishnan and M.A. Prasad, *Radiat. Res.* **80**, (1979) 225.

[Va74a] D.W. Vande Putte, *Electron Energy-Loss and Multiple-Scattering Distributions below 2 MeV*, South Africa Atomic Energy Board report PEL-235, (1974).

[Va74b] D.W. Vande Putte, *Nucl. Instrum. & Methods* **115**, (1974) 117.

[Va83] S. Valkealahti and R.M. Nieminen, *Appl. Phys. A* **32**, (1983) 95.

[Va84] S. Valkealahti and R.M. Nieminen, *Appl. Phys. A* **35**, (1984) 51.

[Wa70] D.W. Walker, *Adv. Phys.* **20**, (1970) 257.

[We27] G. Wentzel, *Z. Physik* **40**, (1927) 590.

[Wh39] J.A. Wheeler and W. E. Lamb, *Phys. Rev.* **55**, (1939) 858.

[Wi35] E. J. Williams, *Kgl. Danske Videnskab. Selskab. Mat.Fys. Medd.* **13**, (1935) No. 4.

[Wo56] C.R. Worthington and S.G. Tomlin, *Proc. Phys. Soc. A* **69**, (1956) 401.

[Ya76] Y. Yamazaki, R. Shimizu, and H. Hashimoto, *J. Phys. Soc. Japan* **41**, (1976) 721.

[Ye54] D.R. Yennie, D.G. Ravenhall and R.N. Wilson, *Phys. Rev.* **95**, (1954) 500.

CHAPTER III

EVALUATION OF CUMULATIVE SCATTERING DESCRIPTIONS

This chapter evaluates cumulative scattering descriptions pertaining to prediction of the energy loss and angular deflection of electrons passing through a finite thickness of a given material. The goal is to make statements about the range of validity of the various formalisms with respect to incident electron energy, target atomic number and electron tracklength. The methodology of the evaluations in the sections of this chapter are laid out analogously to those in the preceding chapter on the evaluation of single scattering cross sections. First, the relevant analytical and numerical techniques for determining cumulative scattering distributions are examined, and an attempt is made to predict the various ranges of validity based on the physical and numerical assumptions underlying the derivations. Previous investigators' use of cumulative scattering descriptions are then surveyed. Next, experiments to be used in evaluating the numerical results of the various theories are listed, and finally the results of the comparison of numerical and experimental results are presented, thus predicting the the ranges of validity of the various distributions.

3.1 Energy Loss Using the Continuous Slowing Down Approximation

The most widely used method for describing the energy loss of an electron as it traverses a given track length is by use of the continuous slowing down approximation. In this technique energy loss is considered to occur continuously along the electron path, at a rate dependent on the nature of the medium and the electron energy. Such a treatment seems reasonable since the distance between individual collisions resulting in some energy loss is small compared with the typical material thickness being investigated. If the rate of energy loss is given by $-\frac{dE}{dx}$, then the total energy loss in traversing a given material thickness s is then given by

$$\Delta E = \int_0^s ds' \left| \frac{dE}{dx} \right|. \tag{3.1}$$

Note that since the electron loses energy as it moves, the derivative $\frac{dE}{dx}$ is negative. The stopping power of the medium is defined in units of energy *loss* per tracklength, and so is a positive quantity given by $-\frac{dE}{dx}$. Several formulations of the stopping power are examined here.

3.1.1 The Bethe Formula for Collisional Losses

If $\sigma(E;Q)$ is the cross section for electrons with initial energy E which lose energy Q in a single collision, then the stopping power is given by

$$-\frac{dE}{dx} = \int_0^E N\sigma(E;Q)\, Q\, dQ. \tag{3.2}$$

Bethe [Be32] has evaluated this expression by dividing the integral into high and low energy transfer regions, delimited by some energy transfer Q_0 yielding

$$-\frac{dE}{dx} = \int_0^{Q_0} dQ\, N\sigma(E;Q)\, Q + \int_{Q_0}^E dQ\, N\sigma(E;Q)\, Q. \tag{3.3}$$

Q_0 is chosen large enough such that the target electrons can be considered to be free for the purposes of modeling energy transfers greater Q_0. This allows substitution of the Møller cross section for $\sigma(E;Q)$ in the high transfer regions to give for the high energy transfer portion

$$\begin{aligned}\int_{Q_0}^{E} dQ\, N\sigma(E;Q)\, Q &= \tfrac{2\pi N e^4 Z}{mv^2}\int_{Q_0}^{E/2} dQ\, Q\left[\tfrac{1}{Q^2}+\tfrac{1}{(E-Q)^2}+\tfrac{2\tau+1}{(\tau+1)^2}\tfrac{1}{Q(E-Q)}+\tfrac{1}{(E+mc^2)^2}\right] \\ &= \ln\frac{E}{4Q_0}+1-\frac{2\tau+1}{(\tau+1)^2}\ln 2+\frac{1}{8}\frac{\tau^2}{(\tau+1)^2}. \qquad (3.4)\end{aligned}$$

Note that because the Møller cross section was derived under the assumption that the two ejected electrons are indistinguishable that the maximum energy transfer is $E/2$, and that τ is given by E/mc^2. For the low energy transfer portion, Bethe uses the fact that energy transferred to the atom must coincide with excitation of discrete electron energy levels to rewrite the the first integral of 3.3 as

$$\int_{Q_0}^{E} dQ\, N\sigma(E;Q)\, Q = \sum_{n=0}^{\infty}(E_n - E_0)\int_{Q_{min}}^{Q_0}\sigma_n(E;Q)dQ. \qquad (3.5)$$

where $\sigma_n(E;Q)$ represents the differential cross section for an incoming electron of energy E losing energy Q and exciting the atom to state n. As seen in chapter II, the differential cross section is often written as

$$\sigma_n dQ = \frac{2\pi e^4 Z}{mv^2}\,|F_n(q)|^2\,\frac{dQ}{Q^2}$$

where F_n is the inelastic form factor and q represents the momentum transfer when a free electron at rest which absorbs energy transfer Q. In a correct relativistic treatment, the expression for $d\sigma_n$ should be [Fa64]

$$\sigma_n dQ = \tfrac{2\pi e^4 Z}{mv^2}\left\{\frac{|F_n(q)|^2}{Q^2(1+Q/2mc^2)^2}+\frac{|\beta_t G_n(q)|^2}{[Q(1+Q/2mc^2)-(E_n-E_0)^2/2mc^2]^2}\right\}\left(1+\tfrac{Q}{mc^2}\right)dQ, \qquad (3.6)$$

where the second term in this expression represents a contribution due to the emission and reabsorption of virtual photons, and β_t is proportional to the component of the

incident electron velocity vector perpendicular to the momentum transfer direction. In evaluating this cross section under the condition of low Q, the inelastic form factor can be approximated by

$$|F_n(q)|^2 = f_n \frac{Q}{E_n - E_0} \tag{3.7}$$

and the virtual photon exchange term as

$$|\beta_t G_n(q)|^2 = f_n \frac{\beta_i^2 (E_n - E_0)}{2mc^2} \tag{3.8}$$

where f_n is the dipole oscillator strength. The dipole oscillator strength, f_n, is closely related to the generalized oscillator strength $f_n(K)$ discussed in chapter II, and is in fact the limit of $f_n(K)$ as $K \to 0$. For the sake of convenience, throughout this chapter the dipole oscillator strength has been normalized so that

$$\sum_{n=0}^{\infty} f_n = 1.$$

The cross section can finally be expressed as

$$\sigma_n dQ = \frac{2\pi N e^4 Z}{mv^2} \frac{f_n}{E_n - E_0} \left[\frac{dQ}{Q} + \frac{\beta^4 \sin^2 \psi}{(1 - \beta^2 \cos^2 \psi)^2} d(\cos^2 \psi) \right] \tag{3.9}$$

where $\cos^2 \psi$ is defined as

$$\cos^2 \psi = \frac{Q_{min}(Q_{min} + 2mc^2)}{Q(Q + 2mc^2)} \tag{3.10}$$

and where the minimum energy transfer Q_{min} is given by $(E_n - E_0)/2mv^2$. The angle ψ is the angle between the incident electron and the momentum transfer. Equation 3.5 can be evaluated to yield

$$\int_{Q_0}^{E} dQ\, N\sigma(E;Q)\, Q = \frac{2\pi N e^4 Z}{mv^2} \ln \frac{Q_0 2mv^2}{1 - \beta^2} - \beta^2 - 2 \sum_{n=0}^{\infty} f_n \ln(E_n - E_0). \tag{3.11}$$

Bethe now defines a quantity I, the mean ionization potential, as

$$\ln I = \sum_{n=0}^{\infty} f_n \ln(E_n - E_0). \tag{3.12}$$

Combining 3.4, 3.11, and 3.12, Bethe arrives at

$$-\frac{dE}{dx} = \frac{2\pi Ne^4 Z}{mv^2} \ln \frac{mv^2 E}{2I^2(1-\beta^2)} + 1 - \beta^2 - \frac{2\tau+1}{(\tau+1)^2} \ln 2 + \frac{1}{8}\frac{\tau^2}{(\tau+1)^2}. \quad (3.13)$$

In evaluating this expression, the parameter I is taken from fits to experimental data. For this work, values are taken from the compilation supplied by Berger and Seltzer [Be82].

Because of the interaction between the atomic electrons of the constituent atoms in compounds, simple weighting by the mass fraction (usually referred to as Bragg additivity) is not always accurate. In this work, a prescription devised by Berger and Seltzer [Be82] in which the constituent mean ionization potentials are multiplied by 1.13 before weighting is used. Berger also suggests the use of a separate set of ionization potentials when certain elemental gases are found in gaseous compounds and yet another set when these elements are found in condensed media, but this approach is not used here.

Often in Monte Carlo calculations it is desirable to know the stopping power for collisions resulting in energy transfers less than a given value Q_r, which lies between $E/2$ and Q_0. In order to calculate this quantity, called the restricted stopping power, $-\left(\frac{dE}{dx}\right)_{res}$, Q_r is substituted as the upper limit in the integral over the Møller cross section. If we define $\epsilon_r = Q_r/E$, we have for the restricted stopping power

$$-\left(\frac{dE}{dx}\right)_{res} = \frac{2\pi Ne^4 Z}{mv^2} \ln \frac{E\,mv^2}{2I^2(1-\beta^2)} - 1 - \beta^2 + \frac{\tau^2}{(\tau+1)^2}\frac{\epsilon_r^2}{2} + \frac{2\tau+1}{(\tau+1)^2}\ln(1-\epsilon_r) + \ln[4\epsilon_r(1-\epsilon_r)] + \frac{1}{1-\epsilon_r} \quad (3.14)$$

The Density Effect

As first shown and quantified by Fermi [Fe40], the cross sections used above in the derivation of the formula for the stopping power assume incorrectly that the polarized

electric field of a condensed media target does not perturb the field of the impingent particle. In some cases this perturbation (called the density effect) is found to cause a significant decrease in the stopping power of the medium. Sternheimer [St52, St56, St66] has developed a model based on a quantum electro-dynamical model of the projectile-target system which is in general use. In Sternheimer's formulation the change in the stopping power is given by

$$\Delta\frac{dE}{dx} = \frac{2\pi Ne^4Z}{mv^2}\left[\sum_i f_i \ln\frac{l_i^2+l^2}{l_i^2} - l^2(1-\beta^2)\right]. \tag{3.15}$$

In this expression f_i is the oscillator strength of the ith transition and l_i is defined as

$$l_i = \left[\bar{\nu}_i^2 + \frac{2}{3}f_i\right]^{1/2} \tag{3.16}$$

where $\bar{\nu}_i$ is frequency ν_i associated with the ith transition divided by the plasma frequency of the media, ν_p, which is defined as in chapter II as $(n_e e^2/\pi m)^{1/2}$. The final component of 3.15 is a frequency l which is the solution to

$$\frac{1}{\beta^2} - 1 = \sum_i \frac{f_i}{\bar{\nu}_i^2 + l^2}. \tag{3.17}$$

In evaluating these expression, the energies $h\nu_i$ corresponding to the frequencies ν_i are given in a first approximation by the binding energies of the atomic subshells and the oscillator strengths f_i by the occupation numbers divided by the number of electrons. A correction for this crude approximation is provided by recalling that according to Bethe's definition of the mean ionization potential I, we should find

$$\ln I = \sum_i f_i \ln h\nu_p l_i. \tag{3.18}$$

We introduce a correction μ_{st} to the $\bar{\nu}_i$,

$$\bar{\nu}_i = \mu_{st}\frac{\nu_i}{\nu_p} \tag{3.19}$$

such that if this new expression for $\bar{\nu}_i$ is used in th e definition of l_i, then 3.18 holds. Compounds are treated by considering all atomic subshells of all constituents as being part of a single system.

A parameterization of calculated values of the density effect correction has been presented by Sternheimer and Peierls [St71] and Sternheimer, Berger and Seltzer [St84], but has been found to be somewhat inaccurate, and so throughout this work values for δ, the term in the brackets of equation 3.15, are calculated by the method described above. Treated are shells K through O in their entirety, and subshells P–I through P–V and Q–I through Q–II. The values of the binding energies are taken from [Ca75] and the occupancy of the shells is assumed to be regular, except for 17 elements whose shells are considered to be filled according to the prescription found in [Le59].

For the case of conducting materials (in the present work, all (and only) solid, single element materials are considered conductors) the conduction electrons must be treated specially [St56]. The conduction electrons are assumed to be completely unbound but to be responsible for energy loss through plasmon excitation, as described in chapter 2. If j represents the total number of oscillators (including the plasmon) then the transition frequency for the plasma oscillator, ν_j is taken to be zero and the strength f_j, given by the number of conduction electrons divided by the total number of electrons, is taken to be simply the normal valence number (divided by Z) for the element as given in [We85]. Additionally, the factor 2/3 in l_j is replaced by unity. Thus for conducting materials the correction factor μ_{st} is given by the solution of

$$\ln I = \sum_{i=1}^{j-1} f_i \ln\left[(\mu_{st} h\nu_i)^2 + \frac{2}{3} f_i (h\nu_p)^2\right]^{1/2} + f_j \ln(f_j^{1/2} h\nu_p). \qquad (3.20)$$

This equation is solved numerically by the *regula falsi* technique. Sternheimer claims

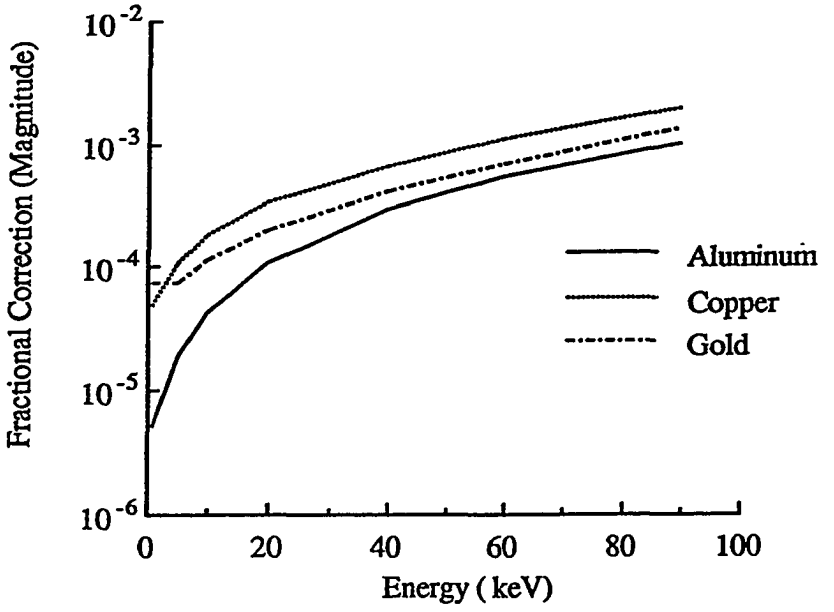

Figure 3.1: Fractional Density Effect Correction vs. Energy

that the correction μ_{st} can be described physically as taking into account excitations (ionizations) of bound electrons into continuum states involving energies greater than the absorption edge energies (the $h\nu_i$'s). For insulators (in which $\bar{\nu}_j \neq 0$) it is seen that there is no non-zero solution for l in equation 3.17 at velocities less than β_0 given by

$$\beta_0 = \left[\sum_i f_i \bar{\nu}_i^2\right]^{1/2} \tag{3.21}$$

and so δ is taken to be zero at all energies such that $v/c \leq \beta_0$.

Values of $(\Delta\frac{dE}{dx})/\frac{dE}{dx}$ calculated from this method are given as a function of energy in figure 3.1 for several elements. It is seen that the correction decreases at low velocities, due to the fact that the use of experimentally determined values of I in the stopping power formula already accounts for the density effect at low energies, so that at all energies pertinent to this work, the effect is negligible.

Flynn's Correction at Low Energy

It is apparent from equation 3.13 that in the limit of $\beta \rightarrow 0$ the stopping power will become negative as E becomes less than roughly $I\sqrt{\frac{2}{e}}$. For high Z materials, this cutoff occurs at energies in the range of a few keV. As this is in conflict with experiment and theory, some correction must be made in order to apply 3.13 in the present work. Rather than appearing as corrections to derivation of the Bethe formula, most low energy treatments of stopping power are based on either empirical formulations or the complex dielectric constant method. One work, however, a semi-empirical correction due to Flynn [Fl76], is applied as a correction to the ionization potential. Flynn rewrites the expression for the ionization potential 3.12 as

$$\ln I_f = \frac{\sum_{n=0}^{n'} f_n \ln(E_n - E_0)}{\sum_{n=0}^{n'} f_n} \tag{3.22}$$

where n' presents the highest kinematically allow excited state and notes that for high velocities $n' \rightarrow \infty$. He then rewrites this expression as an integral and assumes an oscillator strength of the form

$$f(E) = \frac{E}{Z} e^{-E/I_f} \tag{3.23}$$

and takes the integral from 0 to Q_{max}. In order to generalize the expression for all elements, Flynn assumes the form of I_f proposed by Bloch, $I_f = ZI_p$ in the expression for $f(E)$. After substituting this into 3.22 and integrating and then examining the result at high incident velocities, Flynn shows that his expression for I_f reduces to

$$\ln I_f = \ln ZI_p + 1 - \gamma \equiv \ln I \tag{3.24}$$

where γ is Euler's constant and I is the experimentally determined ionization potential. This gives an expression for the low velocity ionization potential of

$$\ln I_f = \ln I + \gamma - 1 + f(x) \tag{3.25}$$

where $x = Q_{max}/ZI_p$ and

$$f(x) = \frac{1 - \gamma - e^{-x}[1 + (1+x)\ln x] - E_i(x)}{1 - (1+x)e^{-x}} \tag{3.26}$$

in which $E_i(x)$ is the exponential integral function. The function $f(x)$ is the exact form of the integral of 3.22, and reduces to $1-\gamma$ at high velocity. At this point three semi-empirical corrections are added. First, as the binding energy of the electrons will reduce the value of Q_{max}, it is arbitrarily reduced by a factor of $e^{\gamma-1}$, so that $x = Q_{max}/I_0$. Second, as the actual value of Q_{max} will fluctuate because of the distribution of atomic electron velocities, a term $g(x)$ is added to the expression for $\ln I_f$ of the form $g(x) = Ae^{-x}$. It can be shown that in order to maintain consistency at low velocities that $A = 3/2 - \gamma$. Finally, Q_{max} is adjusted in order that the stopping power be zero at zero velocity. We depart here somewhat from Flynn and note that this assumption requires

$$Q_{max}^{eff} = \frac{Ee^{(1-\beta^2)/2}}{\sqrt{2}} \tag{3.27}$$

in order that $-\frac{dE}{dx}$ as given by 3.13 approach zero at zero velocity. We are finally left with a correction to the ionization potential of

$$\ln I_f = \ln I + \gamma - 1 + (\frac{3}{2} - \gamma)e^{-Q_{max}^{eff}/I} + f(Q_{max}^{eff}/I). \tag{3.28}$$

Even though Flynn claims that his derivation has at its foundation the idea that the stopping power should be zero at zero energy, it is actually performed under the assumption that the argument of the log term in the stopping power should approach

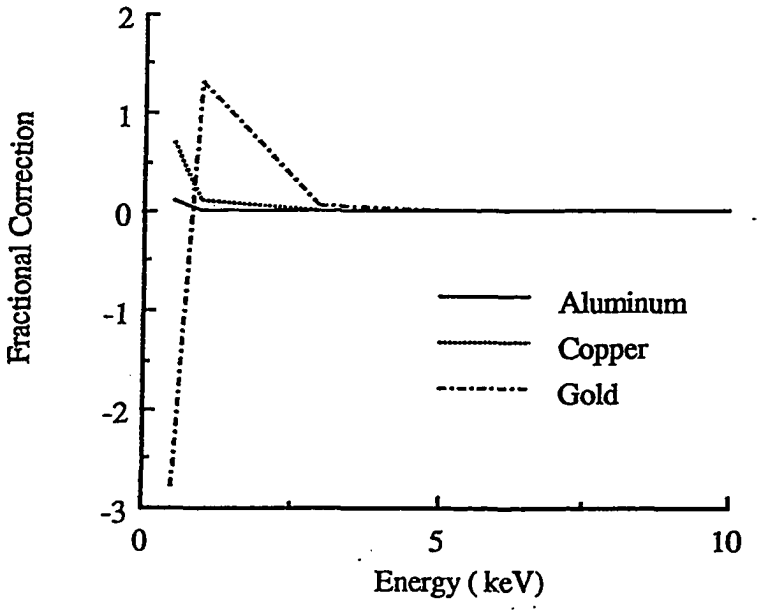

Figure 3.2: Flynn's Correction to Low Energy Stopping Power

unity. Numerically, this leads to a situation in which the log term approaches zero roughly at the same rate as the v^2 term in the denominator of 3.13. Thus, the corrected stopping power of Flynn tends not to zero but to a constant value at zero energy. This effect does not manifest itself however until E becomes less than a few eV.

Values of $\frac{dE}{dx}_f / \frac{dE}{dx}$ as a function of energy and atomic number are given in figure 3.2. It is seen that for high Z materials, the Flynn correction starts to become appreciable around 3 keV. It is interesting to note that its magnitude is greater than 100% for lower energies, and that it corrects the defect in the Bethe theory which predicts negative stopping power (positive $\frac{dE}{dx}$) at very low velocities.

3.1.2 Empirical Stopping Power Formulations at Low Energies

Several investigators have devised empirical formulations of the stopping power at low energies, and two often used examples are given here. Love, Cox and Scott [Lo77]

used in a Monte Carlo investigation the following formula, which they attribute to Rao-Sahib and Wittry [Ra74], for electrons with energy less than 6.338 times the ionization potential:

$$-\frac{dE}{dx} = \frac{6.236\times10^4\rho Z}{A(EI)^{1/2}}. \tag{3.29}$$

This formula is based on a simple, parabolic extrapolation of the Bethe formula so that the inverse of the stopping power becomes infinite at zero energy. Note that this is somewhat at odds to the usual assumption that the stopping power tends to zero at zero energy.

The second widely cited empirical formulation of low energy stopping power is given by Kanaya and Okayama [Ka72]. From an empirically based derivation of the energy transfer cross section, they determine a stopping power given by

$$-\frac{dE}{dx} = \lambda_s \frac{3\times 2^{5/3}\pi a^{1/3}e^{10/3}}{E^{2/3}}\frac{\rho N_a Z}{A} \tag{3.30}$$

in which λ_s is an empirically determined constant, N_a is Avagodro's number and a is the effective screened radius of the atom, $.8853a_H Z^{-1/3}$, with a_H the Bohr radius of the hydrogen atom. From range data, Kanaya and Okayama have determined λ_s to be 0.182. It is noted again that in this approximation, the stopping power becomes infinite at small energies.

3.1.3 Stopping Power by Complex Dielectric Constant Technique

Stopping powers may be calculated in a way analogous to that used to determine the differential inverse mean free path as seen in Chapter II, using the complex dielectric constant. Following the derivation for the differential inverse mean free path by use of the complex dielectric constant, an expression for the stopping power

can be written as

$$-\frac{dE}{dx} = \int_0^{E-E_F} d(\hbar\omega)\,\hbar\omega\,\tau(E,\hbar\omega) \tag{3.31}$$

where $\tau(E,\hbar\omega)$ is the differential inverse mean free path of an electron for energy E in the medium in question and is determined from the complex dielectric constant. As in chapter II, despite the success of this formulation in modeling low energy stopping powers, because of the absence of a suitable, universally applicable formalism, this technique was not pursued in this work.

3.1.4 Models Used by Previous Investigators

Models of continuous energy loss or restricted continuously loss used by previous investigators working in the kilovolt energy region are given in table 3.1. Not surprisingly, the Bethe theory is the most widely used technique, because of the simplicity of its mathematical expression and its accuracy except at quite low energies and at high atomic number. Those investigators working at high Z and/or low energy have been forced (or should have been forced) to employ other techniques. Techniques listed here which have not been examined generally involve empiricisms peculiar to an individual material.

3.1.5 Stopping Power Experiments at Low Energies

Although quite a number of investigations of the scattering of transmitted beams of mono-energetic electron have been performed, in very few instances are the results reported in terms of the stopping power, since corrections for several important experimental effects must be made. Typically, electrons are passed through a thin foil and their emergent energies are measured and the average loss determined. The

Continuous Energy Loss Treatment	Monte Carlo Authors
Bethe theory	Love, Cox and Scott [Lo77] Murata, Kyser and Ting [Mu81] Reimer and Krefting [Re76] Sidei *et al.* [Si57] Ichimura *et al.* [Ic80] Vande Putte [Va74] Berger [Be63] ETRAN [Be68] EGS [Fo78, Ne85] Heńoc and Maurice [He76] Green [Gr63] Bishop [Bi67] Murata *et al.* [Mu71] Mæhlum and Stadsnes [Mæ67] Mukoyama and Watanabe [Mu77] Leiss, Penner and Robinson [Le57] Hawryluk,Hawryluk and Smith [Ha74] Shinoda, Murata and Shimizu [Sh68] Myklebust *et al.* [My76]. Kulkarni and Supe [Ku84] Reimer [Re68] Shimizu and Murata [Sh71] McDonald, Lamki and Delaney [McD71] Matsukawa *et al.* [Ma73]
Bethe Theory with Plasma losses	Gorelik and Rozin [Go72]
Rao-Sahib and Wittry empirical [Ra74]	Love, Cox and Scott [Lo77] Kotera, Murata and Nagami [Ko81b] Murata *et al.* [Mu79a]
Kanaya and Okayama empirical [Ka72]	Kotera *et al.* [Ko81a, Ko81b] Murata *et al.* [Mu79a]
Green and Peterson Empirical [Gr68]	Berger, Seltzer and Maeda [Be70]
Spencer-Fano Theory [Br69]	Murata *et al.* [Mu79b]

Table 3.1: Continuous Collisional Energy Loss Treatments Used in Monte Carlo Electron Transport Codes

approximation that the foil is thin enough such that

$$\frac{dE}{dx} = \frac{(\Delta E)_{ave}}{\delta x}$$

is then used to determine the stopping power. Obviously, many approximations have been made. First, a multiple scattering adjustment correcting for the actual electron tracklength (as opposed to the foil thickness) must be made. This correction is often as large as the measurement itself [Al83]. Second, for low energies or large foil thicknesses, the electron slows appreciably as it passes through the target foil, and so the measured energy loss is actually the average loss over the initial and final energies, and not the instantaneous loss rate of the initial energy applied uniformly through the foil. Table 3.2 lists those experiments in which the results have been suitably corrected to allow direct comparison with calculated values of the stopping power, for initial electron energies less than 100 keV.

3.1.6 Evaluations and Conclusions

The experiments of Al-Ahmad and Watt were chosen for comparison with theoretical calculations. It is hard to predict validity ranges strictly on the basis of approximations made in the derivations (the first Born approximation cross section is not expected to be accurate at low energies) because of the use of the empirical ionization potential.

Results of runs using the Bethe theory both with and without Flynn's correction, as well as some CDCM results of Ashley are shown in figures 3.3 through 3.5. The semi-empirical expressions of Rao-Sahib and Wittry and of Kanaya and Okayama, because of their defect of predicting infinite stopping power at zero velocity, were not included.

Authors	Material (Z)	Initial Energy (keV)
Al-Ahmad and Watt [Al83]	Al (13)	1–10
	Ni (28)	2–10
	Cu (29)	2–10
	Ag (47)	3–10
	Au (79)	4–10
Fittig [Fi74]	Al (13)	.8–4
Garber [Ga65]	Al (13)	.58–1.045
Hubbell and Birkhoff [Hu82]	Al(13)	11–127
	Cu (29)	11-127
Ishigure *et al.* [Is78]	Al (13)	2–10.9
Pugachev and Valkov [Pu79]	Al (13)	40, 50, 60
	Ag (47)	40, 50, 60
	Au (79)	40, 50, 60

Table 3.2: Stopping Power Experiments in the Kilovolt Energy Range

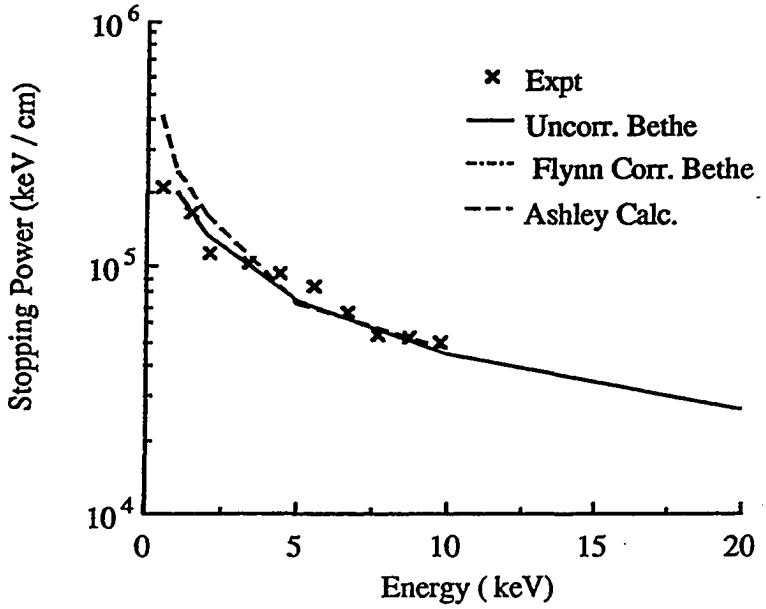

Figure 3.3: Comparison of Stopping Power Formulations with Experiment for Aluminum

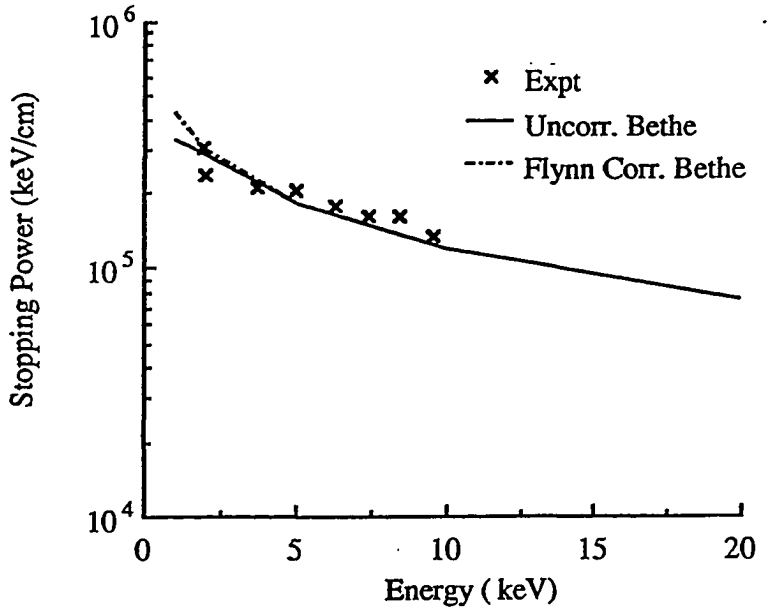

Figure 3.4: Comparison of Stopping Power Formulations with Experiment for Silver

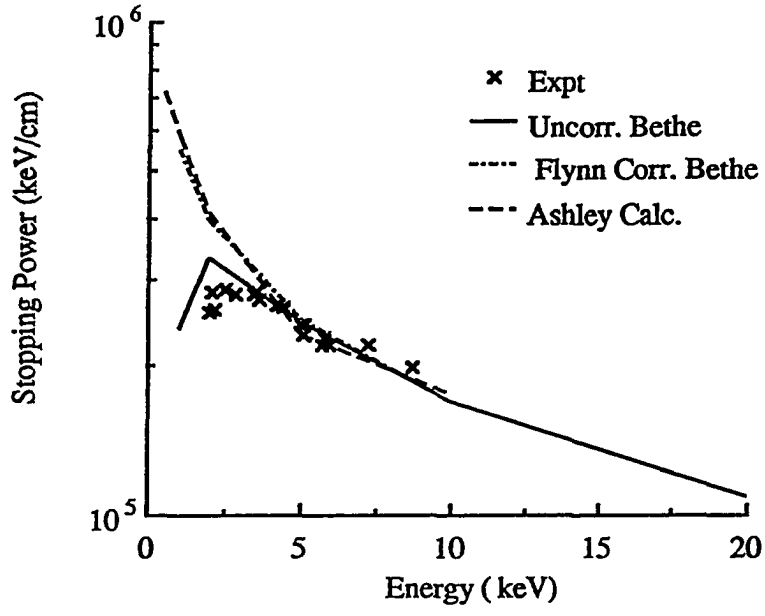

Figure 3.5: Comparison of Stopping Power Formulations with Experiment for Gold

It is seen that except for high Z materials, the Bethe theory is sufficient, without correction, to describe the stopping power of electrons down to 1 keV. A problem is seen in the evaluation for gold. The experimental results appear to agree quite well with the uncorrected Bethe theory. This is particularly worrisome because it comes after the maximum in the theory, at which point the theory is assumed by most authors to be incorrect. Scrutinization of the Al-Ahamad data shows that the same foil thicknesses were used for the high energy and low energy experiments, and that the multiple scatter correction is an order of magnitude greater than the foil thickness for the low energy cases. Therefore, this very low energy data is suspect and so is here discounted, and the Flynn correction, because of its agreement with the detailed stopping power calculation of Ashley, is used for all energies and elements studied in this work.

3.1.7 Treatment of Radiation Losses

Even though the fraction of energy lost by kilovolt electrons as they pass through matter is small, it is not negligible and the production of bremsstrahlung photons is an important effect to model in some applications. Like collisional ionization and excitation losses, losses due to bremsstrahlung can be treated in the continuous slowing down approximation. The stopping power due to radiation losses is determined again by integration of the energy loss times the differential cross section, this time for bremsstrahlung, as

$$-\left(\frac{dE}{dx}\right)_{rad} = \int_0^E dQ\, N\, \sigma_B(E,Q)\, Q. \tag{3.32}$$

Recently, Seltzer and Berger have reviewed differential cross sections for energy loss due to bremsstrahlung and have devised bremsstrahlung stopping power formulations in the energy range from 1 keV to 10 GeV for elements 1 to 100, using the most accurate available formulations in each of several energy regions [Se82]. As their method employs the the best available data and extends fully through the energy range of interest, their results are used exclusively throughout this work, and a review of other available formulations is not undertaken. Additionally, a literature survey has found that only higher energy production codes such as EGS and the ETRAN derivatives typically treat bremsstrahlung losses, and so a summary of previously used models is not included.

Seltzer gives the total stopping power as

$$-\left(\frac{dE}{dx}\right)_{rad} = \frac{\rho\alpha r_e^2 N_a Z^2}{A}\left(E + mc^2\right)\phi(E,Z) \tag{3.33}$$

in which α is the fine structure constant, r_e the classical electron radius, and $\phi(E,Z)$

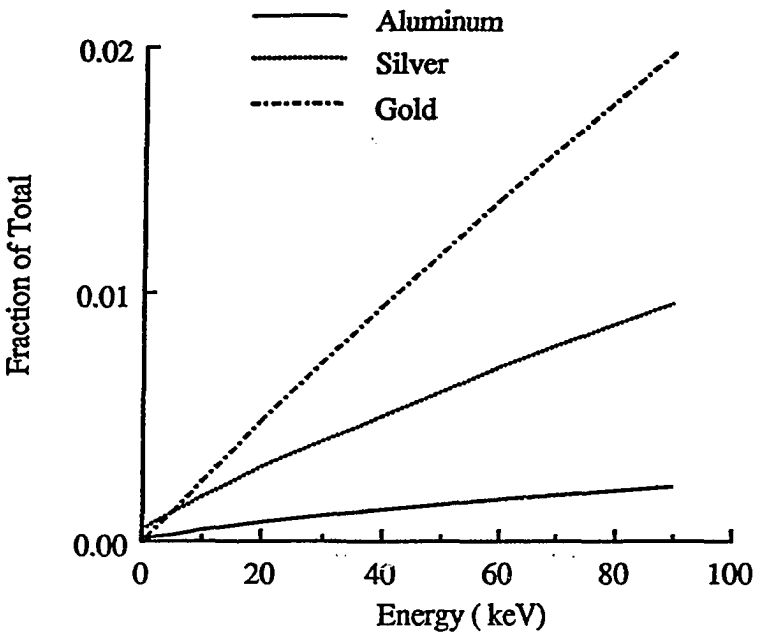

Figure 3.6: Fraction of Energy Loss Due to Radiative Collisions

is given by a fit of the form

$$\phi(E,Z) = d_1(Z)\frac{1+\sum_{i=1}^{4} f_i(Z)(\ln E)^i}{1+\sum_{i=1}^{4} h_i(Z)(\ln E)^i}. \tag{3.34}$$

The values of the constants given by Seltzer include the losses due to electron-electron bremsstrahlung. For the case of compounds, stopping powers are summed in proportion to the weight fractions of the constituents, as in

$$-\left(\frac{dE}{dx}\right)_{rad,tot} = \sum_j -w_j\left(\frac{dE}{dx}\right)_{rad,j}. \tag{3.35}$$

Plots of the magnitude of this effect, given in terms of the fraction of energy loss due to radiative collisions as a function of energy for various elements are given in figure 3.6.

As with the stopping power due to collisional losses, it is sometimes desirable to

use the restricted radiative stopping power,

$$-\left(\frac{dE}{dx}\right)_{rad}^{res} = N\int_0^{E_c} dQ\,\sigma_B(E{:}Q)\,Q. \tag{3.36}$$

Indeed, for the case of bremsstrahlung losses, the energy loss due to relatively high energy collisions represents a large part of the total radiative losses. A fitted expression for the restricted stopping power losses based on the cross sections recommended by Seltzer and Berger has been developed by Urban [Br87] as part of the GEANT high energy physics Monte Carlo code. He gives

$$\left(\frac{dE}{dx}\right)_{rad}^{res} = \frac{Z(Z+\xi)(E+mc^2)^2}{E+2mc^2}\left[\frac{Q_r C_M}{E}\right]^{\beta} F_{EL} \tag{3.37}$$

In the above expression C_M is the Midgal correction factor given by

$$C_M = \frac{1}{1+\dfrac{N_e r_e \lambda\!\!\!^{-2}_0 (E+mc^2)^2}{\pi Q_r^2}} \tag{3.38}$$

where N_e is the number density of the electrons in the medium, and $\lambda\!\!\!^{-}_0$ is the reduced Compton wavelength of the electron, $\hbar/mc$. The factor F_{EL} in equation 3.37 is the parameterization given by

$$F_{EL} = S_1(X,Y) + ZS_2(X,Y) \tag{3.39}$$

in which $X = \ln((E+mc^2)/mc^2)$ and $Y = \ln(Q_r/v(E+mc^2))$ and the functions $S_1(X,Y)$ and $S_2(X,Y)$ are given by

$$S_1(X,Y) = \sum_{i=0}^{5}\sum_{j=0}^{5} C_{i,j}X^iY^j \tag{3.40}$$

$$S_2(X,Y) = \sum_{i=0}^{4}\sum_{j=0}^{4} D_{i,j}X^iY^j. \tag{3.41}$$

The constants β, ξ and v are given as .99, 2.51 and 0.00004, respectively, and the coefficients in the polynomial expansions for S_1 and S_2 are provided in the GEANT

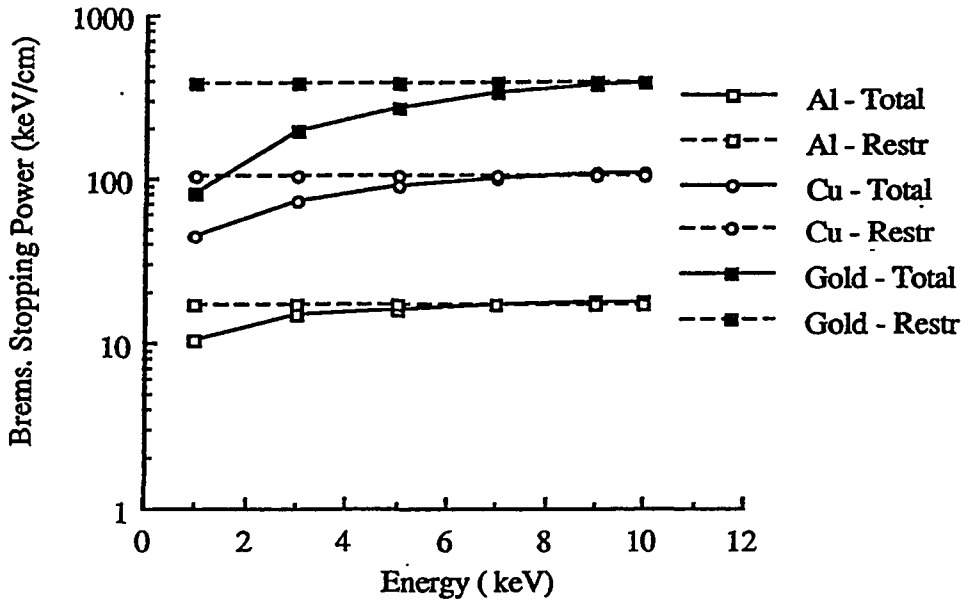

Figure 3.7: Total Radiative Stopping Power Below 10 keV by Extrapolation and Calculation

source code. The fit given by Urban is limited to energies greater than 10 keV, and professes accuracy within 10%. For the present work, the Seltzer expression is used for the total stopping power and Urban's formula only when a restricted bremsstrahlung loss treatment is needed. For restricted stopping powers below 10 keV, a simple constant extrapolation is used. The validity of this extrapolation is examined in figures 3.7, which compares this extrapolation of 3.37 (using $Q_r = E$ to get the total stopping power at 10 keV) with the accurate calculations of 3.33. It is seen that at 10 keV,the two formalisms yield almost identical results, and that at lower energies the assumption of a constant stopping power is not too bad for low Z, but not good for heavier elements. The effect of this should be small however, since the fraction of losses due to bremsstrahlung is very small in this regime.

Figure 3.8, which shows the effect of the extrapolation on the trends of the reduced stopping power at $Q_r = 1$ keV. Again, the effects of errors should be small because of the low probability of bremsstrahlung.

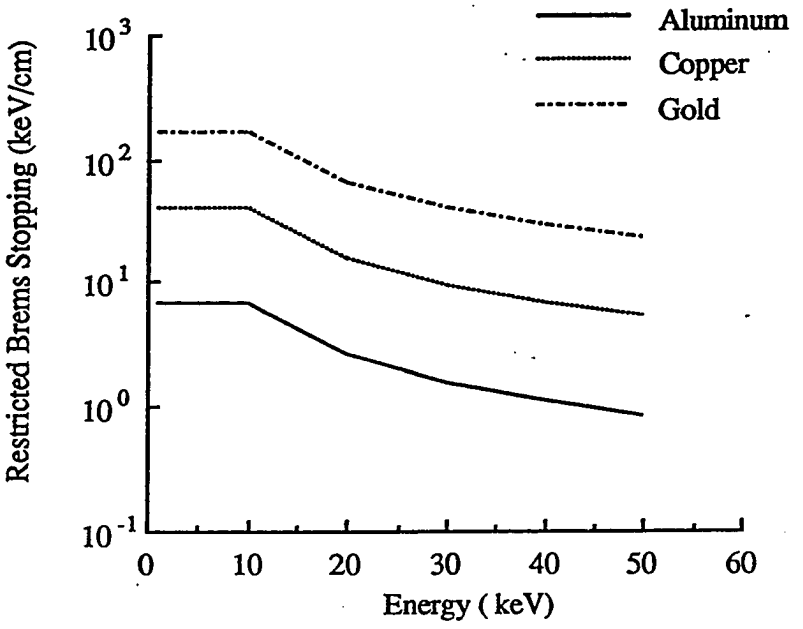

Figure 3.8: Reduced Radiative Stopping Power Using Extrapolation

3.2 Energy Loss Distributions

An obvious drawback to the continuous loss approach is that for a given thickness of material traversed, a single energy loss is predicted for every electron traversing the same thickness of material, as given by the integral 3.1. In reality, a distribution of energy losses is seen, the result of the stochastic nature of the loss process. Expressions describing the relative frequency of the fluctuating losses can be derived, starting with the appropriate form of the transport equation,

$$\frac{\partial f(E,x)}{\partial x} = \int_0^b dQ\, f(E+Q,x)\,\sigma(E+Q \rightarrow E) - \int_0^{Q_{max}(E)} dQ\, f(E,x)\,\sigma(E \rightarrow E-Q) \tag{3.42}$$

where $f(E,x)dE$ is the distribution of electrons at x with energies between E and $E+dE$ and $\sigma(E_1 \rightarrow E_2)$ is the probability that an electron with energy E_1 which undergo a collision from which it will emerge with energy E_2. The integration limit $Q_{max}(E)$ represents the maximum kinematically allowed energy which an electron with energy E can transfer in a single collision, and b the maximum transfer which can produce an electron with energy E. It is usually more convenient to describe the loss phenomena using the variable Δ, which represents the energy loss, E_0-E, (E_0 is the initial energy). Further, it is commonly assumed that $E_0 \gg \Delta$ and so $\sigma(E+Q \rightarrow E) = \sigma(E \rightarrow E-Q) = \sigma(E_0;Q) = \sigma(Q)$ and the integration limit becomes $Q_{max}(E_0)$ for the second integral and b is given by Δ if $\Delta < Q_{max}(E_0)$ and $Q_{max}(E_0)$ otherwise. Thus we have

$$\frac{\partial f(\Delta,x)}{\partial x} = \int_0^b dQ\, f(\Delta-Q,x)\,\sigma(Q) - \int_0^{Q_{max}(E_0)} dQ\, f(\Delta,x)\,\sigma(Q) \tag{3.43}$$

3.2.1 Landau's Derivation

The first proposed solution to 3.43 has been developed by Landau [La44]. Landau argues that the integration limits can both be taken to be ∞, since in the first integral, $f(\Delta-Q,x)$ is by definition zero for $Q > \Delta$ and in the second integral, $\sigma(Q)$ tends to zero for large Q. Thus the contributions of the large Q section of the integrals are small and we can write

$$\frac{\partial f(\Delta,x)}{\partial x} = \int_0^\infty dQ\,\sigma(Q)\,[f(\Delta-Q,x) - f(\Delta,x)] \tag{3.44}$$

This can be solved by a Laplace transform method, yielding

$$f(\Delta,x) = \frac{1}{2\pi i}\int_{a-i\infty}^{a+i\infty} dp\,\exp\left[p\Delta - x\int_0^\infty dQ\,\sigma(Q)\,(1-e^{-pQ})\right] \tag{3.45}$$

where a is an arbitrary constant. Equation 3.45 may now be solved by making an assumption about the form of the cross section $\sigma(Q)$. Typically, if J is defined as the integral over Q, J can be split into a high transfer and low transfer part, as in Bethe's derivation of stopping power. In the low transfer integral it can be assumed that $1-e^{-pQ}$ can be approximated as pQ yielding

$$J = p\int_0^{Q_1} dQ\,Q\,\sigma(Q) + \int_{Q_1}^\infty dQ.\,\sigma(Q)\,(1-e^{-pQ}) \tag{3.46}$$

The low transfer integral is seen to be identical to p times equation 3.5 and so can be evaluated as

$$J_{low} = p\frac{2\pi Ne^4Z}{mv^2}\left[\ln\frac{2mv^2}{I^2(1-\beta^2)} + \ln Q_1 - \beta^2 - \delta\right]. \tag{3.47}$$

In evaluating the high transfer portion, J_{high} Landau assumes that the cross section can be taken to be

$$\sigma(Q) = \frac{2\pi Ne^4Z}{mv^2}\frac{1}{Q^2}. \tag{3.48}$$

This form of the cross section is related to the Møller cross section used in Bethe's evaluation of the contribution of high transfer collisions to the stopping power, but neglects several terms. In this case, J_{high} can be evaluated by direct integration to be

$$J_{high} = \frac{2\pi Ne^4Z}{mv^2}\left[\frac{1}{Q_1} - \frac{e^{-pQ_1}}{Q_1} + pE_i(pQ_1)\right] \tag{3.49}$$

where $E_i(x)$ is the exponential integral function. Again using the idea that pQ_1 is small, Landau expands each of the last two terms above in a Taylor series to obtain

$$J_{high} = \frac{2\pi Ne^4Z}{mv^2}p(1 - \gamma - \ln pQ_1) \tag{3.50}$$

in which γ is Euler's constant. If we define ξ as $x\frac{2\pi e^4NZ}{mv^2}$ we have for $f(\Delta, x)$

$$f(\Delta, x) = \frac{1}{2\pi i}\int_{a-i\infty}^{a+i\infty} dp \exp\left\{p\left[\Delta - \xi(1 - \gamma - \ln p + \ln\frac{2mv^2}{I^2(1-\beta^2)} - \beta^2 - \delta)\right]\right\}. \tag{3.51}$$

Landau defines a single parameter λ_L, given by

$$\lambda_L = \frac{1}{\xi}\left[\Delta - \xi(1 - \gamma + \ln\frac{2mv^2}{I^2(1-\beta^2)} - \beta^2 - \delta)\right] \tag{3.52}$$

This allows the formulation of a universal function $\phi(\lambda_L)$ in which the single parameter λ completely describes both the electron and the target, and ϕ is given by

$$\phi(\lambda_L) = \frac{1}{2\pi i}\int_{c-i\infty}^{c+i\infty} du e^{u\lambda_L + u\ln u} \tag{3.53}$$

and $f(\Delta, x)$ is taken from

$$\begin{aligned} f(\Delta, x) &= \phi(\lambda_L)\frac{d\lambda_L}{d\Delta} \\ &= \frac{1}{\xi}\phi(\lambda_L). \end{aligned} \tag{3.54}$$

The function ϕ must be evaluated numerically, and has been tabulated for values of λ from -4 to 100 by Borsch-Supan [Bo61], and this tabulation is used in the current

work for evaluation of $f(\Delta, x)$. Compounds are accounted for by taking the properly weighted values of ξ and I, as in the case of the evaluation of the collisional stopping power.

3.2.2 Vavilov's Derivation

Vavilov [Va57] has shown that regardless of the value of b in 3.43, ($b = \Delta$ or $b = Q_{max}(E_0)$) the same Laplace transform technique can be used to obtain an analogous form of 3.45 in which the upper limit in the integral over Q can be taken as Q_{max} rather than as ∞. In this treatment, the integral J is rewritten in the form

$$J = p\overline{\Delta} + x\int_0^{Q_{max}} dQ\,\sigma(Q)\left(1 - e^{-Qp} - Qp\right) \tag{3.55}$$

where

$$\overline{\Delta} = x\int_0^{Q_{max}} dQ\,Q\,\sigma(Q)$$

is the average energy loss over the pathlength (note that this assumes that the energy is constant over the pathlength). Vavilov then assumes a cross section of the form

$$\sigma(Q) = \frac{\xi}{x}\left[\frac{1}{Q^2} - \frac{1-\beta^2}{2mc^2}\frac{1}{Q}\right] \tag{3.56}$$

The integral J can now be evaluated (without the Taylor expansions used by Landau) to yield

$$f(\lambda_V, x) = \frac{e^{\kappa(1+\beta^2\gamma)}}{2\pi i Q_{max}}\int_{c-i\infty}^{c+i\infty} du\,\exp\left\{u\lambda_V + \kappa\left[(u+\beta^2)(\ln u - E_i(u)) - e^{-u}\right]\right\} \tag{3.57}$$

where $\kappa = \xi/Q_{max}$ and λ_V, which is related to Landau's λ_L parameter, is given by

$$\lambda_V = \frac{\Delta - \overline{\Delta}}{Q_{max}} - \kappa(1 + \beta^2 - \gamma) \tag{3.58}$$

The complex integral can be shown by a branch cut technique to reduce to a real integral

$$f(\lambda_V, x) = \frac{1}{2\pi Q_{max}} e^{\kappa(1+\beta^2\gamma)} \int_0^\infty dy\, e^{\kappa f_1(y)} \cos[y\lambda_V + \kappa f_2(y)] \qquad (3.59)$$

where

$$\begin{aligned} f_1 &= \beta^2 \ln y - \mathrm{Ci}(y) - \cos y - y\,\mathrm{Si}(y) \\ f_2 &= y \ln y - \mathrm{Ci}(y) - \sin y - \beta^2\,\mathrm{Si}(y) \end{aligned}$$

where Ci and Si are the cosine and sine integral functions respectively.

The finite limit, Q_{max}, on the integral in equation 3.43 allows the determination of a restricted energy loss distribution, analogous to the restricted stopping power, for use in Monte Carlo transport calculations. This is significant since such a result can not be derived in Landau's formalism.

Throughout this work 3.59 is evaluated by numerical integration. The integrand is an oscillating, damped function of y, and is integrated by summing the partial integrals between the zeros of the integrand until the partial integrals become less than .01% of the total. It has been found that if each partial integral is broken into roughly 10 steps, Simpson's rule is adequate to describe the integral accurate to an absolute magnitude of roughly 10^{-6}. Schorr [Sc74] gives a prescription for evaluating 3.59 as Fourier series, accurate to three decimal points, but his method is not used here. He also proves that the Vavilov distribution reduces to the Landau distribution for $Q_{max} \rightarrow \infty$.

3.2.3 Blunck and Leisegang's Correction to Landau

Blunck and Leisegang [Bl50] have included the quadratic term in the Taylor expansion used by Landau in evaluating the integral J. The expression for $\phi(\lambda_L)$

ν	c_ν	$\lambda\nu$	γ_ν
1	0.174	0.0	1.8
2	0.058	3.0	2.0
3	0.019	6.5	3.0
4	0.007	11.0	5.0

Table 3.3: Parameters for Blunck-Leisegang fit to Landau's $\phi(\lambda_L)$

under this approximation can be shown to be given by

$$\phi_{BL}(\lambda_L) = \frac{b}{\sqrt{2\pi i}} \int_{c-i\infty}^{c+i\infty} du\, \phi_L(\lambda_L - u)\, e^{-u^2 b^2} \tag{3.60}$$

where ϕ_L is Landau's $\phi(\lambda_L)$ and $b^2 = \dfrac{\overline{Q^2} x}{2\xi}$ with

$$\overline{Q^2} = \int_0^{Q_1} dQ\, Q^2\, \sigma(Q). \tag{3.61}$$

Blunck and Westphal [Bl51] give an approximate expression for $\overline{Q^2}$ as

$$\overline{Q^2} = \frac{q\overline{\Delta} Z^{4/3}}{2x} \tag{3.62}$$

in which $\overline{\Delta}$ is the average energy loss over the path and q is a constant given as roughly 20 eV. In order to carry out the integral of 3.60, Blunck and Leisegang approximate Landau's universal function ϕ_L by a sum of 4 Gaussians,

$$\phi_L(\lambda_L) = \sum_{\nu=1}^{4} c_\nu \exp\left[-\left(\frac{\lambda_L - \lambda_\nu}{\gamma_\nu}\right)^2\right] \tag{3.63}$$

Values of the constants c_ν, λ_ν and γ_ν are given in table 3.3.

Findlay and Dusautoy [Fi80] have shown that values of the constants given by Blunck and Leisegang do not faithfully approximate Landau's result, and have proposed a 9 Gaussian sum of identical form. The constants used in this fit are given in table 3.4. This more accurate fit is used throughout the present work. Using the

ν	c_ν	$\lambda\nu$	γ_ν
1	0.0386	-1.48	.737
2	0.0843	-0.738	.947
3	0.0882	0.170	1.23
4	0.0647	1.33	1.68
5	0.0359	2.95	2.40
6	0.0164	5.39	3.68
7	0.0064	9.40	6.18
8	0.0021	16.8	12.3
9	0.0006	30.8	39.7

Table 3.4: Parameters for Findlay-Dusautoy fit to Landau's $\phi(\lambda_L)$

sum of Gaussians form for ϕ_L in 3.60 allows analytical integration, yielding

$$\phi_{BL}(\lambda_L) = \sum_\nu \frac{c_\nu \gamma_\nu}{\sqrt{\gamma_\nu^2 + b^2}} \exp\left[-\frac{(\lambda - \lambda_\nu)^2}{\gamma_\nu^2 + b^2}\right]. \tag{3.64}$$

3.2.4 Shulek's Correction to Vavilov

Shulek *et al.* [Sh67] have extended Vavilov's work in a similar fashion. Recalling that Vavilov expressed the integral J as

$$J = x \int_0^{Q_{max}} dQ\, \sigma(Q) \left(1 - e^{-Qp} - Qp + -Qp\right) \tag{3.65}$$

and then used the definition of stopping power to replace the integral over the positive Qp term by $\overline{\Delta}$, Shulek added and subtracted a quadratic term $\frac{(Qp)^2}{2}$ and used a definition of $\overline{Q^2}$ given by Livingston and Bethe [Li37], to remove the contribution of the positive quadratic term, and integrated. The expression for $\overline{Q^2}$ used by Shulek is

$$\overline{Q^2} = \xi \left[Q_{max}\left(1 - \frac{\beta^2}{2}\right)\sum_s f_s + \sum_s \frac{8}{3} I_s f_s \ln\frac{2mv^2}{I_s}\right] \tag{3.66}$$

Distributed Energy Loss Treatment	Monte Carlo Authors
Landau	Berger [Be63] Hebbard and Wilson [He55] Heńoc and Maurice [He76] Perkins [Pe62] Vande Putte [Va74] Sundararaman *et al.* [Su73]
Modified Landau for Ionization losses	Leiss *et al.* [Le57]
Blunck and Leisegang	ETRAN *et al.* [Be68] Berger [Be63] Vande Putte [Va74] Mukoyama and Watanabe [Mu77]

Table 3.5: Energy Loss Distribution Functions Used in Monte Carlo Electron Transport Codes

where the sums are taken over only those subshells for which the ionization energy, I_s is less than the incident electron energy, and f_s represents the fraction of electrons in the given subshells. Shulek shows that the expression for $f(\lambda, x)$ becomes

$$f(\lambda_V, x) = \frac{1}{2\pi Q_{max}} e^{\kappa(1+\beta^2\gamma)} \int_{\infty}^{0} dy\, e^{\kappa(f_1(y)-\lambda_S y^2)} \cos\left[y\lambda_V + \kappa f_2(y)\right] \tag{3.67}$$

where $f_1(y), f_2(y)$ and λ_V have the same definition as in Vavilov's derivation and λ_S is given by

$$\lambda_S = \frac{1}{2}\left[\kappa\left(1 - \frac{\beta^2}{2}\right) - \frac{\overline{Q^2}}{Q^2_{max}}\right] \tag{3.68}$$

The expression 3.67 for $f(\lambda_V, \lambda_S, x)$ must be evaluated numerically.

3.2.5 Models Used by Previous Investigators

Models of energy loss distribution functions used by previous investigators are given in table 3.5.

3.2.6 Energy Loss Experiments at Low Energies

Although quite a number of investigations of the scattering of transmitted beams of mono-energetic electron have been performed, in very few instances are the results reported in terms of the distribution in energy of the emergent particles, *i. e.*, as plots of $f(E)$ or $f(\Delta E)$ versus E or ΔE. Table 3.6 lists those experiments in which the results are given in a form suitable for direct comparison with energy loss distribution theories.

3.2.7 Evaluations and Conclusions

The experiments of Cosslett and Thomas, Fittig, and Vyatskin and Khramov have been chosen for comparison with the various theories. Since it is impossible to compare restricted loss distributions, the calculations of the Vavilov distribution use as the maximum modeled loss the full incident energy. Table 3.7 compares the foil thickness from the experiments used in the analysis with typical condensed history Monte Carlo step sizes, which generally allow for a 4.25% energy loss.

It is seen that none of the experiments used foils as thin as the pathlengths seen in condensed history Monte Carlo runs. Most were several score thicker than a single Monte Carlo step. The greatest difference is seen in the silicon experiment, in which the foil was 100 times thicker than a typical step, and the smallest in two gold experiments, which used foils roughly 25 thicker than a usual Monte Carlo step. Thus, any conclusions about the effectiveness of the various distribution functions at modeling energy loss must be tempered when selecting models for Monte Carlo applications.

Results of runs modeling the chosen experiments are given in figures 3.9 through 3.14.

Authors	Material (Z)	Initial Energy (keV)	Thickness ($\times 10^{-6}$ cm)
Cosslett and Thomas [Co64c]	Al (13)	18.0	44.5–180.
	Au (79)	18.0	6.21–34.9
Fittig [Fi74]	Al (13)	0.8–4.0	2.20
Fittig [Fi75]	Be (4)	1.5–4.0	8.0
	Ge (32)	2.0–4.0	8.0
Ishigure *et al.** [Is78]	Al (13)	3.0	2.
Kwei [Kw84]	C (6)	0.6, 1.0	0.8
Lanteri *et al.* [La80]	Al (13)	1.0–3.0	1.5
Reimer *et al.* [Re78]	Al (13)	20.2	44.5–167.
	Au (79)	20.5	12.8–33.6
Shimizu *et al.* [Sh75]	Al (13)	15.0	10.–104.
	Cu (29)	20.0	17.40
Shulman *et al.* [Sh64]	Al (13)	3.0, 4.0	5.5, 10.
Vyatskin and Khramov [Vy74]	Si (13)	3.5	10.7
	Au (79)	3.5	.785
Young [Yo57]	$Al_2\ 0_3$ (8,13)	3.0–10.0	6.05

* angularly dependent data

Table 3.6: Energy Loss Distribution Experiments in the Kilovolt Energy Range

Experiment	Experimental Thickness (cm)	Typical Monte Carlo Step
Beryllium at 4 keV	8.00×10^{-6}	$.17 \times 10^{-6}$
Aluminum at 18 keV	88.9×10^{-6}	1.81×10^{-6}
Silicon at 3.5 keV	10.7×10^{-6}	$.102 \times 10^{-6}$
Germanium at 4 keV	5.70×10^{-6}	$.107 \times 10^{-6}$
Gold at 3.5 keV	$.785 \times 10^{-6}$	$.032 \times 10^{-6}$
Gold at 18 keV	12.4×10^{-6}	$.468 \times 10^{-6}$

Table 3.7: Comparison of Condensed History Step Sizes and Experimental Foil Thicknesses

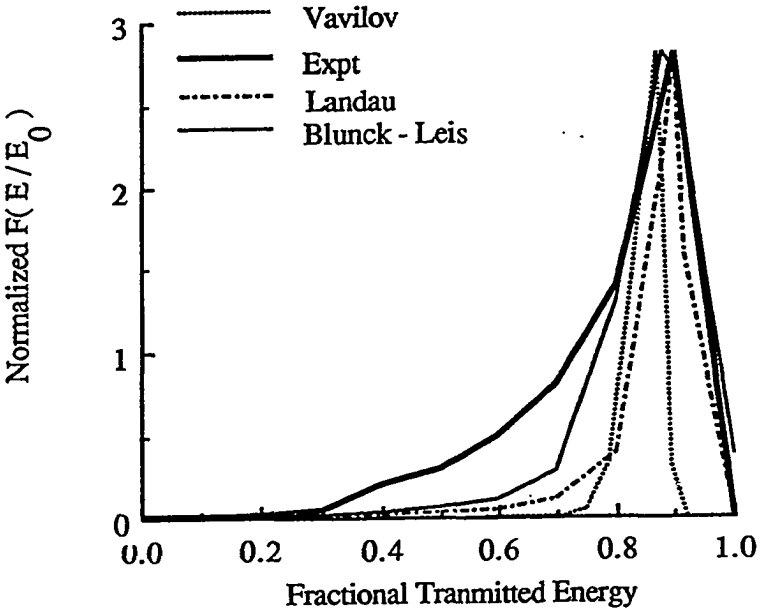

Figure 3.9: Comparison of Energy Loss Distribution Formulations with Experiment for Aluminum at 18 keV

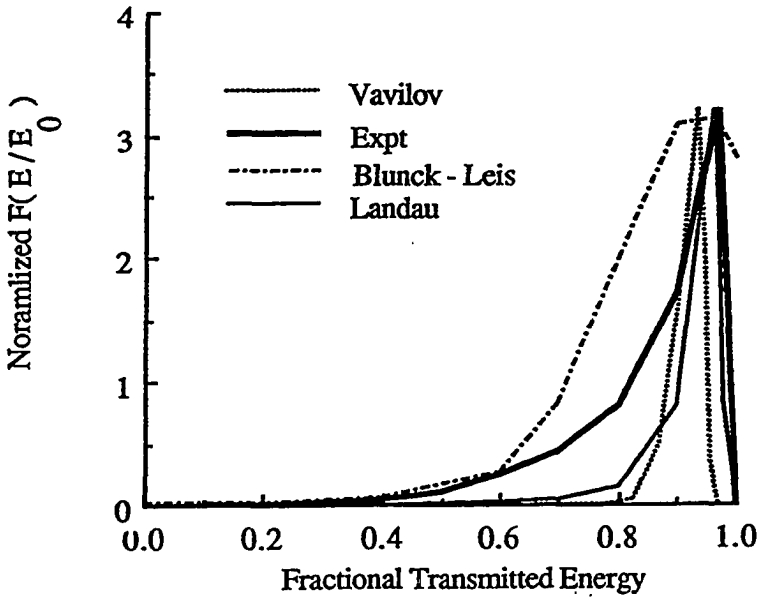

Figure 3.10: Comparison of Energy Loss Distribution Formulations with Experiment for Gold at 18 keV

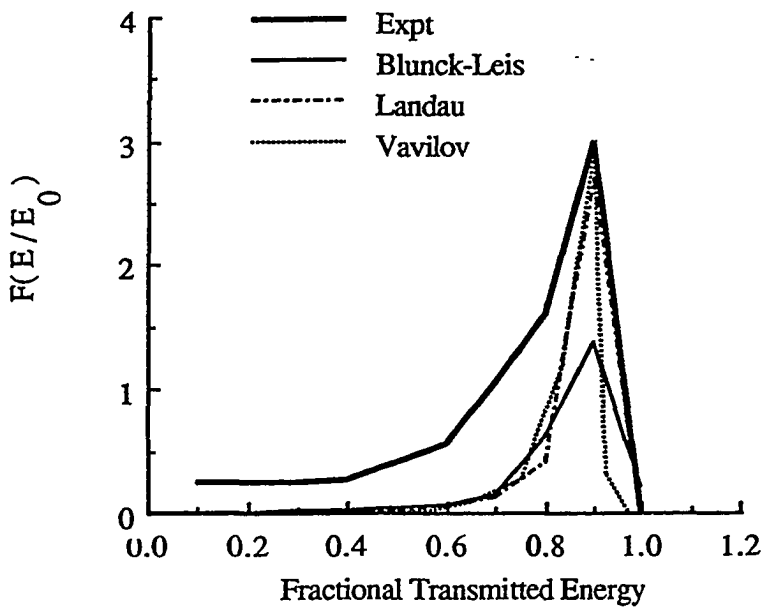

Figure 3.11: Comparison of Energy Loss Distribution Formulations with Experiment for Beryllium at 4 keV

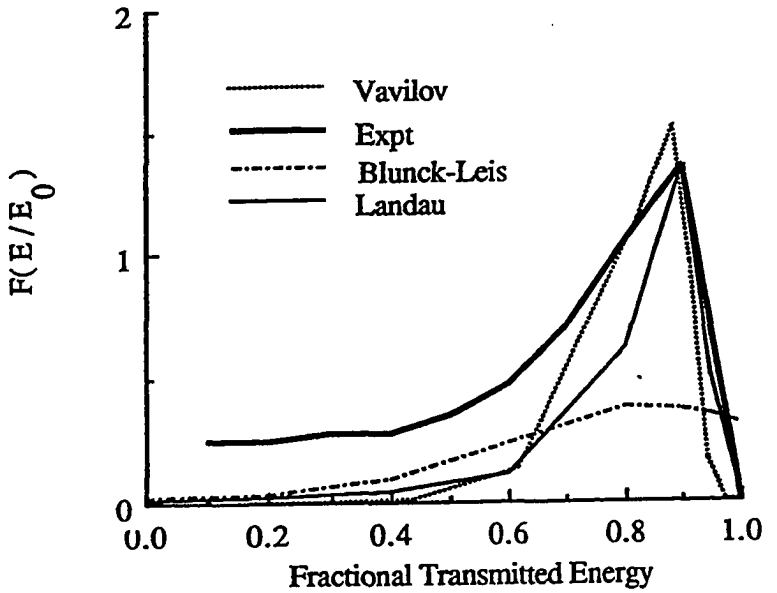

Figure 3.12: Comparison of Energy Loss Distribution Formulations with Experiment for Germanium at 4 keV

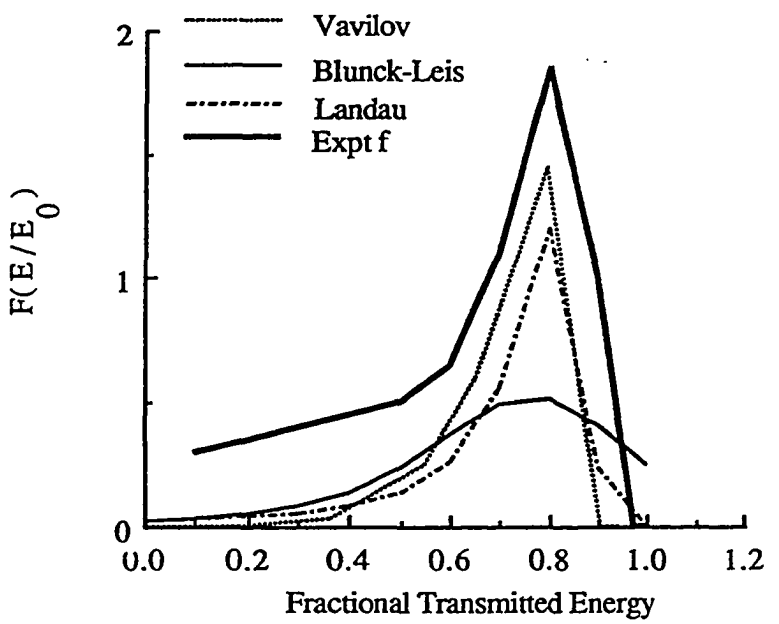

Figure 3.13: Comparison of Energy Loss Distribution Formulations with Experiment for Silicon at 3.5 keV

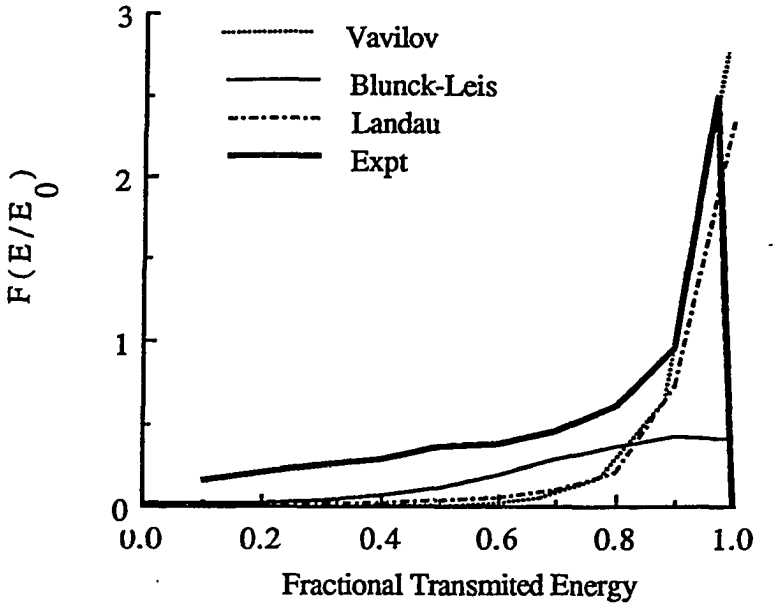

Figure 3.14: Comparison of Energy Loss Distribution Formulations with Experiment for Gold at 3.5 keV

It is seen from the figures that the Landau and Vavilov distributions model the position of the peak quite well in all instances at low energies, but only the Landau predicts this accurately at higher energies. The Blunck and Leisegang calculation does well only for the aluminum experiment at 18 keV. It most instances, the broadening that it adds to the model is over done, and the peak hard to discern. In no case was the tail of the distribution, represented by the large energy loss electrons, well modeled, even by Blunck and Leisegang. Finally, the Vavilov distribution at lower energies in general predicts a slightly wider peak with a gentler slope on the large loss side an a more rapid decline on the loss energy loss side than the Landau, which is a somewhat better approximation to the experimental data.

Additionally, calculations of the average energy loss predicted by the distribution functions, determined by numerically integrating $\Delta E f(\Delta E) d\Delta E$ and given in table 3.8, show that the Vavilov distribution did a remarkable job in predicting the average

Experiment	Blunck-Leis	Landau	Vavilov	CSDA
Beryllium at 4 keV	0.625	0.617	0.594	0.595
Aluminum at 18 keV	2.828	2.792	2.721	2.721
Silicon at 3.5 keV	1.100	0.986	0.997	0.998
Germanium at 4 keV	1.165	0.800	0.743	0.743
Gold at 3.5 keV	0.886	0.347	0.262	0.228
Gold at 18 keV	2.848	1.651	1.479	1.479

Table 3.8: Average Energy Losses (in keV) Predicted from Theories

energy loss which would otherwise be found by integrating the inverse stopping power over the foil size. While average loss values from distribution functions are not be expected to agree with experimentally determined values because of multiple scattering in the foil, they are expected agree with integrated stopping power losses, as they have as their underpinnings the same cross section shape and the assume the same track length.

3.3 Multiple Elastic Scattering Distributions

The differential equation defining the distribution of electrons $f(\theta, s)$ which travel through a material a distance s and scatter into $d\theta$ about θ is given by

$$\frac{\partial f}{\partial s} = -Nf(\theta,s)\int d\chi\,\sigma(\chi)\,\sin\chi + N\int d\chi\, f(\theta-\chi,s)\,\sigma(\chi)\,\sin\chi \qquad (3.69)$$

in which $\sigma(\chi)\sin\chi\,d\chi$ is the probability of a single scattering at an angle χ into $d\chi$. Note that the dependencies of f and σ on energy are implied by the explicit dependencies on the pathlength. Two methods are generally used to attack this problem, the first employing the small angle approximation [Mo48] on the above

equation and the second using a heuristic approach to cast the problem in a different formalism [Go48a, Pe83].

3.3.1 Molière's Method - Small Angle Approximation

Molière [Mo48] solved 3.69 for electron nuclear scattering in the small angle approximation (assuming $\sin\chi \sim \chi$), by a Bessel transform technique. Very lucid descriptions detailing the assumptions, approximations and range of applicability of Molière's technique are given by Bethe [Be53], and by Scott [Sc63], who also describes Fano's [Fa54] extension of theory to include the effect of scattering from the atomic electrons and the treatment of amorphous compounds. By assuming that $\sigma(\chi)$ is independent of s, which is equivalent to assuming no energy loss over the path, Molière arrives at

$$f(\theta,s) = \int_0^\infty d\eta\,\eta\,J_0(\eta\theta)\exp\left\{-Ns\int_0^\infty d\chi\,\chi\,\sigma(\chi)[1-J_0(\eta\chi)]\right\} \tag{3.70}$$

where η is the transformation variable. At this point assumptions must be made about the form of the scattering cross section. Molière (as amended by Scott) takes the inelastic plus elastic differential scattering cross section, $\sigma(\chi)\,\chi\,d\chi$ in a form very similar to that of the Rutherford cross section, given by

$$N\,s\,\sigma(\chi)\,\chi\,d\chi = 2\chi_c^2\frac{Z}{Z+1}\frac{1}{\chi^4}\left[q(\chi)+\frac{S(\chi)}{Z}\right] \tag{3.71}$$

where $q(\chi)$ represents the deviation of the true elastic scattering cross section from the Rutherford cross section and $S(\chi)$ the inelastic form factor, in effect the deviation of the shape of the differential inelastic cross section from that of the Rutherford cross section. In the above expression, χ_c^2 is given by

$$\chi_c^2 = \frac{4\pi e^4 NZ(Z+1)}{p^2v^2}s, \tag{3.72}$$

or, in the case of compounds,

$$\chi_c^2 = s \sum_i \frac{4\pi e^4 N_i Z_i (Z_i+1)}{p^2 v^2}. \tag{3.73}$$

To eliminate the dependence on $q(\chi)$, Molière now defines a characteristic screening angle χ_a which is a function of only the factor $q(\chi)$. In an analogous fashion, Fano has defined an inelastic characteristic angle, χ_{in}, which is a function of only the inelastic scattering factor. These can be combined to form a composite characteristic angle $\overline{\chi_a^2}$ given (for compounds) by

$$\ln \overline{\chi_a^2} = \frac{1}{\chi_c^2} \sum_i \frac{4\pi e^4 N_i Z_i (Z_i+1)}{p^2 v^2} t \left[\frac{Z_i}{Z_i+1} \ln \chi_{a_i}^2 + \frac{1}{Z_i+1} \ln \chi_{in_i}^2 \right] \tag{3.74}$$

where the summation is over the number of elements in the compound. The only property of $q(\chi)$ assumed through the rest of the derivation is that $q \rightarrow 0$ for small angles and $q \rightarrow 1$ for large χ. This permits splitting the integral in the exponent of 3.70 into a low χ region in which an expansion can be used for the Bessel function and a high χ region which can be evaluated analytically, and allows substitution of the expression for $\overline{\chi_a^2}$ into 3.70. A parameter b is defined as

$$b = \ln(\chi_c^2/\overline{\chi_a^2}) + 1 - 2\gamma \tag{3.75}$$

in which γ is Euler's constant. Upon substitution into 3.70, this yields

$$f(\theta)\theta d\theta = \lambda d\lambda \int_0^\infty dy\, y\, J_0(\lambda y) \exp\left[\frac{1}{4} y^2 (-b + \ln \frac{1}{4} y^2)\right] \tag{3.76}$$

in which $y = \chi_c \eta$ and $\lambda = \theta/\chi_c$. This equation can be evaluated by defining a second parameter

$$B - \ln B = b \tag{3.77}$$

and transforming into a new variable $\vartheta = \theta/(\chi_c \sqrt{B}) = \lambda/\sqrt{B}$ to yield

$$f(\theta)\, \theta\, d\theta = \vartheta\, d\vartheta \sum_{n=0}^{\infty} \frac{1}{B^n} f^{(n)}(\vartheta) \tag{3.78}$$

where

$$f^{(n)}(\vartheta) = \frac{1}{n!}\int_0^\infty du\, u\, J_0(\vartheta u) \exp\left\{-\frac{1}{4}u^2\left[\frac{1}{4}u^2 \ln \frac{1}{4}u^2\right]^n\right\} \tag{3.79}$$

in which $u = y\sqrt{B}$. The $n = 0$ term is simply $2e^{-\vartheta}$, and typically only up to the $n = 2$ term is required for satisfactory evaluation of 3.78. Bethe has evaluated and tabulated $f^{(1)}$ and $f^{(2)}$ for 29 values of ϑ. In the present work, the value of B is determined from 3.77 by the *regula falsi* technique, which has been found to converge to better than .1% in less than 10 and typically only 2 or 3 iterations. The values of $f^{(1)}$ and $f^{(2)}$ are interpolated from Bethe's tables.

The energy dependence of the cross section may be taken into account by defining χ_c by

$$\begin{aligned} \chi_c^2 &= \int_0^s ds'\, \chi_c^2(s') \\ &= \int_{E(s'=0)}^{E(s'=s)} dE' \left|\frac{dE}{dx}\right|^{-1} \chi_c^2(E') \end{aligned} \tag{3.80}$$

and similarly $\overline{\chi_a^2}$ by

$$\ln \overline{\chi_a^2} = \frac{1}{\chi_c^2}\int_{E(s'=0)}^{E(s'=s)} dE' \left|\frac{dE}{dx}\right|^{-1} \chi_c^2(E')\left[\frac{Z}{Z+1}\ln \chi_a^2 + \frac{1}{Z+1}\ln \chi_{in}^2\right] \tag{3.81}$$

where the sum over constituents for compounds is implied and $\left|\frac{dE}{dx}\right|$ is the stopping power.

Bethe [Be53] has derived a large angle correction factor of the form $(\theta/\sin\theta)^{1/2}$, which should be multiplied by the distribution function in 3.78 to extend the validity to large angles.

Definition of the Characteristic Angles χ_{a_i} and χ_{in_i}

Molière's original expression of the characteristic angle shows that it is given by

$$-\ln \chi_a = \lim_{k\to\infty}\left[\int_0^k d\chi \frac{q(\chi)}{\chi} + \frac{1}{2} - \ln k\right], \tag{3.82}$$

which depends only of the definition of $q(\chi)$. Not surprisingly, Molière chose to use χ_a from his own approximate numerical evaluation of 3.82 in which he used a fitted Thomas-Fermi potential and the first Born approximation, which is of suspect validity for low atomic number elements and low energies, as discussed in chapter II.

It was stated earlier that for the purposes of the derivation of $f(\theta)$, the only restriction on $q(\chi)$ and hence on χ_a is that $q \rightarrow 0$ for small angles and $q \rightarrow 1$ for large χ. The appealing aspects of this 'definition' of $q(\chi)$ by Molière are that the above criteria are satisfied in the Born approximation by any potential which assumes exponential screening ($V(r) \sim (1/r)e^{-r/a}$) and that we obtain $\chi_a = \chi_0$ exactly, since we have (in the small angle approximation),

$$q(\chi) = \frac{\chi^4}{(\chi^2 + \chi_0^2)^2}, \tag{3.83}$$

where $\chi_0^2 = \lambda\!\!\!^{-}/a$ if a is the effective screened radius of the atom, and $\lambda\!\!\!^{-}$ is the electron wavelength divided by 2π. It is instructive to recall that this simple expression for $q(\chi)$ leads to the screened Rutherford cross section in which the screening parameter η_s is simply related to χ_0, as explained in chapter II. This suggests a method for determining an accurate χ_a, somewhat along the lines of Molière's suggestion as related by Scott, that any value could be substituted for χ_0 in 3.83 and called χ_a. Since accurate data for the single scattering cross section is available, it is proposed here that χ_a be determined from reliable (partial wave) cross section data by requiring that χ_a be set so as to correspond to the screening parameter which would be determined either if the first Born cross section is set equal to a partial wave cross section at $\theta = 0$ degrees, or if the total Born cross section is set equal to the total partial wave cross section. In other words, we set $\chi_a^2 = 4\eta_s$ where η_s is determined

either from

$$\frac{Z^2e^4}{p^2v^2}\frac{1}{(1-\cos 0+2\eta_s)^2}=\sigma_{PW}(0) \tag{3.84}$$

or from

$$\frac{2\pi Z^2e^4}{2\eta_s(1+\eta_s)p^2v^2}=2\pi\int_0^{\pi}\sigma_{PW}(\theta)\sin\theta d\theta. \tag{3.85}$$

The first method insures that the approximated and actual cross sections are roughly equal at small angles at which the majority of the collisions occur, and the second that the large angle collisions, which may be the most important, are accounted for.

Fano defined the inelastic characteristic angle, χ_{in}, in analogy with Molière's definition of χ_a,

$$-\ln\chi_{in}=\lim_{k\to\infty}\left[\int_0^k d\chi\frac{S(v(\chi))}{\chi}+\frac{1}{2}-\ln k\right]. \tag{3.86}$$

Here the variable v, given by

$$v=\frac{1}{3}Z^{-2/3}\left(\frac{pa_0}{\hbar}\right)[2(1-\cos\chi)]^{1/2},$$

is used for convenience, with a_0 the Bohr radius. Applying the small angle approximation to the previous expression and changing variables, Fano deduces

$$\ln\chi_{in}^2=u_{in}-2\ln\left[\frac{1}{3}Z^{-2/3}\left(\frac{pa_0}{\hbar}\right)\right] \tag{3.87}$$

where

$$u_{in}=\lim_{U\to\infty}\left[\int_{-\infty}^{U}du\,S(\exp\frac{1}{2}u)+1-U\right]. \tag{3.88}$$

The Z dependent values of u_{in} can be numerically evaluated from scattering function data. In this work values published by Vande Putte [Va74] have been used.

Summary of Molière's Approximations

Approximations used here can be classified into two categories, those incurred in order to analytically evaluate the expression for f and those caused by inconsistent

modeling of the physics, although the effects often overlap. Both kinds of approximations are expected to be more burdensome in the energy range treated in this work than at higher energies for which Molière's method has been generally been successfully applied. The physics approximation are summarized here:

1. The use of a exponentially screened first Born cross section to describe the both the elastic and inelastic scattering laws. It was shown is chapter II that at low energies and high atomic numbers in particular, elastic scattering is not well defined by first Born scattering laws, and particularly when used in conjunction with the screening parameters typically used in evaluating Molière's distribution.

2. The pathlength equals thickness assumption. As has been maintained throughout this work, at low energies and especially at high atomic numbers, the increase in large angle scattering makes the average tracklength of an electron traversing a material much larger that the foil thickness. This effect will be investigated in detail in a later chapter.

The major mathematical approximations in the derivation are best summarized by Bethe [Be53] and include the following:

1. The use of the small angle approximation. At the energies treated here, large angle scattering is significant and the assumption of $\sin\theta \sim \theta$ leads to underestimation of the large angle scattering. It has been observed that an exact expansion (see the next section) will lead to Molière's result in the small angle approximation if a substitution is made of a Bessel function for a Legendre polynomial, $P_l(\theta) = J_0[(l+\frac{1}{2})\theta]$. Bethe notes that Molière has shown that a more most accurate substitution would be $P_l(\theta) = (\theta/\sin(\theta)^{1/2} J_0[(l+\frac{1}{2})\theta]$,

and therefore suggests that a correction factor of $(\theta/\sin\theta)^{1/2}$ be multiplied by Molière's distribution, as noted above.

2. Splitting the integral into $q(\chi)\rightarrow 0$ and $q(\chi)\rightarrow 1$ parts. Bethe has shown that this approximation leads spuriously to increasing integrands in 3.76 above a given value of y, and asserts that the the expression for $f(\theta, s)$ will be valid only if it is clear that the there would be little contribution to the total integral of the (accurate) partial integral past this minimum, i. e. if the integrand is very small here. The value of the integrand at the inflection is given by $\exp(-e^{b-1})$, which is $\sim e^{-\Omega_0/e}$, where Ω_0 is the number of collisions over the path and is given by roughly $(\chi_c/\overline{\chi_a})^2$. Bethe suggests that Ω be roughly 20 or greater ($e^{-20/e} \leq$ 1%) to insure that 3.76 is accurate. Because of the typically requirement in condensed history Monte Carlo electron transport models that the transport step size be short to keep the average deflection small, the number of collisions in low energy transport steps is often small and the condition $\Omega_0 \geq 20$ is not always met. Noting that in typical condensed history simulation a typical multiple scattering distribution will be calculated for a step corresponding to a 4.24% energy loss, (corresponding to a 50% loss in 16 steps), plots of Ω_0 (using χ_a determined by 3.84 to conform with a partial wave cross section at $\theta = 0$) are given for pathlengths corresponding to a 4.24% fractional energy losses at several initial energies and for several elements in figure 3.15. It is seen in the figures that the threshold for satisfying the number of collisions condition is falls from roughly 8 keV for aluminum to 3 keV for gold. It must be noted that a 4% energy loss over a single step for a 3 keV electron traveling in gold may violate the small deflection transport assumption, and so smaller energy loss steps are likely to be required by this constraint, contrary to the 20 collision

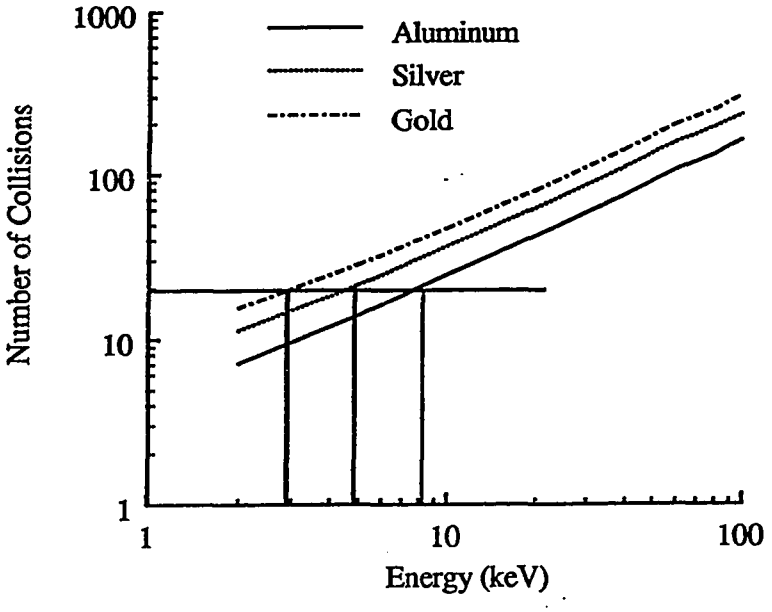

Figure 3.15: Number of Elastic Collisions over a 4.24% Energy Loss Step condition.

Other approximations, as discussed by Bethe and Scott, are expected to be small.

3.3.2 Goudsmit and Saunderson's Method - Legendre Expansion

Goudsmit and Saunderson [Go48a] have derived an expression in which the multiple scattering distribution is given in terms of a Legendre polynomial expansion,

$$f_{GS}(s,\theta) = \sum_l (l+\frac{1}{2})\, G_l(s)\, P_l(\cos\theta) \tag{3.89}$$

where the expansion coefficients are given by

$$\begin{aligned} G_l(s) &= \exp\left[-2\pi N \int_0^s ds' \int_0^\pi \sin\theta' d\theta' \sigma(s',\theta')\,(1-P_l(\cos\theta'))\right] \\ &= \exp\left[-2\pi N \int_0^s ds'\, g_l(s')\right] \end{aligned} \tag{3.90}$$

with (obviously)

$$g_l(s') = \int_0^\pi \sin\theta' d\theta' \sigma(s',\theta')\,(1-P_l(\cos\theta'))\,. \tag{3.91}$$

It can be easily seen from the derivation (especially as related by Peterson, [Pe83]) that the only requirements for this expansion to retain exactness are that the scattering law not change from one collision to the next (equivalent to requiring either small sensitivity of σ with respect to energy or little change in energy over the transport step) and that distribution in the number of collisions undergone by particles traveling a distance s be given by a Poisson distribution. Both conditions are well met in nearly all typically encountered circumstances, and, unlike the Molière distribution, the accuracy of this distribution improves for transport steps which encompass very few collisions. Since the faithfulness of the accordance with the second condition is dependent upon the relationship between the pathlength and the transport thickness, the distribution requires small steps at low initial energies. Additionally, the accuracy of this distribution function is usually dependent on the accuracy of the single scattering cross section used in determining the coefficients, $g_l(s')$.

Numerically, the $g_l(s')$ coefficients are difficult to evaluate. Spencer [Sp55] has developed recursion functions which can be used in conjunction with expansions for the cross section $\sigma(\theta')$ which are in terms of integer and and half integer powers of $(1-\cos\theta'+2\eta_s)$ and/or in terms of Legendre polynomials to quickly evaluate the inner integral term, $g_l(s')$. Taking $\mu=\cos\theta'$, Spencer defines a recursion function $p_{m,l}$ as

$$p_{m,l}=\int_{-1}^{+1}d\mu\,(1-\mu+2\eta_s)^m(1-P_l(\mu)) \tag{3.92}$$

in which m is any integer or half integer. Note that $p_{m,0}=0$ for all l. A recursion relation between $p_{m+1,l}$ and the $p_{m,l}$'s can be derived as

$$p_{m+1,l}=(1+2\eta)p_{m,l}+p_{m,1}-\frac{l+1}{2l+1}p_{m,l+1}-\frac{l}{2l+1}p_{m,l-1}. \tag{3.93}$$

In order to apply this, a relation for the $p_{m,l+1}$ term which is lowest order in m in

terms of the prior l terms for the same m is needed. This can be shown to be

$$(l-m-2)\,p_{m,l+1} = (1-l+m)\,p_{m,l-1} + (1+2\eta_s)(2l+1)\,p_{m,l} - (2l+1)2\eta_s \int_{-1}^{+1} d\mu\,(1-\mu+2\eta_s)^m \qquad (3.94)$$

The lowest order l terms needed to start the recursion can be found by direct analytical integration of 3.92.

For a given θ the $p_{m,l}$'s are severely dependent functions of η_s, as can be seen from their definitions. Values of η_s are typically on the order of 10^{-3} or less, resulting numerically in the use of the sums and differences of very small numbers and very similar numbers, and as much as one significant digit can be lost per l in the march through the recursion in some situations. Thus, even though it would seem impractical to perform numerical integration over the the entire angle range and over the pathlength for each l, Berger and Wang [Be89] have recently reported results in which a quadrature technique was used in order to subvert the roundoff problem encountered in using the recursion functions. They report that convergence could be obtained in less than 999 terms for thicknesses as low as 20 mean free paths in gold and copper for initial energies of about 1 MeV, and at as few as 6 mean free paths for "lower" energies. Direct integration of 3.91 has been briefly investigated in the current work. A 3 point Gaussian quadrature routine was used for the integration, working with tabulated values of the Riley elastic scattering cross section. It was found that the computation time required to evaluate 500 coefficients rose from roughly 400 milliseconds using Spencer's recursions to 15.5 minutes using direct integration, independent of the electron initial energy, material or pathlength. It was also found that the round off problems encountered in evaluating the coefficients in low energy and short pathlength regimes were not alleviated by this

simple scheme, although they were not worsened either (results comparing distribution functions calculated with directly integrated values of G_l and those using the recursively determined $G_l's$ agreed to < 1.5 % in all instances in which convergence was achieved). A more accurate integration technique employing a packaged integration program (still a Gauss quadrature but with more elaborate error checking) and not using pre-calculated cross section values, was explored but was not implemented, as the additional increase (above the increase already encountered) in computation time was felt to render the calculation impractical for the current problem. Thus, Spencer's recursion technique is employed throughout this work.

Applicable Cross Sections

Cross sections of form suitable for use with Spencer's recursion functions must be in the form

$$\sigma(s,\mu) = \sum_i A_i P_i(\mu) + \sum_j B_j (1 - \mu + 2\eta_s)^{m_j} \tag{3.95}$$

in which A_i, B_j and η_s are usually functions of energy and hence functions of s. When such an expansion is substituted for $\sigma(\mu)$ in the integral for $g_l(s)$ in 3.90 we find

$$g_l(s) = \int_{-1}^{+1} d\mu \left[\sum_i A_i P_i(\mu) (1 - P_l(\mu)) + \sum_j B_j (1 - P_l(\mu)) (1 - \mu + 2\eta_s)^{m_j} \right]. \tag{3.96}$$

Given that

$$\int_{-1}^{+1} d\mu \, P_i(\mu) P_l(\mu) = \frac{2}{2i+1} \delta_{li}$$

the first summation in this expression can be written as

$$2A_0 - \sum_i \frac{2}{2i+1} A_i \delta_{li}.$$

The terms in the second summation are obviously of the form of the $p_{m,l}$'s and we have

$$g_l(s) = 2A_0 - \sum_i \frac{2}{2i+1} A_i \delta_{li} + \sum_j B_j p_{m_j,l}. \tag{3.97}$$

Three types of cross sections expansions are applicable to this methodology. Obviously, the screened first Born cross section,

$$\sigma(\theta) = \frac{4\pi e^4 Z^2}{p^2 v^2 (1-\mu+2\eta_s)^2},$$

has the desired form, with the all the A_i's being zero and only one B_j term ($m_j = -2$) present. In this case we have for the g_l's

$$g_l(s) = \frac{4\pi e^4 Z^2}{p^2 v^2} p_{-2,l}. \tag{3.98}$$

As noted earlier, the recursion relation for lowest order m terms must be evaluated using 3.94, giving in this case it is required for $m = -2$, giving

$$p_{-2,l+1} = -\left(\frac{l+1}{l}\right) p_{-2,l-1} + \left(\frac{2l+1}{l}\right)(1+2\eta_s)\, p_{-2,l} - \frac{2l+1}{l(1+\eta_s)} \tag{3.99}$$

with $p_{-2,1}$ evaluated from 3.92 to be $\ln(1+\eta_s^{-1}) - (1-\eta_s)^{-1}$

Recognizing that this form of the cross section is inaccurate at large angles, Berger has used an exact cross section from Mott ($\sigma_{M,uns}$) corrected for screening by multiplying by the ratio of a screened first Born cross section using the Molière's screening parameter ($\sigma_{R,scr}$) and the unscreened cross section ($\sigma_{R,uns}$), as described in chapter II. In order to employ this cross section in 3.97 it is rewritten as

$$\begin{aligned} \sigma(s,\mu) &= \sigma_{R,scr} \frac{\sigma_{M,uns}}{\sigma_{R,uns}} \\ &= \sigma_{R,scr} \left[1 + \frac{\pi Z\alpha}{\sqrt{2}\beta} \cos\gamma (1-\mu+2\eta_s)^{1/2} + h(\mu)\right] \end{aligned} \tag{3.100}$$

in which $\cos\gamma$ is defined as in the expression for Mott's cross section and $h(\mu)$ is given by

$$h(\mu) = \frac{\sigma_{M,uns}}{\sigma_{R,uns}} - 1 - \frac{\pi Z\alpha}{\sqrt{2}\beta} \cos\gamma (1-\mu+2\eta_s)^{1/2}. \tag{3.101}$$

Such a definition is useful because $h(\mu)$ can be expanded to a high degree of accuracy as

$$h(\mu) = \sum_j h_j (1-\mu+2\eta_s)^{j/2}. \tag{3.102}$$

(Colbert has suggested that only non-negative, even values of j need be used [Co74], but this seems to be of small consequence.) Noting that there is a $(1-\mu+2\eta_s)^{-2}$ factor in $\sigma_{R,scr}$, it is easily seen that $\sigma(s,\mu)$ fits the form of 3.95 with no sum over the i terms and with $m_j = (j-4)/2$, and the B_j coefficients given by

$$\begin{aligned} B_0 &= \frac{4\pi e^4 Z^2}{p^2 v^2}(1+h_0) \\ B_1 &= \frac{4\pi e^4 Z^2}{p^2 v^2}\left(\frac{\pi Z\alpha}{\sqrt{2}\beta}\cos\gamma + h_1\right) \\ B_2 &= \frac{4\pi e^4 Z^2}{p^2 v^2} h_2 \\ \vdots &= \quad \vdots \\ B_j &= \frac{4\pi e^4 Z^2}{p^2 v^2} h_j. \end{aligned} \tag{3.103}$$

The coefficients h_j can be determined by a least squares fit to values of $h(\mu)$ calculated from 3.101. Typically only 30 or so angles and the $j = 1 \ldots 5$ coefficients are sufficient to model the expanded cross section to within .1% of the actual value at all angles. Tests over a wide range of energies and atomic numbers confirmed this.

In this expansion, using $j = 1 \ldots 5$, we need two low order m recursions, since both integer and half integer values of m are present. The lowest order integer term has $m_0 = -2$ and so equation 3.99 can be used, and for the lowest order half integer term, $m_1 = -3/2$, we have

$$p_{-3/2,l+1} = \eta_s' p_{-3/2,l} + p_{-3/2,l-1} \tag{3.104}$$

in which $\eta_s' = 1-2\eta(\sqrt{1+1/\eta_s}-1)$. The starting term $p_{-3/2,1}$ is given by

$$2(2\eta_s')^{3/2}(1+\eta_s')^{-1}.$$

A third candidate cross section is that given by Riley *et al.*, who parameterized their exact, screened calculations precisely in the form of 3.95, specifically for implementation in the Goudsmit-Saunderson distribution, with $i = 0 \ldots 6$ and $j = -4 \ldots -1$, with $m_j = j$. For this case, the recursion relation for $p_{-4,l+1}$ is given by

$$p_{-4,l+1} = -\left(\frac{l+3}{l-2}\right) p_{-4,l-1} + \left(\frac{2l+1}{l-2}\right)(1+2\eta_s)\, p_{-4,l} - \left(\frac{2l+1}{l-2}\right)\left[\frac{\eta_s}{12(1+\eta_s)^3} - \frac{1}{12\eta_s^2}\right]. \tag{3.105}$$

We see that in addition to the starting $l = 1$ term, we will also need to explicitly evaluate the $l = 3$ term, since there are an $l-2$ expressions in the denominators of several of the terms. For convenience, we can derive all of the first 3 terms, which are given by

$$\begin{aligned} p_{-4,1} &= \frac{1+3\eta_s}{24\eta_s^2(1+\eta_s)^3} \\ p_{-4,2} &= \frac{3(1+\eta_s)}{24\eta_s^2(1+\eta_s)^3} \\ p_{-4,3} &= \frac{5}{2}\ln\left(\frac{1+\eta_s}{\eta_s}\right) + \frac{6\eta_s - 12\eta_s^2 - 110\eta_s^3 - 150\eta_s^4 - 60\eta_s^5}{24\eta_s^3(1+\eta_s)^3} \end{aligned} \tag{3.106}$$

The next step in the evaluation of $f_{GS}(s,\theta)$ is the determination of the integral of the g_l's over the pathlength. Two methods have been examined here. In the first, the integrals are done as were similar integrals over path in the evaluation of Molière's distribution, using the inverse stopping power and employing the trapezoid rule. This should be a reasonable approximation when the cross section and hence the g_l's are insensitive to the energy loss. We have

$$G_l(s) = \exp\left[-2\pi N \int_{E(s'=0)}^{E(s'=s)} dE' \left|\frac{dE}{dx}\right|^{-1} g_l(E')\right] \tag{3.107}$$

As an alternative method, Spencer has shown that $g_l(s)$ can be approximated by

$$g_l'(s') = g_1(s')\frac{g_l(s'=0)}{g_1(s'=0)} \tag{3.108}$$

and that $g_1'(s')$ can be approximated as

$$g_1'(s') = \frac{c_1}{t(s')(t(s') + c_2)} \tag{3.109}$$

where t is defined by

$$t(s') = \frac{r_0 - s'}{r_0} \tag{3.110}$$

in which r_0 is the total residual range. The constants c_1 and c_2 are evaluated from $g_1(1)$ ($t = 1$ at $s' = 0$) and $g_1(t(s))$, and are given by

$$\begin{aligned} c_2 &= \frac{g_1(1) - t^2 g_1(t)}{t g_1(t) - g_1(1)} \\ c_1 &= (1 + c_2) g_1(1). \end{aligned} \tag{3.111}$$

Equation 3.109 can be substituted into 3.90 which can then be evaluated analytically to yield

$$G_l(s) = \frac{r_0 c_1}{c_2} \frac{g_l(1)}{g_1(1)} \ln\left[\frac{t + c_2}{t(1 + c_2)}\right]. \tag{3.112}$$

This method will allow faster evaluation of $G_l(s)$ as only the $l = 1$ term in the $g_l(s)$ series needs to be evaluated. Tables 3.9 through 3.11 show values of the average scattering cosines of distributions calculated by numerical integration (equation 3.107) and by Spencer's transformation, (3.112). for various values of s, Z, E and l. It is seen that little variation is found throughout the entire range of energies, pathlengths, and atomic numbers examined, except at very thick paths that are much longer than typical condensed history steps, and even then the variation is only a few percent. What is interesting to note is the large amount of scattering for high Z materials.

The last step in the evaluation of $f_{GS}(s, \theta)$ is the summation of the series itself. In general, $f_{GS}(s, \theta)$ converges very slowly, with the problems becoming worse at low energies, short tracklengths and low atomic numbers. It has been proposed by

Fraction of Total	200 keV		60 keV		5 keV	
Range Traversed	Num. Int.	Spenc.	Num. Int.	Spenc.	Num. Int.	Spenc.
.005	.9905	.9905	.9896	.9896	-	-
.050	.9036	.9037	.8982	.8982	.8880	.8878
.200	.6411	.6427	.6244	.6260	.5873	.5890

Table 3.9: Variation of $< \cos\theta >$ for Aluminum at Various Energies and Thicknesses

Fraction of Total	200 keV		60 keV		5 keV	
Range Traversed	Num. Int.	Spenc.	Num. Int.	Spenc.	Num. Int.	Spenc.
.005	.9628	.9628	.9630	.9630	-	-
.050	.6756	.6757	.6748	.6749	.7114	.7115
.200	.1800	.1815	.1798	.1814	.2274	.2292

Table 3.10: Variation of $< \cos\theta >$ for Silver at Various Energies and Thicknesses

Fraction of Total	200 keV		60 keV		5 keV	
Range Traversed	Num. Int.	Spenc.	Num. Int.	Spenc.	Num. Int.	Spenc.
.005	.9331	.9331	.9391	.9391	-	-
.050	.4926	.4927	.5197	.5197	.6169	.6169
.200	.0458	.0465	.0583	.0591	.1232	.1246

Table 3.11: Variation of $< \cos\theta >$ for Gold at Various Energies and Thicknesses

Felder [Fe69] that the transformation of Yennie *et al.* [Ye54] be applied to speed the convergence of this series, as in the evaluation of the exact Mott cross section series. In general, the transformation greatly speeded convergence of the series, especially at large angels. However, it was found that in some instances that the transformation did not speed but rather slowed and sometimes even inhibited the convergence for small angles. In no instances did the application of the the transform at low angles provide a vehicle for the convergence of series which would not converge without the transform. Therefore, only for angles less than 10 degrees is this transformation applied. Plots of the number of terms which must be summed before the succeeding terms are less than .01% of the total sum are given in figures 3.16 through 3.21 for various values of s, Z, E and m, where m is the order of the transformation. The maximum number of terms used was limited by the number of non-decreasing $g_l'(s)$'s, with a maximum of 500 terms, and the minimum was limited to 20, which is necessary to trap false convergence in few terms at scattering angles of 90 degrees. It is seen that a transform order of 3 allows convergence in a few instances when the second order transform does not, so for all cases inr this work a third order transformation is used. What is striking about the results is that no convergence is achieved for reasonably large energy loss steps at low energy.

A further numerical trick to speed convergence (at the penalty of introducing error which must later be accounted for) has been devised by Berger and Seltzer. They note that the expansion of equation 3.89 is valid in theory even for the case of no collisions (or zero thickness), for which the result should be a delta function at $\theta = 0$. Indeed, in this instance all of the G_l's are equivalent (and equal to G_0, which

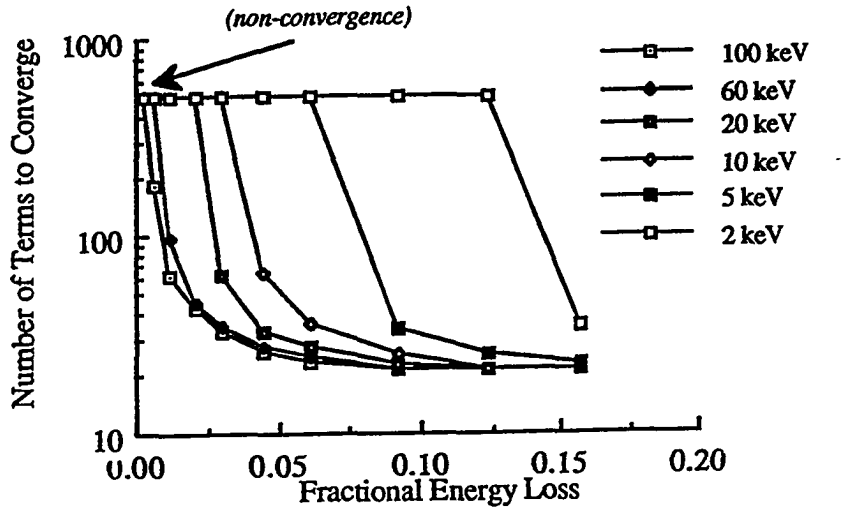

Figure 3.16: Number of Terms for Convergence of $f_{GS}(s,\theta)$ for Aluminum, $m = 2$, vs. Energy, Path

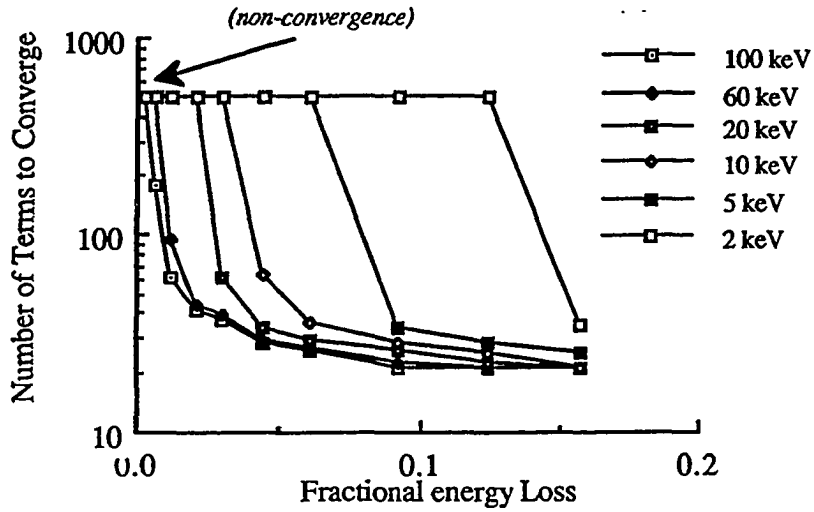

Figure 3.17: Number of Terms for Convergence of $f_{GS}(s,\theta)$ for Aluminum, $m = 3$, vs. Energy, Path

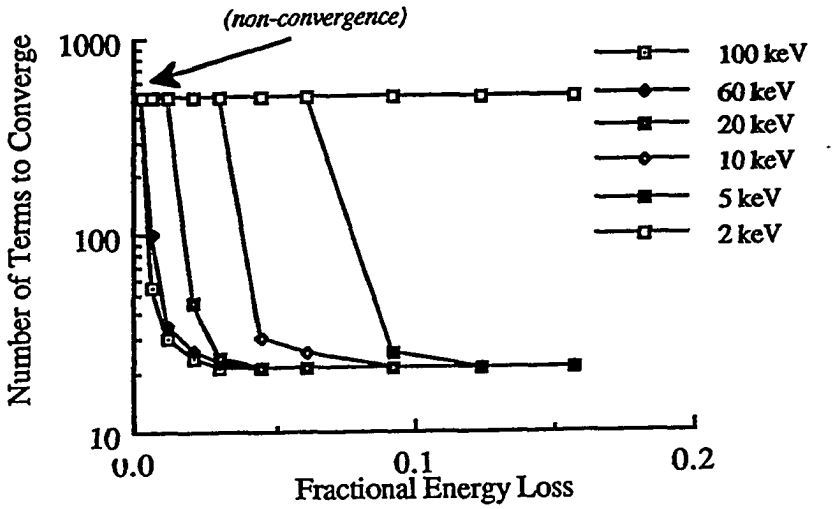

Figure 3.18: Number of Terms for Convergence of $f_{GS}(s,\theta)$ for Silver, $m = 2$, vs. Energy, Path

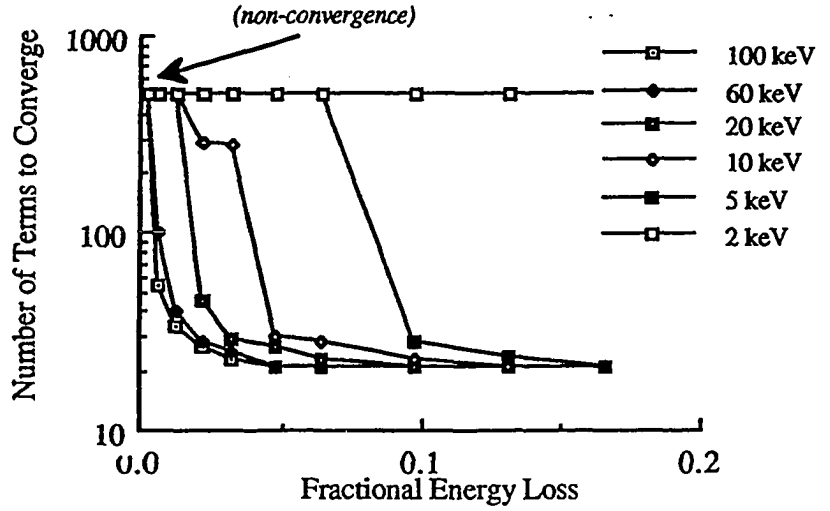

Figure 3.19: Number of Terms for Convergence of $f_{GS}(s,\theta)$ for Silver, $m = 3$, vs. Energy, Path

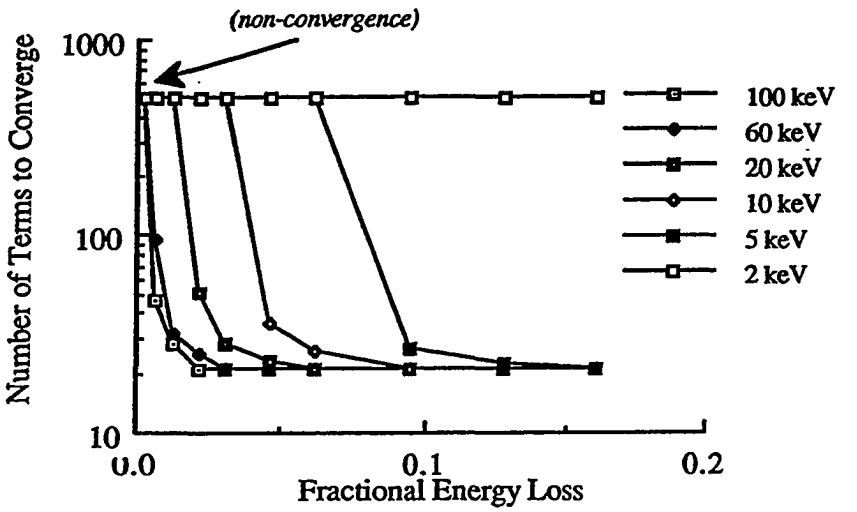

Figure 3.20: Number of Terms for Convergence of $f_{GS}(s,\theta)$ for Gold, $m = 2$, vs. Energy, Path

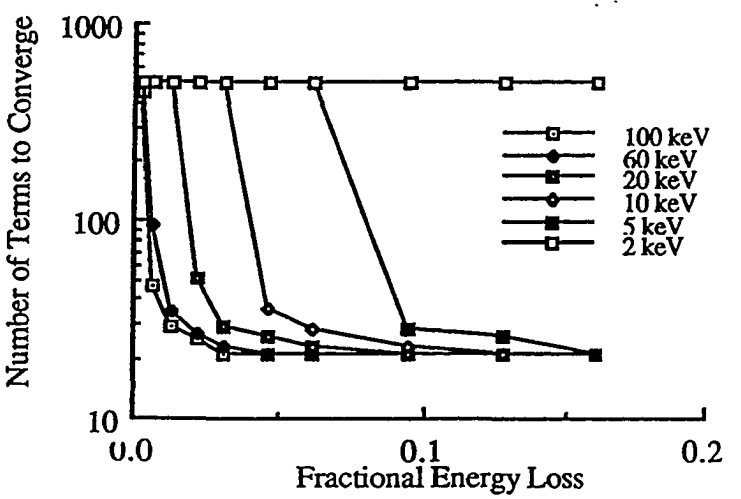

Figure 3.21: Number of Terms for Convergence of $f_{GS}(s,\theta)$ for Gold, $m = 3$, vs. Energy, Path

is = 1), and it can be shown that

$$G_0 \sum_{l=0}^{\infty} (l + \frac{1}{2}) P_l(\theta) = \delta(\theta),$$

although an infinite number of terms is required for this result. At small but non-zero number of collisions (short paths), a similar situation occurs, as the difference between successive coefficients becomes numerically indeterminate as l increases, owing to machine precision. If L is the last numerically correct coefficient, it is argued that the distribution can be approximated by

$$\begin{aligned} f_{GS}(s,\theta) &= \sum_{l=0}^{\infty} (l + \frac{1}{2}) G_l(s) P_l(\theta) \\ &= \sum_{l=0}^{\infty} (l + \frac{1}{2}) [G_l(s) - G_L(s)] P_l(\theta) + G_L(s) \sum_{l=0}^{\infty} (l + \frac{1}{2}) P_l(\theta) \\ &\sim \sum_{l=0}^{L} (l + \frac{1}{2}) [G_l(s) - G_L(s)] P_l(\theta) + G_L(s) \delta(\theta). \end{aligned} \tag{3.113}$$

Since numerically $G_l = G_L$ for all $l \geq L$, the first term sum need be taken only out to L. The second term is the no-scatter delta function, which can be taken into account by ignoring it in the determination of $f_{GS}(s,\theta)$ and instead determining a no-scattering probability (given by $P_{ns}(s) = e^{-\Sigma s}$) at $\theta = 0$ and invoking multiple scattering in Monte Carlo runs only when appropriate. In practice, Berger and Seltzer employ the above technique to calculate the distribution in all instances in the ITS code series. They use an empirical expression based on the screening parameter, rather than a comparison of the last few G_l's, to estimate the number of terms required, and they further artificially constrain L to be between 51 and 242. The series terms always 'converges,' since the last coefficient, given by $G_L - G_L$, is always equal to zero. In practice, there is often still significant deviation between G_L and G_{L+1}, which somewhat invalidates the approximation of truncating the first term in equation 3.113 at $l = L$. Test runs were made to examine the effect of

this approximation on the accuracy of the distribution function. Truncation was performed when the first decreasing g_l (and hence increasing G_l coefficient) was reached. It was found that in all cases in which convergence was achieved for the full series, the truncated results were identical. This was to be expected since full series results converge only for long pathlengths, when the no scatter probability is small. Further comparisons, between unconverged full series and truncated series results revealed that the truncated and unconverged full series results are roughly equivalent (within a few percent in the worst cases) at large angles, but that at small angles the truncated series results significantly underestimate the scattering. ('Unconverged' results are those that did not converge at *every* angle.) In most instances, the unconverged series converged for all but a few angles, with those usually limited to within a few degrees of $\theta = 0$ Thus, the difference between the truncated and unconverged sums approximates, but does not equal, a delta function, because of the errors in approximations of equation 3.113, as described above. An example of the difference in a truncated and a non-truncated but unconverged series is shown in figure 3.22. It is clear from the figure that the majority of the error is at the small angles, and so could be modeled by adding a no scatter component. The magnitude of no scatter probabilities are shown in figures 3.23 and 3.24 for several elements and various pathlengths at low energies. It is seen in the figures that throughout the range of elements the no scattering probability at low initial energies can sometimes be quite large, but only for paths as thick as those encountered in high energy condensed history simulations. It is noted, however, that successful low energy condensed history simulations will require the short paths over which the no scatter probability is large. Despite the theoretical hand waving involved, since full series do not converge at short paths and low energy, the approximation of adding

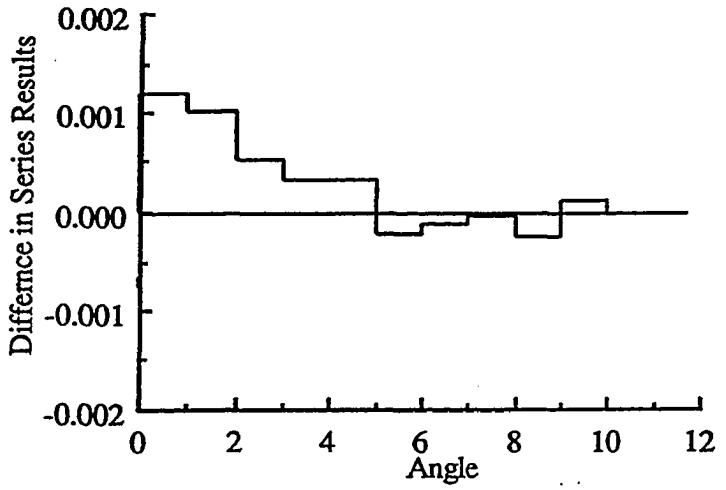

Figure 3.22: Truncated vs. Unconverged Series of $f_{GS}(s,\theta)$ for Aluminum at 4.24 % Energy Loss

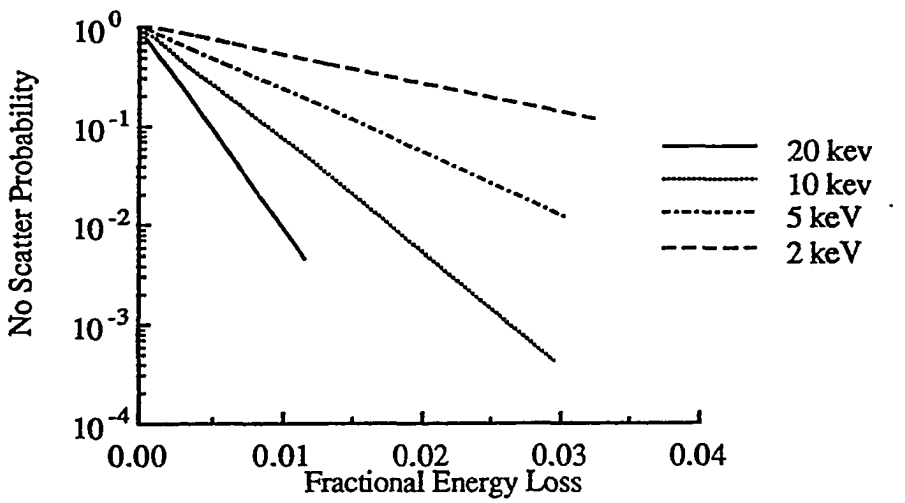

Figure 3.23: No Scatter Probability for Aluminum vs Energy Loss

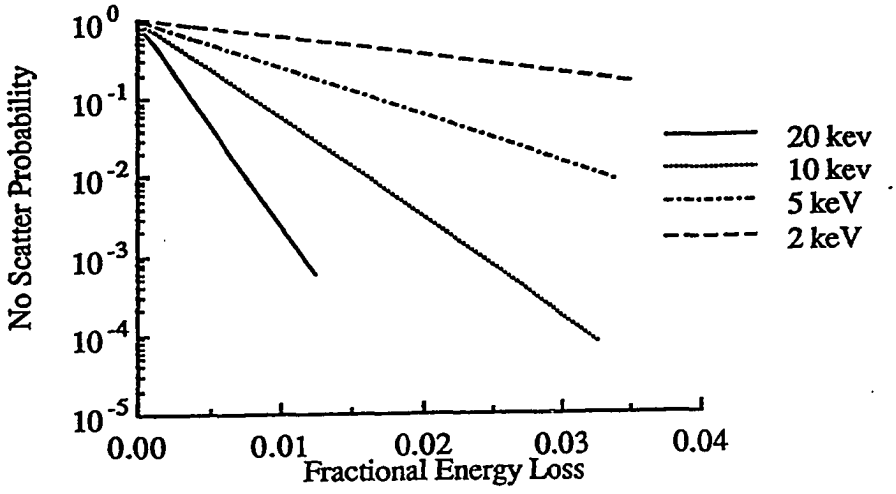

Figure 3.24: No Scatter Probability for Gold vs Energy Loss

a no scatter probability to multiple scattering distribution function seems to be the best way to model scattering at the small steps.

3.3.3 Models Used by Previous Investigators

A list of multiple scattering distributions used by previous investigators is given in table 3.12. Because of the numerical difficulties encountered in calculating the various distribution functions, there are unique features to almost every implementation listed. It is instructive to comment on some special characteristics of one of the two most widely used formats, the Molière formalism of EGS. In the form employed by EGS, the characteristic angle χ_a and parameter B are calculated each time the distribution is sampled, and a cumulative form of the expansion functions $f^{(0)}+f^{(1)}+f^{(2)}$ is numerically inverted. Additionally, the approximation that $\beta \rightarrow 1$ is employed in the calculation of χ_a. This is clearly not true at low energies, although in practice it results in a much less worse approximation of χ_a than would a strict adherence to

Molière's original formula for χ_a, as will be seen in the next section.

3.3.4 Multiple Elastic Scattering Experiments at Low Energies

Although quite a number of investigations of the scattering of transmitted beams of mono-energetic electron have been performed, in very few instances are the results reported in terms of multiple scattering distribution functions (as plots of $f(\theta)d\theta$ versus θ). Most often, results showing the dependence of the average and most probable scattering angles on thickness, energy and/or atomic number are presented. Table 3.13 lists those experiments in which the results are given in a form suitable for direct comparison with multiple scattering theories.

3.3.5 Evaluations and Conclusions

For the purpose of comparison, two versions of the Molière distribution and two of the Goudsmit-Saunderson are examined, as listed in table 3.14.

The experiments from table 3.13 which are modeled are those of Cosslett and Thomas [Co64a], and Inada [In71]. Results are presented in figures 3.25 through 3.28. The Cosslett and Thomas experiments are of particular interest because they focused on the 'plural scattering' region, in which the number of collisions is small. The average energy loss over the foils for these experiments can be calculated to be 1.89% for the aluminum experiment, 1.56% for the copper run and 0.65 % for the gold experiment. All of these represent smaller loss than typically encountered in Monte Carlo simulations. for For the As expected, in this regime not all of the different types of distribution functions converged at all angles. In fact, the Goudsmit-Saunderson distribution with the Berger/Mott/Molière cross section did not produce reliable results, and the Molière using Molière's screening parameter *never* yielded consistent

Multiple Scattering Formalism	Monte Carlo Authors
Molière	Hebbard and Wilson [He55] Sidei *et al.* [Si57] Perkins [Pe62] Berger [Be63] Mukoyama and Watanabe [Mu77] Vande Putte [Va74] EGS [Fo78, Ne85]
Goudsmit and Saunderson with σ_{Ruth} and Molière screening	ETRAN [Be68] Vande Putte [Va74] Gorelik and Rozin [Go72] Berger [Be63]
Goudsmit and Saunderson with σ_{Mott} and Molière screening	Berger [Be63] ETRAN [Be68] Sundararaman *et al.* [Su73] Kulkarni and Supe [Ku84] Vande Putte [Va74]
Goudsmit and Saunderson with σ_{Ruth} and Wentzel screening	Heńoc and Maurice [He76] Bishop [Bi67]
Gaussian distribution after Rossi	Leiss *et al.* [Le57]
Goudsmit and Saunderson with σ_{Ruth} and Nigam Screening	Shinoda, Murata and Shimizu [Sh68] Shimizu and Murata [Sh71]
Goudsmit and Saunderson with σ_{Riley}	ITS (Berger and Seltzer) [Ha84]
Bothe [Bo27] for $\theta < \pi/2$, empirical for $\theta > \pi/2$	Green [Gr63]
Unscreened Rutherford, empirically adjusted, randomly sampled impact parameters [Cu71]	Love,Cox and Scott [Lo77] Myklebust *et al.* [My76] Newbury *et al.* [Ne80]
Rossi and Greisen [Ro41]	Hebbard and Wilson [He55]
Fixed Angle Methods [Li77, Li78a]	Liljequist [Li77, Li78a] Liljequist *et al.* [Li78b]
Lewis multiple scattering model, $\theta < 10°$, Single scattering [Re71] $\theta > 10°$	Reimer and Krefting [Re76]

Table 3.12: Multiple Scattering Distributions Used in Monte Carlo Electron Transport Codes

Authors	Material (Z)	Energy (keV)	Thickness ($\times 10^{-6}$ cm)	Angles (deg)
Cosslett and Thomas [Co64a]	Al (13)	20	6.07–35.6	.45 – 45
	Cu (29)	20	2.15–8.99	.45 – 45
	Au (79)	20	.64–4.1	.45 – 45
Cosslett and Thomas [Co64b]	Cu (29)	20	2.15–19.2	0 – 180
Haefer [Ha60]	C (6)	40,80	6.25–87.5	.79–3.87
Inada *et al.* [In71]	Al (13)	5,10,15,30	7.95–13.7	.05–35
	Polyst. (1,6,8)	15	10.7–19.6	.05–35
Kamiya [Ka58]	C (6)	47	3.5–44.	.57–6.88
Klemperer *et al.* [Kl60]	Al_2O_3 (8,13)	.81–6.0	2.08	9–17.83
Lanteri *et al.* [La80]	Al (13)	1.0–3.0	1.5–7.85	0–180
Leisegang [Le52]	Al (13)	20,40,68	2.7	0-7
	Ag (47)	20,40,68	1.2–4.5	0-15
	Au (79)	40,68	1.5	0-13

Table 3.13: Multiple Elastic Scattering Experiments in the Kilovolt Energy Range

1. Molière distribution with Molière screening parameter
2. Molière distribution with EGS/Molière screening parameter
3. Goudsmit-Saunderson distribution with Berger/Mott/Molière cross section
4. Goudsmit-Saunderson distribution with Riley cross section

Table 3.14: Multiple Scattering Distributions Tested In this Work

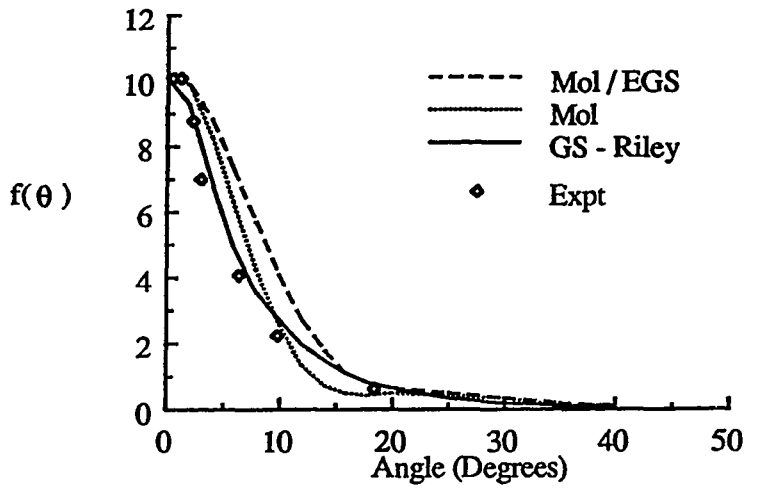

Figure 3.25: Comparison of Multiple Scattering Distributions with Experiment for Aluminum at 20 keV

results, and in fact most often was faced with a regime in which the b parameter was indeterminate. It is seen that only the the Goudsmit-Saunderson distribution using the Riley cross section gives results that approach the experimental data in these short steps which must be used in low energy condensed history simulations. Also seen is a significant amount of scattering at very small angles not modeled by the theory, as expected.

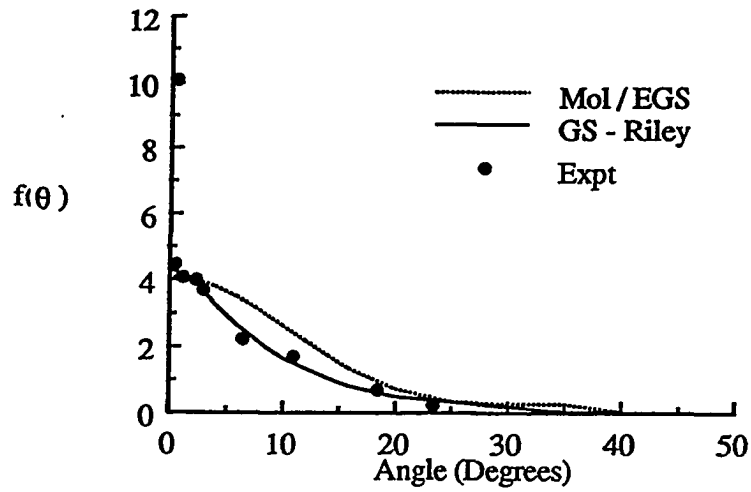

Figure 3.26: Comparison of Multiple Scattering Distributions with Experiment for Copper at 20 keV

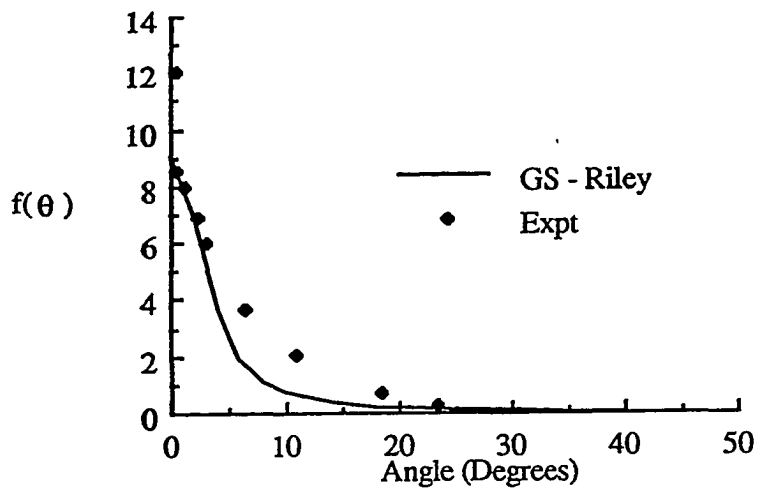

Figure 3.27: Comparison of Multiple Scattering Distributions with Experiment for Gold at 20 keV

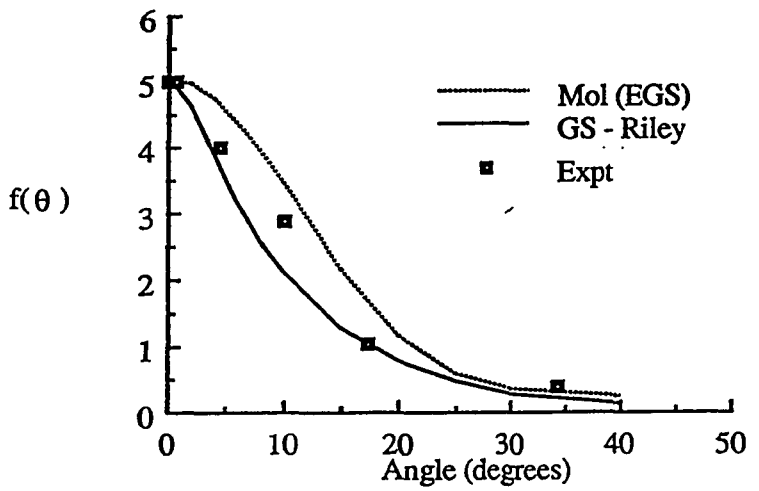

Figure 3.28: Comparison of Multiple Scattering Distributions with Experiment for Aluminum at 10 keV

References

[Al83] K.O. Al-Ahmad and D. E. Watt, *J. Phys. D* **16**, (1983) 2257.

[Be32] H.A. Bethe, *Z. Physik* **76**, (1932) 293.

[Be53] H.A. Bethe, *Phys. Rev.* **89**, (1953) 1256.

[Be63] M.J. Berger, "Monte Carlo Calculation of the Penetration and Diffusion of Fast Charged Particles," in *Methods in Computational Physics*, vol. 1, B. Adlu, S. Fernbach, M. Rotenberg, eds., Academic Press, New York (1963) 135.

[Be68] M.J. Berger and S.M. Seltzer, *Monte Carlo Code System for Electron and Photon Transport through Extended Media*, Oak Ridge Natioanl Laboratory Radiation Shielding Information Center document CCC-107 (1968).

[Be70] M.J. Berger, S.M. Seltzer and K. Maeda, *J. Atmos. Terrestial Phys.* **32**, (1970) 1015.

[Be82] M.J. Berger and S.M. Seltzer, *Stopping Powers and Ranges for Electrons and Positrons*, National Bureau of Standards Report NBSIR 82-2550 (1982).

[Be89] M. J. Berger and R.Q. Wang, *Monte Carlo Transport of Electrons and Photons*, T. M. Jenkins, W. R. Nelson and A. Rindi, Eds., Plenum Press, New York (1989)

[Bi67] H.E. Bishop, *Brit. J. Appl. Phys.* **18**, (1967) 703.

[Bl50] O. Blunck and S. Leisegang, *Z. Physik* **128**, (1950) 500.

[Bl51] O. Blunck and K. Westphal, *Z. Physik* **130**, (1951) 641.

[Bo27] W. Bothe, *Handb. d. Phys.* **24**, (1927) 18.

[Bo61] W. Borsch-Supan, *J. Research NBS* **65B**, (1961) 245.

[Br69] D.B. Brown, D.B. Wittry, and D.F. Keyser, *J. Appl. Phys.* **40**, (1969) 1627.

[Br87] R. Brun, F. Bruyant, M. Maire, A.C. McPherson and P. Zanarini, *GEANT3 User's Guide*, CERN Data Handling Division Document DD/EE/84-1 (1987).

[Ca75] T.A. Carlson, *Photoelectron and Auger Spectroscopy*, Plenum Press, New York (1975).

[Co64a] V. E. Cosslett and R. N. Thomas, *Brit. J. Appl. Phys.* **15**, (1964) 235.

[Co64b] V. E. Cosslett and R. N. Thomas, *Brit. J. Appl. Phys.* **15**, (1964) 883.

[Co64c] V. E. Cosslett and R. N. Thomas, *Brit. J. Appl. Phys.* **15**, (1964) 1283.

[Co69] A. Cohn and A.G. Caledonia, *Bull. Am. Phys. Soc.* **14**, (1969) 523.

[Co74] H. M. Colbert, *SANDYL A Computer Program for Calculating Combined Photon-Electron Transport in Complex Systems*, Sandia Report SLL-74-0012 (1974).

[Cu71] L. Curgenven and P. Duncumb, *Simulation of Electron Trajectories in a Solid Target by a Simple Monte Carlo Technique*, Tube Investments Report No. 303 (1971).

[Eg75] E. Eggarter, *J. Chem. Phys.* **56**, (1975) 833.

[Fa54] U. Fano, *Phys. Rev.* **93**, (1954) 117.

[Fa64] U. Fano, *Ann. Rev. Nucl. Sci.* **13**, (1964) 1.

[Fe40] E. Fermi, *Phys. Rev.* **57**, (1940) 485.

[Fe69] R.M. Felder, *MOGUS - A Code for Evaluating the Mott Scattering Cross Section and the Goudsmit-Saunderson Angular Multiple-Scattering Distribution for Use in Electron Transport Calculations*, Brookhaven National Laboratory Report BNL 50199 (T-549), 1969.

[Fi74] H.-J. Fittig, *Phys. Stat. Sol. A* **26**, (1974) 525.

[Fi75] H.-J. Fittig, *J. Phys. D* **8**, (1975) 1480.

[Fi80] D.J.S. Findlay and A.R. Dusautoy, *Nucl. Instrum. & Methods* **174**, (1980) 531.

[Fl76] M.J. Flynn, *Ph.D. Theis*, University of Michigan (1976).

[Fo78] R.L. Ford and W.R. Nelson, *The EGS Code System: Computer Programs for the Monte Carlo Simulation of Electromagnetic Cascade Showers (Version 3)*, Stanford Linear Accelerator Center Report SLAC-210 (1978)

[Ga65] F.W. Garber, Oak Ridge National Laboratory report ORNL-TM-1153 (1965).

[Go48a] S. Goudsmit and J.L. Saunderson, *Phys. Rev.* **57**, (1940) 24.

[Go48b] S. Goudsmit and J.L. Saunderson, *Phys. Rev.* **58**, (1940) 36.

[Go72] G.E. Gorelik and S.G. Rozin, *J. Eng. Phys.* **22**, (1972) 772.

[Gr57] A.E.Grün, *Z. Naturf.* **12a**, (1957) 89.

[Gr63] M. Green, *Proc. Phys. Soc.* **82**, (1963) 204.

[Gr68] A.E.S. Green and L.R. Peterson, *J. Geophys. Res.* **72**, (1968) 3975.

[Ha60] R.A. Haefer, *Optik* **17**, (1960) 213.

[Ha74] R.J. Hawryluk, A.M. Hawryluk, and H.I. Smith, *J. Appl. Phys.* **45**, (1974) 2551.

[Ha84] J. A. Halbleib and T. A. Mehlhorn, *ITS: The Integrated TIGER Series of Coupled Electron/Photon Monte Carlo Transport Codes*, Sandia National Laboratories Report SAND84-0573 (1984)

[He55] D.F. Hebbard and P.R. Wilson, *Australian J. Phys.* **8**, (1955) 90.

[He76] J. Heńoc and F. Maurice, National Bureau of Standards Special Publication 460, (1976) 61.

[Hu82] H.H. Hubbell Jr. and R. D. Birkhoff, *Phys. Rev. A* **26**, (1982) 2460.

[Ic80] S. Ichimura, M. Aratama and R. Shimizu, *J. Appl. Phys.* **51**, (1980) 2853.

[In71] T. Inada, K. Hashino, H. Matsuzawa, *Phys. Med. Biol.* **16**, (1971) 25.

[Is78] N. Ishigure, C. Mori and T. Watanabe, *J. Phys. Soc. Japan* **44**, (1978) 973.

[Ka58] Y. Kamiya, *J. Phys. Soc. Japan* **13**, (1958) 1144.

[Ka72] K. Kanaya and S. Okayama, *J. Phys. D* **5**, (1972) 43.

[Kl60] O. Klemperer, A. Thetford and F. Lenz, *Proc. Phys. Soc. (Lond.)* **76**, (1960) 705.

[Ko81a] M. Kotera, K. Murata and K. Nagami, *J. Appl. Phys.* **52**, (1981) 997.

[Ko81b] M. Kotera, K. Murata and K. Nagami, *J. Appl. Phys.* **52**, (1981) 7403.

[Ku84] R.N. Kulkarni and S.J. Supe, *Phys. Med. Biol.* **29**, (1984) 185.

[Kw84] C. M. Kwei, *Thin Solid Films* **111**, (1984) 83.

[La44] L. Landau, *J. Phys. U.S.S.R.* **8**, (1944) 20.

[La80] H. Lanteri, R. Bindi, and P. Rostaing, *Thin Solid Films* **65**, (1980) 293.

[Le52] S. Leisegang, *Z. Physik* **132**, (1952) 183.

[Le57] J.E. Leiss, S. Penner and C.S. Robinson, *Phys. Rev.* **107**, (1957) 1544.

[Le59] R.B. Leighton, *Prinicples of Modern Physics*, McGraw-Hill Book Company, New York, (1959).

[Li37] M.S. Livingston and H.A. Bethe, *Rev. Mod. Phys.* **9**, (1937) 245.

[Li77] D. Liljequist, *J. Phys. D* **10**, (1977) 1363.

[Li78a] D. Liljequist, *J. Phys. D* **11**, (1978) 839.

[Li78b] D. Liljequist,T. Ekdahl and U. Bäverstam , *Nucl. Instrum. & Methods* **155**, (1978) 529.

[Lo77] G. Love, M.G.C. Cox, V.D. Scott, *J. Phys. D* **10**, (1977) 7.

[Mæ67] B. Mæhlum and J. Stadsnes, *Phys. Norv.* **2**, (1967) 111.

[Ma73] T. Matsukawa, K. Murata and R. Shimuzu, *Phys. Stat. Sol. B* **55**, (1973) 371.

[McD71] I.R. McDonald, A.M. Lamki and G.F.G. Delaney, *J. Phys. D* **4**, (1971) 1210.

[Mo48] G. Molière, *Z. Naturforsch.* **3a**, (1948) 78.

[Mu71] K. Murata, T. Matsukawa and R. Shimizu, *Jap. J. Appl. Phys.* **10**, (1971) 678.

[Mu77] T. Mukoyama and Y. Watanabe, *Bull. Inst. Chem. Res. Kyoto Univ.* **55**, (1977) 46.

[Mu79a] K. Murata, M. Kotera and K. Nagami, *Microbeam Analysis–1979*, D.E. Newbury, ed., San Fransicso Press, San Fransisco (1979) 35.

[Mu79b] K. Murata, E. Nomura, K. Nagami, T. Kato, H. Nakata, *J. Vac. Sci. Technol.* **16**, (1979) 1734.

[Mu81] K. Murata, D.F. Kyser and C.H. Ting, *J. Appl. Phys.* **52**, (1981) 4396.

[My76] R.L. Myklebust, D.E. Newbury and H. Yakowitz, National Bureau of Standards Special Publication 460, (1976) 105.

[Ne80] D.E. Newbury, R.L. Myklebust and K.F.J.Heinrich, *Proceedings of the Eighth International Conference on X-Ray Optics and Microanalysis*, D. Beaman, R. Ogilvie, D. Wittry, eds., Pendell Publishing Co., Midland, MI, (1980) 57.

[Ne85] W.R. Nelson, H. Hirayama and D.W.O. Rogers *The EGS4 Code System*, Stanford Linear Accelerator Center Report SLAC-265 (1985)

[Pu79] A. T. Pugachev and Ya. A. Valkov, *Sov. Phys. Solid State* **21**, (1979) 1518.

[Pe62] J.F. Perkins, *Phys. Rev.* **126**, (1962) 1781.

[Pe83] M.A. Peterson, *Phys. Rev. A* **28**, (1983) 135.

[Ra74] T.S. Rao-Sahib and D. B. Wittry, *J. Appl. Phys.* **45**, (1974) 5060.

[Re68] L. Reimer, *Optik* **27**, (1968) 86.

[Re71] L. Reimer, H.G. Badde, H. Seidel and W. Bühring, *Z. Angew. Physik* **31**, (1971) 145.

[Re76] L. Reimer and E.R. Krefting, National Bureau of Standards Special Publication 460, (1976) 45.

[Re78] L. Reimer, K. Brockman and U. Rhein, *J. Phys. D* **11**, (1978) 2151.

[Ro41] B. Rossi and K. Greisen, *Rev. Mod. Phys.* **13**, (1941) 240.

[Sc63] W.T. Scott, *Rev. Mod. Phys.* **35**, (1963) 231.

[Sc74] B. Schorr, *Comp. Phys. Comm.* **7**, (1974) 216.

[Se82] S.M. Seltzer and M.J. Berger, *Int. J. Appl. Radiat. Isot.* **33**, (2982) 1219.

[Sh64] A.R. Shulman, I.R. Kanicheva and B.F. Barzdo, *Radioenginnering and Electron Physics* **9**, (1964) 255.

[Sh68] G. Shinoda, K. Murata, and R. Shimizu, National Bureau of Standards Special Publication 298, (1968) 155.

[Sh67] P. Shulek, B.M. Golovin, L.A. Kulyukina, S.V. Medved and P. Pavlovich, *Soviet J. Nucl. Phys.* **4**, (1967) 400.

[Sh71] R. Shimizu, K. Murata, *J. Appl. Phys.* **42**, (1971) 387.

[Sh75] R. Shimizu, Y. Kataoka, T. Matsukawa, T. Ikuta, K. Murata, and H. Hashimoto, *J. Phys. D* **8**, (1975) 820.

[Si57] T. Sidei, T. Higashimura and K. Kinosita, *Mem. Fac. Eng. Kyoto Univ.* **19**, (1957) 270.

[Sp55] L.V. Spencer, *Phys. Rev.* **98**, (1955) 1507.

[St52] R.M. Sternheimer, *Phys. Rev.* **88**, (1952) 851.

[St56] R.M. Sternheimer, *Phys. Rev.* **103**, (1956) 511.

[St66] R.M. Sternheimer, *Phys. Rev.* **145**, (1966) 247.

[St71] R.M. Sternheimer and R.F. Peierls, *Phys. Rev. B* **3**, (1971) 3681.

[St84] R.M. Sternheimer, M.J. Berger and S.M. Seltzer, *At. Dat. Nuc. Dat. Tables* **30**, (1984) 261.

[Su73] V. Sundararaman, M.A. Prasad, and R.B. Vora, *Phys. Med. Biol.* **18**, (1973) 208.

[Un79] K. Unnikrishnan and M.A. Prasad, *Radiat. Research* **80**, (1979) 225.

[Va57] P.V. Vavilov, *Soviet Physics JETP* **5**, (1957) 749.

[Va74] D.W. Vande Putte, *Electron Energy-Loss and Multiple-Scattering Distributions below 2 MeV*, South Africa Atomic Energy Board report PEL-235, (1974).

[Vy74] A. Ya. Vyat-skin and V. Yu. Khramov, *Sov. Phys. Solid State* **16**, (1974) 1188.

[We85] R.C. Weast, Ed., *CRC Handbook of Chemistry and Physics,* 66^{th} *Edition*, CRC Press Inc., Boca Raton (1985).

[Ye54] D.R. Yennie, D.G. Ravenhall and R.N. Wilson, *Phys. Rev.* **95**, (1954) 500.

[Yo57] J. R. Young, *J. Appl. Phys.* **128**, (1957) 524.

CHAPTER IV

MODELS FOR PHOTON PHENOMENA

Because the photons which are generated in various electron scattering interactions can give rise to other energetic electrons and because they have a greater range than electrons of comparable energy and so possess capacity to transport radiation great distances, photon scattering phenomena must be treated in electron transport simulations. In general, the theoretical models and the relevant experimental data bases describing photon scattering are complete and accepted with a high degree of confidence, and so photon scattering and atomic relaxation, although included in this work, have not been examined and evaluated in the rigorous sense in which the differential electron scattering cross sections and cumulative scattering distributions have been. For completeness, a brief description of the processes and the source and substance of formalisms as employed in the current work are presented.

4.1 Photon Scattering

Three types of photon scattering interactions are important in the energy ranges considered here, photoelectric absorption, incoherent (Compton) scattering and coherent (Rayleigh) scattering. Each of the processes is described briefly below, the source of the data and expressions for the pertinent differential cross sections used in

the current work are acknowledged, and any special manipulations are also described.

4.1.1 Photoelectric Absorption

In the photoelectric absorption process an incident photon interacts with an atomic electron, ejecting the electron and resulting in the absorption of the full energy of the incident photon and the creation of a vacancy in the target atom's electron configuration. The cross section for this reaction rises precipitously with energy in the vicinity of the shell energy, and drops to zero at energies less than that of the shell. The general trend among all atomic species is for the maximums in the cross sections (found at the absorption edges) for the various shells to be larger for the outer shells, and to be roughly equal for subshells within a single shell. Photoelectric cross sections vary radically with atomic number, increasing roughly proportional to Z^4 or Z^5.

Data for the photoelectric cross section as used here is taken from the expanded parameterization of Biggs and Lighthill [Bi71]. The Biggs parameterization represents the total cross section data in the form of

$$\sigma_{pe}(Z,E) = \sum_{i=1}^{4} A_i(Z,E)/E^i. \tag{4.1}$$

where there is a different set of A_i's between almost all of the levels and between selected other energy points, beginning at .01 keV. In this expression $\sigma_{pe}(Z,E)$ is the sum of the photoelectric cross sections for each subshell which has an energy level below E. An alternate data set is that of McMaster *et al.* [McM70]. Their parameterization is of the form

$$\ln\left[\sigma_{pe}(Z,E)\right] = \sum_{i=0}^{N_E} A_i(Z,E) \cdot (\ln E)^i, \tag{4.2}$$

where N_E is 2,3, or 4, depending on the energy. This data is not used because it extends down only to the M-I energy level, which is greater than 1 keV for quite a few elements.

Carter and Cashwell [Ca75] have suggested that the total photoelectric cross section can be resolved into individual subshell cross sections by assuming that the ratio between the cross sections for the n^{th} and $n^{th}+1$ levels is constant at all energies greater than E_n and is given by their ratio at E_n. Thus if we have a problem in which the applicable energy range is between E_{min} and E_{max} and a material in this problem with N different cross sections (and so $N-1$ levels; the N^{th} level must be at $E_N < E_{min}$) we would have

$$\sigma_N(E) = \sigma_B^N(E) \qquad E_{min} \leq E \leq E_{N-1}$$

$$\begin{aligned}
\sigma_N(E) &= \sigma_B^{N-1}(E)\frac{\sigma_B^N(E_{N-1})}{\sigma_B^{N-1}(E_{N-1})} \\
\sigma_{N-1}(E) &= \sigma_B^{N-1}(E)\left(1-\frac{\sigma_B^N(E_{N-1})}{\sigma_B^{N-1}(E_{N-1})}\right) \qquad E_{N-1} \leq E \leq E_{N-2}
\end{aligned}$$

$$\begin{aligned}
\sigma_N(E) &= \sigma_B^{N-2}(E)\frac{\sigma_B^N(E_{N-1})}{\sigma_B^{N-1}(E_{N-1})}\frac{\sigma_B^{N-1}(E_{N-2})}{\sigma_B^{N-2}(E_{N-2})} \\
\sigma_{N-1}(E) &= \sigma_B^{N-2}(E)\left(1-\frac{\sigma_B^N(E_{N-1})}{\sigma_B^{N-1}(E_{N-1})}\right)\frac{\sigma_B^{N-1}(E_{N-2})}{\sigma_B^{N-2}(E_{N-2})} \\
\sigma_{N-2}(E) &= \sigma_B^{N-2}(E)\left(1-\frac{\sigma_B^{N-1}(E_{N-2})}{\sigma_B^{N-2}(E_{N-2})}\right) \qquad E_{N-2} \leq E \leq E_{N-3}
\end{aligned}$$

$$\vdots$$

where σ_B^n refers to the Biggs cross section data in energy region n and σ_n refers to the cross section for ionizing the n^{th} level.

Photoelectrons are ejected with energies given by the incoming photon energy minus the binding energy of the shell of the interaction, and at angles roughly given

by a $\sin^2$ distribution,

$$f(\Omega)d\Omega = \frac{1}{4\pi}\left[1-\frac{1}{2}\beta(E)P_2(\cos\theta)\right]\sin\theta d\theta d\phi$$
$$= \frac{1}{4\pi}\left[\left(1-\frac{\beta(E)}{2}\right)+\frac{3\beta(E)}{4}\sin^2\theta\right]\sin\theta d\theta d\phi \qquad (4.3)$$

where $\beta(E)$ is the "asymmetry parameter" which ranges from -1 to $+2$, and is heavily dependent on the ratio of the energies of the particular subshell and the incoming photon and is somewhat dependent on the target atomic number [Ma72]. In the cases treated here, it can be assumed that all electrons of interest are fathered by photons of energies at least 1 keV above the shell energy, and so both dependencies are minimized. For this case, the most widely used expression for the angular dependence of electrons in the low kilovolt energy range is that of Fischer [Co74] and is given as

$$f(\theta)\sin\theta d\theta = \frac{3(1-b^2)^2}{4}\frac{\sin^3\theta}{(1-b\cos\theta)^4}d\theta \qquad (4.4)$$

in which b is defined as

$$b = \frac{\beta}{1+E/2mc^2}, \qquad (4.5)$$

with E the initial photon energy and here β given by v/c for the ejected electron. Equations 4.3 and 4.4 are identical for low velocity electrons, in which $\beta(E)\rightarrow 2$ and $b\rightarrow 0$, and are given exactly by a $\sin^2$ distribution,

$$f(\theta)\sin\theta d\theta = \frac{3}{4}\sin^3\theta d\theta. \qquad (4.6)$$

An alternative method sometimes employed for the extreme ease of its implementation is to assume that the distribution is isotropic.

4.1.2 Compton (Incoherent) Scattering

Compton scattering involves the collision of a photon with an atomic electron. The photon loses an amount of energy which is converted into kinetic energy of the

target electron. The well known Klein-Nishina formula,

$$\sigma_{KN}(E_0, E_1, \theta)\sin\theta d\theta = \pi r_0^2 \left(\frac{E_1}{E_0}\right)^2 \left(\frac{E_1}{E_0} + \frac{E_0}{E_1} + \cos^2\theta - 1\right)\sin\theta d\theta \qquad (4.7)$$

gives the differential cross section for the scattering of a photon from a free electron at rest, (here r_0 is the classical electron radius). From kinematics, a relation between the scattered photon angle and the photon energy loss can be derived,

$$\alpha_1 = \frac{\alpha_0}{1 + \alpha_0(1-\mu)} \qquad (4.8)$$

where μ is the cosine of the scattering angle and the α's are energies divided by the electron rest mass.

Since Klein-Nishina applies only to a scattering from a single free electron at rest, some modification must be made to take into account the population of electrons in the atom and the probability that the electron will be ejected after having absorbed the photon momentum. This can be done by multiplying σ_{KN} by the incoherent scattering function discussed in chapter II, $S(Z,q)$ where again q is related to the momentum transfer and is given by

$$q = \frac{2\pi\sin(\theta/2)}{\lambda\!\!\!^{-}}$$

if $\lambda\!\!\!^{-}$ is the reduced photon wavelength. We thus have for the differential Compton cross section

$$\sigma_{inc}(E, E') = \sigma_{KN}(E, E')S(Z, q). \qquad (4.9)$$

The scattering functions used in this work in this instance are taken from tables produced by Hubbell *et al.* [Hu75] and interpolated as needed. We note that at at low values of q, $S(Z,q)$ is very close to zero, while at high q, $S(Z,q) \rightarrow Z$, and so the effect of $S(Z,q)$ is to decrease the scattering in the forward directions as the energy decreases or the atomic number increases.

4.1.3 Coherent Scattering

The rather general term "coherent scattering" is meant in the present sense to include only elastic scattering from the bound atomic electrons, sometimes referred to as Rayleigh scattering. Because the electrons are considered bound, their target mass is essentially the mass of the atom, and little energy is available for transfer in this type of collision. The scattering is coherent since the electrons are essentially indistinguishable and reflected photons can interfere constructively. The cross section for Rayleigh scattering is given as the classically derived Thomson formula for the elastic scattering of a photon by a particle at rest,

$$\sigma_T(\theta) = \frac{\pi e^2}{2mc^2}(1 - \cos^2\theta) \tag{4.10}$$

times the square of the atomic form factor $F(Z,q)$ (again, as defined in chapter II) so that we have

$$\sigma_{coh}(E,\theta) = \sigma_T(\theta)[F(Z,q)]^2. \tag{4.11}$$

Note that the Thomson formula is independent of the photon energy, and is in fact valid for the scattering cross section at non relativistic velocities. The form factors used in this work, like the scattering functions, are taken from tabulated data of Hubbell *et al.* [Hu75]. $F(Z,q)$ is 0 at $q=0$ and as $q \rightarrow \infty$, $F(Z,q) \rightarrow 0$, so that the effect is to decrease the cross section at large angles, high energy and low atomic number.

Recent work [Br89] has shown that in the low keV range, the effect of molecular binding on the coherent cross section can be large, and simple additivity assuming free atoms, as in done throughout this work, may not be valid for compounds. The importance of this effect is not investigated.

4.1.4 Other Scattering Mechanisms

A technique for classifying all the possible scattering mechanisms is given by Fano [Fa53] and an excellent description of the processes and their relative importances is given in [Ev55]. Among the other processes which are significant for certain problems but are not treated in the current work are pair production, nuclear photo-absorption and coherent nuclear scattering. Although pair production, in which a photon interacts with the field of the either the nucleus or the atomic electrons (a less likely occurrence) to produce a positron-electron pair, is the dominant stopping mechanism at very high energies, the threshold for the reaction is twice the rest mass of the electron, and so it does not occur at energies considered here. Nuclear Thomson scattering is also possible, but negligible except at very high energies. Similarly, nuclear photo-absorptions, which can lead either to fission or the emission of energetic neutrons, is a small effect and appreciable only in the MeV range.

4.2 Atomic Relaxation (De-Excitation)

Recalling that in many of the interactions modeled in electron transport an electron is expelled from a shell of a target atom and that the target subsequently rearranges its electrons into a lower energy state and emits radiation in some form or another, an important phenomenon to consider in coupled electron photon transport is this relaxation or de-excitation. Two types of rearrangement phenomena are possible, both of which begin with a vacancy in an inner shell being filled by an electron from a outer shell. In the first situation, a photon may be emitted with energy given by the difference in the energy of the levels of the initial hole and the subshell providing the filling electron. The second case also begins with the transition of an outer electron into an inner shell, but in this instance it is followed by the ejection of a

second outer electron, leaving two outer shell vacancies. This process is called Auger emission and the ejected electron referred to as an Auger electron. If the ejected electron came from the same shell as the one which filled the initial vacancy, the transition is called a Coster-Kronig transition. In general, the smaller the difference in energy level, the more probable that a subshell will sacrifice its electron. Thus L to K transitions are more prevalent that N to K transitions.

The data presented by Halbleib and Morel [Ha78] and used in the P-codes (extended relaxation) of the ITS series has been used here. This data is tabulated in a form for easy manipulation by a conventional, history based Monte Carlo program and required extensive manipulation in order to produce a full set of decay mode probabilities for use in the present work. The raw data is listed in table 4.1.

From this data probabilities for various decay channels can be determined for vacancies in the K, L-I, L-II, L-III and average M subshells, and are listed in tables 4.2 through 4.6.

Several assumptions have been made in compiling these relaxation modes. First, because data is not available, transitions involving electrons outside the N shell must be ignored, regardless of the shell of the original vacancy. This is, however, consistent for the most part with the general lower energy limit of 1 keV placed on this work, as only in the range of $Z \sim 90$ are N shell energies above 1 keV, and any transitions involving these shells would produce daughters with energy below the 1 keV cutoff anyway. A second assumption is that the relative frequency of K-MM, K-MN, and K-NN Auger decays may be taken for all elements to be .91, .045, and .045, respectively, as suggested by Halbleib. Third, the source of the second electron in all L-II to L-I Coster-Kronig transitions is assumed to be the N shell, in L-III to L-I transitions the M shell, and in L-III to L-II transitions the N shell. And lastly, because of some

Total probability of K fluorescence
Relative fraction of K fluorescence from L-II, L-III, and M average transitions
Fraction of K Augers involving two L transitions
Relative fraction of K LL Augers for various L subshell combinations
Fraction of K Augers involving one L and one outer transition
Relative fraction of K L-Outer Augers involving M shells
Relative fraction of K LM Augers for various L subshells
Relative fraction of K LN Augers for various L subshells
Total probability of L-I fluorescence
Fraction of L-I fluorescence from M average transitions
Fraction of L-I Augers involving an L (Coster-Kronig) transitions
Relative fraction of L-I L Augers involving L-II and L-III
Relative fraction of L-I Augers involving MM and MN average transitions
Total probability of L-II fluorescence
Fraction of L-II fluorescence from M average transitions
Fraction of L-II Augers involving an L-III (Coster-Kronig) transitions
Relative fraction of L-II Augers involving MM and MN average transitions
Total probability of L-III fluorescence
Fraction of L-III fluorescence from M average transitions
Relative fraction of L-III Augers involving MM and MN average transitions
Total probability of Average M fluorescence

Table 4.1: ITS P-Code Relaxation Data

K to L-II fluorescence
K to L-III fluorescence
K to M-Average fluorescence
K to N-Average fluorescence
K to L-I L-I Auger emission
K to L-I L-II Auger emission
K to L-I L-III Auger emission
K to L-II L-II Auger emission
K to L-II L-III Auger emission
K to L-III L-III Auger emission
K to L-I M-Average Auger emission
K to L-I N-Average Auger emission
K to L-II M-Average Auger emission
K to L-II N-Average Auger emission
K to L-III M-Average Auger emission
K to L-III M-Average Auger emission
K to M-Average M-Average Auger emission
K to M-Average N-Average Auger emission
K to N-Average N-Average Auger emission

Table 4.2: K Shell Decay Channels Treated

L-I to M-Average fluorescence
L-I to N-Average fluorescence
L-I to L-II N-Average Auger emission
L-I to L-III M-Average Auger emission
L-I to M-Average M-Average Auger emission
L-I to M-Average N-Average Auger emission
L-I to N-Average N-Average Auger emission

Table 4.3: L-I Shell Decay Channels Treated

L-II to M-Average fluorescence
L-II to N-Average fluorescence
L-II to L-III N-Average Auger emission
L-II to M-Average M-Average Auger emission
L-II to M-Average N-Average Auger emission
L-II to N-Average N-Average Auger emission

Table 4.4: L-II Shell Decay Channels Treated

L-III to M-Average fluorescence
L-III to N-Average fluorescence
L-III to M-Average M-Average Auger emission
L-III to M-Average N-Average Auger emission
L-III to N-Average N-Average Auger emission

Table 4.5: L-III Shell Decay Channels Treated

M-Average to N-Average fluorescence
M-Average to N-Average N-Average Auger emission

Table 4.6: Average M Shell Decay Channels Treated

errors in the tabulation, in several instance for elements from $Z \sim 15$ to $Z \sim 30$ the partial probabilities of the L decay modes add up to more than unity. When this occurs, they are simply renormalized.

In modeling the filling of vacancies through the transitions described above, new vacancies are often produced in outer (yet still important) subshells. These vacancies must then be relaxed until all new vacancies lie in untreated channels, either those with energy less less than the cut-off or those lying outside the M shell. Once this stage is reached a certain amount of de-excitation energy is still available to the atom, and throughout this work it considered to be deposited locally.

The use of average M shell quantities to treat M shell vacancies, as required by the limited data set, presents somewhat of a problem. Because of the extensive photoelectric and electron ionization cross section data which is available, scattering models may be sometimes be defined in which vacancies are excited in explicit M subshells. It would be desirable to model the relaxations exactly, but only average M transition data is available, and this causes the following potential problem. Because the 5 M subshells can be separated by up to 2 keV for high Z materials, it usually happens that the average relaxation energy, $E_{\bar{M}} - E_{\bar{N}}$, is not given by the energy of the explicitly excited shell (E_{M_i}) minus the average N binding energy. Using the average transition numbers destroys the energy balance, and so in the present work a certain residual error energy, given by $E_{\bar{M}} - E_{M_i}$ is introduced when modeling the relaxation. Whenever a specific M subshell is excited, the residual energy (which can be negative) is deposited locally, the vacancy is treated as being in the average M shell, and the only allowed transition is with the average N electron. This feature is invoked for only materials which have M shell energies greater than 1 keV, which starts at roughly $Z \sim 50$.

References

[Br89] D.A. Bradley, D.R. Dance, S.H. Evans, and C.H. Jones, Med. Phys. **16**, (1989) 851.

[Bi71] F. Biggs and R. Lighthill, *Analytical Approximations of X-Ray Corss Section II*, SC-RR-710507, (1971).

[Ca75] L.L. Carter and E.D. Cashwell, *Particle Transport Simulation with the Monte Carlo Method*, TID-26607, (1975).

[Co74] H. M. Colbert, *SANDYL A Computer Program for Calculating Combined Photon-Electron Transport in Complex Systems*, Sandia Report SLL-74-0012 (1974).

[Ev55] R.D. Evans, *The Atomic Nucleus*, McGraw Hill Book Co., New York (1955).

[Fa53] U. Fano, *Nucleonics* **11(8)**, (1953) 8.

[Ha78] J. A. Halbleib Sr. and J. E. Morel, *Improved Atomic Shell Excitation and Relaxation in the Tiger Series Codes*, Sandia Laboratory Report SAND-78-0580, (1978).

[Hu75] J. H. Hubbell, W. J. Veigle, E. A. Briggs, R. T. Brown, D. T. Cromer and R. J. Howerton, *J. Phys. Chem. Ref. Data* **4**, (1975) 471.

[Ma72] S. T. Manson, *J. Electron Spectrosc.* **1**, (1972) 413.

[McM70] W. H. McMaster, N. K. Del Grande, J. H. Mallett and J. H. Hubbell, *Compilation of X-Ray Cross sections*, Lawrence Livermore Laboratory Report UCRL-50174, (1970).

CHAPTER V

CURRENT MONTE CARLO CODE, SKEPTIC

The third aspect of this work involves the examination of the accuracy and computational efficiency of Monte Carlo simulations of electron transport problems using various single scattering cross sections and multiple scattering distribution functions. The development of a set of programs suitable to this task and labeled the SKEPTIC (Simulated Kilovolt Electron and Photon Transport In Condensed media) package is described in this chapter.

Given the many fine references already cited, it would seem inappropriate to present here a detailed examination of either the Monte Carlo method or its specific application to the simulation of electron and photon transport. However, understanding the justification for certain techniques which have been employed in SKEPTIC in order to simultaneously create a general algorithm and improve computational alacrity requires a basic knowledge of the principles of the Monte Carlo technique. Thus, those fundamental concepts cited in the course of describing the methods used in this work are reviewed in some detail. Additionally, a general knowledge of the basic Monte Carlo particle transport simulation algorithm is essential in comprehending the differences in the classes of electron transport algorithms described briefly in the first chapter. Thus a review of the fundamental particle transport simulation

algorithm is presented, along with a new scheme for classifying the variations from the basic algorithm for the case of electron transport. Thirdly, as efficient use of the available vector computation facilities mandates alteration of the basic transport algorithm, a review of vector computation concepts is presented in effort to elucidate the logic underlying the final SKEPTIC program flow.

5.1 Basic Elements of the Monte Carlo Technique

As noted in chapter one, the premise of Monte Carlo transport simulation is the generation and compilation of enough statistically determined case histories so that the average result of the many individual particle simulations approximates the solution to the problem at hand. The underlying procedure in history generation is the simulation of every event outcome by using random numbers to 'sample' from probability distribution functions appropriately describing the events. It is instructive to examine basic Monte Carlo sampling schemes in order to appreciate how the SKEPTIC package has come to be fashioned around general sampling techniques.

Three main types of sampling schemes are examined here, with special focus on the subsets of the third method. While the first two techniques are meant to give exact results, the third method, except in special cases for which it is actually a subset of the first technique, involves some error introducing approximations which are examined here and quantified in a loose analytical fashion as well as by numerical example.

For the sake of clarity, some definitions should be set forth at the outset. These definitions are not meant to adhere to rigorous mathematical convention, but rather to provide a foundation for the current discussion. Thus, a probability density or distribution function is defined as the function describing the probability of occur-

rence of a given outcome x of an event and designated $p(x)$. An example of a density function would be an scattering cross section differential in angle. The 'event' is scattering at some angle and the outcomes are all possible angles θ in the interval from 0 to π radians.

A cumulative probability density or distribution function $P(x)$ for an event is defined as

$$P(x) = \int_{x_{min}}^{x} dx' \, p(x'). \tag{5.1}$$

We note that the normalized distribution, defined by $P(x)/P_{max}$,where

$$P_{max} = \int_{x_{min}}^{x_{max}} dx \, p(x)$$

is monotonically increasing on the interval $[0, 1]$.

5.1.1 Direct Sampling

The basic technique involved in determining the outcome of a given event is the equating of a number ξ, chosen at random from a uniform distribution on the interval $[0, 1]$, and the normalized probability distribution function of the possible outcomes of the event. The distribution function is then inverted to determine at which outcome the normalized distribution function is equal to the random number, as

$$x = P^{-1}(\xi) \tag{5.2}$$

where P^{-1} represents the inverted function such that

$$\xi = P(x).$$

Theoretically, if enough events are sampled, the normalized frequency with which the specific outcomes are chosen will match the normalized density function from which

the distribution function is derived. A common application of this technique is the determination of the distance to collision for a particle in free flight. The possible outcomes are distances s traversed prior to the collision for which the density function is given by

$$p(s) = \Sigma e^{-\Sigma s}$$

where Σ is the total cross section. The cumulative distribution is given by

$$P(s) = 1 - e^{-\Sigma s}$$

and so if ξ is a random number the outcome chosen would be

$$s = \frac{1}{\Sigma} \ln (1 - \xi).$$

Note that $(1 - \xi)$ is uniformly distributed over $(0, 1]$, and so just ξ is commonly used as the argument of the log term.

While inversion sampling reproduces the density function exactly for an infinite number of samples, a crippling disadvantage of this technique arises when the distribution function is not invertible in closed analytical form. Thus, this technique is not universally applicable and other methods must sometimes be employed.

5.1.2 Rejection Sampling

A second method, called the rejection technique, involves the comparison of a random number with the density function normalized to have maximum value of one (as opposed to integral value of one) and evaluated at a possible outcome determined by a preceding random number. If the second random number is less than the density function at the given point, then the point is chosen as the outcome. If not, it is rejected, and a different possible outcome chosen using a third random number and

tested by comparing the normalized density at that point with a fourth random number and so on. In theory, all possible outcomes will be initially tested uniformly but chosen as successful outcomes in proportion to their relative probability. The angle of Compton scattering is usually sampled in this manner in conventional Monte Carlo photon transport codes. Although this technique is applicable to all situations, its efficiency, defined as the fraction of successful samplings, will be low when the density function deviates significantly from uniformity. This is clear from figure 5.1, if we note that the efficiency is equal to the fractional area under the normalized density function. For the top figure, a rather uniform density, potential outcomes are rarely rejected and the technique is efficient. For the bottom, sharply peaked density curve, the potential outcome will most likely be rejected unless it lies in the narrow band under the peak, and so sampling will be inefficient and time consuming. Consequently, a good deal of effort goes into determining variable transformations under which the density functions can be sampled efficiently (see for example, [Ka56] or [Fo78]). The difficulty in developing such transformations has a large impact on the SKEPTIC package. Because the purpose of the work is cross section and distribution function comparison, and since very few distribution functions can be inverted, retaining exactness in sampling would require that rejection techniques be used. Since most of the cross sections and distributions tested have not been widely (if at all) used in prior Monte Carlo calculations, efficient rejection schemes are not available, and would have to be developed for each cross section or distribution used. The effort involved in such an undertaking would be substantial, and the Monte Carlo transport simulation portion of the package would be different for each case tested. As a universally applicable sampling scheme is sought, a third type of sampling must be examined.

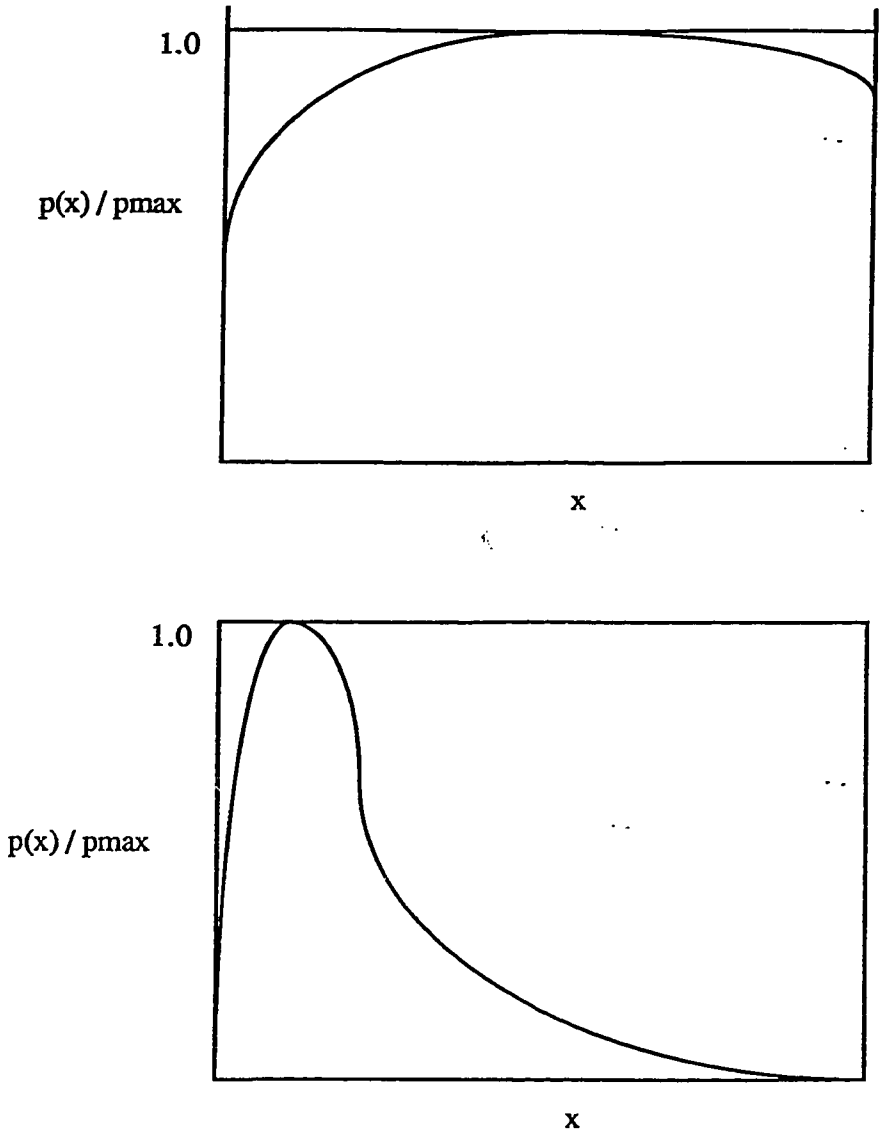

Figure 5.1: Sample Functions in the Rejection Technique

5.1.3 Discrete Sampling Schemes

A third scheme arises in two situations, the first for the case in which the number of possible outcomes is finite and the second in the case for which a continuous set of outcomes is approximated by a discretization of the outcomes and the density function defining them. In the first instance, the technique is actually a subset of the direct inversion sampling scheme, and in the second, a combination of rejection sampling with unit efficiency employing specially processed densities and an approximation using direct inversion.

Sampling Techniques for Densities with Discrete Outcomes

A common application of the first instance is in determining which type of interaction has occurred at a scattering point from the set of all possible scattering interactions. If σ_i represents the microscopic cross section for interaction type i, the normalized (by integral value of one) density function $p(x_i)$ (or simply p_i) for outcome x_i is given by σ_i/σ_{tot} and the cumulative density is defined by

$$P(x_i) = P_i = \sum_{j=1}^{i} p_j. \tag{5.3}$$

In determining an outcome, a random number ξ is compared with the distribution function and outcome x_i is chosen for

$$P_{i-1} < \xi \leq P_i. \tag{5.4}$$

Two methods of determining x_i from a table of P_i and a random number are available, the first involving a simple table search and the second sampling from an artificially created uniform distribution, as proposed by Walker [Wa77] (in which the technique was called alias sampling) and extended to Monte Carlo particle transport

simulations by Brown [Br82]. In this work, schemes which use alias sampling to permit arbitrarily spaced bins will be refered to either as arbitrary schemes or Brown schemes. The table search involves sifting through the outcomes (usually using a binary search technique) until the appropriate outcome is found. This can be very slow when a large number of outcomes are possible, requiring two tests and three index assignments at each step for $\log_2 N_t$ steps, where N_t is the number of elements in the table. Alias sampling consists of the construction of a uniform distribution function with an accompanying dual index list and binary probability function. Essentially all points in a discrete probability density function are normalized to the mean by considering them to be comprised of portions of two components of the density. Thus a density function with N points and average value $\bar{p}$ will be represented by a uniform distribution of N points χ_i and density $\bar{p}$, and each χ_i will have a corresponding dual index list I_i and J_i, where the index lists point to two points x_k and x_l of the original distribution, and a probability ρ_i which equals the fractional contribution of the point I_i to the distribution average. The set-up algorithm involves finding the mean and then using the point with the smallest density, x_s and the point with the largest density x_l. Thus $I_1 = s$ and $J_1 = l$ and $\rho_1 = p_s/\bar{p}$. For the next pass, x_s is removed from the list of possible outcomes and the density of x_l is reduced to $p_l - (\bar{p} - p_s)$. The average of the updated density is still $\bar{p}$ and the number of points is $N - 1$. It is clear than N sets of points will be generated after N passes. It can be seen that for all occurrences of a given point x_j in the index lists I and J

$$\sum_{i=1}^{N} \delta(x_j - x_{I_i})\,\bar{p}\,\rho_i + \delta(x_j - x_{J_i})\,\bar{p}\,(1-\rho_i) = p_j$$

where p_j is the original probability density function. The main advantage of this method is the computational savings in sample time. Sampling is a two step operation, with the first index to be used determined by $i = N\xi + 1$ and the actual index

I_i used for $\rho_i \leq \eta$ and J_i otherwise, where ξ and η are random numbers. In practice, the amount of stored information can be reduced from three to one full word array by ordering the i's so that $I_i = i$ and by storing ρ_i and J_i as their floating point sum, $\rho_i' = J_i + \rho_i = J_i.\rho_i$. The additional preprocessing required in generating the pseudo uniform distribution is not great, and the method will be faster than a table search whenever there are more than a few possible outcomes. Because of the increase in computing speed gained by employing this method, it is always employed for sampling initially discrete distributions in SKEPTIC. Note that for the case of initially discrete densities, both the table search and alias sampling methods are exact for an infinite number of trials.

Discretely Sampling Densities with Continuous Outcomes

The second case in which discrete sampling might be employed is that for which a continuous distribution is discretized. An example would be assuming that only certain values of scattering angles are allowed, for example, every one degree from 0 to 180. In the discretization approximation some sort of numerical integration scheme is necessary in determining the discrete function from the continuous density. Noting that we are determining probabilities for finite intervals or bins rather than individual points, if we define the endpoints of bin m as χ_m and χ_{m+1} and the probability of choosing the bin as Π_m, we obtain

$$\Pi_m = \int_{\chi_m}^{\chi_{m+1}} dx\, p(x). \tag{5.5}$$

If we normalize the Π_m's by $\Pi_m = \Pi_m / \Pi_{tot}$ where Π_{tot} is given by

$$\Pi_{tot} = \sum_{m=1}^{M} \Pi_m,$$

we chose a bin by

$$\Pi_{m-1} < \xi \leq \Pi_m$$

as in the true discrete case. Obviously, the table search method (applied to cumulative densities of course) and alias sampling are applicable for determining the outcome bin from the discrete set of bin probabilities, and clearly the table search method will be much slower than alias sampling for every realistic application. In addition to alias sampling, a fast sampling scheme which uses preprocessing to select the endpoints χ_m so that all Π_m are equal may be employed. In this technique, if ξ is a random number to be used in selecting the bin, the bin index is given by $m = M\xi + 1$ where an integer multiplication is assumed. This has the advantage over alias sampling in that is requires less data storage per bin (a set of the bin endpoints versus a set of endpoints and a set of probabilities) and requires only one sampling step instead of two, but has some disadvantages in that more bins are required to accurately describe the distribution, especially if it has a long tail. The storage per bin and run time efficiency versus accuracy and preprocessing time loss trade-offs between the two methods will be explored in depth later in this chapter. Note that the equally probable bin method is not applicable to the true discrete case because in that case the bin probabilities are fixed *a priori.*

In addition to the two schemes described above for discrete sampling, three methods, two of which reintroduce continuity of the outcomes, have been used here to determine an outcome from inside the sampled bin. The first involves simply choosing the midpoint value of the bin as the sampled point. The second assumes that all points within the bin are equally probable (constant density), and sampling is done accordingly. The third assumes that the points are distributed with linear probability through the bin.

In general, the probability of sampling a point χ' which lies in bin m is given by $\Pi_m \cdot \pi_m^s(\chi')$ where $\pi_m^s(\chi)$ represents the density of the outcomes in bin m and the superscript s refers to one of the three interbin interpolation schemes. In all three interbin sampling schemes the densities are later normalized so that

$$\int_{\chi_m}^{\chi_{m+1}} d\chi\, \pi_m^s(\chi) = 1. \tag{5.6}$$

In the first two cases only the shape of the density survives normalization, so no additional constants need be assigned. In the third case, the slope and intercepts must be determined before normalization. We require that the values of π_m^{lin} at the bin endpoints be set such that

$$\frac{\pi_m^{lin}(\chi_{m+1})}{\pi_m^{lin}(\chi_m)} = \frac{p(\chi_{m+1})}{p(\chi_m)}$$

and the slope of the linear density, μ_m, be determined so that the integral of π_m^{lin} over the bin is equal to the integral of the actual density function over the bin. Thus we have

$$\begin{aligned} \pi_m(\chi_{m+1}) &= \frac{2\,\Pi_m\, p(\chi_{m+1})}{(\chi_{m+1} - \chi_m)\,(p(\chi_{m+1}) + p(\chi_m))} \\ \pi_m(\chi_m) &= \pi_m(\chi_{m+1})\,\frac{p(\chi_m)}{p(\chi_{m+1})} \\ \mu_m &= \frac{\pi_m(\chi_{m+1}) - \pi_m(\chi_m)}{\chi_{m+1} - \chi_m} \end{aligned} \tag{5.7}$$

Note that the requirement of maintaining consistent bin integrals may also be imposed for the first two interbin sampling techniques, but the constants are trivially factored out in normalization. Normalized expressions for the π^s's are given in table 5.1 and expressions for determining an outcome from a sampled bin given a random number ξ for a given scheme are given in table 5.2. Although the inversion scheme for the linear case of table 5.2 is correct, a scheme which skirts the use of square roots

Interpolation Scheme	$\pi_m^s(\chi)$
Mid point	$\delta(\chi - \frac{\chi_{m+1} + \chi_m}{2})$
Constant	$\frac{1}{\chi_{m+1} - \chi_m}$
Linear	$\frac{\mu_m(\chi - \chi_m) + \pi_m(\chi_m)}{\frac{1}{2}[\pi_m(\chi_{m+1}) + \pi_m(\chi_m)](\chi_{m+1} - \chi_m)}$

Table 5.1: Interbin Interpolation Probability Densities

Interpolation Scheme	$x(\xi)$
Mid point	$(\chi_{m+1} + \chi_m)/2$
Constant	$\chi_m + (\chi_{m+1} - \chi_m) \cdot \xi$
Linear	$\chi_m + \left(\sqrt{\xi(\pi(\chi_{m+1})^2 - \pi(\chi_m)^2)} - \pi(\chi_m)\right)/\mu_m$

Table 5.2: Inverted Interbin Interpolation Probability Distributions

and reduces the necessary amount of data may be used instead. In this scheme, a point is chosen from a linear density on the interval -1 to +1 according to the formula

$$\chi' = 1 - 2 \cdot |\xi_1 - \xi_2|$$

The final answer is given by

$$\chi = \frac{\chi_{m+1} + \chi_m}{2} \pm \frac{\chi_{m+1} - \chi_m}{2} \cdot \chi'$$

with the positive term containing χ' chosen for $\frac{1}{2}(\chi_{m+1} - \chi_m) \cdot \pi_m(\chi_{m+1}) \geq \xi_3$ and negative otherwise. (In this example, ξ_1, ξ_2 and ξ_3 are random numbers.) Although this scheme is marginally slower than the previous one using square roots, it reduces the data requirements for linear sampling from three to one item per bin, and so has been employed exclusively throughout this work.

For all sampling schemes, as the interbin densities have all been normalized, if we have M constructed bins, we have consistency in that

$$\int_{\chi_1}^{\chi_{M+1}} d\chi\, \pi(\chi) = \sum_{m=1}^{M} \Pi_m \int_{\chi_m}^{\chi_{m+1}} d\chi\, \pi_m^s(\chi) = \int_{x_{min}}^{x_{max}} dx\, p(x). \qquad (5.8)$$

Note that $\pi(\chi)$ may be discontinuous at mesh endpoints, but this has no bearing on the accuracy of sampling.

Discretization of Continuous Functions The determination of the specific points in a continuous set of outcomes at which to define discrete bins requires some scheme relying on minimizing the error created in using the discrete rather than continuous distribution. Two subroutines for splitting distribution functions into bins, each using the same error estimation logic, have been written. The error prediction algorithm devised here relies on calculation of the relative root mean square difference between the input function and the approximating function. The

input function is a finely meshed set of points which will be interpolated as necessary. Some *a priori* knowledge of the function behavior, particularly of local maximums and minimums, is necessary when selecting the finely spaced input base points. In most cases, such knowledge is available and base points can be set in an almost arbitrary manner and still not skew the calculation. It should be noted that there is no way to circumvent the use of base points, and it is impossible to assure that no local maximums or minimums will be wholly contained within a set of adjacent base points for an arbitrary continuous function. Thus we assume that the input function consists of a tabulated set of N points x_n and values of the density $p(x_n) = p_n$. The root mean square (rms) error in approximating the density function within a given bin is determined as follows. As the interbin schemes are developed assuming that the input density is exact, that Π_m comes from integrating the density itself, and that the created densities are normalized so that they have the same area as the exact density over the input base points, no error is incurred in sampling for the proper bin, and so all of the sampling error arises in selecting an outcome once the bin has been identified. The run time sampled density function will be equal to the constructed function (given enough histories), so that the runtime probability of choosing point χ from bin m using interpolation scheme s is given by $\Pi_m \cdot \pi_m^s(\chi)$, while the actual probability is given by $p(\chi)$ (interpolated from the input fine mesh) and therefore the total square error introduced by discretization in bin m for interpolation scheme s is given by

$$(E_m^s)_{tot}^2 = \int_{\chi_m}^{\chi_{m+1}} d\chi \, (p(\chi) - \Pi_m \pi_m^s(\chi))^2 . \tag{5.9}$$

Related quantities are the relative square error,

$$(E_m^s)_{rel}^2 = \int_{\chi_m}^{\chi_{m+1}} d\chi \left(\frac{p(\chi) - \Pi_m \pi_m^s(\chi)}{p(\chi)} \right)^2 , \tag{5.10}$$

the relative root mean square error,

$$E_{rel,rms} = \left[\frac{\left(\sum_{m=1}^{M} (E_m^s)_{tot}^2 \right) / (\chi_{M+1} - \chi_1)}{\left[\left(\int_{\chi_1}^{\chi_{M+1}} d\chi\, p(\chi) \right) / (\chi_{M+1} - \chi_1) \right]^2} \right]^{1/2}, \tag{5.11}$$

and the root mean square relative error,

$$E_{rms,rel} = \left[\frac{\sum_{m=1}^{M} (E_m^s)_{rel}^2}{(\chi_{M+1} - \chi_1)} \right]^{1/2}. \tag{5.12}$$

There is some question concerning whether the relative rms error (equation 5.11) or the rms relative error (equation 5.12) is a better indicator of the error in the constructed density. The relative rms error represents the root of the total square error relative to the average square value of the function, while the rms relative error represents the root of the average relative error in the function at each point. Thus relative rms is a measure of mean relative total error and rms relative is a measure of mean instantaneous relative error. It is clear that using instantaneous relative error will predict large error at small function values and small error at large function values, even though the actual difference in the densities may be comparable or even reversed relative to this prediction. Using instantaneous relative error as a basis for bin determination will predict very closely spaced bins with small absolute error when the density is small and widely spaced bins with large absolute error where the density is large. In the worst case of applying this method, actual densities with a zero would exhibit infinite error unless the constructed densities also had zero value at that point. An illustrative example of the differences resulting from application of the two definitions of error is the case of screened Rutherford scattering discretized into linear bins. Using rms relative error, the distribution would be broken into many

smaller bins than in the case of keying on relative rms error. It can be concluded in general that for equal number of bins, using relative rms error gives a closer overall fit at all outcomes, while using the rms relative error would ensure better accuracy at the small probability events. For situations in which the low probability outcomes have enormous effect on final results, defining error as the rms relative deviation may be superior. Unfortunately, it is usually not known beforehand when the low probability events are so important as to justify a technique resulting in poorer absolute error in the high probability cases. Thus, throughout this work, relative rms deviation (equation 5.11) has been adopted as the figure of merit for determining accuracy. Note that no matter how the error is defined, using the midpoint interpolation scheme leads analytically to infinite error. However, if the final Monte Carlo simulation tally bins are more coarsely spaced than the input discrete distribution bins, using the midpoint interpolation scheme may actually produce quite good results. When the midpoint sampling technique is to be applied, the bin end points are determined by minimizing the error predicted for one of the other schemes.

Using the above formalism for quantifying error, two routines for discretization of continuous functions have been written and tested. Both use LaGrangian interpolation of a user specified order *nord* to determine various necessary function values from the tabulated input, and both use a $(nord+1)/2$ point Gaussian quadrature scheme (exact for evaluating the integrals of *nord* degree polynomials) to perform integrals of both the bin probability and rms error.

Subroutine EQCHOP constructs equal probability bins from the input distribution. Options exist to request either a specified number of bins regardless of the error, or a code determined number of bins, depending on the selected inter-bin interpolation scheme and the input maximum allowable total rms error between the constructed

distribution and the input distribution. The subprogram in EQCHOP which performs the actual calculation, NEQUAL, computes equal probability bin endpoints given that the distribution is broken into a preset number of bins. Its algorithm begins by integrating over the input base points until the preset equal bin probability, determined by dividing the integral of the input density by the number of bins to use, is exceeded. This determines which input base point interval contains the next output bin endpoint. An iteration scheme based on the *regula falsi* technique determines the bin endpoint by successively integrating over portions of the base point interval until a point is found which yields the desired bin probability. The *regula falsi* procedure usually takes no more than 2 or 3 iterations. For cases in which the code is requested to determine the minimum number of bins for a given error, an initial guess of the number of bins is made, the bin spacing for this guess determined by NEQUAL and the error calculated. An outer iteration scheme based on halving the interval from the previous guess to the minimum or maximum allowed number of bins is followed until the fewest number of bins (plus or minus an input number tolerance) for the given error is found. This entire technique relies on the assumption that the error always decreases as the number of bins increases. This is not strictly true, but is a reasonable assumption for smooth functions and has been found to hold for all distribution functions treated in this work. Obviously, there are some free parameters in addition to the given error tolerance, which effect the results. The order of the integration and interpolation schemes have some bearing on the final results, and the number of bins initially guessed greatly effects the computation time. In order to test the dependency of the results on these parameters tests were run on 5 example functions: a constant function, a linear function, a sine function, an exponential function and a sawtooth function with equivalently shaped teeth. The routine always correctly

selected one bin for use in sampling the constant function with constant interpolation and for sampling the linear function with linear interpolation, regardless of the error tolerance. For the more variant functions, the routine always predicted more bins for constant rather than linear interpolation for the same allowed error, and more bins for smaller tolerated error using the same interpolation scheme. For the same tolerated error, the number of bins and their spacing was found to be somewhat dependent, and the execution time to be greatly dependent, on the order of interpolation and integration schemes, especially at lower orders. In general it was found that a 5^{th} order scheme for both cases produced roughly the same results as higher order schemes, with a substantial saving in computation time. An interesting problem presented itself for the case of the input sawtooth shaped density, which is an example of a function for which increasing the number of bins may not lower the error. For instance, if the initial guess on the number of bins happens by chance to be an integral multiple of the number of teeth, the code will correctly predict that the error is zero. If it then tries a smaller number of bins which is not an integral multiple, the error will increase, and so the code will end up converging on the initial guess, which is not the true minimum. In addition, as only the tooth end points were input as base points, any scheme requiring more than two base points for the interpolation caused program abort due to calculation of negative probabilities. This problem was caused by the program trying to fit smooth polynomial functions to the sawtooth end points and needing negatively valued functions for the fit. No realistic density function will be this poorly determined however.

Subroutine CHOP constructs bins of arbitrary probability for use in alias sampling and in constructing tables of cumulative densities. Input options allow the user to specify either the bin endpoints or the maximum rms error allowed in a single

bin. In the case of code determined bin endpoints, the algorithm searches the input base points until it locates the interval containing the point which, when included in the bin, will exceed the allowed error for that bin. A *regula falsi* technique is then employed to determine the exact endpoint. This scheme again assumes that the larger the bin the greater the error, which is again a reasonable approximation for most functions. It should be noted that as this scheme calculates error for individual bins rather than the entire distribution, and since the bins all have the maximum allowed relative error and the squares of the bin errors add, the total error is given by the allowed error in a single bin times the square root of the number of bins. Using the test functions it was again found that that 5^{th} order interpolation and integration produce the same results as higher order schemes with great savings in computation time. In this instance, if asked to use a first order interpolation scheme, the routine always accurately predicted that the sawtooth function should be cut at the tooth end points. The same problems which arose in the equal probability case were evident here when higher order interpolation schemes were used for the sawtooth test problem.

Application of Discretization Schemes to Practical Cases The discretization procedure will clearly have an impact on the speed, accuracy, and data storage requirements of the calculation. Data storage is a concern because of main memory limitations involved in using the Cray X-MP/48, as explained in a later section. The problem however must be addressed here as some bin schemes are potentially space limited. Speed and accuracy are obviously interdependent, as the more accurate sampling schemes (such as linear interbin interpolation) are slower. Speed for accuracy trade-offs are also influenced on the data limitations, as faster schemes re-

quire more data for the same modeling accuracy. Thus the effect of discretization on accuracy, sampling speed and data handling for the binning schemes and the three interpolation methods should be examined.

The sampling time per outcome and the size of data structure required for a given accuracy for each of the discretization and interbin interpolation sub-cases can however be examined, and results compared with similar computations using both direct sampling cases and table search schemes. As it is assumed that discretization will be desirable in instances for which determination of a single point in a differential cross section by inversion or by rejection is time consuming, it is instructive to examine for the sake of comparison cross sections with varying complexity in analytical form. Additionally, as indications are sought of the difficulty of discretization (manifested by the required number of bins), cross sections with of varying degrees of non-uniformity should be examined. The examples chosen here are the Rutherford elastic scattering cross section, because it may also be sampled by direct inversion and is quite smooth, even though varying over several orders of magnitude; the Compton photon scattering distribution, because it has been widely studied and well documented rejection sampling schemes are available; the Riley cross section for elastic scattering at high Z and low energy, because it exhibits non-uniformity of shape and so should prove a hardy test to any discretization scheme and because it must be sampled using a table search of the cumulative density. The cross sections are sampled for initial particle energy of 10 keV in gold, and graphical representations of the density functions for the three cases are presented in figures 5.2, 5.3, and 5.4.

The distributions to be sampled were processed by the discretization routines using various input error tolerances. Results showing the number of bins generated as a function of input error E_m^s for all three cross sections for both equally and

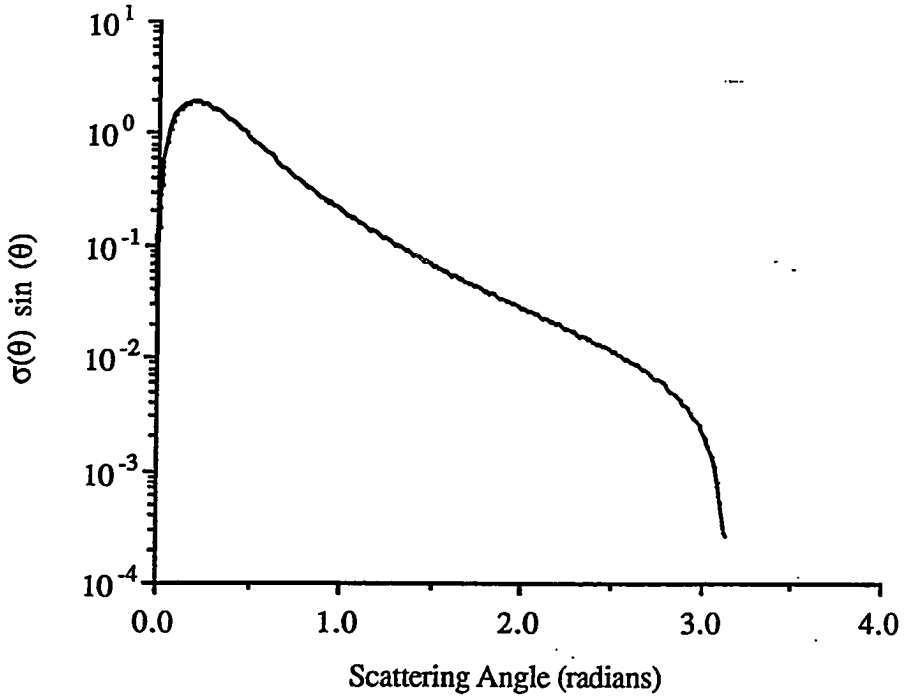

Figure 5.2: Screened Rutherford Cross Section in Gold at 10 keV.

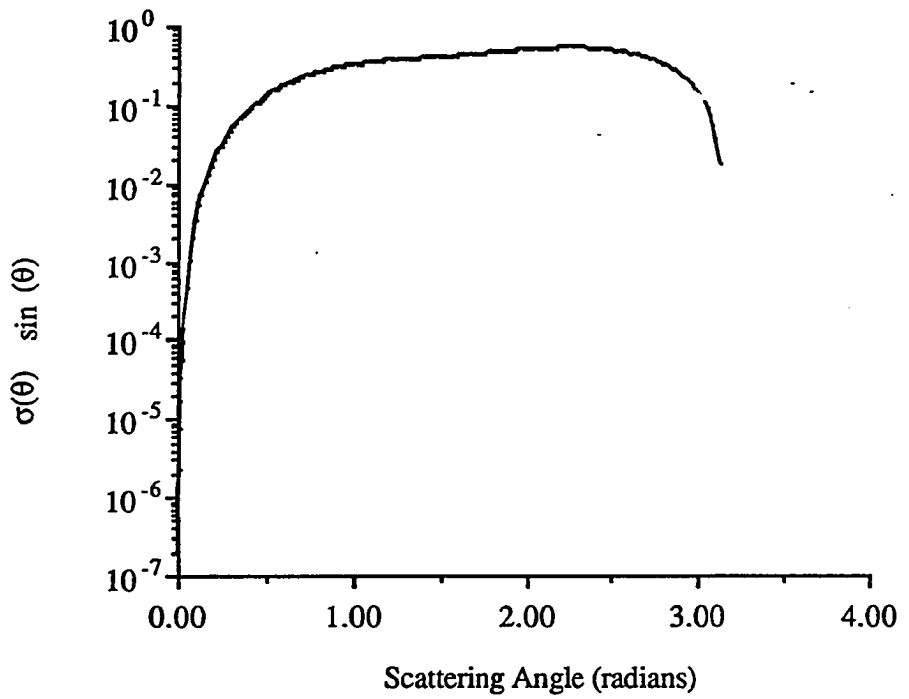

Figure 5.3: Compton Scattering Cross Section in Gold at 10 keV.

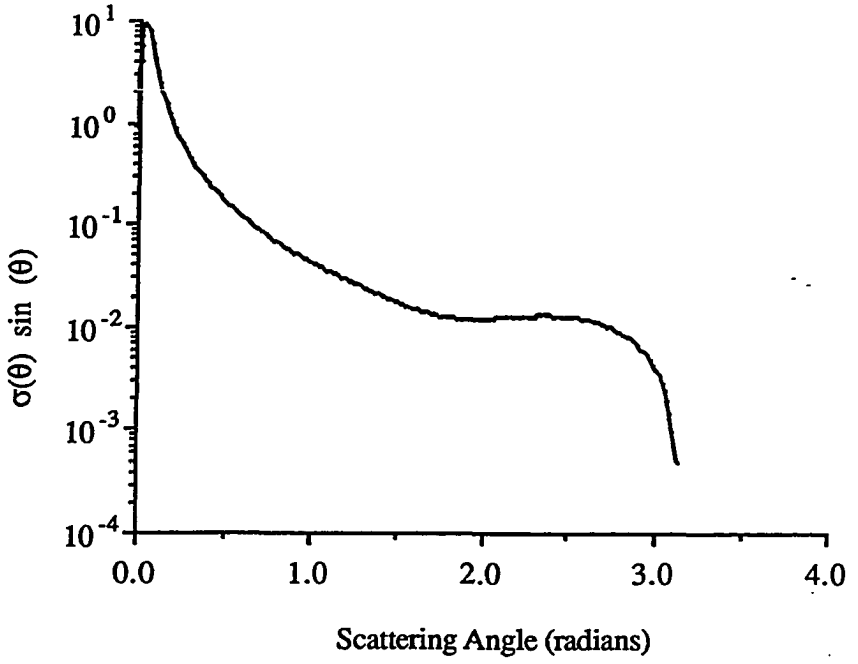

Figure 5.4: Riley Elastic Cross Section in Gold at 10 keV.

arbitrarily probable bins and both constant and linear interbin sampling schemes are plotted in figures 5.5, 5.6, 5.7 and 5.8. The same results grouped by cross section thus comparing the number of bins between the sample schemes are shown in figures 5.9, 5.10 and 5.11.

As expected from the experience with the test functions, for lower error tolerance, more bins are needed, and linear interpolation requires fewer bins than constant for a given error in all cases. Somewhat surprisingly, the results show that constant interpolation schemes appear unsuitable for required error tolerances of less than 5% or so in all cases, owing to the extremely large number of bins required. On the opposite extreme, relatively few bins give quite good accuracy for either bin scheme using linear interpolation, with one exception described later. Also consistent with earlier experience is that the number of bins required to fashion equally probable bins is much larger than for the arbitrary probability case. The number is so much larger that the total data storage required for the equally probable case exceeds that

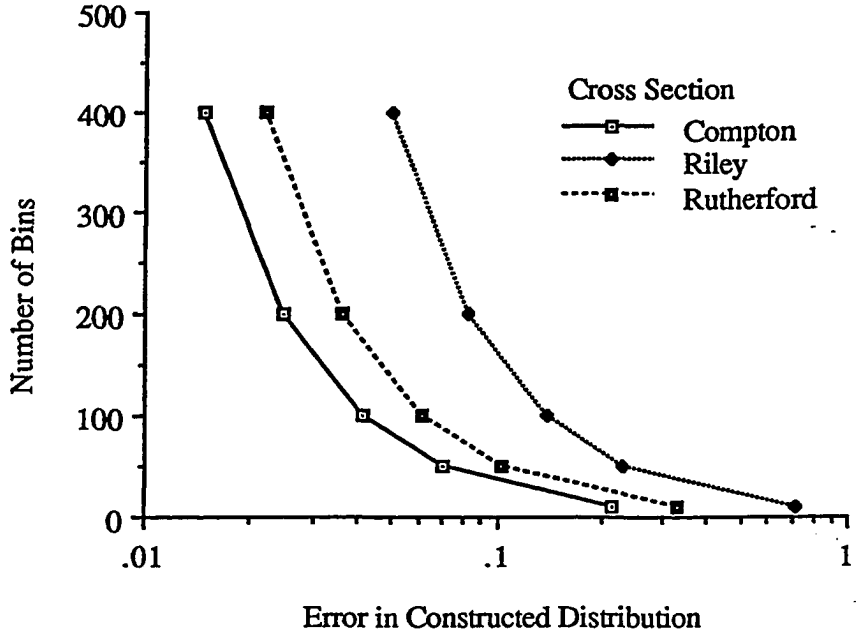

Figure 5.5: Number of Bins versus Error, Equally Probable Bins, Constant Interbin Interpolation

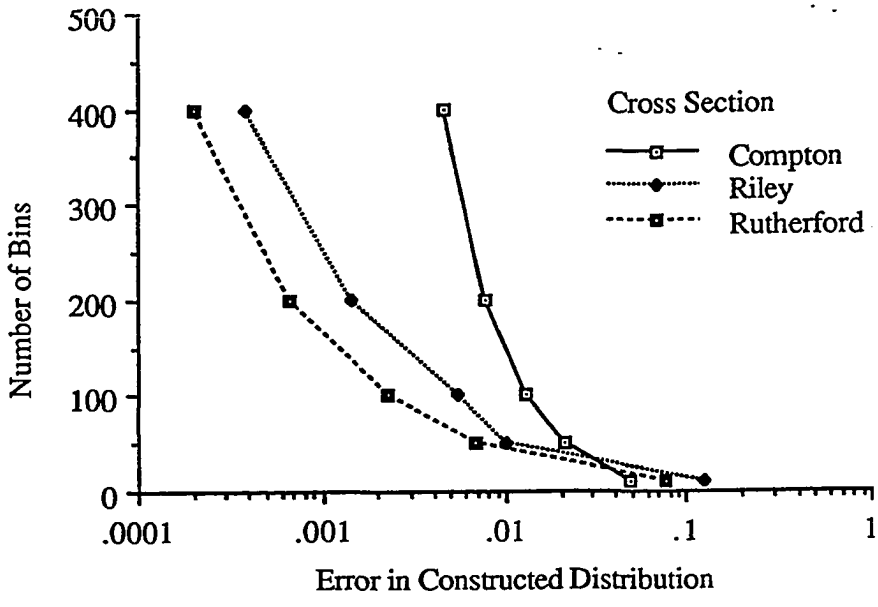

Figure 5.6: Number of Bins versus Error, Equally Probable Bins, Linear Interbin Interpolation

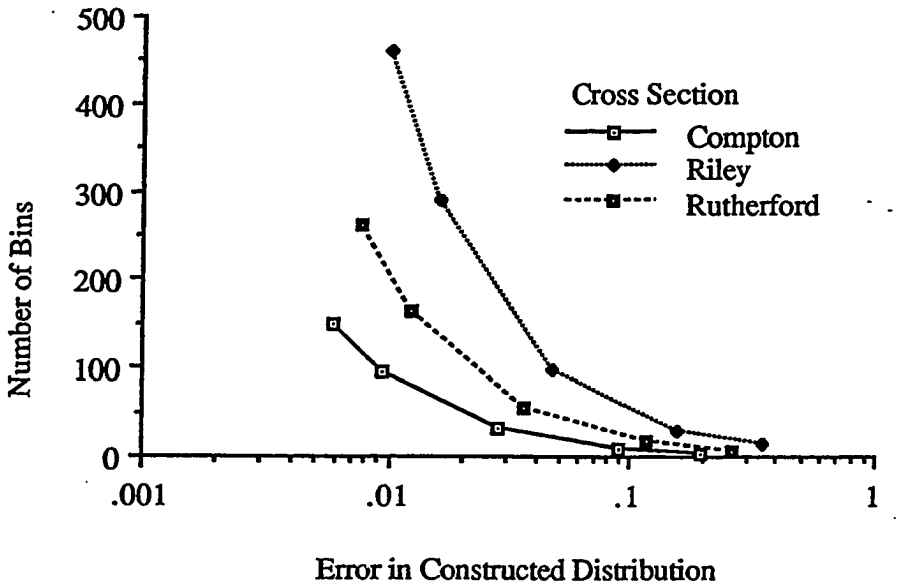

Figure 5.7: Number of Bins versus Error, Arbitrarily Probable Bins, Constant Interbin Interpolation

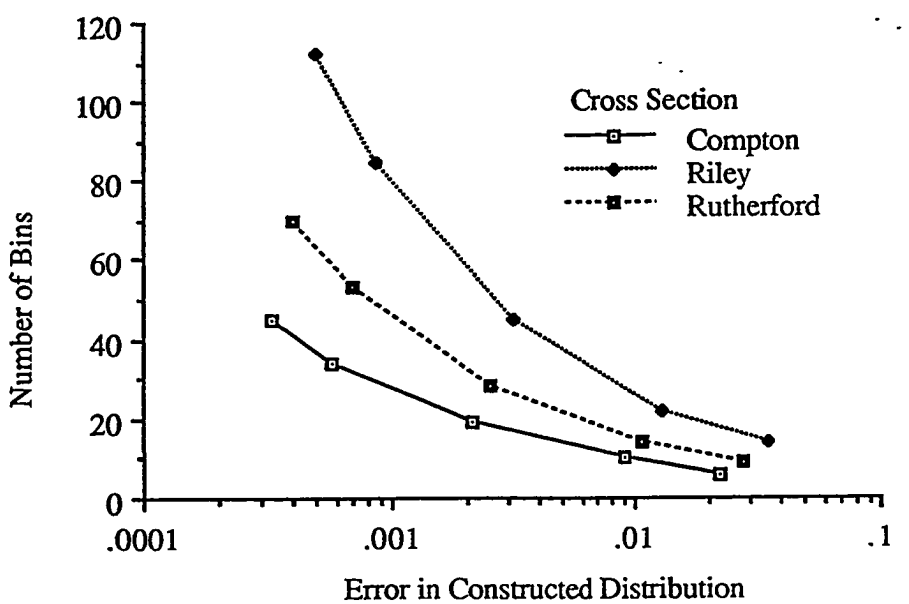

Figure 5.8: Number of Bins versus Error, Arbitrarily Probable Bins, Linear Interbin Interpolation

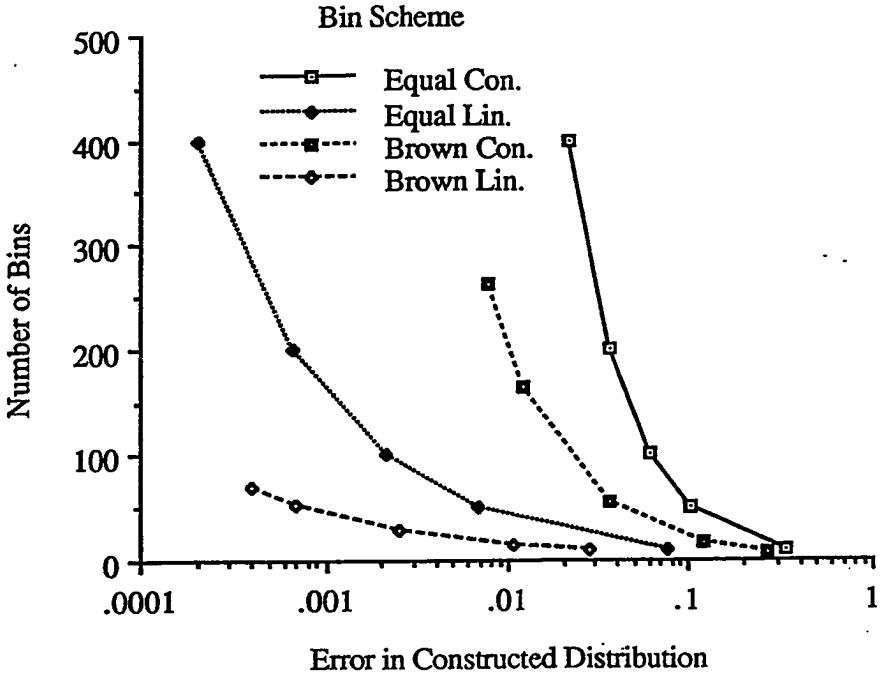

Figure 5.9: Number of Bins versus Error, Rutherford Scattering Cross Section, All Sampling Schemes

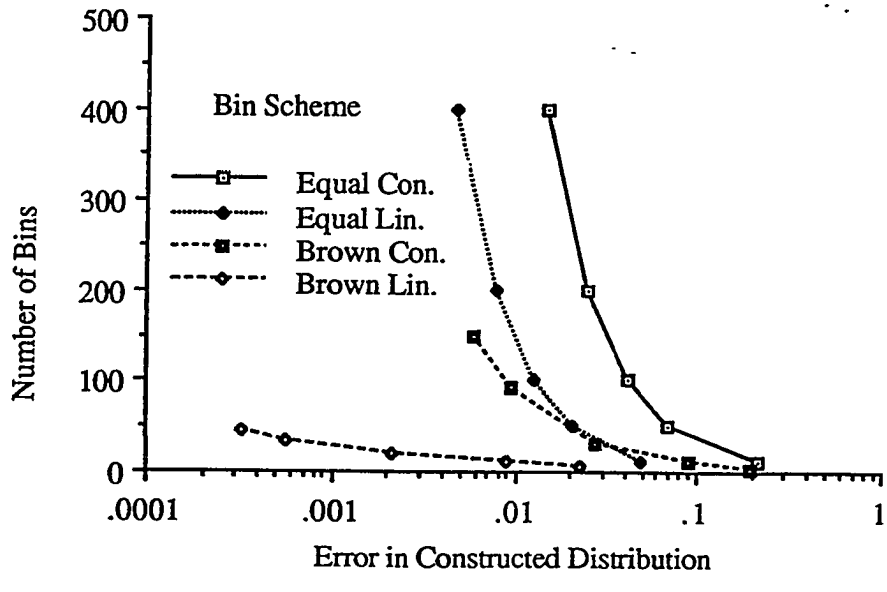

Figure 5.10: Number of Bins versus Error, Compton Scattering Cross Section, All Sampling Schemes

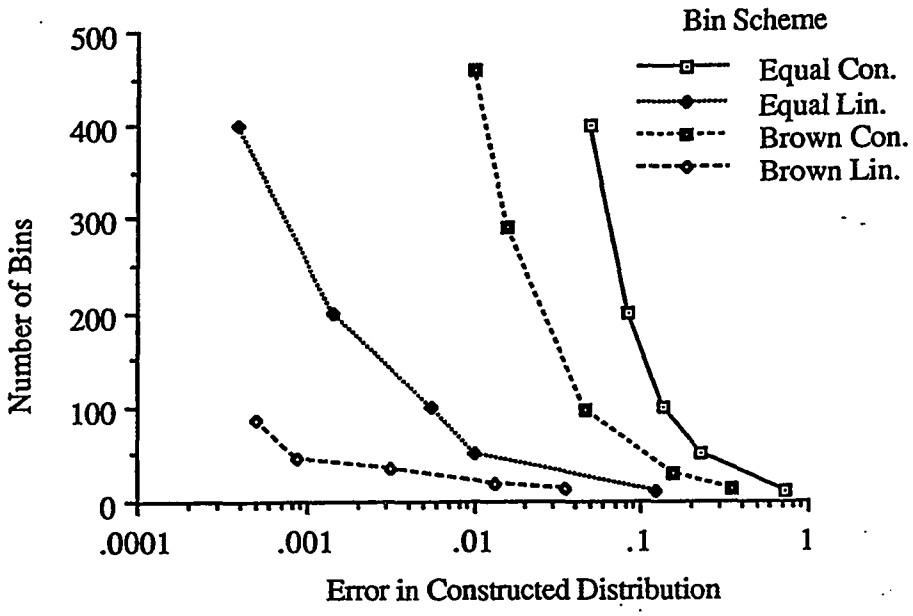

Figure 5.11: Number of Bins versus Error, Riley Elastic Scattering Cross Section, All Sampling Schemes

of the arbitrary case, even though the arbitrarily probable bin case requires twice as much data per bin. The inherent data storage requirements for the various schemes are given in table 5.3 and the specific results for the three test distributions (in terms of number of full words) are given in table 5.4.

It is seen from these results that for both bin schemes, the extra data storage required for linear interbin interpolation is more than offset by the saving in the number of bins, producing a net *decrease* in total space required for a linear interbin scheme versus a constant scheme at the same input accuracy. One other interesting fact revealed through these simple test cases is the unsuitability of the equally probable bin case for discretizing the Compton scattering distribution. The large number of bins results because of the large error involved in modeling the first bin, as $\sigma(\theta)\sin\theta d\theta$ is very small and very non-linear for small θ. The first bin must be kept short in order to satisfy the error requirement, and so has low probability. Since

Scheme	Data Elements Required
Table Search	Π_m, χ_m
Uniform Distribution	χ_m
Arbitrary Probability Distribution	χ_m, ρ'_m
Midpoint Interpolation	$(\chi_{m+1} + \chi_m)/2$
Constant Interpolation	χ_m
Linear Interpolation	$\chi_m, \pi'_m(\chi_{m+1})$

Table 5.3: Data Requirements for Bin Schemes and Interbin Sample Schemes

Scheme	Input Error	Compton	Riley	Rutherford
Table Search (Linear)	1%	20	52	30
Uniform, Const. Interp	6%	62	310	103
Arbitrary, Const. Interp	6%	30	156	68
Uniform, Linear Interp	1%	288	98	78
Arbitrary Linear Interp	1%	30	78	45

Table 5.4: Number of Full Words of Data Storage Required for Example Distributions

Sample Scheme	Interp. Scheme	Input Error	Computation Mode		
			Apollo	Cray Scalar	Cray Vector
Inversion	-	-	68.72	1.924	0.190
Table Search	-	1%	355.7	11.48	1.719
Equal Prob.	Midpoint	-	42.83	1.996	0.254
	Constant	6%	63.34	2.149	0.308
	Linear	1%	159.4	4.463	0.556
Arb. Prob.	Midpoint	-	76.00	2.723	0.367
	Constant	6%	108.3	3.789	0.490
	Linear	1%	194.7	5.869	0.702

Table 5.5: Sample Time per Outcome (μsec) for Sampling from the Rutherford Scattering Distribution at 10 keV in Gold

all other bins must have the same probability, a great number are required.

The discretized bin results at a given error tolerance of roughly 1% total rms error for the sample cross sections discussed above were then used in sampling 3500 values using vectorized algorithms which include all the necessary sampling overhead (both the details of the vectorization and the source of the overhead are explained later in this chapter) on an Apollo DN-4000 and a Cray X-MP/48 in both scalar and vector mode. Results showing the average sample time per outcome as a function of sampling scheme are presented for all three cross sections in all three computation modes in tables 5.5, 5.6, 5.7.

As expected, both the equally probable bin method and alias sampling method yielded faster sample times than the table searches and the rejection cases. Likewise,

Sample Scheme	Interp. Scheme	Input Error	Computation Mode		
			Apollo	Cray Scalar	Cray Vector
Rejection	-	-	3942.	102.2	17.84
Table Search	-	1%	313.7	9.943	1.488
Equal Prob.	Midpoint	-	40.86	2.041	0.255
	Constant	6%	63.22	2.192	0.288
	Linear	1%	157.7	4.585	0.524
Arb. Prob.	Midpoint	-	88.93	2.668	0.375
	Constant	1%	108.7	3.867	0.478
	Linear	1%	193.5	6.038	0.664

Table 5.6: Sample Time per Outcome (μsec) for Sampling from the Compton Scattering Distribution at 10 keV in Gold

Sample Scheme	Interp. Scheme	Input Error	Computation Mode		
			Apollo	Cray Scalar	Cray Vector
Fine Search	-	-	688.8	8.890	2.010
Table Search	-	1%	369.0	11.81	1.747
Equal Prob.	Midpoint	-	41.18	2.009	0.262
	Constant	6%	63.58	2.236	0.291
	Linear	1%	150.2	4.574	0.535
Arb. Prob.	Midpoint	-	76.52	2.679	0.361
	Constant	6%	109.2	3.859	0.458
	Linear	1%	194.8	6.026	0.668

Table 5.7: Sample Time per Outcome (μsec) for Sampling from the Riley Elastic Scattering Distribution at 10 keV in Gold

the equally probable bin scheme proved faster for all interpolation schemes than the arbitrary case. Surprisingly, equally probable sampling was comparable in speed to the simple direct inversion involved in sampling the Rutherford cross section.

The conclusions drawn from the results of applying discrete sampling schemes to continuous functions can be summarized as follows:

1. Constant and midpoint interpolation schemes require excessive amounts of storage space for error tolerances less than 5%.

2. Even though the arbitrary probability method requires more data elements per bin than the equal probability technique, the total data needed for the same error tolerance is actually smaller. In certain instances, the equal probability method requires unsuitable amounts of data storage, even when employing linear interpolation.

3. The number of bins required for a given error tolerance and a given scheme is highly dependent on the cross section.

4. The sampling speed for the various discrete schemes is roughly independent of the number of bins.

5. Sampling with a discrete method is 2 - 8 times faster than a table look up for scalar computations, and 2 - 7 times faster for vector computations. It appears to be faster than all but the simplest schemes for direct sampling.

6. Sampling from equally probable distributions is 30 to 50% faster than from arbitrary probability bins.

7. The maximum allowed error which results in sufficiently accurate transport simulations must be determined from simulations. If it is found that large errors

may be allowed, equally probable schemes may be preferred because of their speed. If high degrees of accuracy must be maintained in the discretization, then arbitrary probability schemes may be necessary to reduce data storage requirements.

Discretization in Energy Once the decision is made to use tabulated density functions for energy loss or angular deflection, some scheme must be concocted for handling the variation in the densities with respect to energy. The most obvious scheme involves another layer of discretization. Distribution functions are tabulated at given energies throughout the applicable range and the density for an event involving a particle with a given energy sampled from the density tabulated at the nearest energy. In the interest of saving main memory space, the energy binning scheme should minimize the number of base points for a desired level of accuracy. Several timing considerations impact the energy bin (or ladder) scheme. First, it is desirable to have uniform spacing (typically either logarithmic or linear) so that the bin index of the nearest base point can be calculated directly rather than determined from a table search. Second, it would save computations if each cross section or distribution function had the same energy ladder, and so the proper bin need be determined just once per particle per track. Of these two considerations, the first is far more important. The use of non-uniform ladders would require a table search to determine a distribution energy index at each sampling, and would be very time consuming. Non-uniform ladders with the same spacing for each distribution would require only one such table search per particle per event, but would require that the all distributions be tabulated at as many points as the least accurate one and hence would impose a data space penalty. This same storage penalty would be imposed

in the case of using a single, uniformly spaced ladder for all of the distributions, but this implementation would save some computations in that the energy index could be calculated instead of determined from a search. This option is employed in a production code, the SANDYL derivative of ETRAN, in which the base points are fixed in a uniform course mesh at every 8.30% energy loss (corresponding to a reduction to half energy every 8 base points) and, at the user's discretion, possibly at more widely spaced base points [Co74]. The final alternative is the use of uniform, distribution dependent ladders.

The attempt to optimize ladder spacing for an individual distribution function begins with an examination of the error induced by ladder schemes. The sampling error introduced can be measured by equations 5.9 and 5.11 with $p(\chi)$ equal to the actual density and $\Pi_m \pi_m^s(\chi)$ the tabulated density at the nearest energy. The magnitude of the error depends on the sampling scheme, the difference in energy between the actual energy and the energy for which the tabulation is made and on the tabulation's energy base point itself, if the derivative of the density varies with energy. Families of curves denoting the relative rms error as a function of particle energy using different base points for the tabulation for several sampling schemes for each of the three test densities are given in figures 5.12 through 5.20. The energy base points at which the densities are tabulated are 100, 50, and 10 keV for several values of initial error tolerance.

The following observations about the error introduced by using functions tabulated at energies differing from the actual particle energy can be drawn from these figures:

1. The error introduced by energy laddering increases with the change in energy, as expected.

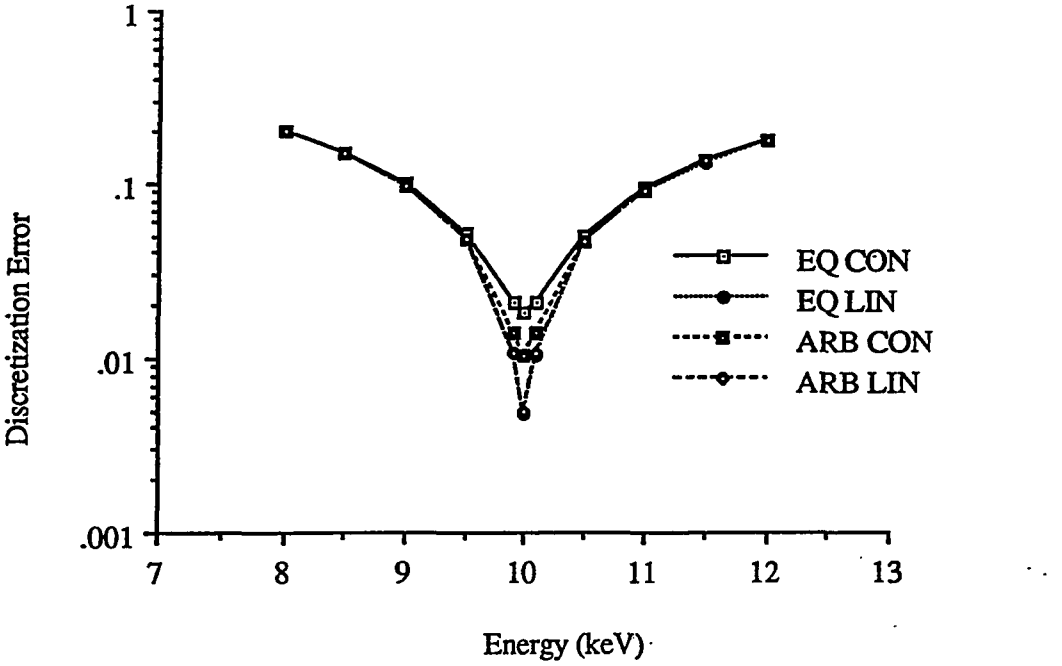

Figure 5.12: Discretization Error vs. Energy for Rutherford Elastic Scattering Cross Section at 10 keV

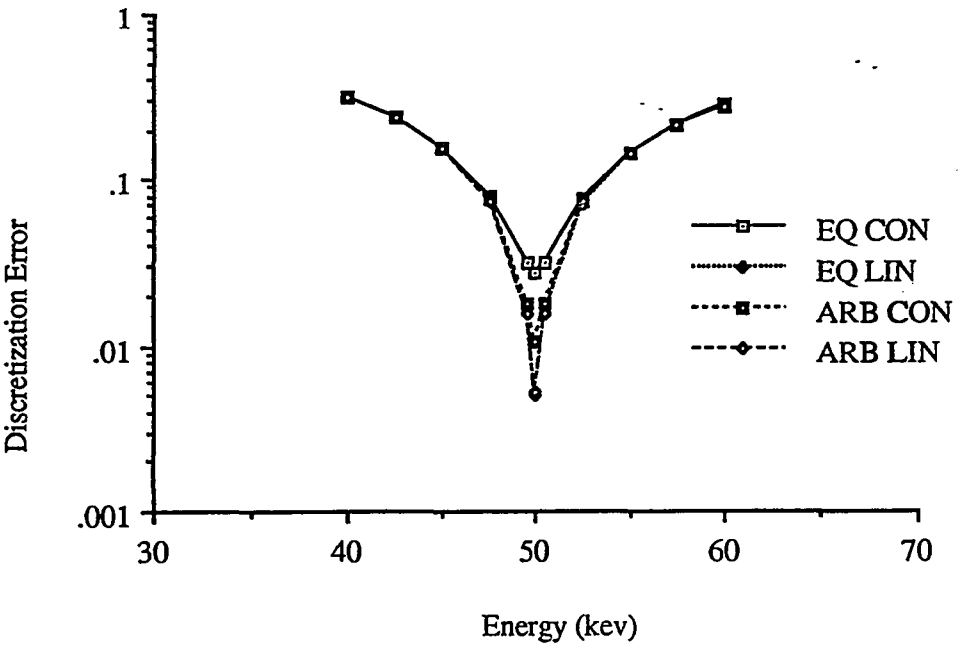

Figure 5.13: Discretization Error vs. Energy for Rutherford Elastic Scattering Cross Section at 50 keV

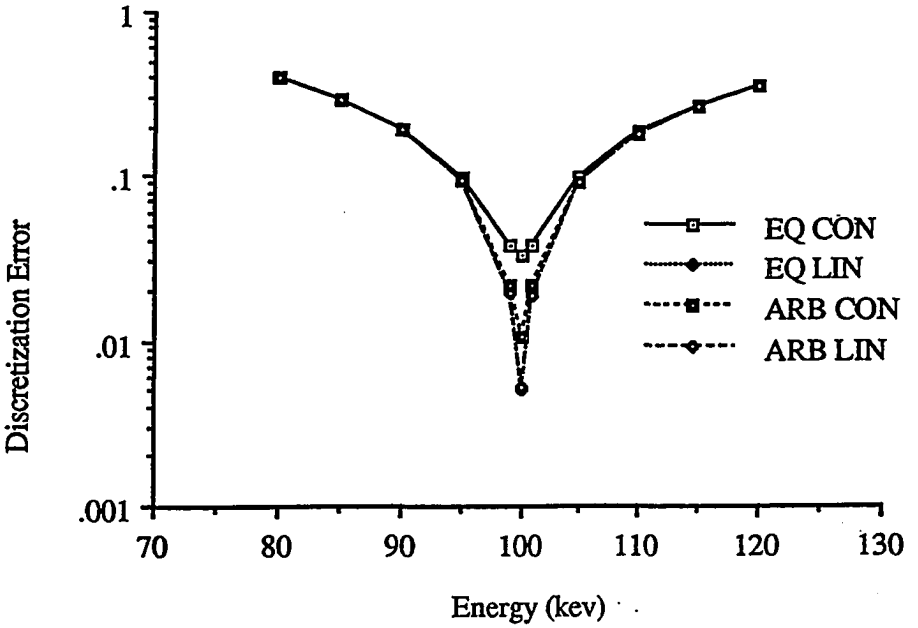

Figure 5.14: Discretization Error vs. Energy for Rutherford Elastic Scattering Cross Section at 100 keV

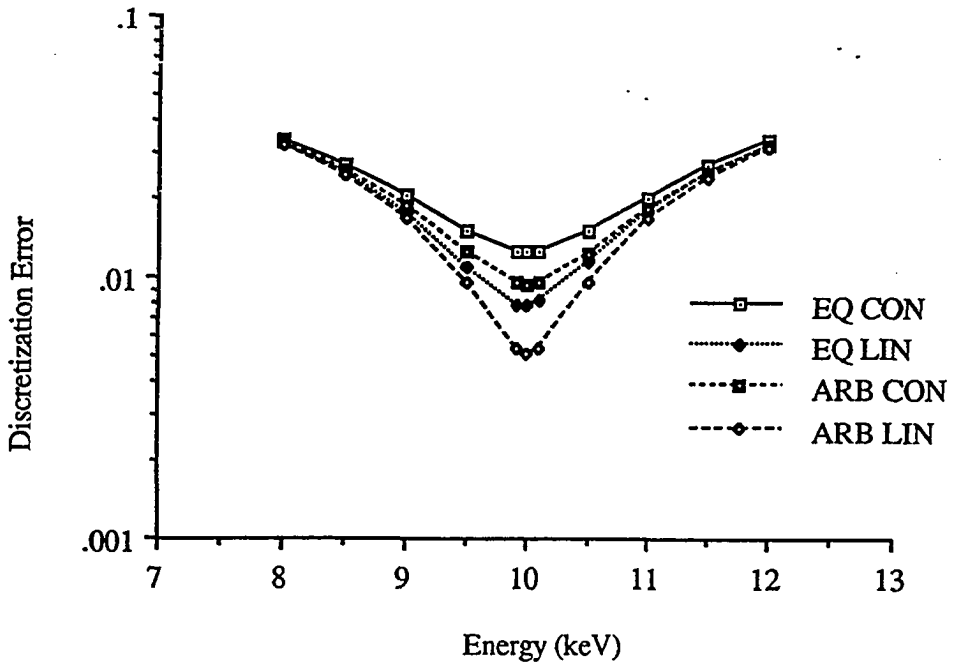

Figure 5.15: Discretization Error vs. Energy for Compton Cross Section at 10 keV

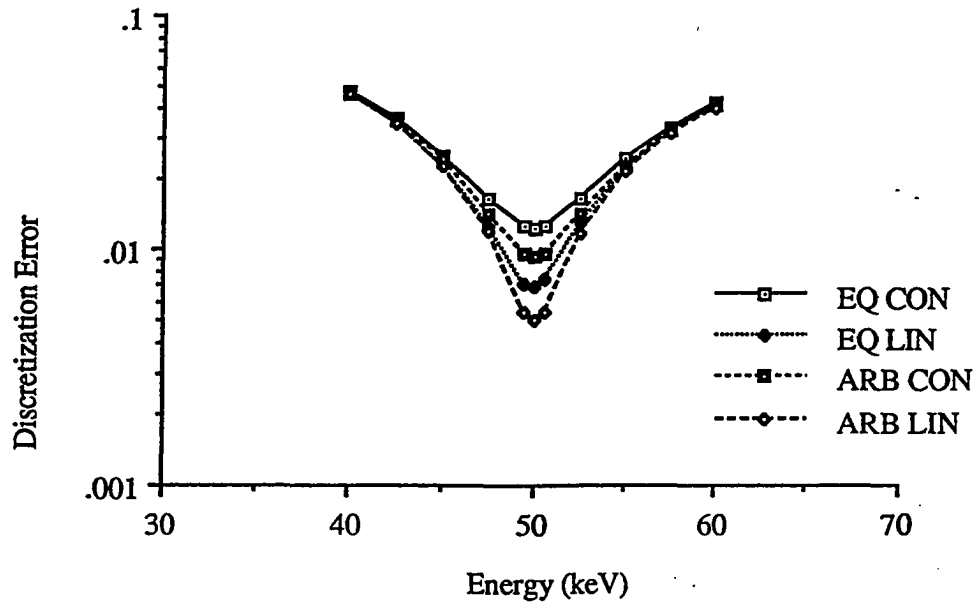

Figure 5.16: Discretization Error vs. Energy for Compton Cross Section at 50 keV

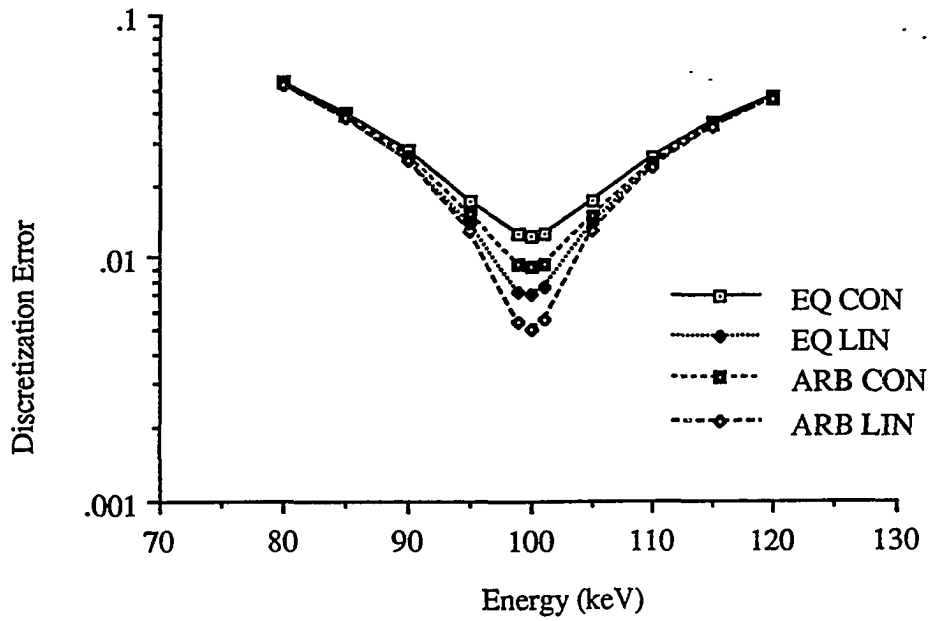

Figure 5.17: Discretization Error vs. Energy for Compton Cross Section at 100 keV

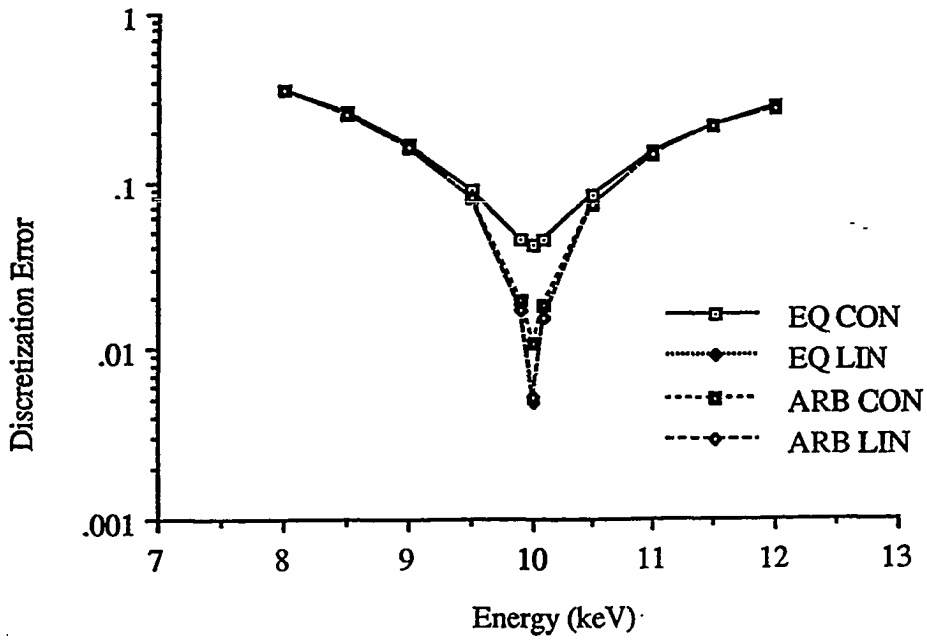

Figure 5.18: Discretization Error vs. Energy for Riley Elastic Scattering Cross Section at 10 keV

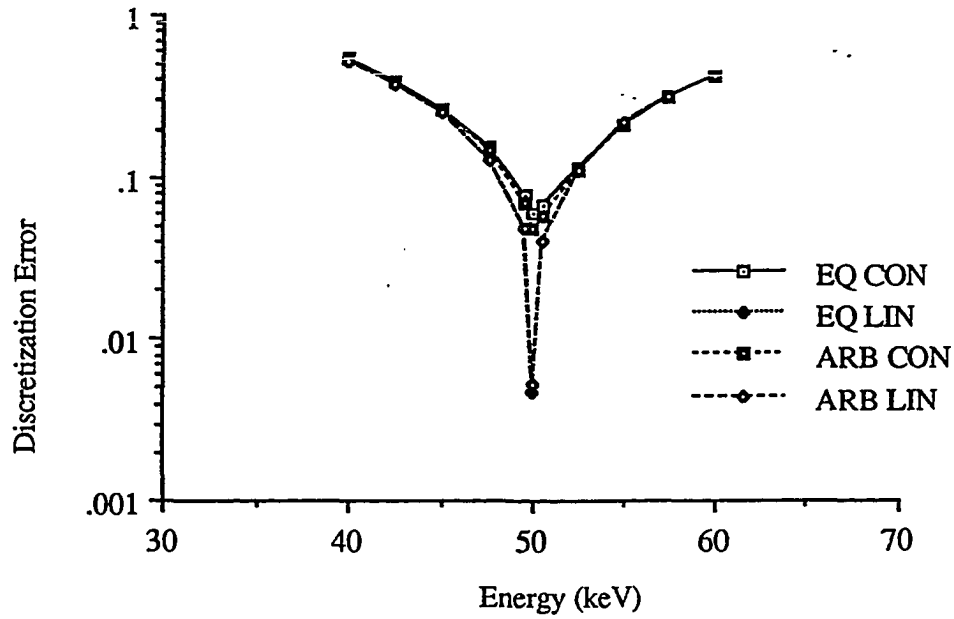

Figure 5.19: Discretization Error vs. Energy for Riley Elastic Scattering Cross Section at 50 keV

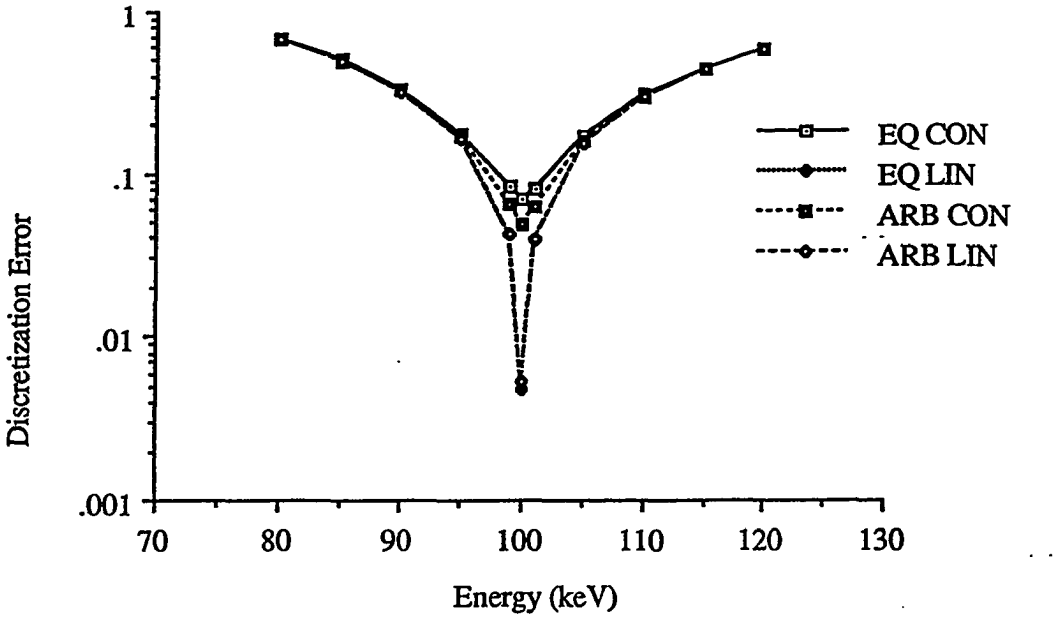

Figure 5.20: Discretization Error vs. Energy for Riley Elastic Scattering Cross Section at 100 keV

2. The error is extremely cross section dependent. This implies that if memory availability is the most critical modeling criteria, each distribution should have an independent set of energy base points.

3. The laddering error is slightly less pronounced at lower initial energies for the same fractional change in energy. This implies that the optimal mesh scheme lies somewhere between logarithmically spaced base points (the optimal spacing when error change is completely independent of energy for the same fractional change) and linear spacing.

4. The rate of error change is much steeper for smaller initial errors. This implies that more widely spaced points are suitable for larger tolerance cases, as expected. The extent to which this was found to hold is somewhat surprising.

5. The error change appears to be bin scheme independent. For the same scheme

and the same tolerance, the error incurred in using a discrete scheme calculated at a different energy is driven by the actual differences in the densities and not inaccuracies in discretization.

6. The error change is for the most part symmetric with respect to negative and positive energy differences. If it were skewed, the approximation of using the density function tabulated at the nearest base point would have to be adjusted to take into account the asymmetry.

7. A highly accurate discretization at the energy base points is not much more effective than a low accuracy scheme at small incremental energies away from the base point for a moderate allowed error ($\gtrsim 6\%$). This implies that unless extremely high accuracy in the inter-energy distributions is required, crude base point distributions will perform almost as well as fine ones with a significant savings in data storage.

8. High accuracy will require an extremely fine mesh of energy base points.

The last two points imply that it may be worth the loss in computing speed to gain accuracy with respect to the faithfulness of the distribution approximations by interpolating between energies. This would involve sampling both the upper and lower energy density using the same random number and then performing a linear interpolation. This technique is unnecessary for direct sampling schemes and is incompatible with alias sampling (the alias results at different energies are not correlated), but can be used for both table searches and equally probable bin sampling, with midpoint, constant and linear interbin interpolation. Timing runs similar to those performed for presentation in tables 5.5 through 5.7 were repeated and the resultant slow down due to inter-energy interpolation computed. Since the slow down,

Sample Scheme	Interp. Scheme	Computation Mode		
		Apollo	Cray Scalar	Cray Vector
Table Search	-	616.8 (2.0)	18.92 (1.9)	2.855 (1.9)
Equal Prob.	Midpoint	69.47 (1.7)	2.292 (1.1)	0.365 (1.4)
	Constant	114.9 (1.8)	2.909 (1.3)	0.475 (1.6)
	Linear	288.3 (1.8)	8.538 (1.9)	0.938 (1.8)

Table 5.8: Sample Time per Outcome (μsec) and Slowdown Factor for Sampling from the Compton Distribution at 10 keV in Gold using Inter-energy Interpolation

like the sampling speed, was found to be independent of the cross section, only the results for the Compton scattering tests are presented here, in table 5.8. The actual sample times as well as the slowdown (given by the increase in computation time) are given. The input error tolerances for the discretizations are equivalent to those for the non-interpolated case. As expected, it is seen from these results that the usual trade-offs of run time for space saving and accuracy are present. One interesting point to note is that the expected slowdown of a steady factor of 2 is not seen for the Cray X-MP for sample schemes requiring only a small amount of arithmetic operations. In these instances, much of the computing time is involved in pipeline startup and in processing the vectors according to index (the third section in this chapter examines this in detail), and so loops containing twice the arithmetic (which is always present) do not require twice the run time. As the computation becomes more involved (for the more detailed interpolation schemes) the startup and vector processing operations take up less of the total computation time and the slow down

does approach a factor of 2.

Based on the conclusions drawn from these preliminary tests and the results described above, several schemes for determining the number and spacing of the energy points were examined. As noted earlier, the optimal scheme will lie between linear spacing, for which the l^{th} energy base point is given by

$$E_l = E_1 + (l-1) \cdot \Delta E \tag{5.13}$$

and logarithmic spacing, for which

$$E_l = k^{(l-1)} \cdot E_1. \tag{5.14}$$

We assume that E_i and E_f, the smallest and largest energies, are known, and that $E_1 = E_i$ and $E_{N_b} = E_f$, if N_b is the number of base points. For the above formalisms, the current energy index l for a particle of energy E is given by

$$l = (E - E_1)/\Delta E + 1 \tag{5.15}$$

in the linear case and

$$l = \ln(E/E_1)/\ln k + 1 \tag{5.16}$$

for the logarithmic case.

Since previous results have shown that the absolute energy change required to maintain constant error decreases dramatically as the energy decreases for most instances, the spacing constants ΔE for the linear case is determined by the maximum allowed difference between E_1 and E_2, and is given by

$$\Delta E = E_2 - E_1 \tag{5.17}$$

and so the number of base points is given by

$$N_b = (E_{N_b} - E_1)/\Delta E + 1. \tag{5.18}$$

Since the fractional (as opposed to absolute) allowed spacing increases as the energy decreases, in the logarithmic case the constant will be determined by the fractional difference between the the last two base points,

$$k = E_{N_b}/E_{N_b-1} \tag{5.19}$$

and the number of points given by

$$N_b = \ln\left[\frac{E_{N_b}}{E_1}\right] / \ln k + 1. \tag{5.20}$$

A simple algorithm for determining the spacing constants in these two cases has been devised. For the linear case, it is necessary to determine only E_2, and for the logarithmic case, E_{N_b-1}. To do this, an input density function is first discretized using the allowed base point error at either E_i or E_f for the linear and logarithmic spacing cases respectively. Relative average root mean square differences between this discrete density and actual densities calculated at several nearby energies are then determined. Assuming that the error incurred in using a discrete density to model densities at other energies increases with the energy difference, the energy at which the maximum allowed rms inter-energy error is reached can be interpolated from data giving errors as a function of energy. Since earlier results have shown that the error is relatively symmetric with respect to energy change, the initially determined point is taken as the *midpoint* of the bin. Hence the nearest energy base point (E_2 or E_{N_b-1}) can be assumed to be located at an energy difference from the base point which is twice the absolute difference between the determined midpoint and the initial base point. Either constant or linear interbin interpolation may be employed when no inter-energy interpolation is assumed, in which case densities are treated as if they were piecewise constant with respect to energy.

For the case of employing inter-energy interpolation, the algorithm is very similar.

Discretizations are performed at several energies near the initial one, and rms errors in linearly interpolated discrete densities are calculated at energies midway between the test energies and the initial base point energy. The energy base point for which linear inter-energy interpolation at the midpoint (assumed to be the least well modeled) produces the maximum desired error can be determined from the test data. As noted earlier, for arbitrarily spaced densities inter-energy interpolation is not possible using alias sampling. It is however, possible to use inter-energy interpolation in conjunction with a table search technique for sampling.

As stated above, it is assumed that the error increases as the energy bin spacing gets larger, and this has been found to hold or nearly hold for all instances. It sometimes fails when the errors found at large energy deviations are large and vary little from one another, which can be assumed to be a numerical artifact. In such instances, the data at small energy deviations, for which the calculated errors are close to the maximum desired error, is used in determining the energy base points.

Some initial calculations were made to determine the number of energy points required as a function of the maximum allowed error at the base point energies and the maximum deviation at the energy midpoints, using both linear and logarithmic spacing for equally and arbitrarily probable bin schemes using both constant and linear interpolation, but without interpolation in the energy dimension. In all instances, the tests were performed on the Compton, Rutherford and Riley scattering cross sections, assuming an initial energy of 100 keV and a final energy of 1 kev. Results of the number of energy bins required under the conditions of 5% base point and 7.5% interbin error for constant interpolation and of 1% and 2.5% errors for linearly interpolated distributions for are given in table 5.9.

The most important conclusion ascertained from these initial tests is that poten-

Sample Scheme	Rutherford		Compton		Riley	
	Lin.	Log.	Lin.	Log.	Lin.	Log.
Equal. Prob, Const. Interp.	417	84	< 248[1]	< 11[1]	1152	575[2]
Equal. Prob, Linear Interp.	958	188	< 248[1]	23	3537	511
Arb. Prob, Const. Interp.	410	79	< 248[1]	< 11[1]	1077	164
Arb. Prob, Linear Interp.	958	188	< 248[1]	23	3090	523

[1] Larger fractional energy differences not tested

[2] Basepoint Error = 6.8% (5% error required < 500 discrete angle bins)

Table 5.9: Number of Energy Base Points for Different Bin Schemes

tial memory limitation problems will be driven not by the number of bins necessary to discretize a distribution at a given energy (except of course for constant interbin interpolation schemes with small errors), but by the number of energy base points required to support high accuracy. The use of linearly spaced base points results in unnecessarily fine energy bins at the high energies, and logarithmic spacing produces too much detail at the lower energies. In fact, the linear energy bin scheme is almost precluded from use because of inordinate number of base points required, except in the Compton scattering case. It could be argued that the linear base point spacing ΔE for the requested accuracy be determined from that necessary at a higher energy (ΔE would be larger, thus reducing the number of energy points) and because the particles are nearly stopped at the lower energies, the large errors introduced by the wide relative spacing at the lower energies may not have a severe effect on overall

Sample Scheme	Rutherford		Compton		Riley	
	Bins	ϵ	Bins	ϵ	Bins	ϵ
Equal. Prob, Const. Interp.	29	18.14 %	$< 6^1$	> 5.71 %	119[2]	8.47 %
Equal. Prob, Linear Interp.	67	7.31 %	$< 10^1$	> 3.25 %	248	3.46 %
Arb. Prob, Const. Interp.	27	19.73 %	$< 6^1$	> 5.14 %	78	11.28 %
Arb. Prob, Linear Interp.	67	7.30 %	$< 10^1$	> 3.25 %	248	3.45 %

[1] Larger fractional energy differences not tested

[2] Basepoint Error = 6.8% (5% error required < 500 discrete angle bins)

Table 5.10: Number of Linearly Spaced Energy Base Points and Resultant Error at 10 keV using 50 keV for ΔE

results. If we apply this reasoning to the three distributions above by taking the ΔE from the spacing required at 50 keV for the error tolerances requested, we find that although the number of required energy points is greatly reduced, the number is still prohibitively large for the Riley elastic scattering cross section, and the errors at energies as high as 10 keV have already grown quite large for the Rutherford case (recall, the desired input tolerance was 7.5 % for the constant interpolative schemes and 2.5 % for the linear ones) and are certain to be larger at the lower energies. Thus it is assumed that linear spacing of energy basepoints is not practical. The data supporting these findings is summarized in table 5.10.

It is therefore proposed that a third base-point scheme be tried, using quadratic spacing. In this case, the energy bins are defined by

$$E_l = E_1 + (l-1)\cdot C_1 + (l-1)^2 \cdot C_2 \tag{5.21}$$

For this case, the current energy index l for a particle of energy E is given by

$$l = \frac{\sqrt{4C_2(E - E_1) + C_1^2} - C_1}{2C_2} + 1. \tag{5.22}$$

The constants C_1 and C_2, and the number of bins N_b can be determined in such a way that the energy spacing at E_i and E_f is optimal with respect to the input error tolerances. We find

$$\begin{aligned} N_b &= \frac{2(E_{N_b} - E_1)}{(E_{N_b} - E_{N_b-1}) + (E_2 - E_1)} + 1 \\ C_2 &= \frac{(E_{N_b} - E_{N_b-1}) + (E_2 - E_1)}{2(N_b - 2)} \\ C_1 &= (E_2 - E_1) - C_2. \end{aligned} \tag{5.23}$$

There is one drawback to this scheme, however, in that the first several bins after the first one are wider on a fractional basis than the first bin, leading to a slight increase in deviations of the midpoint distributions from the base-point discrete densities, above the original inter-energy error tolerance. This is clearly not an artifact of using quadratic spacing, but rather is due to the way in which the constants are chosen, and can be alleviated (at the expense of adding more bins) by requiring a slightly smaller input inter-energy error tolerance.

With this in mind, a routine ENCHOP was written to determine the energy bin spacing as a function of the base point error tolerance, the inter-energy error tolerance, the discretization scheme, the interbin interpolation scheme and the inter-energy interpolation scheme. Additionally, features were added to this routine which print warnings and adjust the input base-point error tolerance if a preset maximum number of allowed bins in the discretized densities is exceeded, and which adjust the inter-energy error if an allowed maximum number of energy base points would be exceeded. Test runs were performed which calculated the total number of bins

required and the error at energy midpoints as a function of the error tolerances and sample schemes. The maximum number of bins for these tests was set to the practical limits of 100 energy points (note that none of the examples in the previous test cases met this limit) and 200 secondary ladder points. The input base point error tolerances tested were 2.5% and 5% for discretization schemes using constant interpolation and .5% and 1% for those employing linear interpolation. Maximum requested inter-energy error was set to be 1.2, 1.5 and 2.0 times the base point error for the constant interpolation cases and 1.5, 2.5 and 5.0 times the base point error for the linear interbin interpolation case. These error limits were the same for the schemes using inter-energy interpolation between the base point data and those simply using the nearest base point data, and all three of the test case cross sections were used, making a total of 84 test runs (6 error schemes and 2 energy base point spacing methods for each of 4 constant and 3 linearly interpolated inter-energy sample scheme) for each of the three test cross sections. These tests were designed to explore the validity of the following assumptions:

1. Smaller requested errors at energy midpoints will require closer spacing of the energy base points.

2. The use of inter-energy interpolation will decrease the number of energy base points required.

3. The use of quadratically spaced base points will decrease the number of energy base points required.

4. Spacing constants can be calculated using data at only one set of energy points because the error at the energy midpoints monotonically decreases with energy for a given spacing scheme.

Because of the limitations placed on the total number of energy points and the total number of bins at each point, not all of tests were completed within the requested input error. In all cases however, the ENCHOP program determined a bin scheme within the preset size limitations with either the requested error or a "minimum" possible error, as described above.

As expected, the total number of base points required decreases as the midpoint error tolerance decreases. Figures 5.21 through 5.23 present results for the three test case scattering cross section in gold, modeling stopping from 100 to 1 keV. Only the inter-energy interpolation test results are shown, for all possible sampling types and for quadratically spaced base points. Results are similar when the "nearest base point" method and/or logarithmically spaced base points are used, but more numerical artifacts are present because the size limitation feature of the program was invoked more often. The leveling off at high errors seen in the figures is caused by a limitation of algorithm in that no energy differences of greater that 50% were tested, implying a minimum of 4 base points. One interesting feature evident from the figures is that for the same error, the number of energy base points required is independent of the sample scheme. Therefore, the sampling scheme requiring the minimum storage will be determined solely from the number of bins needed in modeling the distribution at the base points.

As noted above, requested error tolerances (.5% at the base points and .75% at the midpoint for the linear interpolation schemes and 2.5% and 3.0% for the constant interpolation schemes) were not always attainable. The "best" errors for the 3 cross sections with and without inter-energy interpolation for the permitted sample schemes with logarithmic spacing is given in table 5.11. Note that the linear interpolation scheme with arbitrarily spaced bins can be used only with table searches,

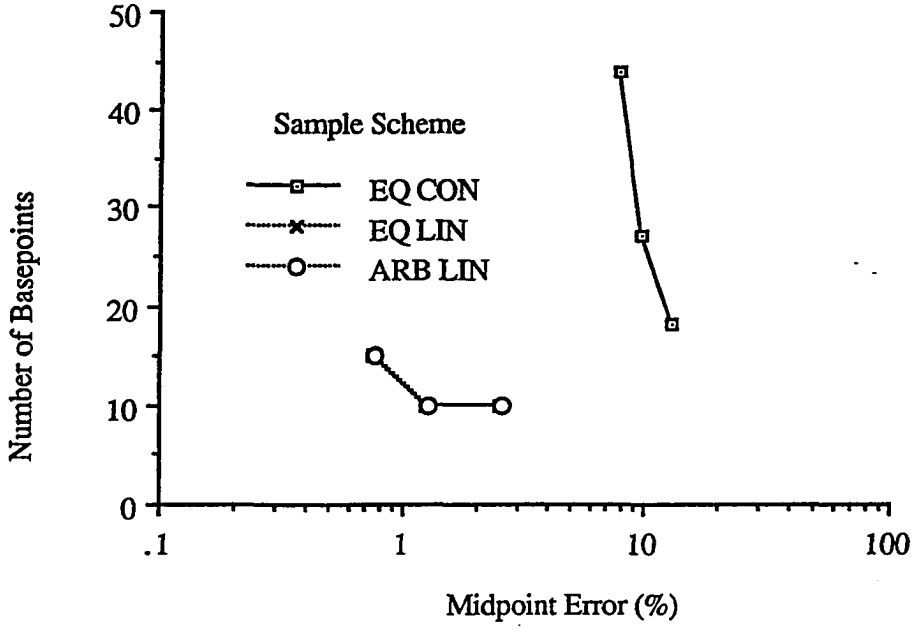

Figure 5.21: Number of Basepoints vs. Midpoint Error, Rutherford Cross Section, Slowing in Gold from 100 to 1 keV.

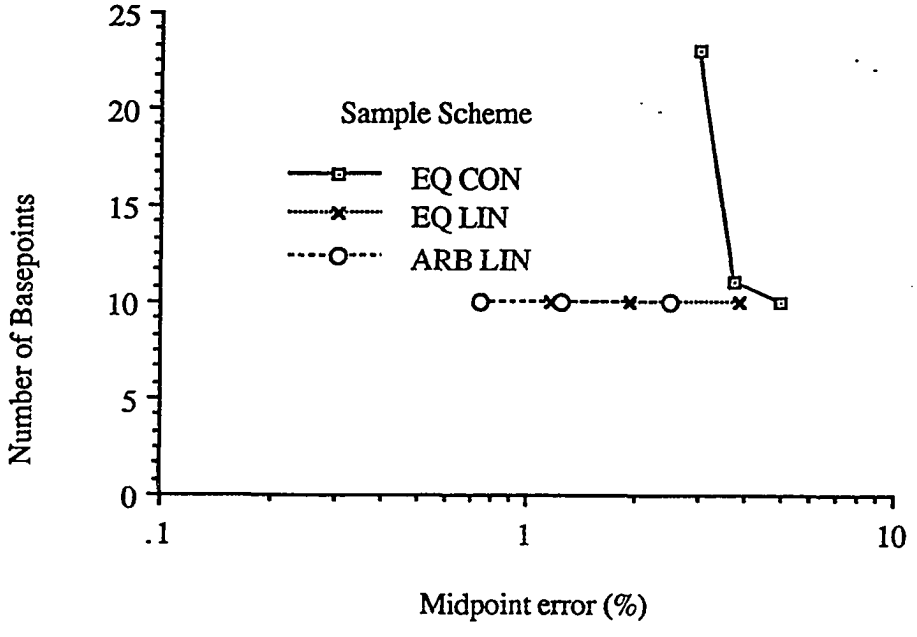

Figure 5.22: Number of Basepoints vs. Midpoint Error, Compton Cross Section, Slowing in Gold from 100 to 1 keV.

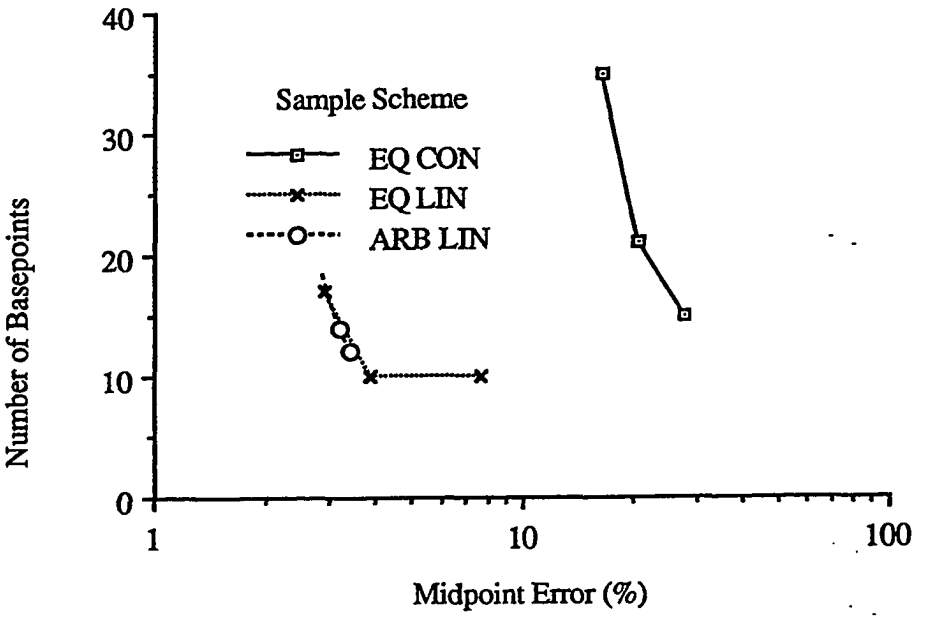

Figure 5.23: Number of Basepoints vs. Midpoint Error, Riley Cross Section, Slowing in Gold from 100 to 1 keV.

and not alias sampling methods.

The results show that in several cases when the non-inter-energy interpolative scheme was to be used, the requested midpoint error could not be obtained using the 100 energy point limit, but it could be obtained if interpolation were used. As could be expected from previous tests, results show that arbitrarily probable discretizations can more easily meet stringent space requirements, in both the interpolation and nearest basepoint cases. One artifact of the CHOP algorithm is evidenced by table 5.11, that being that since the error is calculated for the arbitrary spacing case bin by bin, the final total error can not be known in advance. One iteration is performed, using a guess of the individual bin error needed to produce the desired total error, based on the initial total error and the first cut number of bins. As this procedure is not always accurate, the result shown in the table which seems to indicate that for constant interbin interpolation, equally probable bins lead to higher accuracy for the

Sample Scheme	Rutherford		Compton		Riley	
	ϵ_{Base}	ϵ_{Inter}	ϵ_{Base}	ϵ_{Inter}	ϵ_{Base}	ϵ_{Inter}
Without Inter-energy Interpolation:						
Eq Prob, Const Interp	6.555 %	7.866 %	2.501 %	3.001 %	13.87 %	16.64 %
Eq Prob, Linear Interp	0.496 %	1.939 %	0.779 %	1.168 %	1.528 %	4.476 %
Arb Prob, Const Interp	3.672 %	4.407 %	3.194 %	3.833 %	3.936 %	5.904 %
Arb Prob, Linear Interp	0.515 %	1.887 %	0.499 %	0.749 %	0.551 %	4.204 %
With Inter-energy Interpolation:						
Eq Prob, Const Interp	6.555 %	7.866 %	2.501 %	3.001 %	13.87 %	16.64 %
Eq Prob, Linear Interp	0.496 %	0.745 %	0.779 %	1.168 %	1.528 %	2.773 %
Arb Prob, Linear Interp	0.515 %	0.773 %	0.499 %	0.749 %	0.551 %	2.775 %

Table 5.11: Requested or Resultant Errors Within Maximum 100 Energy Points and 200 Bins per Point

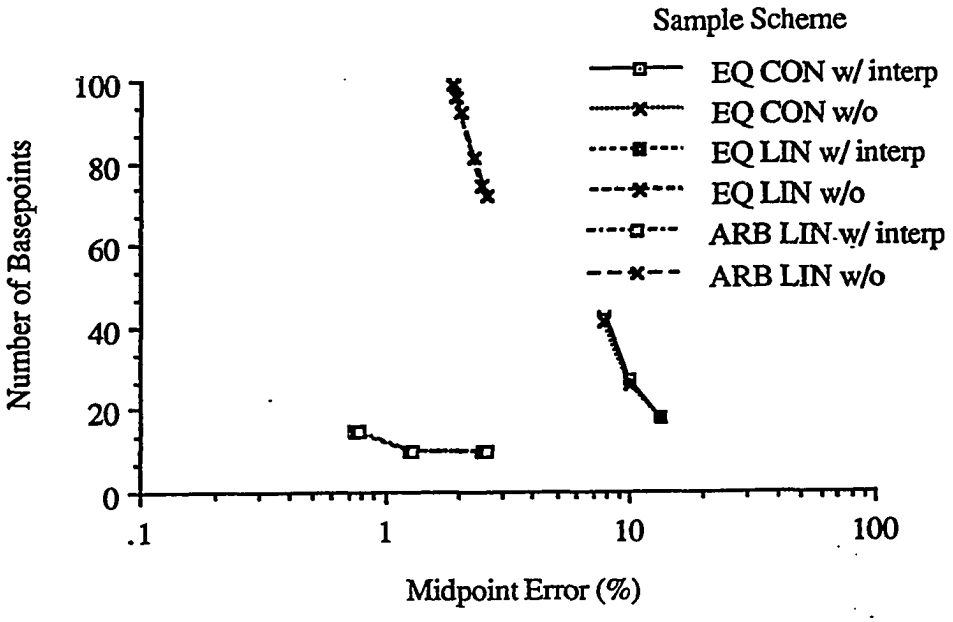

Figure 5.24: Number of Basepoints vs. Midpoint Error, with and without Inter-Energy Interpolation, Rutherford Cross Section, Slowing in Gold from 100 to 1 keV.

Compton cross section is not true. In this case the error after one iteration, although requested to be 2.50 %, was 3.19 %. It is certain that lower error could be found for this case with this scheme, if more iterations were employed.

A related consequence of the use of inter-energy interpolation is that the required number of energy base points is smaller, as expected. This is illustrated in figures 5.24 through 5.26 which plot a pair of curves for each sampling scheme, representing the number of base points versus interbin error for both the interpolative and nearest base point methods. The data presented is restricted to the larger base point error case and quadratic spacing, although again the results are similar for logarithmic spacing. The magnitude of the effect is quite dramatic.

Figures 5.27 through 5.29 show that quadratic spacing does indeed reduce the number of base points needed, and by a considerable amount. Results are present for the test cases using the nearest base point method. Note the roughly uniform

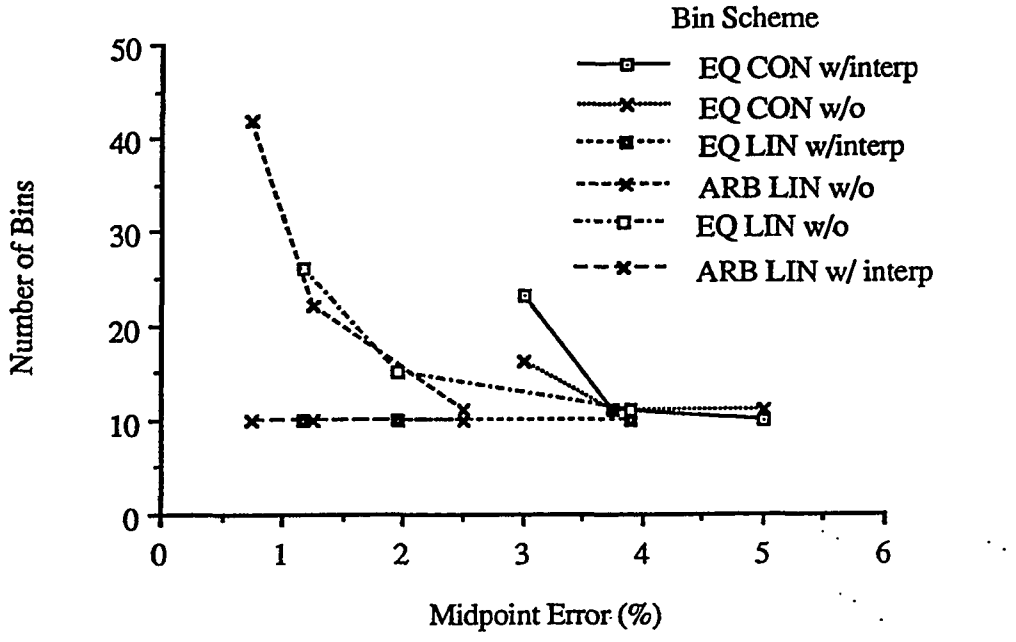

Figure 5.25: Number of Basepoints vs. Midpoint Error, with and without Inter-Energy Interpolation, Compton Cross Section, Slowing in Gold from 100 to 1 keV.

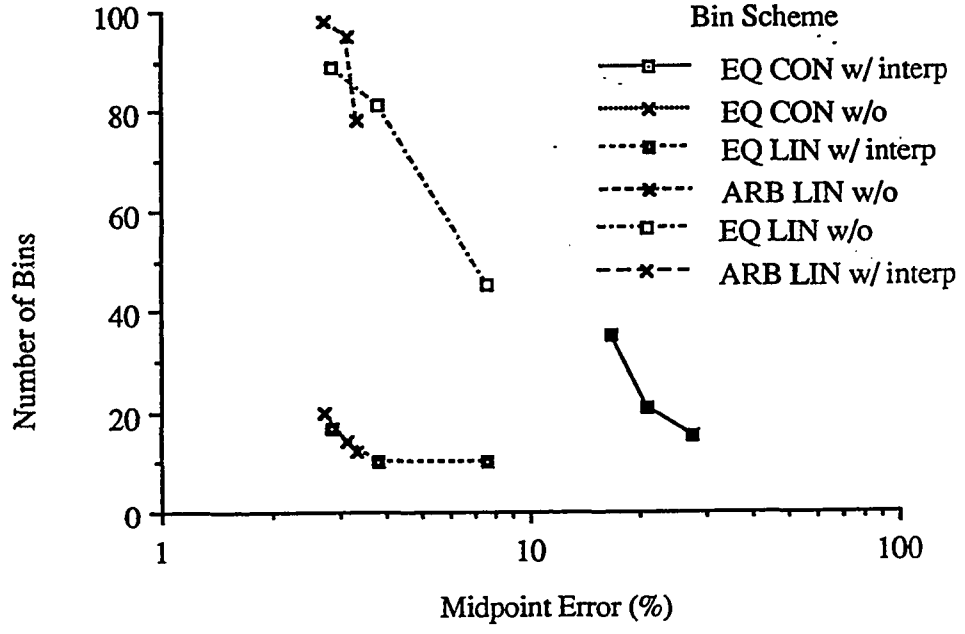

Figure 5.26: Number of Basepoints vs. Midpoint Error, with and without Inter-Energy Interpolation, Riley Cross Section, Slowing in Gold from 100 to 1 keV.

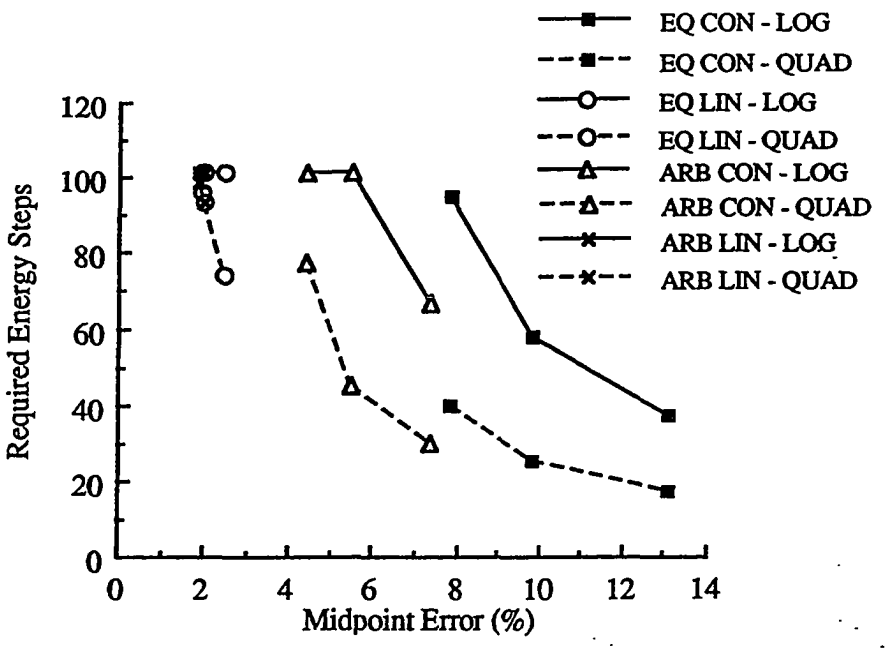

Figure 5.27: Number of Basepoints vs. Midpoint Error for Quadratic and Logarithmic Spacing, Rutherford Cross Section, Slowing in Gold from 100 to 1 keV.

factor of two difference in the number of basepoints, independent of the error or the cross section.

Recall that it is assumed that in determining the energy spacing schemes, the error at the energy *midpoints* decreases with energy for the same fractional energy difference between the base points. Several examples of the change in midpoint error are shown in figures 5.30 through 5.32, and the expected behavior is for the most part evident. Note the artifacts at low energy for the quadratic cases caused by the large bin sizes. In instances when very few numbers of base points are predicted, the algorithm clearly fails, as unacceptably large errors occur at the midpoints of other than the first and last bins. And even in instances in which more than a few (20 or so) energy points are chosen, the errors at the low energy midpoints are still higher than the input tolerance. Note also that because of the close energy point spacing in the logarithmic cases, the midpoint errors are very close to the *basepoint* errors at low

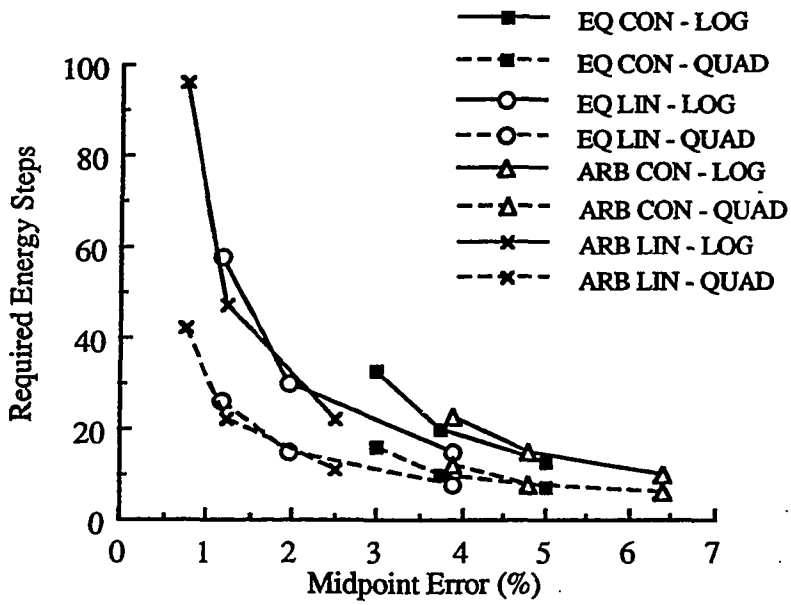

Figure 5.28: Number of Basepoints vs. Midpoint Error for Quadratic and Logarithmic Spacing, Compton Cross Section, Slowing in Gold from 100 to 1 keV.

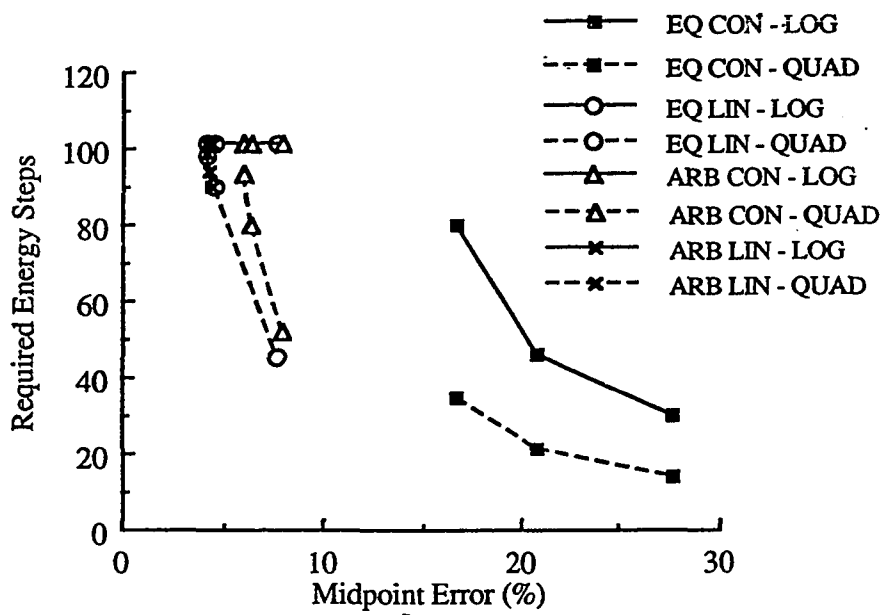

Figure 5.29: Number of Basepoints vs. Midpoint Error for Quadratic and Logarithmic Spacing, Riley Cross Section, Slowing in Gold from 100 to 1 keV.

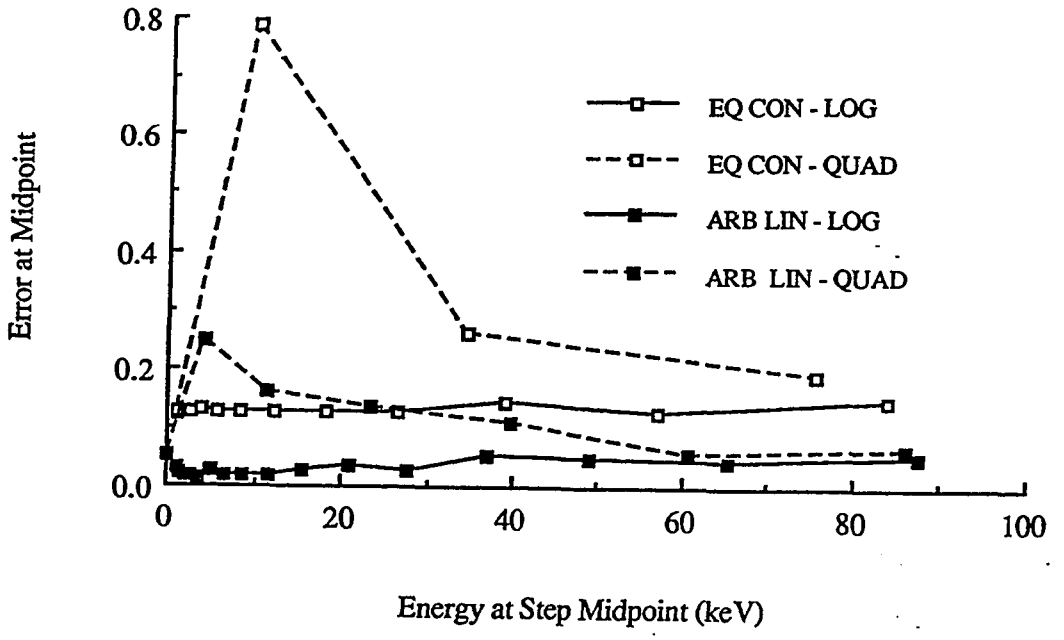

Figure 5.30: Discretization Error at Midpoint versus Energy, Rutherford Cross Section, Slowing in Gold from 100 to 1 keV.

energies. The trade-off between logarithmic and quadratic spacing schemes is thus assured accuracy at lower energies for a factor of two savings in the data set size. In light of this, the energy chopping algorithm has been modified so that if the number of energy basepoints in less than 20 for the quadratic case, logarithmic spacing will be substituted. If the number is greater than twenty and bin minimization is required, quadratic spacing will be used and the somewhat larger than input errors will be tolerated at the low energies.

To illustrate the dramatic effect that the spacing, sampling and inter-energy interpolation scheme can have on the total storage requirement, the total number of bins (summed over all energies) required for similar error tolerances are presented in table 5.12 for several different combinations of sample scheme, energy interpolation technique and base point spacing algorithm.

In interpreting all of the above results is is important to note that the arbitrarily

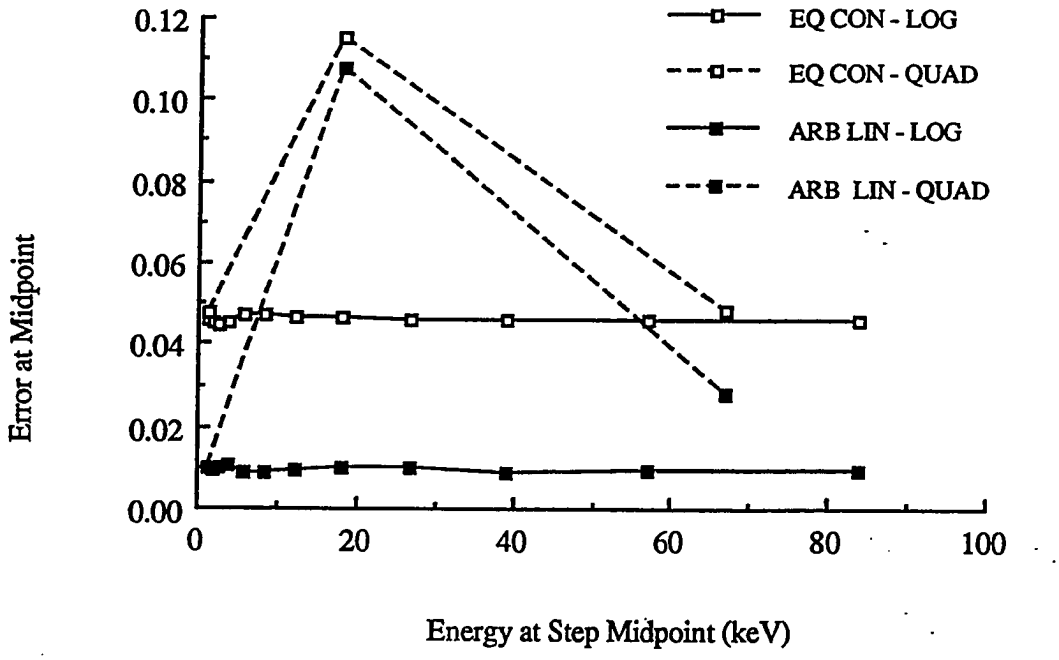

Figure 5.31: Discretization Error at Midpoint versus Energy, Compton Cross Section, Slowing in Gold from 100 to 1 keV.

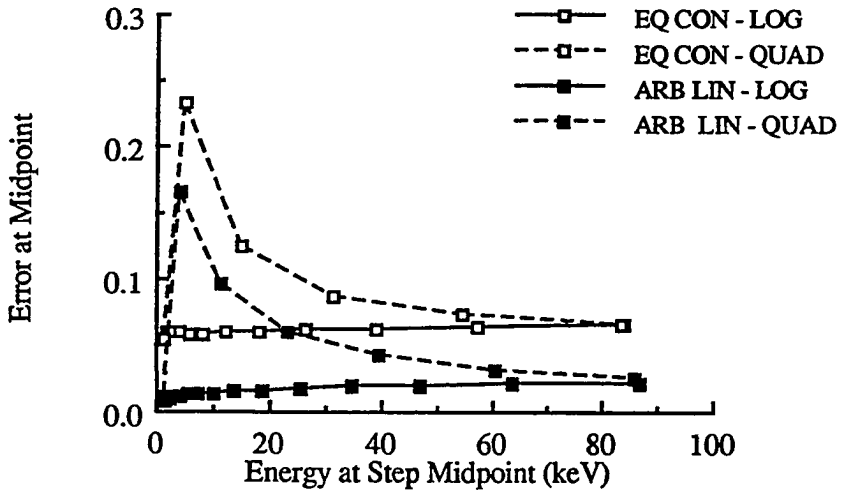

Figure 5.32: Discretization Error at Midpoint versus Energy, Riley Cross Section, Slowing in Gold from 100 to 1 keV.

Scheme	Rutherford			Compton			Riley		
	ϵ_{Base}	ϵ_{Inter}	Bins	ϵ_{Base}	ϵ_{Inter}	Bins	ϵ_{Base}	ϵ_{Inter}	Bins
Equally Probable Bin Schemes:									
Con Near Quad	6.555	7.886	5201	2.501	3.001	3184	13.685	16.638	4665
Con Near Log	6.555	7.886	10016	2.501	3.001	6567	13.685	16.638	8958
Con Int Quad	6.555	7.886	839	2.501	3.001	796	13.685	16.638	608
Con Int Log	6.555	7.886	1385	2.501	3.001	2587	13.685	16.638	1465
Lin Near Quad	0.496	1.931	8300	0.779	1.168	4815	1.528	4.202	5761
Lin Near Log	0.496	1.931	7062[1]	0.779	1.168	11025	1.528	4.202	6319[1]
Lin Int Quad	0.496	0.745	1348	0.779	1.168	932	1.528	2.773	1216
Lin Int Log	0.496	0.745	2522	0.779	1.168	2467	1.528	2.773	6319[1]
Arbitrarily Probable Bin Schemes:									
Con Near Quad	3.672	4.407	3925	3.194	3.833	249	3.936	5.904	9278
Con Near Log	3.672	4.407	4404[1]	3.194	3.833	503	3.936	5.904	8946[1]
Lin Near Quad	0.515	1.886	2231	0.499	0.749	532	0.551	4.177	3659
Lin Near Log	0.515	1.886	2016[1]	0.499	0.749	1207	0.551	4.177	3591[1]
Lin Int Quad	0.515	0.773	353	0.449	0.749	87	0.551	2.755	709
Lin Int Log	0.515	0.773	699	0.449	0.749	164	0.551	2.755	1566

[1] Did not meet 100 energy point limit

Table 5.12: Total Bins Needed to Meet Same Error Requirement

probable case is included in the inter-energy interpolation case only because it can be used to model distribution functions sampled by table searches. It can not be used in conjunction with alias sampling. Inter energy interpolation is seen to be so effective that the reduction in the number of energy basepoints lowers the total required number of bins for the equally probable case to the point where *fewer* words of storage are required than for alias sampling using the nearest energy point, for some of the distributions. What was initially seen as a trade-off of sacrificing 50% speed for space in going to arbitrarily probable bins has reversed itself. Alias sampling using the nearest energy point is 50% faster than using equally probable bins with interpolation, but in some instances requires more storage.

The 200 bin per basepoint and 100 basepoint limits should have allowed 20000 total bins, but because some distributions can be easily modeled (few bins) at base points, this limit was never reached. Therefore, if bin minimization is the goal, ENCHOP should allow a floating number of basepoints to be used given by the maximum number of bins allowed divided by the average number of bins per base point, rather than fixing the number of energy points.

The following conclusions are drawn regarding the data set size as a function of cross section type, sample scheme, interbin sampling scheme, inter energy sampling treatment, energy base point spacing scheme, base point error tolerance and energy midpoint error tolerance.

1. The number of energy base points required for a given discretization error is strongly effected by the distribution type.

2. Substantial savings in data can be made through the use of inter-energy interpolation, at a cost in computation time.

3. Outstanding savings can be attained by use of quadratic energy base point spacing, at the expense of decreased accuracy in several of the lowest energy bins.

4. Small errors both in the base point and midpoint densities are not obtainable for some sample schemes and some densities for a manageable (20,000 bin) data set size.

So far in this chapter, seven variables have been identified as having effect on data storage and computation time, as well as being possible sources of numerical error in transport calculations. The effects of the ladder spacing scheme, cross section type, sampling scheme, interbin sampling scheme, inter energy sampling scheme, base point error tolerance, and midpoint error tolerance on data set size and execution time within sampling loops themselves have been well quantified in this section. The overall effect on the speed and accuracy of transport calculations are presented in chapter 6.

5.2 Monte Carlo Electron Transport Simulation Algorithms

In chapter I the two main Monte Carlo electron transport algorithms, based on the single scattering and condensed history models, were described briefly. Here they are examined more fully and in the context of their relationship to the basic algorithm for simulating the transport of particles by the Monte Carlo method.

Although special considerations arise in the modeling of electron transport, the underlying scheme varies only slightly from the basic particle transport algorithm shown in figure 5.33. (The format for presenting algorithms throughout this section is borrowed from Brown [Br82].) The algorithm starts with data reading, geometry set up, and tally initialization before entering a double outer loop (the first over

the number of batches, and the second over the number of particles per batch) over the total desired number of input events. The main components of the loop over particles involve sampling from a source distribution to get the initial particle parameters such as energy, position, and direction of propagation, tracing the particle and its daughters by looping over a tracking algorithm until the particle is absorbed, escapes or is stopped, and tallying the results before moving on to the next input particle. The first part of the tracking loop involves determining the distances to the nearest cell boundary and to the next potential collision. It is then assumed that the particle collided if the distance to collision is smaller and crossed the boundary if that distance is smaller. If a crossed cell boundary is one which demarks different materials (and hence different cross sections), the particle material index must be updated for the next tracking pass. Particle parameters (position, direction, energy, etc.) are updated after each collision or boundary crossing, the appropriate tallies performed, and the status of secondary particles determined. When secondary particles are produced, their state parameters, along with those of the primary particle, are stored in ordered arrays called 'stacks.' Stacks are typically emptied by tracking the lowest energy particle in the stack first. This prevents rapid buildup and potential overflow of the stacks, since low energy particles can produce only lower energy secondaries and thus will produce fewer progeny than higher energy particles. However, for particles in the energy range of interest here, this is usually not a concern as the probability of producing secondary particles is small. Particles are removed from the stacks when they are absorbed, slow to energies below a preset cutoff energy or escape from the volume. When the stacks are empty, the next source particle parameters are retrieved. The problem is finished when the stacks have emptied subsequent to the final initiating source event, and final tallying and output have been produced.

- read collision data
- read and prepare geometry
- initialize batch tallies
- loop over desired number of batches
    - ∇ initialize current tallies
    - ∇ loop over desired number of source particles
        - ⋆ load new source particle parameters onto top of stacks
        - ⋆ process a single track
            - ◇ determine distance to nearest boundary
            - ◇ determine distance to collision
            - ◇ determine if crossing or collision
            - ◇ update position
            - ◇ if collision:
                - ♯ determine collision type
                - ♯ sample collision parameters
                - ♯ absorbed or slowed below cutoff?
                    - o no - update parameters
                    - o yes - delete from stacks
                - ♯ add any secondaries to stacks
                - ♯ tally
            - ◇ if cell boundary crossing:
                - ♯ escaped active volume?
                    - o no - update parameters
                    - o yes - delete from stack
                - ♯ tally
            - ◇ load parameters of current particle (if any) onto top of stacks
            - ◇ return to get next track (if any particles)
        - ⋆ return to get next source particle
    - ∇ tally batch results
    - ∇ return to get next batch
- do final tallies
- output
- stop

Figure 5.33: Generalized Monte Carlo Tracking Algorithm

Class I: Condensed history technique with no single scattering

- **A.** Base energy loss and angular deflection distributions on preset tracklength values (this allows energy straggling and transverse displacement)
- **B.** Base tracklength and angular deflection distributions on preset energy loss values (this allows tracklength straggling and transverse displacement)

Class II: Condensed history technique with single scattering for large energy loss events and reduced loss distributions.

Figure 5.34: Berger's Classification of Electron Transport Algorithms

Obviously, many details have been omitted from this schematic. In particular, no mention has been made of variance and run time reduction techniques which are commonly used but which do not significantly alter the algorithm.

Berger [Be63] presented the earliest attempt to systematically classify electron transport algorithms during his original work on the condensed history algorithm. Two main classifications were given, with sub-classes for the first group, as given in figure 5.34 but with the current terminology applied..

To these two classifications, which can be combined in the single category of condensed history algorithms, two types of single scattering classes must be added. The first involves situations in which inelastic scattering events are treated as discrete collisions with finite total cross section, even though the energy loss function and mean free path may be determined empirically. The second new class includes the scheme in which inelastic collisions are treated as continuously occurring events between elastic and 'special interest' inelastic collisions. The three schemes are now listed in figure 5.35 in order of decreasing adherence to the true analog simulation algorithm.

The top level portions of the transport simulation algorithm of figure 5.33 (input,

Class I: Single scattering elastic and inelastic collision technique

Class II: Stochastically determined step size using total elastic plus partial inelastic scattering cross sections, with continuous energy loss between collisions

Class III: Condensed history technique, with or without single scattering for large energy loss events and reduced loss distributions.

Figure 5.35: Current Classification of Electron Transport Algorithms

output, batching and sourcing) are applicable to all three classes. The inner loop over individual tracklengths (demarked by $\Diamond$'s) is dependent on the class of algorithm, and is directly applicable to class I schemes only. It should be noted that the Monte Carlo simulation of photon transport is almost performed using a class I scheme. The other classes are only to charged particle transport simulations.

The algorithm for class II schemes differs from the pure single scattering method of class I schemes in several respects. First, as the particle is assumed to be losing energy continuously while in 'free' flight, it loses energy in traveling to boundary crossing events, and therefore its state parameters must be updated even when there is no collision. The deflection due to the inelastic collisions which take place between elastic events must be neglected, but it is usually small and should not effect the results dramatically. More importantly, as the total scattering cross section is energy dependent, it is not constant over the simulated flight distance. If this variation is ignored, the average distance to a collision, given by

$$\bar{x} = \int_0^\infty dx\, e^{-\Sigma(x)x}\, \Sigma(x)\, x \tag{5.24}$$

will be over-estimated somewhat, since Σ increases with x at low energies. The magnitude of this deviation is investigated here. When the energy dependence of $\Sigma(x)$ is ignored, the (over-estimated) average distance to a collision is given by $1/\Sigma(x_0)$,

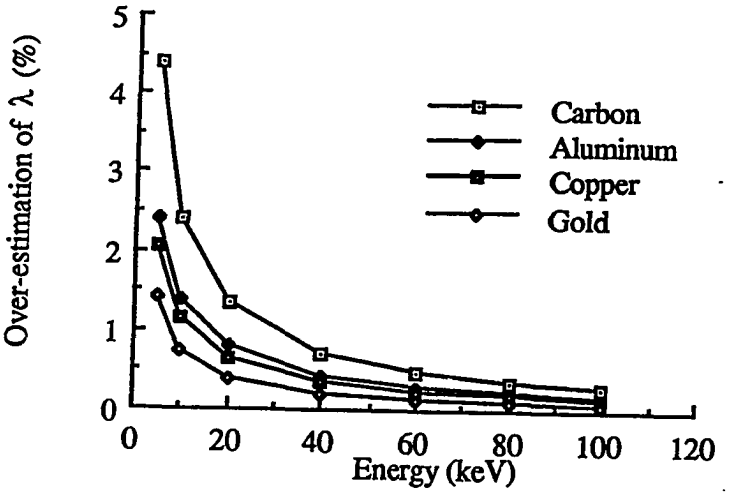

Figure 5.36: Effect of Ignoring Energy Dependency on Elastic Scattering Mean Free Paths

if $\Sigma(x_0)$ is the cross section at the starting point. The actual values of $\bar{x}$ can be determined by numerical integration of equation 5.24, after the appropriate transformation to energy variables, as the distance dependence of Σ is in fact due to an energy dependence which is pathlength determined. The results of this calculation are shown in figure 5.36 for several elements at various initial energies. The figure shows that the discrepancy is greatest ($\sim$ 4 %) at low Z and low energy, and rapidly becomes negligible with increasing energy and atomic number. At high energy this diminution in the error results from the small relative energy loss after travel through a large number of mean free paths, and the accompanying small absolute change in the cross section. At lower energy, the stopping power is larger so that travel through the same number of mean free paths yields a large relative energy loss, which, when coupled with the higher variation in the cross section with energy in this region, produces the slight over-estimation of the average collision distance. At high atomic

numbers, the cross section is so great that travel through a large number of mean free paths is a very small distance and the energy loss is small, as the stopping power does not increase as rapidly with Z as the cross section (roughly a Z vs. Z^2 dependence). Hence the cross section does not change with distance as rapidly and the over-estimation of the mean free path is smaller than at low atomic numbers. It can be concluded that the effect of ignoring the energy variation of the elastic cross section in model II electron transport algorithms may be of significance only for low initial energies and low Z materials.

The energy dependence of the cross section can be taken into account by using a method employing 'fictitious' cross sections. In this scheme, an energy-dependent cross section $\Sigma_{fict}(x)$ is constructed such that $\Sigma'(x)$, defined by

$$\Sigma'(x) = \Sigma_{real}(x) + \Sigma_{fict}(x), \tag{5.25}$$

is constant over the range of the particle, with value Σ'. The distance to a collision is sampled in the standard way by $s = -\ln(\xi)/\Sigma'$. and the type of collision, real or fictitious, is then determined based on the ratio of $\Sigma_{real}(x)$ and $\Sigma_{fict}(x)$ at s. If a fictitious collision is determined to have occurred, the particle is simply transported the predicted distance and returned to the stack for the next pass, with no other action. Real collisions are processed normally.

In order for this method to give exact results, the value of the constant Σ' must be determined by the maximum in the cross section over the applicable range of energy. The number of fictitious collisions encountered will have some bearing on the run time since actual transport steps will be taken for particles seeing false collisions, and a new distance to a real collision determined in the next step. The fraction of

real encounters, f_{real}, is given by

$$f_{real} = \int_0^\infty dx\, \Sigma' e^{-\Sigma' x} \frac{\Sigma_{real}(x)}{\Sigma'}. \tag{5.26}$$

For the trivial case of constant cross sections, $\Sigma' = \Sigma_{real}$ and f_{real} will be equal to one, as no particles undergo fictitious collisions. For the case in which the cross section decreases as the energy decreases (and hence with distance, since the particles lose energy with distance), the real collision fraction will be high since the ratio of Σ_{real}/Σ' is large at the short distances most likely to be sampled. In the case of cross sections which increase with energy loss, the real collision fraction will be low since Σ_{real}/Σ' will be small at the distances most likely to be tested.

A formal theory of this technique has been developed by Carter, *et al.* [Ca72]. In that work, fictitious collision are rejected and real collision determined at a distance greater than that of the fictitious one. Additionally, in an effort to increase the sampling efficiency for the case of increasing cross sections by setting what is equivalent to the constant value of Σ' to a small number, Carter's scheme sometimes involves assigning negative weights to particles. A negatively weighted collision increases the variance in the result, but if Σ' is chosen correctly the time gained by more efficient sampling will offset the time lost in forcing extra real collisions in order to make up for the increased variance. Rather than employing fictitious cross sections, Carter's method involves introducing a modifying function $C(x)$ which is defined so that the cross section is constant as in $\Sigma(x)C(x) = \Sigma'$. Fictitious collisions are not treated as events, but rather new distances are immediately sampled (at a greater distance) based on the ratios of $\Sigma', C(x)$ and $\Sigma(x)$. This method reduces to the simple technique described when there are no negative collisions and when fictitious collisions are accepted as simple translation events rather than rejected. Assuring that no negative collisions occur requires that $C(x) \geq 1$ everywhere, in other words

setting Σ' equal to the maximum value of the cross section and then of course using $C(x) = \Sigma'/\Sigma(x)$. The number of rejections increases with the value of $C(x)$ at the initial point, $C(x_0)$. For the case of decreasing cross sections we have $C(x_0) = 1$, and the number of rejections is small. In the case of electron elastic scattering (for which the cross section increases with distance), since there is a small but finite probability that an electron would slow to the problem cutoff energy without undergoing any elastic scatters, the maximum cross section would be that at the cutoff energy, and so we would have $\Sigma' = \Sigma(x(E_{cut}))$ and $C(x_0) = \Sigma(x(E_{cut}))/\Sigma(x_0)$. This may make $C(x_0)$ on the order of several powers of ten (even at low initial energies), producing unacceptably low sampling efficiencies.

A simple scheme is presented which retains exactness, insures a high fraction of real collisions and avoids the computational complexities introduced by negative weighting. The scheme proposed here forces good sampling efficiency by defining a maximum distance ζ to which particles may be transported during the current step. The best value of Σ' is obviously $\Sigma(\zeta)$, which amounts in Carter's method to defining, $C(x_0)$ as $\Sigma(\zeta)/\Sigma(x_0)$. If ζ is not too large, $C(x_0)$ is close to 1 and the real collision fraction will be high. There is a trade off however in that any collision which would have occurred at a distance greater than ζ is ignored until the next pass, and so extra transport steps are required.

A prescription for choosing ζ is described here. The fraction of all possible events which are modeled as real collisions is determined by

$$f_{real} = \int_0^{\zeta} dx\, e^{-\Sigma(\zeta)x}\, \Sigma(x) \tag{5.27}$$

Here all particles predicted to travel beyond ζ instead are assumed to undergo fictitious collisions at ζ. The values of ζ should be chosen such that the average distance

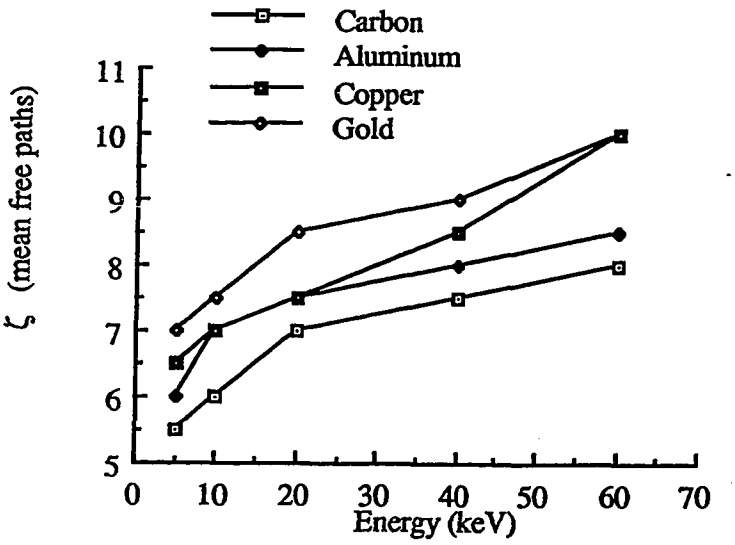

Figure 5.37: ζ (in mean free paths) vs. E for Several Materials

traveled by particles undergoing their first real collisions, given by

$$\overline{x_{real}} = \int_0^{\zeta} dx\, e^{-\Sigma(\zeta)x}\, \Sigma(x)\, x \tag{5.28}$$

is maximized. A maximum in $\overline{x_{real}(\zeta)}$ is expected because at small ζ the most likely event is transport to ζ without any collision, so $\overline{x_{real}(\zeta)}$ will be small, and at very large ζ, the number of fictitious encounters at small x will be great because of the large difference between $\Sigma(\zeta)$ and $\Sigma(x_0)$, and so again $\overline{x_{real}(\zeta)}$ will be small. Figure 5.37 shows predicted values of ζ (in terms of number of initial mean free paths) for several Z over a wide range of energies.

Particularly interesting inelastic collision processes, such as bremsstrahlung or inner shell ionization may be included along with elastic scattering as individual events, so long as their contribution to the total stopping power is removed from the calculation of $\frac{de}{dx}$, as described in the presentation of restricted stopping power in chapter III. Since this cross section decreases with decreasing energy, inclusion of

- ◇ determine distance to boundary
- ◇ determine distance to collision using Σ'
- ◇ determine if crossing or collision
- ◇ update position
- ◇ update energy from continuous loss
- ◇ if collision:
  - ♯ determine if real collision or not
  - ♯ if real collision:
    - o determine collision type
    - o sample collision parameters
    - o update energy
    - o slowed below cutoff ?
      - • no - update angle parameters
      - • yes - delete from stack
    - o add any secondaries to stack
    - o tally
- ◇ if cell boundary crossing:
  - ♯ escaped active volume?
    - o no - update cell number
    - o yes - delete from stack
  - ♯ tally
- ◇ load parameters of current particle (if any) onto top of stacks
- ◇ return to get next track (if any particles)

Figure 5.38: Tracking algorithm for Class II schemes

explicit inelastic events tends to lessen the over-estimation of the mean free path. The final tracking algorithm (inner loop) for Class II algorithms takes the form shown in figure 5.38.

Because the effect of ignoring the over-estimation of the mean free path is small except for low E and Z, and because in all important applications of alogithms of this class, especially interesting inelastic scattering events are included, thus lessening the over-estimation effect, the techinques described above have not been implemented.

Class III schemes, which most of the widely used Monte Carlo electron transport programs employ, use the condensed history algorithm discussed in Chapter I, but also allow distinct collisions to be treated independently. Again, the collisions of special interest are inelastic collisions resulting in energy transfer above a certain cutoff, and so restricted stopping power or distribution functions, as described in chapter III, must be used in determining energy loss. Three important new aspects of simulation technique arise in this class of calculation, the most significant being that a step may conclude not only with a collision or boundary crossing but also with movement through a preset distance, as defined by limits on the length of a track for which multiple scattering distributions are valid. Since energy loss and angular deflection are then sampled almost as if a collision had occurred (but from cumulative rather than single scattering distributions), these events are referred to here as 'pseudo' collisions. The second added dimension arises in that an angular deflection must be determined at every transport step, at boundary crossings and prior to analysis of major inelastic events. Finally, pathlength straggling may be modeled for this class of algorithms.

There seems to be two conflicting methods of implementation of this scheme, the first found in ETRAN [Be63, Co74, Se89] and its descendants, and the second found in EGS [Fo78, Ne85] and GEANT [Br87]. In the first case, data for cumulative scattering distributions is tabulated into equally probable bins assuming that preset distance have been traversed, and then these discrete distributions are sampled. This introduces a problem with boundary crossing events as discussed below. Additionally, ETRAN does not model collision distances nor analyze the collisional effects on the incident particle in explicit and completely consistent manners. Secondary particle parameters are typically determined using rejection schemes, but

primary parameters only sometimes updated consistently [Se89]. EGS and GEANT, in contrast, always use rejection schemes to determine multiple scattering angles and to analyze collisions, and so always conserve momentum in inelastic events. The tradeoff is speed (ETRAN method) for accuracy (EGS and GEANT method). The implementation of this work is a hybrid of these two, employing the pre-calculated cumulative scattering distributions found in ETRAN and the explicit single scattering collision analysis (but with interpolative sampling of tabulated data rather than rejection sampling) found in EGS and GEANT.

As mentioned above, boundary crossings (and discrete collisions) present problems for this method because the multiple scattering and energy loss fluctuation distributions must be pre-calculated using preset tracklengths and are not valid for the shorter than anticipated distances traversed prior to these events. In determining the energy loss, the stopping power, with simple numerical integration, can be used in place of energy loss fluctuations, as in class II schemes. For the angular deflection, two simple methods may be employed, the first involving ignoring the deflection altogether if the distance to the boundary is less than half of the preset tracklength for multiple scattering and using the full tracklength distribution otherwise; and the second involving a semi-direct inversion sampling from a Gaussian distribution [Ev83]. The implications of the use of these two approximations are examined in chapter VI.

Class III schemes are the first for which pathlength straggling may be a necessary procedure. The method for straggling adopted here is based on that presented by Berger [Be63]. Formulae valid for small values of the scattering angle θ given azimuthal scattering angle ϕ is given by

$$\Delta y = \frac{1}{2}\Delta s\left(\sin\theta\cos\phi + \xi_N\sqrt{2-2\cos\theta}\right) \qquad (5.29)$$

$$\Delta z = \frac{1}{2}\Delta s\left(\sin\theta\sin\phi + \eta_N\sqrt{2-2\overline{\cos\theta}}\right)$$
$$\Delta x = \Delta s\frac{1+\cos\theta}{2}$$

where Δs is the preset tracklength and ξ_N and η_N are taken from a normal distribution with mean zero and variance unity and $\overline{\cos\theta}$ is the average scattering angle over the current step. Straggling presents a problem in that if a particle is traveling near a boundary, it may be transported across the cell division by straggling. This may lead to deposition of energy in incorrect regions, if the majority of the track was determined to have taken place in the crossed into region. Several methods are routinely employed to account for this, but often it is ignored. An outstanding analysis of this effect is given by Bielajew and Rogers [Bi86].

Thus the class III algorithm for tracking electrons is described by figure 5.39.

5.3 Impact of Vector Supercomputer Facilities

The large number of collisions and the resultant lengthy computations involved in single scattering Monte Carlo electron transport simulations demand the use of fast computers in order to achieve tolerable variances in the results in reasonable real time. An obvious candidate machine for such a problem is a vector supercomputer. In addition to the impressive speed inherent to such machines because of their fast clocks, it has been shown by Brown [Br82] and others that the Monte Carlo algorithm can be adapted to take advantage of vector processing facilities and further enhance the speed of calculations. For example, Martin, Nowak and Rathkopf [Ma86] have reported vectorization speedup factors of 4 to 5 for photon transport calculations, and more recently Miura [Mi87] has extended vectorization to electron transport, using the EGS4 code and reports a factor of 8 increase in computing speed. Thus vector supercomputing resources were sought and ultimately made available for this

* loop until stacks empty
  - ◇ determine distance to boundary
  - ◇ determine distance to collision
  - ◇ determine distance to pseudo collision
  - ◇ determine if collision, crossing or pseudo collision
  - ◇ update position
  - ◇ if real collision:
    - ♯ update energy
    - ♯ update direction
    - ♯ straggle position
    - ♯ check for boundary crossing due to straggling
    - ♯ determine collision type
    - ♯ sample collision parameters
    - ♯ slowed below cutoff ?
      - o no - update angle parameters
      - o yes - delete from stack
    - ♯ add any secondaries to stack
    - ♯ tally
  - ◇ if cell boundary crossing:
    - ♯ escaped active volume?
    - ♯ update energy
    - ♯ update direction
    - ♯ straggle position
    - ♯ check for boundary crossing due to straggling
      - o yes - get cell number, material (if new)
    - ♯ tally
  - ◇ if pseudo collision:
    - ♯ update energy
    - ♯ update direction
    - ♯ straggle position
    - ♯ check for boundary crossing due to straggling
    - ♯ tally
  - ◇ load parameters of current particle (if any) onto top of stacks
  - ◇ return to get next track (if any particles)

Figure 5.39: Tracking Algorithm for Class III schemes

project by the San Diego Supercomputer Center, which operated a Cray XMP/48 vector supercomputer until January 1990, and now runs a eight processor Cray YMP. Both machines were used over the course of this project.

Although the primary need for this resource arises because of the timing considerations involved in the class I and II schemes, since this resource was available, and since the techniques involved in implementing vectorized class III schemes parallel those inherent to the single scattering algorithms (particularly given the use of the discretization schemes discussed earlier in this chapter), all three schemes have been implemented in vectorized mode.

Taking advantage of the vector facility requires that several changes be made to the basic particle transport simulation algorithm, as discussed by Brown [Br82]. In addition, the choice of the vectorized sampling algorithm, which greatly influences the speed of the computation, also effects the fundamental vector transport algorithm. Thus before the the vectorized algorithm can be finalized, optimization of the sampling implementation must be performed. In order to explore the differences between various implementations, some basic vector computation concepts must be examined.

5.3.1 Introductory Vector Computation Concepts

A vector processor improves computing speed by performing the same operation on long streams of data in a pipeline procedure. Individual operations (such as addition or multiplication) are broken down at the hardware level into independent components which perform only a portion of the operation. Thus while component n of an procedure which has been broken into N components is operating on data article i, component $n-m$ will be processing datum $i+m$. Obviously there is an initial

startup overhead, after which results emerge produced from the end of the pipeline at every single clock cycle. As the length of data stream approaches infinity, the startup overhead becomes negligible and the time to process M data articles decreases from $N \cdot M$ to M clock cycles. Since vector machines typically break operations into more components than scalar machines, an opposite, slowdown effect is evidenced as the data stream approaches length 1. Clearly there is a break even point in the data stream length below which the vectorization is inefficient and above which speedup occurs. On the Cray XMP/48 this number is roughly 6 to 10, depending on the operation.

Vector pipelines perform the same operation on a continuous stream of data. Because it is desired to perform an operation on a long stream and then branch to various other operations pending the outcome of the first procedure, it is necessary to have some facility for breaking a single stream into component streams for further processing, and for merging the partial streams which have been manipulated by different procedures. The splitting process is commonly called a 'gather' operation, in which elements are collected from a longer stream into a shorter one according to an index list which defines which elements to take. The complimentary merging operation, called a 'scatter', selectively places elements of the short stream into specific slots in the long array, again according to an index list. Gather and scatter may be coded as distinct steps or inferred by indirect addressing, in which pipeline operations are performed only on specific elements of a stream in the pipeline as specified by an index list. As an example of the two techniques, consider a vector `V` of length `N` and an index list `IND` of length `M` containing the indices of those `M` elements of `V` on which the next operation is to be performed, for instance, updating the energy (stored in `V`) of only those particles which underwent collisions (indexed by `IND`). For

the explicit method, we would require first that all of the elements on which the operation is to be performed be collected (into array W, let's say), the calculation be done on the elements of W, and the answers re-inserted into their proper positions in the original V array. This requires the following fortran coding:

```
CALL GATHER(V,W,N,IND,M)
```

Now do the calculation to get the elements in W

```
CALL SCATTER(W,V,N,IND,M)
```

For the case of indirect addressing with implicit gather and scatter, we have simply

```
    DO 10 I=1,M
10    V(IND(I)) = required operation
```

The use of standardized discrete sampling schemes has introduced one level of generality to the SKEPTIC package in that the sampling schemes are independent of the exact formulation of the distributions being used. Complete use of indirect indexing, in addition to maximizing vector lengths, would introduce another layer of generality in that the fundamental algorithm for each class of techniques would be independent of the particular transport model, where the term 'transport model' is taken to mean the number of cross sections, the characteristics of the individual cross sections (whether they produce secondary particles, cause energy loss, angular deflection etc.) and so on. For the gather/scatter implementation, the particular sampling scheme would be implemented in a subroutine which would perform the actual sampling operation. For the indirect indexing scheme, all distributions sampled using the same scheme would be flagged, and after the type of events determined the particles would be indexed according to the form of the sampling scheme and all

particles undergoing events whose results are determined similarly sampled in the same vector loop using indirect indexing to hit the appropriate distribution functions. Instead of requiring a unique set of subroutines designed specifically to sample for a given parameter using a set technique for each model, the general code would contain internally a set of the allowed sampling loops and would require a set of input flags characterizing each cross section or distribution function in order to fully describe the model.

It is clear that the use of complete indirect indexing is desirable from the stand points of code generality and the ease of implementation of a variety of models, critical concerns for this work. It is not clear whether this will slow the calculation down or speed it up. Features tending toward speed up are the increased vector lengths gained in collecting particles to be similarly sampled and the reduced number of software gather, scatter and index list compress calls. Potential slow down arguments are that the total number of the gathers and scatters, although implemented in hardware through indirect indexing, is actually larger, and that the required deep nesting of indices may slow the vector loop. Further, speed up or slow down may be model dependent, influenced by the number of cross sections, the number of different types of sampling schemes, even the shape of the sampled functions (it has been suggested that sharply peaked densities, which produce many hits on the same element of an array, slow down sampling with indirect indexing on some processors.) Clearly the speed advantage gained (if any) in complete indirect indexing would be minimized when a large number of cross sections each with a unique sampling scheme comprised the model. However, given the advantages of generality and the uncertain nature of the effect on computation speed, it was decided that the indirect indexing technique would be used unless it caused unreasonable slow down as determined in some simple

tests.

Because the use of either scheme greatly effects the overall implementation, timing tests must be done not on single loops but on a sizable portion of the algorithm. For the sample tests conducted here, processing begins at that point for which a stack of particles with known energy and energy ladder index are to be tested to determine which collide and which cross boundaries. The colliding particles are to be assigned one of the allowed scattering types and then processed, with the updated energy of all of the particles determined as the desired final result. A representative scattering model consisting of 4 possible collision types was chosen, and a class I (single scattering) scheme implemented. The gather/scatter based algorithm for this problem is given in figure 5.40. The implementation using full indirect indexing is shown in figure 5.41. Note that one level of indirect indexing must be used in the gather/scatter case, as in determining the energy loss it is necessary to use the distribution corresponding to the initial energy. In theory this could be eliminated by gathering according to initial energy before sampling, but in practice this would make it extremely difficult to keep track of the distributions. One effect of the implementation of these schemes on the structure of the code is that it defines the data and I/O structure. The data structure necessary to support the first scheme is listed in table 5.13, and that required in the indirect indexing case given in table 5.14.

Note that even though more stack variables are required for the gather/scatter algorithm, the same number of data bank distribution variables (which take up the majority of the memory) are required for both algorithms.

Two initial energy distributions were tested, the first assuming all particles to have the same energy (50 kilovolts) and the second using a randomly determined

- loop over all particles in stack
  - ⋆ determine energy ladder index
  - ⋆ determine total cross section
  - ⋆ determine distance to collision
  - ⋆ determine distance to boundary
  - ⋆ create index list of which particles collide
  - ⋆ update position of all particles
- gather indices of particles which have collided
- loop over all colliding particles
  - ⋆ determine which type of collision has occurred
  - ⋆ index collision type identifier
- loop over the collision types
  - ⋆ create sub-list of colliders undergoing current collision
  - ⋆ gather index list of particles undergoing collision of current type
  - ⋆ gather energies of particles undergoing collision of current type
  - ⋆ gather energy ladder indices of particles undergoing collision of current type
  - ⋆ call subroutine to get results of collision of current type
    - ◇ loop over all particles undergoing collision of current type
      - o load energy ladder index
      - o determine index of energy loss
      - o determine energy loss
      - o determine new energy
      - o determine index of deflection
      - o determine deflection
      - o determine new direction
  - ⋆ scatter updated energy for particles undergoing collision of current type
  - ⋆ scatter updated directions for particles undergoing collision of current type

Figure 5.40: Gather/Scatter Sampling Algorithm

- loop over all particles in stack
  - ⋆ determine energy ladder index
  - ⋆ determine total cross section
  - ⋆ determine distance to collision
  - ⋆ determine distance to boundary
  - ⋆ create index list of which particles collide
  - ⋆ update positions of all particles
- loop over all colliding particles
  - ⋆ determine which type of collision has occurred
  - ⋆ index collision type identifier
  - ⋆ index energy sampling scheme identifier
  - ⋆ index deflection sampling scheme identifier
- loop over deflection and energy
  - ⋆ loop over all possible sampling schemes
    - ○ create index list of particles using current sampling scheme
    - ○ create index list of collision type identifiers
    - ○ loop over all particles using current sample scheme
      - ◇ load particle index
      - ◇ load collision type index
      - ◇ load energy ladder index
      - ◇ get distribution index from collision type index
      - ◇ determine index of energy loss/deflection
      - ◇ determine energy loss/deflection
      - ◇ determine new energy/direction

Figure 5.41: Indirect Indexing Sampling Algorithm

Main Particle Stack:	
N	Number of particles in the stack
NELAD	Number of energy ladder points
E(1:N)	Energy of particles 1 - N
IELAD(1:N)	Energy ladder index number of particles 1 - N
Secondary Particle Stack:	
NCRASH	Number of particles which collide
ICRASH(1:NCRASH)	Index list of colliding particles
FCOLL(1:NCRASH)	Pointer to collision type
Tertiary Particle Stack:	
NSAMP	No. particles undergoing current collision type
ISAMP(1:NSAMP)	Index list of colliding particles
ESAMP(1:NSAMP)	Energy of colliding particles
IELADS(1:NSAMP)	Energy ladder index of colliding particles
Collision Data Bank:	
NEDISK(1:NELAD)	No. loss points at each energy for collision type k
EDISK(1:NELAD,1:NEDISK)	Energy loss values for collision type k
NADISK(1:NELAD)	No. deflection points, each energy, collision type k
ADISK(1:NELAD,1:NADISK)	Deflection values for collision type k
etc., one pair for each possible collision	

Table 5.13: Data Structure Necessary for Gather/Scatter Sampling Algorithm

Main Particle Stack:	
N	Number of particles in the stack
NELAD	Number of energy ladder points
E(1:N)	Energy of particles 1 - N
IELAD(1:N)	Energy ladder index number of particles 1 - N
Secondary Particle Stack:	
NCRASH	Number of particles which collide
ICRASH(1:NCRASH)	Index list of colliding particles
FCOLL(1:NCRASH)	Collision index of colliding particles
IATYPE(1:NCRASH)	Deflection sampling scheme index of colliders
IETYPE(1:NCRASH)	Energy loss sampling scheme index of colliders
Tertiary Particle Stack:	
NSAMP	Number of particles using current sample scheme
ISAMP(1:NSAMP)	Indices of particles using current sample scheme
Collision Data Bank:	
NCROSS	Number of collision types
FSCHME(1:NCROSS)	Energy loss sample scheme flag for collision type
FSCHMA(1:NCROSS)	Deflection sample scheme flag for collision type
FADIS(1:NCROSS)	Pointer to deflection distribution for collision types
FEDIS(1:NCROSS)	Pointer to energy loss distribution for collision types
NEDIS(1:NCROSS,1:NELAD)	No. loss points at each energy for each collision
EDIS(1:NCROSS,1:NELAD,1:NEDIS)	Energy loss values for each collision, each energy
NADIS(1:NCROSS,1:NELAD)	No. deflection points at each energy for each collision
ADIS(1:NCROSS,1:NELAD,1:NADIS)	Deflection values for each collision, each energy

Table 5.14: Data Structure Necessary for Indirect Indexing Sampling Algorithm

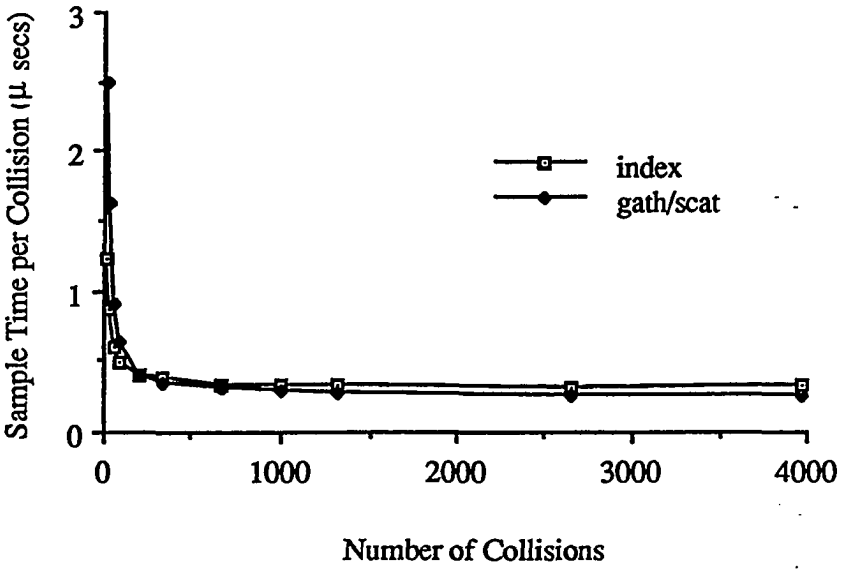

Figure 5.42: Run Time per Particle vs. Initial Number of Particles for Indirect Indexing and Gather/Scatter Sampling Schemes

uniform distribution over the range of 1 to 50 kilovolts with ladder steps in 1 kilovolt increments.

Each input energy distribution was tested for both the indirect indexing and gather/scatter models using a variety of different initial stack sizes. The results comparing average run time per particle as a function of number of initial particles are given in figure 5.42 for both input cases and both schemes, and average result sample time per collision versus number of collisions in figure 5.43. Since the random number generator was reset for each test case and because each technique uses the same method for determining the number and type of collisions, these results will be identical and the timing calculation will not be skewed by different numbers and types of collisions.

The figures clearly show that although sample time is increased by use of the heavily nested indirect addressing technique, the overhead saved in eliminating the

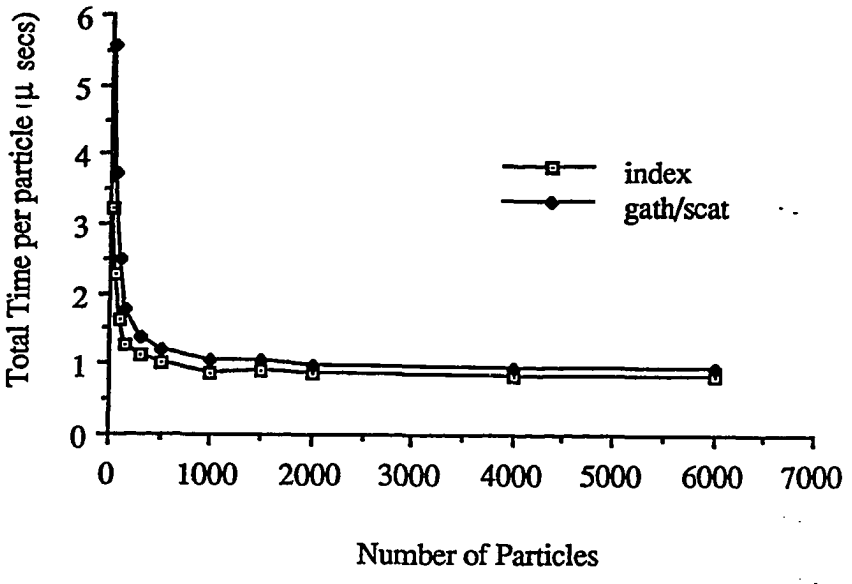

Figure 5.43: Sample Time per Collision vs. Number of Collisions for Indirect Indexing and Gather/Scatter Sampling Schemes

software gather and scatter operations required to circumvent the nesting yields a slight net enhancement of program performance. Thus, hardware gather by indirect addressing of particles undergoing similarly sampled collisions has been universally adopted in SKEPTIC.

All other vectorization schemes employed are standard optimized procedures culled from the suggestions contained in the documentation for the Cray XMP/48. These include the use of the Conditional Vector MerGe (CVMG) functions inside vectorized do loops instead of structured block ifs, use of the WHEN functions to produce index lists from conditions, and so on.

5.3.2 Vectorized Monte Carlo Transport Simulation Algorithm

A standard vectorized version (similar to the gather/scatter test algorithm of figure 5.40) of the basic particle transport simulation algorithm described in the

previous section is given in figure 5.44. The main difference due to vectorization arises in that as the operations are done on the entire particle stack at once, implicit loops over particles exist at each step inside the $\diamond$ and o loops and the main $\star$ loop over source particles is replaced by a loop over batches of particles.. In the scalar case, secondary particles are immediately added to the stacks and processed as soon as the primary is deleted. In the vector situation, secondaries are stored in banks and added only after a sufficient number of holes in the primary stack exist. Similarly, new source particles in the same batch (the number of particles per batch may be longer than the stack length) are added as positions open in the main stack. Re-sourcing, which encompasses the adding of secondaries, is done in SKEPTIC whenever 10% or more of the main stack is free, or, if all source particles have been added, if the number of queued secondaries is more than half the number of active particles. Another difference between the vector and scalar algorithms is that gather operations are required once the event type (collision or boundary crossing) is determined and when the specific type of collision is determined. Branching to different routines to do the collision sampling is then implemented. The operations denoted as occurring inside vector loops may often be done inside the same loop as consequent procedures. Note that as with the scalar algorithm, particle type distinctions need be made only when determining the total cross section and in assigning the proper collision type.

As shown previously, the general discretization schemes used in SKEPTIC alter the tracking loop by gathering particles according to the sampling scheme used to determine the collision parameters rather than by collision type. Additionally, the gathers and scatters are done by indirect indexing, rather than explicit software operations. Thus the general inner tracking algorithm (inside the $\diamond$ loops) of SKEPTIC is quite different that of the general vector tracking algorithm as seen in figure 5.45.

- vector loop - initialize tallies
- read collision data
- read and prepare geometry data
- loop over desired number of batches
  - ∇ initialize current tallies
  - ∇ loop over desired number of source particles
    - ⋆ vector loop - load secondary particles parameters if any
    - ⋆ vector loop - load batch source particle parameters if any
    - ⋆ loop over tracks until re-source condition met
      - ◇ vector loop - determine distances to boundaries
      - ◇ vector loop - determine distances to collisions
      - ◇ vector loop - chose boundary crossings or collisions
      - ◇ vector loop - update positions
      - ◇ gather colliding particle parameters
        - ♯ vector loop - determine collision types
        - ♯ gather by collision type
        - ♯ branch to appropriate collision routines
          - o vector loop - sample collision parameters
          - o vector loop - update parameters
          - o vector loop - remove escaped, absorbed, stopped particles
          - o vector loop - get secondaries and parameters
          - o tally
      - ◇ scatter all collision stack parameters into main stack
      - ◇ tally
      - ◇ return to get next tracks
    - ⋆ return to add more source/secondary particles
  - ∇ tally batch results
  - ∇ return to get next batch
- do final tallies
- output
- stop

Figure 5.44: Generalized Vectorized Monte Carlo Tracking Algorithm

- ⋆ loop over tracks until re-source condition met
  - ◇ vector loop - determine distances to boundaries
  - ◇ vector loop - determine distances to collisions
  - ◇ vector loop - chose boundary crossings or collisions
  - ◇ vector loop - update positions
  - ◇ vector loop - index colliding particles
  - ◇ loop over colliding particles
    - ♯ vector loop - determine collision types
    - ♯ vector loop - index by collision type
    - ♯ vector loop - index by deflection sampling scheme
    - ♯ vector loop - index by energy loss sampling scheme
    - ♯ vector loop - index by secondary production scheme
  - ◇ loop over each energy loss sampling scheme
    - ♯ vector loop - get distribution index if needed
    - ♯ vector loop - sample fractional energy loss
  - ◇ loop over each deflection sampling scheme
    - ♯ vector loop - get distribution index if needed
    - ♯ vector loop - sample deflection
  - ◇ loop over each secondary production scheme
    - ♯ vector loop - get secondary particles
    - ♯ vector loop - index secondaries by energy scheme
    - ♯ vector loop - index secondaries by deflection scheme
  - ◇ loop over each secondary energy scheme
    - ♯ vector loop - get secondary particle energies
    - ♯ vector loop - remove particles created below cutoff
    - ♯ index viable secondaries
  - ◇ loop over each secondary angle scheme
    - ♯ vector loop - get secondary particle angles
  - ◇ vector loop - rotate secondary direction to reference system
  - ◇ vector loop - update primary particle parameters
  - ◇ vector loop - remove escaped, absorbed, stopped particles
  - ◇ tally
- ⋆ return for next set of tracks

Figure 5.45: Generalized SKEPTIC Tracking Algorithm (Class I schemes)

The vectorized tracking schemes for each of the three classes of Monte Carlo electron transport simulation algorithms are now very similar to the general SKEPTIC algorithm, and in fact the scheme for class I models is identical to the general algorithm. In that no change is made in the part of the algorithm which models secondary particle production, the representations of class II and III schemes, shown in figures 5.46 through 5.47, include only the primary particle model. As with the scalar class II and III schemes, the particle type distinction becomes explicit in these classes.

5.4 Current Code Features

This section details the major features of SKEPTIC. The program's capabilities are described, the data structure is detailed, the implemented variance reduction techniques are listed, and a summary is given of the pre-processing model building code.

5.4.1 Capablitities

SKEPTIC is designed to allow the solution of roughly 20 different classes of problems using several different source options. The problem to be solved is specified by the user and typically effects only the tallying and output portions of the programs. Source and problem output options are described below.

Source Options

The types of sources which can be modeled are summarized in table 5.15. Either photon or electron sources can be specified, and provisions exist to model both simultaneously. The user is able to specify an angle of incidence for oblique beam

- ⋆ loop until re-source condition met
  - ◇ vector loop - determine distances to boundaries
  - ◇ vector loop - determine distances to collisions
  - ◇ vector loop - chose boundary crossings or collisions
  - ◇ vector loop - update positions
  - ◇ index electrons
  - ◇ loop over all electrons
    - ♯ vector loop - update energy from continuous loss
  - ◇ vector loop - index colliding particles
  - ◇ loop over colliding particles
    - ♯ vector loop - determine collision types
    - ♯ vector loop - index by collision type
    - ♯ vector loop - index by deflection sampling scheme
    - ♯ vector loop - index by energy loss sampling scheme
    - ♯ vector loop - index by secondary production scheme
  - ◇ loop over each energy loss sampling scheme
    - ♯ vector loop - get distribution index if needed
    - ♯ vector loop - sample fractional energy loss
  - ◇ loop over each deflection sampling scheme
    - ♯ vector loop - get distribution index if needed
    - ♯ vector loop - sample deflection
  - ◇ process secondaries, as before
  - ◇ loop - tally
- ⋆ return for next set of tracks

Figure 5.46: SKEPTIC Vectorized Tracking Algorithm for Class II schemes

Pencil beam, normal incidence, monoenergetic
Pencil beam, normal incidence, distributed energy
Pencil beam, oblique incidence, monoenergetic
Pencil beam, oblique incidence, distributed energy
Point source, isotropic, monoenergetic
Point source, isotropic, distributed energy
Distributed source, isotropic, monoenergetic
Distributed source, isotropic, distributed energy

Table 5.15: Source Options

* loop until re-source condition met
  - ◇ vector loop - determine distances to boundaries
  - ◇ vector loop - determine distances to collisions
  - ◇ vector loop - chose boundary crossings or collisions
  - ◇ vector loop - update positions
  - ◇ index electrons
  - ◇ loop over all electrons
    - ♯ vector loop - determine maximum distances
    - ♯ vector loop - choose real collision/crossing or multiple scatter limit
    - ♯ index colliding/crossing electrons
    - ♯ loop over all colliding/crossing electrons
      - o vector loop - update energy from continuous loss
      - o vector loop - update deflection from skewed distribution
    - ♯ index multiple scatter electrons
    - ♯ loop over all multiple scatter electrons
      - o vector loop - update energy from continuous loss or distribution
      - o vector loop - update deflection from multiple scatter distribution
      - o vector loop - straggle paths
      - o vector loop - check for boundary crossing
  - ◇ vector loop - index colliding particles
  - ◇ loop over all colliding particles
    - ♯ vector loop - determine collision types
    - ♯ vector loop - index by collision type
    - ♯ vector loop - index by deflection sampling scheme
    - ♯ vector loop - index by energy loss sampling scheme
    - ♯ vector loop - index by secondary production scheme
  - ◇ loop over each energy loss sampling scheme
    - ♯ vector loop - get distribution index if needed
    - ♯ vector loop - sample fractional energy loss
  - ◇ loop over each deflection sampling scheme
    - ♯ vector loop - get distribution index if needed
    - ♯ vector loop - sample deflection
  - ◇ process secondaries, as before
  - ◇ loop - tally
* return for next set of tracks

Figure 5.47: SKEPTIC Vectorized Tracking Algorithm for Class III schemes

Determine spatial distribution of energy deposition
Determine transmission fraction from an electron source
Determine energy distribution of transmitted electrons
Determine angular distribution of transmitted electrons
Determine energy and angular distribution of transmitted electrons
Determine the backscattering fraction for an electron source
Determine energy distribution of backscattered electrons
Determine angular distribution of backscattered electrons
Determine energy and angular distribution of backscattered electrons
Determine transmission fraction from a photon source
Determine energy distribution of transmitted photons
Determine angular distribution of transmitted photons
Determine energy and angular distribution of transmitted photons
Determine the backscattering fraction for a photon source
Determine energy distribution of backscattered photons
Determine angular distribution of backscattered photons
Determine energy and angular distribution of backscattered photons

Table 5.16: Problem Options

sources, the energy of monoenergetic source and the distribution in energy of non-monoenergetic sources. Distributed sources are assumed to be uniformly spread throughout the entire problem volume.

Problem Options

Problems which can be solved are listed in table 5.16. Any number of problems can be specified for a single run. When energy distribution functions are desired, the user must input the major angle of the cone in which the particles are to be collected. In all cases, the tally bins are regularly spaced, and the user may input only the total number of bins.

The number and energy of source particles
The number and energy of secondary particles produced
The number and relative frequency of the different collisions
The number of boundary crossings

Table 5.17: Physics Statistical Output

Physics Specifications

Some information about the physics modeling of all problems, listed in table 5.17, is automatically tallied and output by SKEPTIC.

5.4.2 Data Structure

The program data structure can be divided into four main components: geometry, collision data, particle stacks, and auxiliary stacks. Each of these is examined here, with note taken of the typical amount of memory required by each section. Much of the structure is derived as a direct result of either the Cray memory limitations or the indirect addressing technique used to maintain long vector lengths.

Geometry

The first category of data is that required to describe the geometry. Since the main function of SKEPTIC is the evaluation of models and algorithms, the geometry has been kept trivial, limited to boxes of the same size, although not necessarily cubes. Different regions and materials can be specified, but they must align within the basic structure. (Implementing a more sophisticated geometry algorithm would not be difficult, however, since SKEPTIC requires from a geometry package only the distance to the nearest boundary and the cell number on the other side.) If a

Subscript	Function
t	Particle type
i	Material index
j	Distribution index
k	Cross section index
l	Primary energy ladder index
m	Secondary ladder (energy or angle) index
n	Particle index

Table 5.18: Subscript Convention

total of NCELL cells is allowed, and for each cell only the material index, the region index, and the coordinates of the 6 planes delineating the cell must be known, then a total of just 8·NCELL words are used. Typical runs performed here used roughly $10 \times 10 \times 10$ arrays of cells, NCELL = 1000.

Collision Data

By far, the most complicated data structure in SKEPTIC is that which holds the collision and distribution data. The data is broken into several components, including total cross section data, two banks of cross section flags, distribution flags and distribution data, which are described below. A subscript convention described in table 5.18 is used throughout.

The total cross section data set includes the elements listed in table 5.19.

As described earlier, the alias probabilities contain the index of the cross section embedded in their values. If a particle undergoes a collision, a collision index between 1 and NSIG(t,m) is determined, and a final index is set by adding NSECTX(t,m). This way all cross section flags and pointers can be stored in one dimensional contiguous arrays, and need not be indexed by both particle type and material. The flags

XC(t,m)	The total cross section ladder spacing parameter
SIGT(t,m,1)	The total cross section
NSIG(t,m)	The number of cross sections
NSECTX(t,m)	The number of cross sections in previously assigned material
P(t,m,1,k)	Alias probabilities for the various collision types.

Table 5.19: Total Cross Section Data Structure

describing how the collision is to be analyzed are split into two categories, with one set describing how the primary particle is affected by the collision and one set pertaining to the secondaries. These flags and their available options, which encompass all possible ways in which particle interactions are modeled, are described in tables 5.20 and 5.21 below. It should be noted that the 'fictitious' collisions described in section 2 of this chapter are modeled simply by setting both the deflection and energy loss flags corresponding to the fictitious cross section to indicate no change.

The indices pointing from a cross section to its companion distribution and the flags describing the distribution functions are listed in table 5.22.

The actual data describing the distributions is stored as shown in table 5.23. Because distributions require differing numbers of energy points and bins, it would be a waste of allocatable space to dimension the data arrays NJ × NLMAX × NMMAX. Therefore, the data is stored in contiguous arrays with pointers indicating where the data for particular distributions at particular energies begin.

Additional storage is required to model doubly differential bremsstrahlung cross sections. A complete distribution function of scattering angles is required for each possible photon energy at each electron energy. In order to prevent machine storage overflow, an artificial limit of 10 primary electron energy ladders and 10 possible photon energies and 10 angle sets is imposed. Fortunately, the differential cross sec-

Flag		Function and Options
FANG(k)		Angular Deflection
	0 →	No change
	1 →	Table sample
	2 →	Table search with energy interpolation
	3 →	Discrt, equal prob, midpoint interp
	4 →	Discrt, equal prob, midpoint interp, w/energy interp
	5 →	Discrt, equal prob, constant interp
	6 →	Discrt, equal prob, constant interp, w/energy interp
	7 →	Discrt, equal prob, linear interp
	8 →	Discrt, equal prob, linear interp, w/energy interp
	9 →	Discrt, arb prob, midpoint interp
	10 →	Discrt, arb prob, constant interp
	11 →	Discrt, arb prob, linear interp
	12 →	Isotropic distribution
	13 →	Binary collision distribution
	14 →	Compton scattering, base energy on angle
FENER(k)		Energy Loss
	0 →	No change
	1 – 11 →	Look up table, same scheme as angular
	12 →	Lose all energy
	13 →	Lose fixed amount of energy

Table 5.20: Primary Cross Section Flags

Flag	Function and Options
FSEC(k)	Number of Secondaries
	0 → No secondaries
	1 → 1 electron given off
	2 → 1 photon given off
FSECA(k)	Secondary Scattering Angle
	1 → Same as parent initial direction
	2 → Same as parent final direction
	3 → Isotropic
	4 → Elastic kinematic
	5 → Sampled from doubly diff brems dist
	6 → Constant angle bremsstrahlung
FSECE(k)	Secondary Energy
	1 → $E_{sec} = \Delta E_{pri}$
	2 → $E_{sec} = \Delta E_{pri}$ - binding energy
	3 → E_{sec} sampled from diff brems dist
BINDE(k)	Binding energy
XRESID(k)	Extra M Shell Binding Energy, if any
FRELAX(k)	Excitation Flag
	0 → No excitation
	1 → Excitation
ISECR(k)	Index of Relaxation Scheme

Table 5.21: Secondary Cross Section Flags

IADIST(k)	Pointer to the angular distribution
IEDIST(k)	Pointer to the energy loss distribution
FDELAD(j)	Flag signalling linear or quadratic ladder spacing
ELADC(j,2)	Ladder spacing constants

Table 5.22: Distribution Function Pointers and Flags

NTABLE(j,1)	The number of points
XSTART(j,1)	The starting position of the end points
XTABLE(m)	The endpoints of the potential answer bins
PSTART(j,1)	The starting position of the PDF points
PTABLE(m)	The cumulative distribution of the bins
SSTART(j,1)	The starting position of the formatted 'slopes'
STABLE(m)	The specially formatted slopes of the distribution bins

Table 5.23: Distribution Function Data

tion and the shape functions for bremsstrahlung are smooth and well behaved, and generally fewer than 10 bins are required for 1% accuracy in modeling. In order to conform to the general SKEPTIC algorithm, a special storage scheme has been devised. Doubly differential bremsstrahlung cross sections have their energy sampling flag FENER set to indicate midpoint interpolation with arbitrarily spaced bins. The midpoint answers which are sampled are not the fractional energy losses, but pointers to positions in the bremsstrahlung data structure of the form jl+m /10, where jl points to a combination of the bremsstrahlung distribution number and the energy position, and m points to the sampled photon energy answer bin. In the secondary particle processing section of SKEPTIC, the actual value of the fractional energy loss is assigned and the photon angle is sampled from the appropriate distribution as indicated by jl and m. The data structure containing the doubly differential bremsstrahlung data is given in table 5.24. Since there will be only one bremsstrahlung cross section per material, with less than 20 or so primary energy endpoints, and since the number of secondary angles and energies is set to be less than 10, the total amount of data is held below about 2000 words per material.

The total amount of collision data involved in describing a problem is clearly going to be determined by the size of the distribution function data set. A problem

BENER(jl,m)	Fractional energy loss bin endpoints
BESLP(jl,m)	Formatted slopes for energy loss bins
NBA(jl,m)	Number of angle bins at given loss bin
BANGS(jl,m,m2)	Angle bin endpoints
BASLP(jl,m,m2)	Formatted slopes for the angle bins

Table 5.24: Doubly Differential Bremsstrahlung Function Data

involving NM materials with NC constituent elements and NK possible scattering mechanisms, each using a tabulated discrete distribution function to determine collision parameters for angular deflection as well as energy loss at NL energy steps could consume 2 · NM · NC · NK · NL discrete sets of probability, endpoint and formatted slope vectors. A typical problem with a high Z material uses about 20 distributions per constituent, requiring on average about 40 bins with roughly 30 ladder points to model accurately, for a total of 24 kilowords per constituent per material, plus 2 kilowords per material for the bremsstrahlung data.

Particle Stacks

Three sets of particle parameter stacks are employed: primary, secondary and split particle storage arrays. The basic stack structure is given in table 5.25. The secondary stack and the split particle storage stack contain all of the same elements as the primary stack except the index vector, which is not required because these stacks are always contiguous, and the material index, which is not a fundamental parameter (it is uniquely determined from the cell number), but is included in the stack because of the frequent reference to it. Thus if NP is the length of the primary stack, NSP the size of the secondary particle stack and NSPLIT the length of the split particle storage bank, the number of words of stack variables is given by 12· NS

INDEX(n)	List of the currently occupied positions in the stack
ALIVE(n)	Flag describing the particle type
E(n)	Energy of the particle
IMAT(n)	Index of the material in which the particle is traveling
CELL(n)	Current cell number
DIR(n,3)	Array of the 3 direction cosines
POS(n,3)	Array of the 3 Cartesian coordinates
WEIGHT(n)	Particle weight (for variance reduction)

Table 5.25: Primary Stack Variables

+10·(NSP + NSPLIT). Typically, values for the stack lengths would be in the vicinity of 10,000 particles, and so a total of about 320 kilowords must be allocated to stack variables.

Auxiliary Particle Stacks

As the collision analysis proceeds, auxiliary quantities such as change of state variables, lists of particles undergoing certain types of processes and so on must be generated and sometimes stored. All the routines of SKEPTIC are supplied with a 12 element scratch bank, each vector being NP elements long for local particle processing. In addition, roughly 16 additional vectors must be maintained for global access. These include energy loss, collision index, parent particle index, lists of boundary crossing and colliding particles and so on. So roughly 28NP additional words of memory must be allocated.

The total data requirement then can be summarized as follows:

Structure	Words per Unit	Typical Total
Geometry	8 NCELL	80,000
Physics Data	24,000 (NM·NM)	100,000
Bremsstrahlung Data	10,000 NM	20,000
Main Stacks	32 NP	320,000
Auxiliary Stacks	28 NP	280,000

5.4.3 Variance and Run-Time Reduction Techniques

Variances in Tabulated Quantities

Monte Carlo programs determine quantities which must be thought of in terms of the average effect per input particle. If there are N input particles and t_i describes the contribution to event T of input particle i, then the Monte Carlo calculation of $\overline{T}$ is given by

$$\overline{T} = \frac{1}{N}\sum_{i=1}^{N} t_i \tag{5.30}$$

and the "variance" between the Monte Carlo estimate and the actual value of $\overline{T}$ is given by the well known formula

$$S^2(\overline{T}) = \frac{1}{N-1}\left[\left(\frac{1}{N}\sum_{i=1}^{N} t_i^2\right) - \left(\frac{1}{N}\sum_{i=1}^{N} t_i\right)^2\right]. \tag{5.31}$$

It is impractical to tally the contribution t_i of each particle to each of the output quantities being tabulated. For example, when a single particle gives rise to secondaries each of which deposit energy, the deposited secondary energy must be attributed to the primary particle. In vector computations, in addition to requiring additional storage space for a complete set of tallying stacks, the bookkeeping overhead in keeping track of which particle parented which secondary would be substantial. So instead of storing the t_i's, Monte Carlo programs can be run in batches, and the variance in batch average quantities used to determine statistical uncertainty. Thus if the quantity of interest $\overline{T}$ is the number of secondary electrons produced per

incoming particle, rather than keep track of the number of secondaries produced by each of the N particles, the variance can be calculated simply by dividing the N incoming particle into N_b batches of N/N_b particles each and determining the variance from

$$S^2(\overline{T}) = \frac{1}{N_b - 1}\left[\left(\frac{1}{N_b}\sum_{i=1}^{N_b}\overline{T_i}^2\right) - \left(\frac{1}{N_b}\sum_{i=1}^{N_b}\overline{T_i}\right)^2\right] \tag{5.32}$$

where $\overline{T_i}$ is the value of $\overline{T}$ for the i^{th} batch.

The most commonly determined types of quantities calculated in SKEPTIC are normalized distribution functions, such as the distribution in energy of transmitted electrons or the fraction of deposited energy deposited in a certain geometry node. In this instance, the quantity of interest $\overline{F_j}$ (the fraction of $\overline{T}$ taken by the j^{th} tally bin) is given by

$$\overline{F_j} = \frac{\overline{T_j}}{\overline{T_{tot}}}$$

and the variance given from

$$\frac{S^2(\overline{f_j})}{(\overline{f_j})^2} = \frac{S^2(\overline{T_j})}{(\overline{T_j})^2} + \frac{S^2(\overline{T_{tot}})}{(\overline{T_{tot}})^2} \tag{5.33}$$

where $S^2(\overline{T_j})$ and $S^2(\overline{T_{tot}})$ are determined according to 5.32.

Splitting and Particle Weighting

Three run time/variance reduction techniques are allowed in SKEPTIC. These methods were implemented primarily to permit the solution of the problem of determining the energy spectrum of X-rays generated by an electron beam impingent on a thick target and were mandated by the low production rate of photons. Because of the specific nature of the problem, the techniques permitted here, collisional importance sampling, weight splitting, and weight russian rouletting, are limited in application.

First, importance sampling as implemented by the weighting of cross sections is allowed. The user is able to input a set of numbers which correspond to the desired relative weights of the different collision types. A collision type which occurs infrequently (such as bremsstrahlung) but which contributes greatly to the desired problem outcome is artificially weighted to occur more frequently. If p_i is the relative frequency at which collision i occurs, a new frequency p_i', given by p_i/w_i is used, where w_i is the desired weight. The program automatically adjusts the weighted cross sections and the actual weights to maintain the average weight at 1 and keep the relative energy dependent weights equal to the input relative weight. When this technique is employed all source particles are given a starting weight of 1 and have their weight multiplied by the appropriate cross section weight whenever they undergo a collision. Secondary particles are always born with the weight of their parents. Tallying is done by recording $t_i \cdot w_i$ (w_i is the particle weight) rather that just t_i, the quantity of interest.

Also allowed is the splitting (in an inputable proportion) of particles which attain a user specified weight. Since the weight of some of the collisions must be set to be greater than one in order to keep the average at unity, it is possible for particles to attain high weights. This is undesirable from a variance standpoint, as the tally from a single highly weighted particle can overwhelm the tallies generated in the rest of problem and create high variance. This effect can be alleviated by setting a maximum allowed weight w_{max} and modeling each high weight particle as N_s separate, independent particles of weight w_{max}/N_s. This increases run time since more particles are created and tracked, but decreases the variance since the weights are more nearly uniform.

A companion process, Russian roulette, is also allowed. When weighting is used

it is possible that a particle will attain a very low weight, and hence lose its ability to contribute to the solution of the problem being investigated. Such particles are killed or allowed to continue with a user defined probability. Survivors have their weight increased by the reciprocal of the survival probability. This increases variance slightly, but decreases run time by not processing insignificant particles.

5.4.4 The Model Building Algorithm

The global algorithm describing the program which molds together the cross sections, relaxation data, distribution functions, and so on which make up a complete transport model is shown in figure 5.48.

The titles in capital letters denote the names of individual subroutines and functions which comprise the model builder. Some of these (particularly the discretization routines) have been described previously. Most of the routines are generic, but several major routines depend explicitly on the model in question and are described here in some detail. The basic function of PRECAL1 is the setup of global parameters such as the weight fraction and number density of the constituents, the shell energy levels, binding energies and occupation densities, and the relaxation probabilities. A few constants particular to specific models are also set on request in this routine, such as the ionization potential and the Molière screening constants of the constituents, in a holdover from an initial version of the program. PRECAL2 performs similar functions for a few energy dependent quantities, mostly having to do with stopping power and energy losses. The remainder of the routines described in this section are not actually subprograms, but rather Fortran entry points into subprograms entitled EDRIVE and PDRIVE. Each electron or photon model is generated by using different sections (yet possibly very similar) of the EDRIVE and PDRIVE routines. These

* INITE – Initialize a few standard fractional energy loss data sets
* INITA – Initialize a few standard angle sets
* PREIN1 – Read data pertinent to current problem
* PREIN2 – Read data base
* Loop over all materials in the problem
    - ◊ QUEMAT – Pop the current material in the active array
    - ◊ PRECAL1 – Do some global energy independent calculations
    - ◊ Loop over particle types from this point
        - ♯ Pass 1: PELECT – set up the electron model
        - ♯ Pass 2: PPHOT – set up the photon model
        - ♯ Loop over total cross section ladder energies
            - o PRECAL2 – Do some global energy dependent calculations
            - o Pass 1: TELECT – Get total electron cross sections
            - o Pass 2: TPHOT – Get total photon cross sections
            - o ALIAS – Alias the total cross sections
            - o XSTORE – Store total cross section results
        - ♯ Loop over all cross sections and multiple scattering distributions
            - o If there is a distribution to get:
            - o Loop over 16 preset fractional energy endpoints
                - PRECAL2 – Do some global energy dependent calculations
                - Pass 1: DELECT – Get current distribution
                - Pass 2: DPHOT – Get current distribution
            - o Loop over 14 preset fractional energy midpoints
                - PRECAL2 – Do some global energy dependent calculations
                - Pass 1: DELECT – Get current distribution
                - Pass 2: DPHOT – Get current distribution
            - o ENCHOP get energy ladder for the distribution
            - o Loop over the energies determined by ENCHOP
                - PRECAL2 – Do some global energy dependent calculations
                - Pass 1: DELECT – Get current distribution
                - Pass 2: DPHOT – Get current distribution
                - CONCHP – Do the correct discretization
                - DSTORE – Store the results

Figure 5.48: Model Building Program Algorithm

routines have three parallel main sections each, PELECT and PPHOT, TELECT and TPHOT, and DELECT and DPHOT. The 'P-' sections handle the initialization of the source, determine the number of cross sections (for energy dependent phenomena like inner shell ionization, even the number of cross sections of interest is energy dependent), set all of the sampling, flags, secondary particle generating flags, interaction result flags (those listed in tables 5.20,5.21 and 5.22), the values of the argument to be used in getting the distribution, the primary energy ladder and so on. These are called once per material. The 'T-' sections loop over all the cross sections in each material and get the total cross sections, and are called at each energy in the total cross section ladder. The 'D-' sections of the routine return the differential distribution for a single specified cross section or multiple scattering distribution. They are called inside a loop over all the cross sections, and at each of the energy end points and midpoints during the ladder determining (ENCHOP) process and at each ladder point afterward. All adjustable parameters are set, and indeed, even the specification of the physics models are determined by adjusting several signal array flags which are read from the main problem data file.

Discretization with error minimization is an incredibly slow process (almost comparable to short Monte Carlo runs), although it need be done just once per model per material. In some instances, when a model similar to a previous one is being created, it is useful to determine the discretized results for just the new component, rerun the total cross section portion, and insert existing discretizations. Provisions have been made in the program to allow for this.

References

[Be63] M.J. Berger, "Monte Carlo Calculation of the Penetration and Diffusion of Fast Charged Particles," in *Methods in Computational Physics*, vol. 1, B. Adlu, S. Fernbach, M. Rotenberg, eds., Academic Press, New York, (1963) 135.

[Bi86] A. F. Bielajew and D. W. O. Rogers, *PRESTA: The "Parameter Reduced Electron-Step Transport Algorithm" for Electron Monte Carlo Transport*, NRC Canada Document PIRS 042 (1986).

[Bl83] R.N. Blomquist and E.M. Gelbard, *Nucl. Sci. Eng.* **83**, (1983) 380.

[Br82] F. Brown, *Ph.D. Thesis*, University of Michigan, (1982).

[Br87] R. Brun, F. Bruyant, M. Maire, A.C. McPherson and P. Zanarini, *GEANT3 User's Guide*, CERN Data Handling Division Document DD/EE/84-1 (1987).

[Ca72] L.L. Carter, E.D. Cashwell, and W.M. Taylor, *Nucl. Sci. Eng.* **48**, (1972) 403.

[Ca75] L.L. Carter and E.D. Cashwell, *Particle Transport Simulation with the Monte Carlo Method*, TID-26607, (1975).

[Co74] H.M. Colbert, "SANDYL A Computer Program for Calculating Combined Photon-Electron Transport in Complex Systems", SLL-74-0012, (1974).

[Ev83] C.J. Everett and E.D. Cashwell, "A Third Monte Carlo Sampler", LA-9721-MS, (1983).

[Fo78] R.L. Ford and W.R. Nelson, *The EGS Code System: Computer Programs for the Monte Carlo Simulation of Electromagnetic Cascade Showers (Version 3)*, Stanford Linear Accelerator Center document SLAC-210, (1978).

[Ka56] H. Kahn, "Applications of Monte Carlo", AECU-3259, (1956).

[Ma61] G. Marsaglia, *Ann. Math. Stat.* **32**, (1961) 894.

[Ma86] W.R. Martin, P.F. Nowak, J.A. Rathkopf, *IBM J. Research Dev.* **30**, (1986) 193.

[Mi87] K. Miura, *Comp. Phys. Comm.* **45**, (127) 1987.

[Ne85] W.R. Nelson, H. Hirayama and D.W.O. Rogers *The EGS4 Code System*, Stanford Linear Accelerator Center Report SLAC-265 (1985)

[Se89] S. M. Seltzer, *Monte Carlo Transport of Electrons and Photons*, T. M. Jenkins, W. R. Nelson and A. Rindi, Eds., Plenum Press, New York (1989) 153.

[Wa77] A.J. Walker, *ACM Trans. Math. Soft.* **3**, (1977) 253.

CHAPTER VI

RESULTS AND CONCLUSIONS

The preceding chapters have identified the models potentially suited for use in the three classes of kilovolt energy Monte Carlo transport simulation algorithms discussed in chapter V. In this chapter, the best of these models are implemented, evaluated, and compared, with four objectives. First, the best choices of scattering models for each of the three classes of algorithms, based on comparisons with experiment, are sought. Second, the energy and atomic number regimes under which different classes of algorithms are suitable (with respect to both computation time and accuracy), are determined. Next, speed-ups achieved by vectorization of the various algorithm classes are reported. And lastly, purely numerical artifacts, as described in chapter V, regarding the inter-related effects of discretization error (on accuracy) and sample schemes (on speed) are examined.

All calculations reported in this chapter were performed on the San Diego Supercomputer Center Cray YMP.

6.1 Comparison of Scattering Models for Various Algorithms

Cross sections and distribution functions modeling electron scattering phenomena and applicable to the three algorithms types have been explored in chapters II and

III. In some cases, it is clear from the discussion in those chapters that one particular description of a given phenomenon is the best available for use in a certain class of algorithms. In other cases there is some doubt, usually because the phenomenon being modeled is so poorly understood that *a priori* comments about the validity of various models can not be made. In this section, an effort is made to identify the best scattering models for use in each of the three classes of algorithms.

6.1.1 Class I Models

A fully constituted class I (purely single scattering) scheme consists of two basis parts: one single elastic scattering cross section and a complete, inelastic scattering model, which is typically composed of several cross sections describing the various inelastic processes and takes into account the structure of the atom. It is clear from chapter II that only those elastic cross sections derived under the relativistic formulation of quantum mechanics employing the partial wave technique and screened atomic potentials are suitable for use in kilovolt energy electron transport simulations. It is not clear which full inelastic model is most appropriate, nor even which inelastic cross sections are best suited to modeling the various atomic electron collision processes of the various models. Thus, some preliminary evaluation of these models is warranted.

Usually three or four processes are treated by an inelastic models: ionization of inner shells,ionization of outer shells (delta ray production), atomic excitation, and sometimes plasmon excitation. For this work, five single scattering models were chosen, spanning the range from attempts at complete, first principle descriptions of all inelastic processes to primarily empirical models, as listed in table 6.1. In some inner shell ionization models, a two part scheme was adopted, in which the total

Model No.:	Inner Ioniz. Model	Free Electron Model	Excit. Model
1	Gryzinski	Gryzinski	none
2	Sco./Gryzinski	Mod. Møller	Gryz., w/ Quinn Pl.
3	Sco./Gryzinski	Mod. Møller	Streit., w/ Quinn Pl.
4	Pressa/Gryzinski	Møller	$1/(\Delta E)^2$
5	Sco./Mod. Møller	Møller	Mod. Gryz.

Table 6.1: Single Inelastic Scattering Models

cross section was taken from a parameterization, and the density function describing the shape of the differential distribution from one of the available theories.

In evaluating these models for potential use in Monte Carlo simulations, two factors should be examined. First, the average energy loss per pathlength predicted by the model, given by

$$\frac{dE}{dx} = \sum_{all\ processes\ j} N_{e_j} \int \sigma_j(\Delta E)\Delta E d(\Delta E) \tag{6.1}$$

should be very close to the experimental stopping power, and second, the total inelastic cross section should scale properly with the total elastic cross section. (Note that the first condition is met by default for the empirically based models.) The second condition is somewhat difficult to evaluate because data on the ratio of total elastic to inelastic cross section is not widely available. In general, elastic cross sections are thought to scale roughly as Z^2/E^2, and inelastic cross sections as Z/E. However, at the low velocities seen in this work, screening effects on the elastic cross section become very important and the elastic process tends to scale roughly as $Z^{1/2}$ at lower end of the kilovolt energy range, and as $Z^{3/2}$ in the upper regions. Further, for light elements, σ_{el} tends to vary linearly with $1/E$ at high energies, slightly more

slowly near 1 keV, and even less sharply for heavier atoms at all energy ranges. The primary inelastic cross sections tend to retain the expected Z/E dependence at most energies and for most atomic numbers, although the Z dependence is somewhat less than linear for high Z atoms, since the inner electrons become excluded from participating in inelastic processes at low energy. Thus we expect to see the fraction of elastic collisions to be roughly constant with energy at low atomic numbers, and increase as the energy increase for heavy elements, especially at lower energies.

Several interesting effects which influence these evaluations must be noted. Most importantly, for all five scattering models the total cross section (and hence the stopping power) will be strongly dependent upon how the atomic electrons are apportioned among the categories of inner, valence, and conduction electrons. Further, the total cross section and stopping power predicted by those models explicitly describing atomic excitations will be very dependent upon the minimum excitation energy chosen. The manner in which distinctions between the various categorizations of electrons was made for this work is described below. An atomic subshell was considered an inner ionization shell if and only if the relaxation of a vacancy subsequent to ionization could lead to the emission of a traceable particle, i. e., one with energy greater than 1 keV. Several ways of assigning the remaining electrons to cross sections predicting the scattering with bound outer shells, valence shells, and the conduction band were investigated. The options are listed in table 6.2. The effects of using combinations of the various options were also investigated. For the three non-empirical models examined here, various versions of these atomic descriptions options were employed in efforts to best model the stopping power. It should also be noted that the manner in which outer shells are treated has a strong influence on the total data set size for a given problem, through the number of cross sections re-

1. Assume *all* subshells can give rise to excitations as well as ionizations
2. Assume all subshells not treated as inner ionization shells give rise to excitations
3. Assume conduction electrons contribute only to plasmon excitations
4. Assume only subshells with binding energies below 25 eV give rise to excitations
5. Assume a minimum excitation energy of the Fermi level energy
6. Assume a minimum excitation energy of 10 eV
7. Ignore the binding energy of all but the inner shells

Table 6.2: Single Inelastic Scattering Model Assumptions

quired to implement a given scheme. The empirical models, which describe all of the permissible excitation transitions with one cross section, require much less data to fully model inelastic scattering than those models which treat each shell's processes explicitly.

Comparisons of the stopping power calculated by the first three models listed in table 6.1 when employing various the assumptions listed in table 6.2 with the low energy stopping power for carbon, aluminum, copper, and gold at various energies are shown in figure 6.1 through 6.3.

For each of the five models, data is presented only for the particular combination of options which best described both the stopping power and the elastic to inelastic cross section behavior. The assumptions employed are described here.

For the first model, every subshell is treated as an inner ionization shell, by taking the minimum excitation energy to be the electron binding energy. The maximum

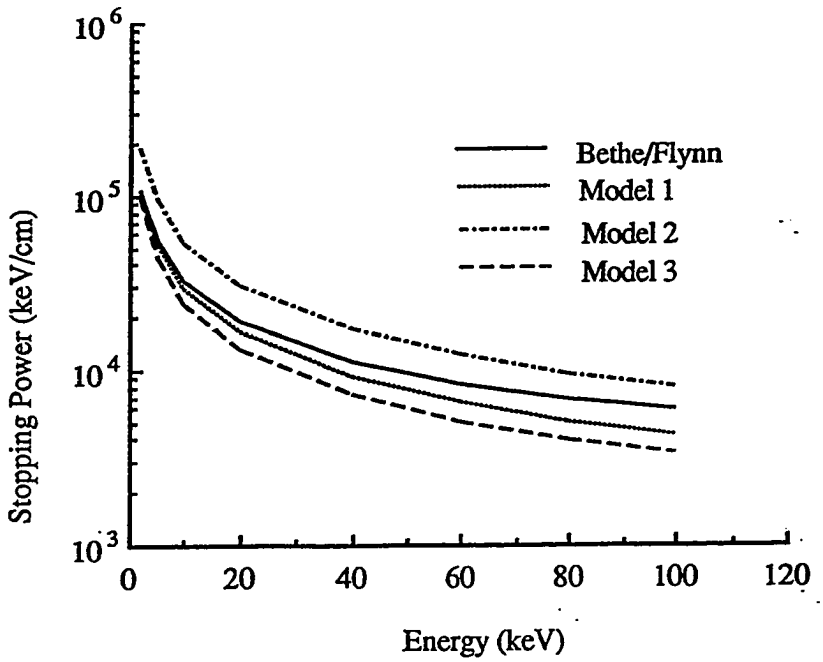

Figure 6.1: Stopping Power for Carbon Predicted by Inelastic Scattering Models

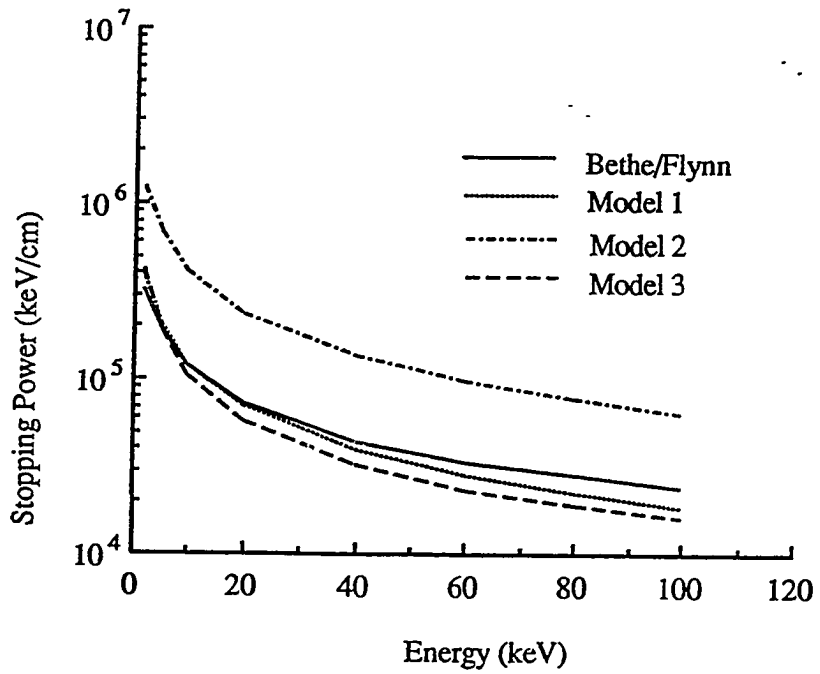

Figure 6.2: Stopping Power for Copper Predicted by Inelastic Scattering Models

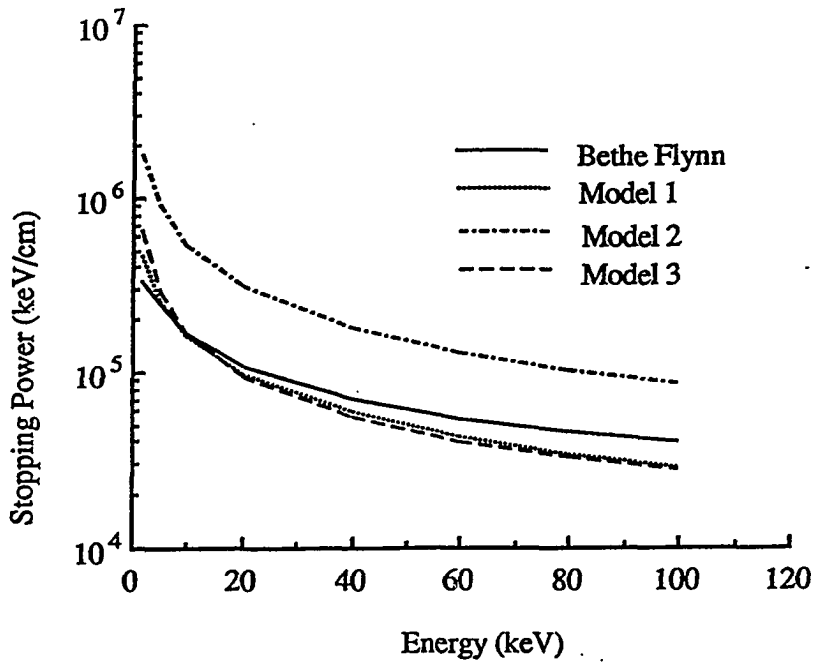

Figure 6.3: Stopping Power for Gold Predicted by Inelastic Scattering Models

transfer is assumed to be the incident electron energy, so that in addition to ionizations, each subshell can give rise to energetic knock-ons. Ignored are all excitations not producing ionizations. It is seen in the figure that the stopping powers are well predicted by this scheme at low energy and underestimated at higher energies, for all elements.

Model 2 from table 6.1 treats all inner ionizations with Gryzinski's cross section shape and Scofield's total cross section. It treats outer shells, defined as those giving rise to vacancies with relaxation energy less than 1 keV, using Gryzinski's cross section to determine the excitations and the modified Møller cross section to model all outer shell ionizations, and treats conduction electrons as giving rise to plasmon excitations as described by Quinn's model. Stopping powers predicted by this model consistently overestimate the stopping power by a large amount, with this trend worsening at low energies. This is seen to be true regardless of the way in which with the atomic structure was modeled, or in size of the minimum energy transfer selected.

The data in figures 6.1 through 6.3 was taken from a best case (lowest predicted stopping power) calculation in which only subshells with binding energies less than 25 eV were considered to contribute to outer shell excitations and ionizations, and in which the minimum loss was also taken to be 25 eV. The results from this evaluation showed this model to be so poorly representative of electron stopping that it was not considered for further analysis.

The 3rd model examined here treats inner shells with a combination of Pressa and Newell's empirical total cross section and Gryzinski's differential cross section, uses the modified Møller cross section to describe all outer shell ionizations, and uses Steitwolf's excitation cross section assuming a minimum excitation loss equal to the Fermi level energy to model outer shell excitations. Stopping powers derived from this model typically model the stopping power well at lower energies, and underestimate them at high energies, similar to model 1, although to a slightly more severe degree.

The remaining two models predict the stopping power exactly because of the empirical excitation functions which they include. The fourth model treats inner ionization processes in the same way as the previous model, but uses a simple Møller cross section for the knock-on delta ray production cross section. All electrons outside of the inner shell are considered to contribute to this process. This model also uses a $1/\Delta E^2$ excitation cross section with the total cross section dictated by the stopping power. Minimum losses of both the Fermi level energy and 25 eV (maximum loss of 1 keV) were tested.

The fifth model uses Scofield's total cross section and the modified Møller differential cross section to describe inner shell processes, and then ignores the binding energy in all outer shells and uses the simple Møller cross section to describe delta ray

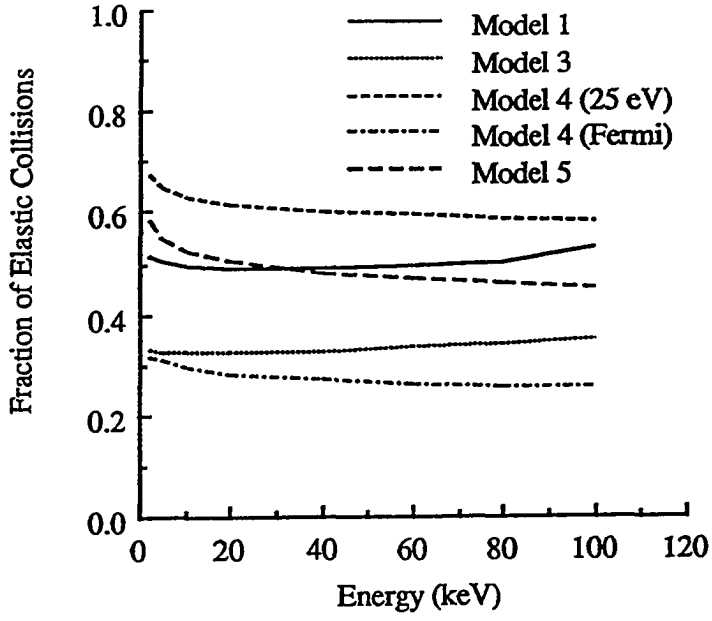

Figure 6.4: Elastic Fraction of Total Cross Section for Carbon

production. It also uses a Gryzinski cross section, modified to include an empirical binding energy so as to preserve the stopping power, to treat outer shell excitation processes. A minimum excitation energy of the Fermi energy and of 25 eV are both examined.

As mentioned before, the other way to evaluate the validity of various scattering models is by examining the total cross sections which they predict. In this work, this is done by comparing the the fraction of the total which is comprised of elastic scattering. Fractional elastic cross sections as functions of energy for each models are shown for various elements in figures 6.4 through 6.6.

Note that all of the models generally produce the anticipated scaling trends. The primary differences lie in the values of the ratio of elastic to total collisions. The validity of the various predictions should become apparent from Monte Carlo calculations.

Thus, of the five models initially examined, four have been found suitable for

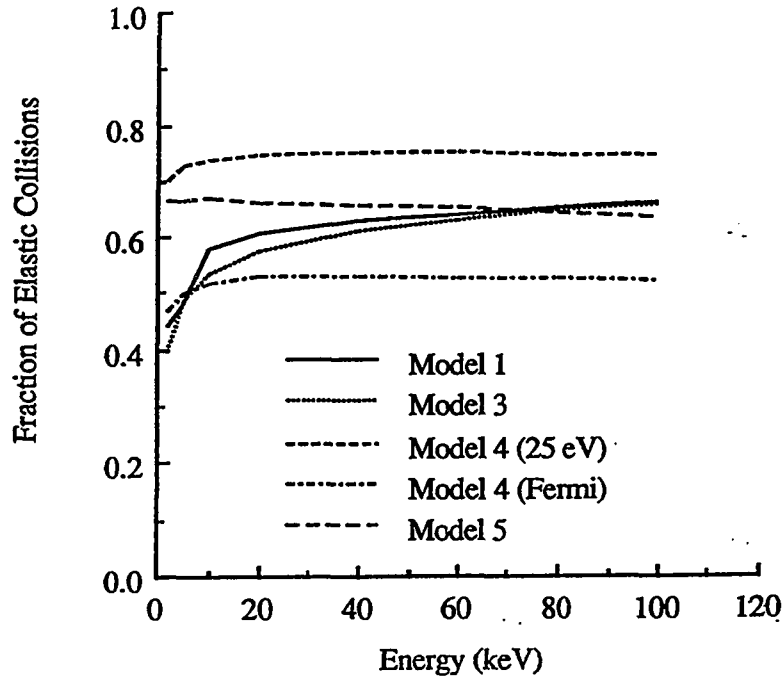

Figure 6.5: Elastic Fraction of Total Cross Section for Copper

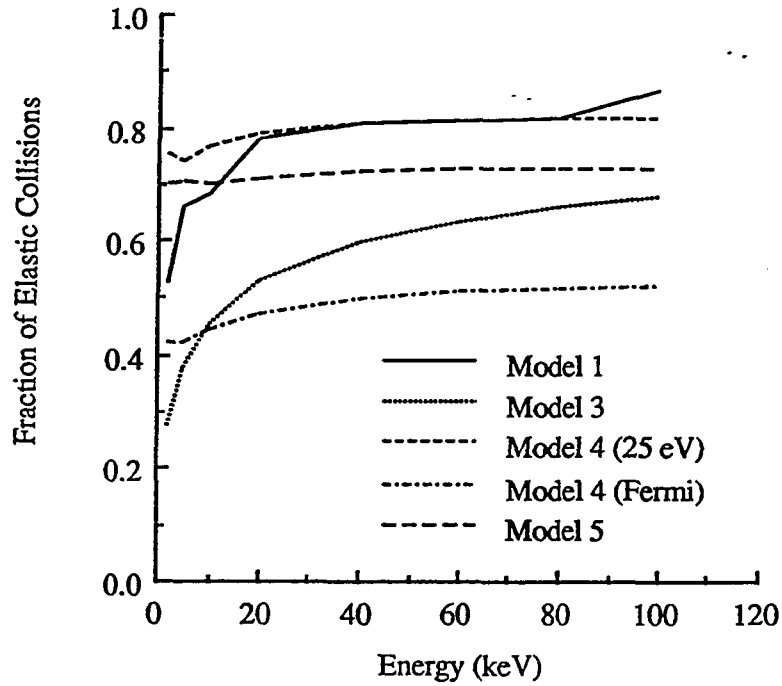

Figure 6.6: Elastic Fraction of Total Cross Section for Gold

evaluation by Monte Carlo calculation based on comparison with low kilovolt energy experiments. The parameters for the data generation were the same as those used in the above analysis, except that all models which had such an option assumed 10 eV minimum excitation losses, and the fourth model (model 5 described above) assumed that only the outermost subshell is involved to the excitation stopping. This last approximation was made because when all the outer shells are allowed to contribute to low energy ionizations and excitations and a small minimum loss been assumed, the empirical Gryzinski binding energy can be indeterminately small at low initial energies and high Z materials.

Three classes of experiments were selected for simulation and evaluation, namely, measurements of total backscattering fraction, x-ray production, and energy distribution of backscattered electrons. Results are described below.

No consensus exists on the best values, as determined by experiment, of total backscattering coefficients throughout the full range of materials at kilovolt energies, although several authors have attempted to define them. Recently, Kalef-Ezra, *et al.* [Ka82] have reviewed the relevant data for low Z materials. Other summaries and/or wide ranging experiments can be found in Neubert and Rogaschewski [Ne80], Liuzzi and Martin [Li79], Darlington [Da75], Darlington and Cosslett [Da72] and Drescher, *et al.* [Dr70]. A comparison of Monte Carlo simulations with experimental results is shown in table 6.3. Wherever more than one experimental result is available, the range of results is presented. (A small variation in the tabulated experimental value should be construed to represent not so much a highly confident figure for the backscattering fraction as a highly uncertain number derived from a single measurement.)

Agreement is generally good, although two anomalies are seen. First, models 1

Experiment	Expt	Model 1	Model 3	Model 4	Model 5
Al at 3 keV	.275	.192	.164	.179	.169
Al at 5 keV	.186 – .25	.206	.191	.186	.178
Al at 10 keV	.157 – .19	.205	.211	.183	.183
Cu at 3 keV	.38	.274	.242	.299	.309
Cu at 5 keV	.352 – .363	.301	.288	.316	.314
Cu at 10 keV	.26 – .35	.320	.325	.321	.318
Au at 3 keV	.525	.408	.328	.414	.452
Au at 5 keV	.43 – .50	.458	.396	.457	.477
Au at 10 keV	.425 – .50	.498	.462	.481	.482

Table 6.3: Backscattered Fractions from Experiment and Monte Carlo

and 3 tend to over-estimate the backscatter somewhat for low Z materials. Most likely, this occurs because these models predict a stopping power for aluminum at 10 keV which is somewhat less than the experimental value. Thus, these models tend to slow the electrons so slowly that too great a fraction manage to escape. For the higher Z test case, for which models 1 and 3 accurately predict the stopping power, and this effect does not exist.

The second incorrect result is a gross underestimation in the total backscattering coefficient at very low energies. The most likely reason for this is that backscattering experiments typically collect all electrons with energies above 50 eV while the simulation considers as stopped all electrons slowing to 1 keV. At high initial energies, the number of electrons expected between .05 and 1 keV is a small fraction of the total backscatter, but for 3 and even 5 keV incident electrons, the backscattered electrons

Experiment	Expt	Model 1	Model 3	Model 4	Model 5
Al at 3 keV	.275	.248	.204	.242	.210
Al at 5 keV	.186 – .25	.223	.208	.206	.203
Al at 10 keV	.157 – .19	.213	.215	.191	.189
Cu at 3 keV	.38	.346	.287	.362	.381
Cu at 5 keV	.352 – .363	.322	.308	.340	.341
Cu at 10 keV	.26 – .35	.328	.328	.332	.325
Au at 3 keV	.525	.462	.379	.499	.518
Au at 5 keV	.43 – .50	.483	.409	.481	.501
Au at 10 keV	.425 – .50	.505	.465	.487	.491

Table 6.4: Corrected Backscattered Fractions from Class I Monte Carlo

ignored by the model may represent significant fraction of the total. This hypothesis is supported by the shape of the energy distribution (see for example, figure 6.7), which shows the *peak* in the distribution near 1 keV. Thus the Monte Carlo results would probably be closer to the experimental results if the low energy cut off were greater. Table 6.4 shows computational results corrected for this effect by assuming that the tail of the backscattered energy distribution is flat extending to 50 eV.

The extrapolation is admittedly crude, (especially at 3 keV), but it does show that the single scattering Monte Carlo results, when based on data well-representative of the medium's characteristics, conform to the general trend of increased backscattering with decreasing energy. Note that at very low energies for the higher Z materials, for which model 1 and particularly model 3 overestimate the stopping power, the predicted backscattering fraction is far too low, even with the correction.

Energy (keV)	Experiment	Model 1	Model 3	Model 4	Model 5
10	.403	.485	.470	.475	.458
15	1.38	1.42	1.83	1.30	1.58
20	2.69	2.12	3.08	1.90	2.70
25	4.29	3.54	4.75	2.86	4.10

(Values in 10^{-4} photons/electron-steradian)

Table 6.5: X-ray Yield for Various Class I Models for 10 – 25 keV Electrons on Chromium

The next experiment modeled was the yield of x-rays from a thick chromium target bombarded by monoenergetic electrons, based on the experimental results of Lifshin *et al.* [Li77]. This calculation tests primarily the accuracy of the inner ionization cross section, since most emitted photons from this target at this energy are K characteristic x-rays. It is seen from the results in table 6.5 that models using Scofield's parameterization (models 3 and 5) are more likely to give correct results than those using Pressa's empirical formulation (model 4) or Gryzinski's total cross section (model 1), both of which predict too great a yield at low energies and too low a yield at high energies. It is also apparent from the table that other portions of the scattering model influence the x-ray yield prediction, as models 2 and 5, which use the same total ionization cross section, predicted different x-ray yields. Recall that the non-empirical model 2 tends to underestimate stopping powers at high energies, and would be expected to predict an increase in the population of high energy electrons after traversal of a given pathlength and hence too large a likelihood of inner shell ionization. Since the underestimation of $\frac{dE}{dx}$ diminishes at low energies, the difference in the predictions of x-ray yield between this model and model 5, which is pinned to

Author	Energy (keV)	Element
Darlington [Da75]	10	13
	10	29
	10	79
Kanter [Ka57]	10	13
	10	79
Sternglass [St54]	1.92	6

Table 6.6: Backscattered Experiments Used in Investigating Class I Algorithm Inelastic Scattering Models

the stopping power, is expected to be smallest in the low energy region.

The final set of evaluations involve the prediction of the energy distribution of backscattered electrons. These experiments, especially those employing obliquely incident electrons, are expected to test the complete model since both the deflection and energy degradation components of the models must conform to actual conditions in order to accurately predict the energy of the ejected electrons. The experiments chosen for this portion of the examination are listed in table 6.6.

As noted before, backscattering data in the energy range of interest here is sometimes contradictory. Table 6.7 gives the total backscattering fraction predicted by the various models for the various experiments, and that given by the experimenters whose distributions measurements are being used.

Agreement between experiment and the Monte Carlo calculations is generally very good. It should be noted that Sternglass's experimental value is generally held to be much too low, 1/3 to 1/2 of the usually accepted value for carbon in this energy range [Da72, Ve77, Ka82], and so the relatively good agreement between the carbon experiment and the models is chance, especially in light of the argument put forth

Experiment	Expt	Model 1	Model 3	Model 4	Model 5
C at 1.92 keV	.065	.0688	.0565	.0622	.0554
Al at 10 keV	.19,.173	.205	.211	.183	.183
Al at 10 keV, 80°	.66	.671	.656	.650	.648
Cu at 10 keV	.312	.322	.326	.322	.317
Au at 10 keV	.48,.479	.498	.462	.481	.482
Au at 10 keV, 80°	.80	.797	.766	.786	.788

Table 6.7: Backscattered Fractions from Experiment and Monte Carlo

earlier concerning the relatively high cut off energy used in the simulations. In the comparisons involving gold and aluminum, the only significant deviation between the Monte Carlo simulations and experimental results arises for models 1 and 3 for normally incident electrons impingent on aluminum, in which case the calculation over-estimates the backscattering. This is expected based on the analysis of the total backscattering results presented earlier. For obliquely incident electrons this effect is limited because of the fewer number of inelastic (as well as elastic) collisions necessary to eject the electron.

Results of distributions calculated by the four models are plotted in figures 6.7 through 6.27.

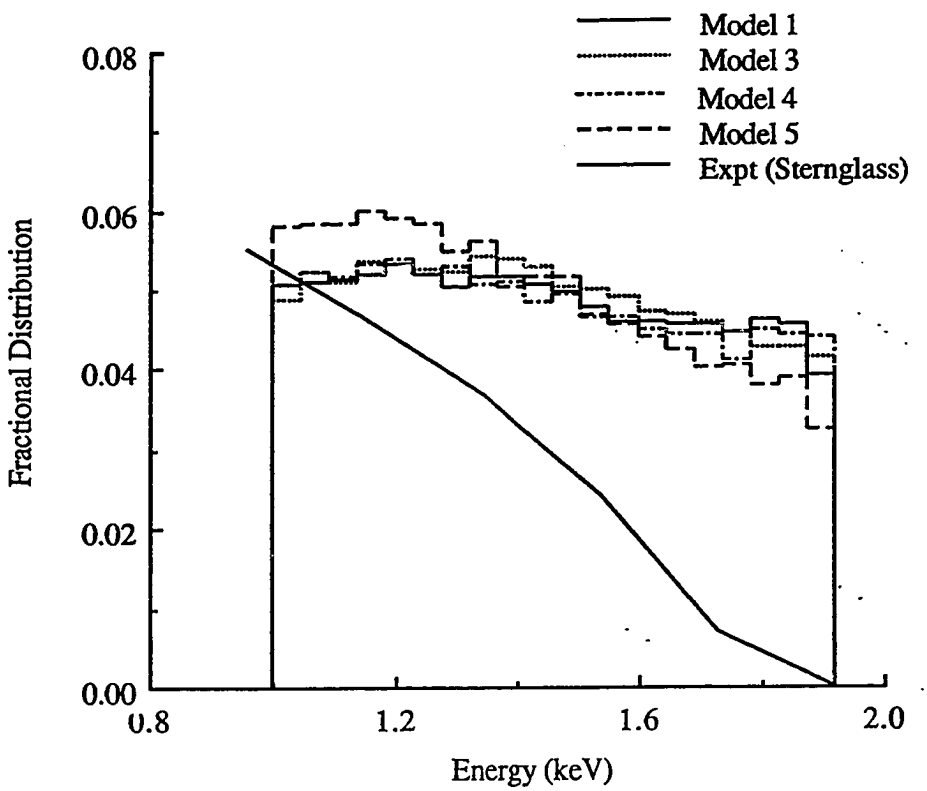

Figure 6.7: Backscattered Electron Energy Distributions for Various Class I Models for 1.92 keV Electrons on Carbon

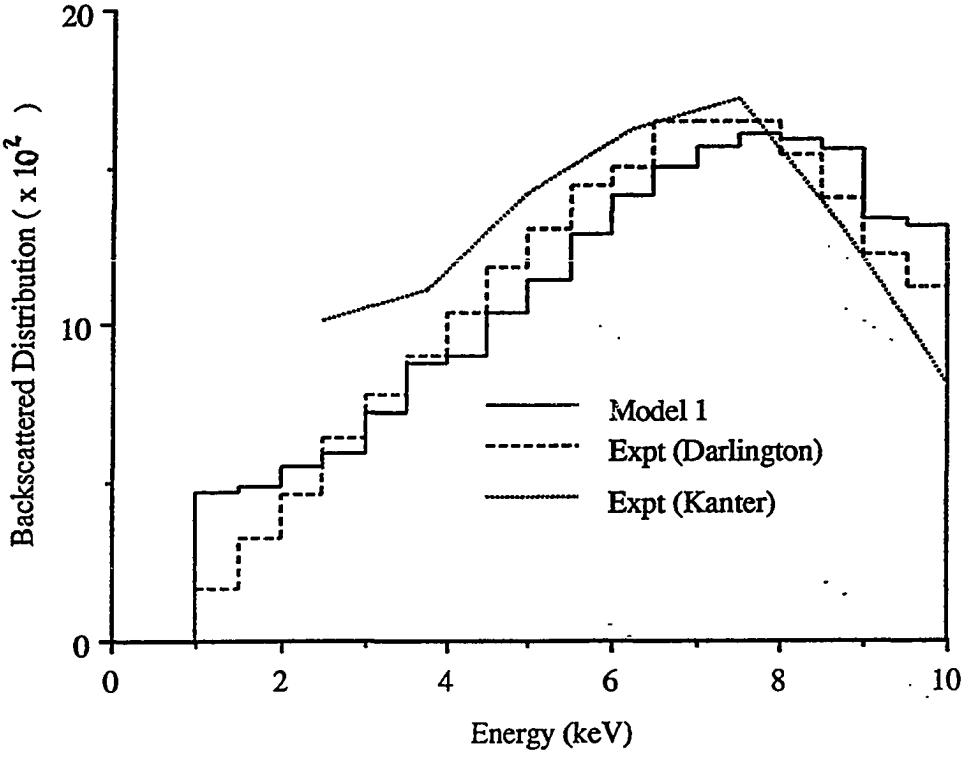

Figure 6.8: Backscattered Electron Energy Distributions for Class I, Model 1 for 10 keV Electrons on Aluminum (Normally Incident)

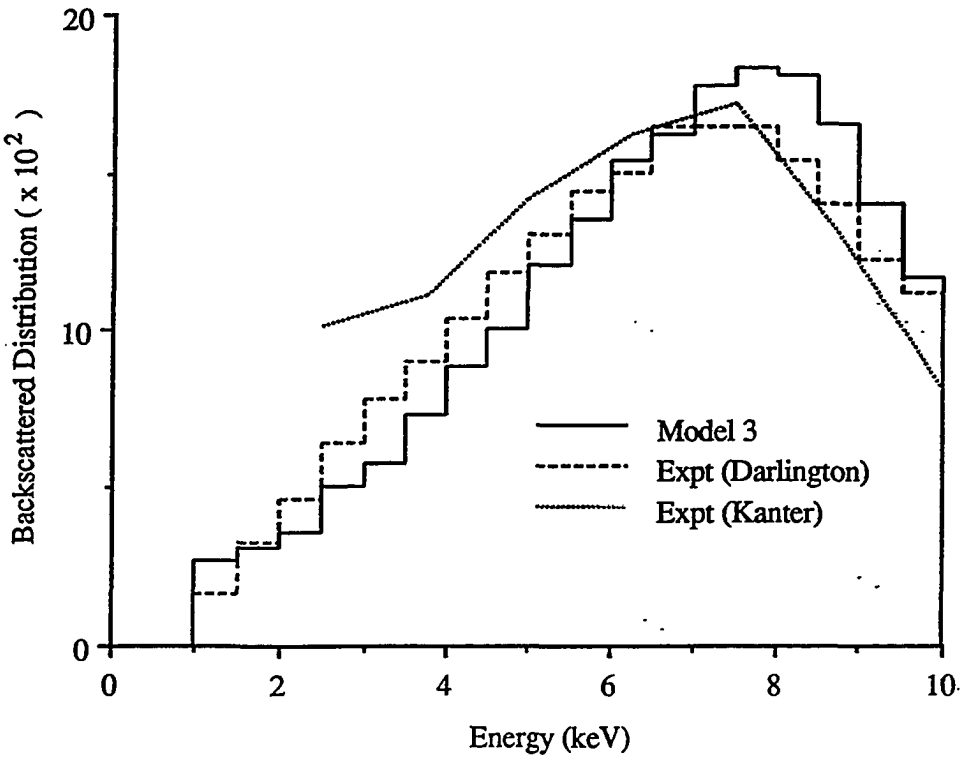

Figure 6.9: Backscattered Electron Energy Distributions for Class I, Model 3 for 10 keV Electrons on Aluminum (Normally Incident)

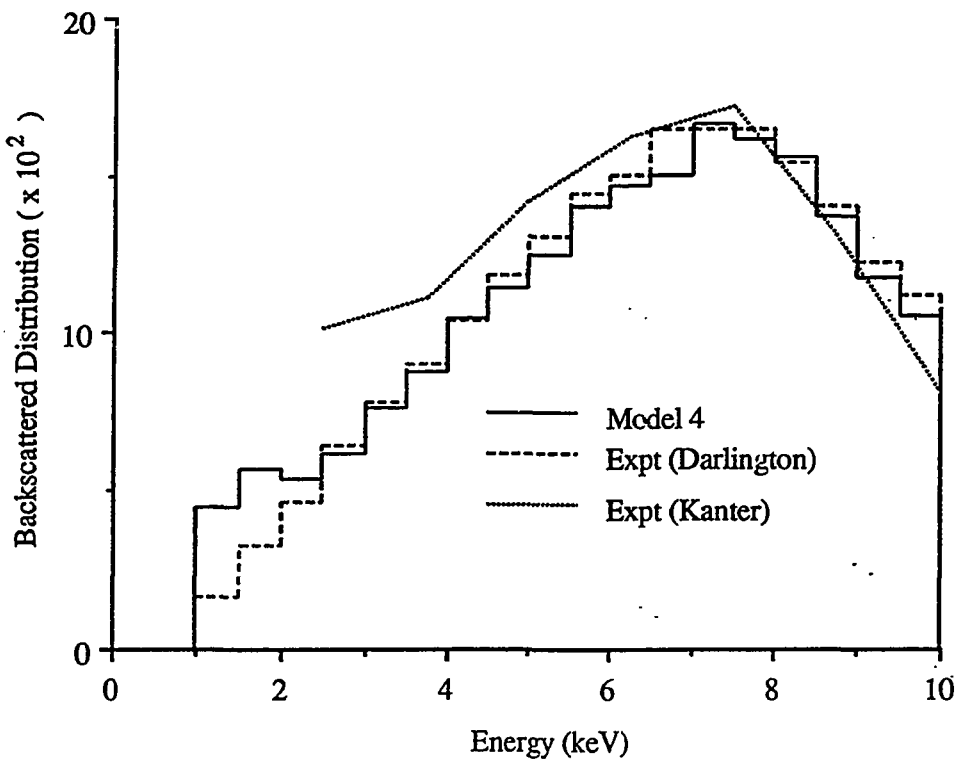

Figure 6.10: Backscattered Electron Energy Distributions for Class I, Model 4 for 10 keV Electrons on Aluminum (Normally Incident)

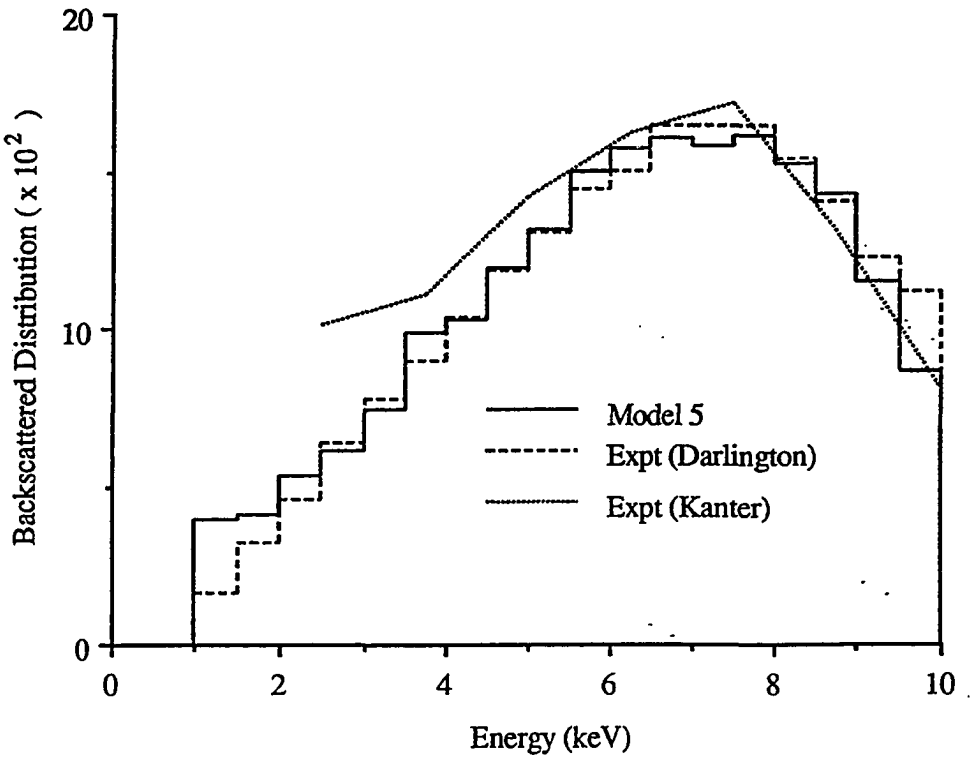

Figure 6.11: Backscattered Electron Energy Distributions for Class I, Model 5 for 10 keV Electrons on Aluminum (Normally Incident)

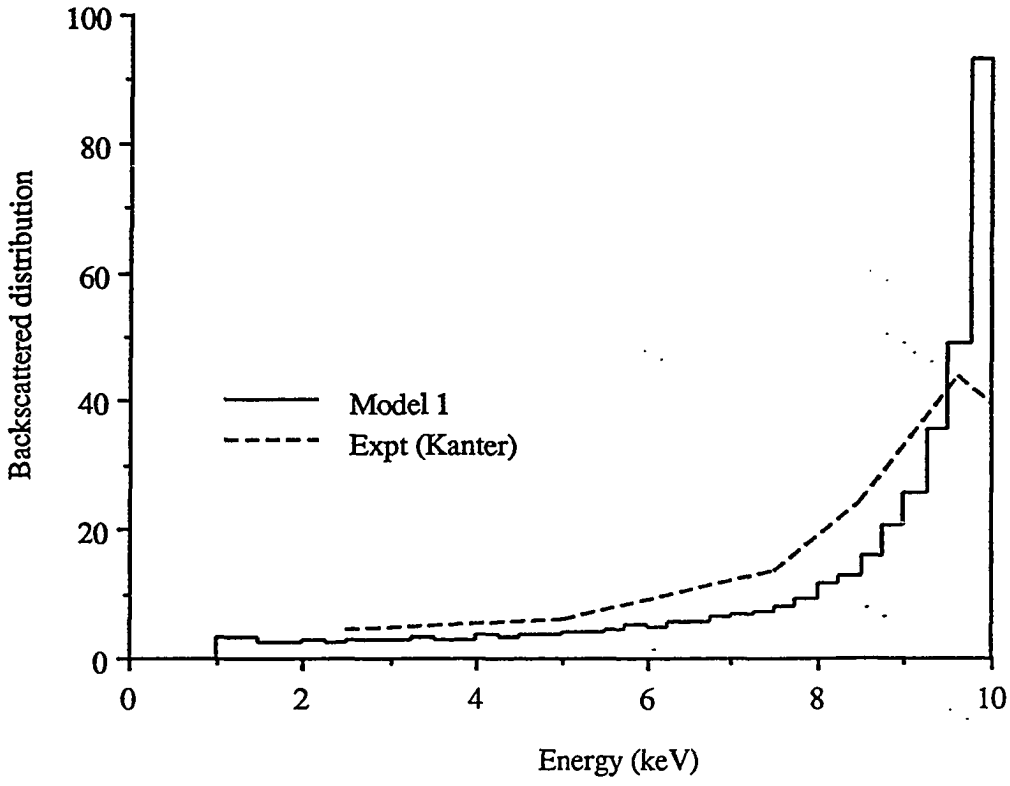

Figure 6.12: Backscattered Electron Energy Distributions for Class I, Model 1 for 10 keV Electrons on Aluminum (80° Incident)

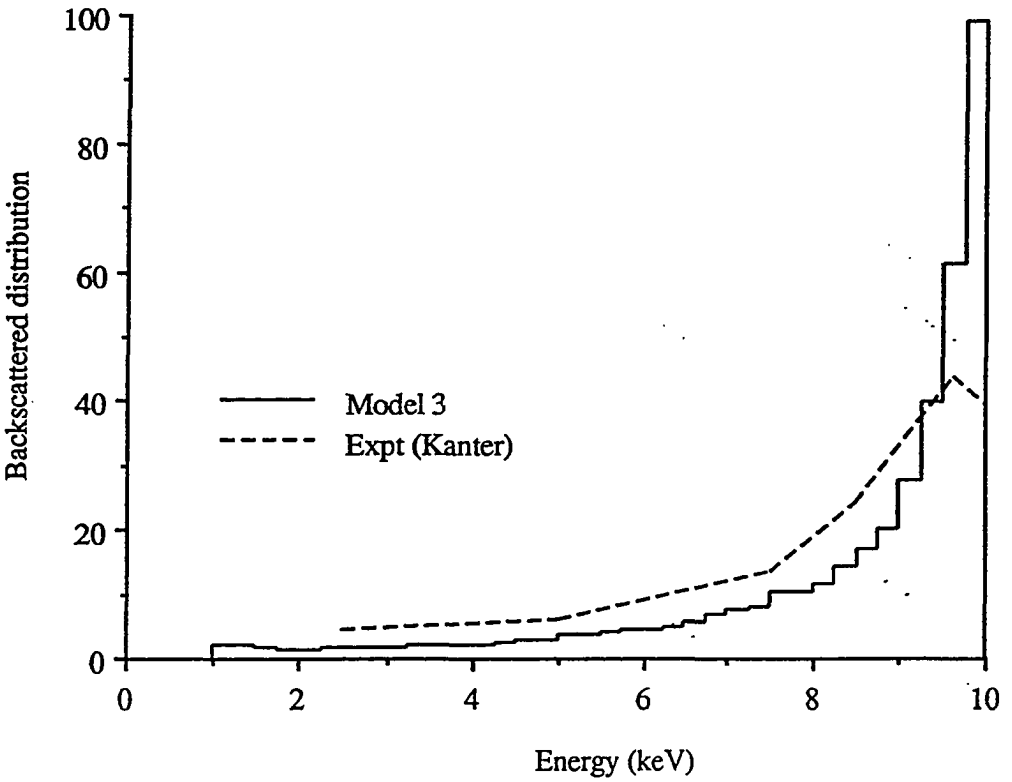

Figure 6.13: Backscattered Electron Energy Distributions for Class I, Model 3 for 10 keV Electrons on Aluminum (80° Incident)

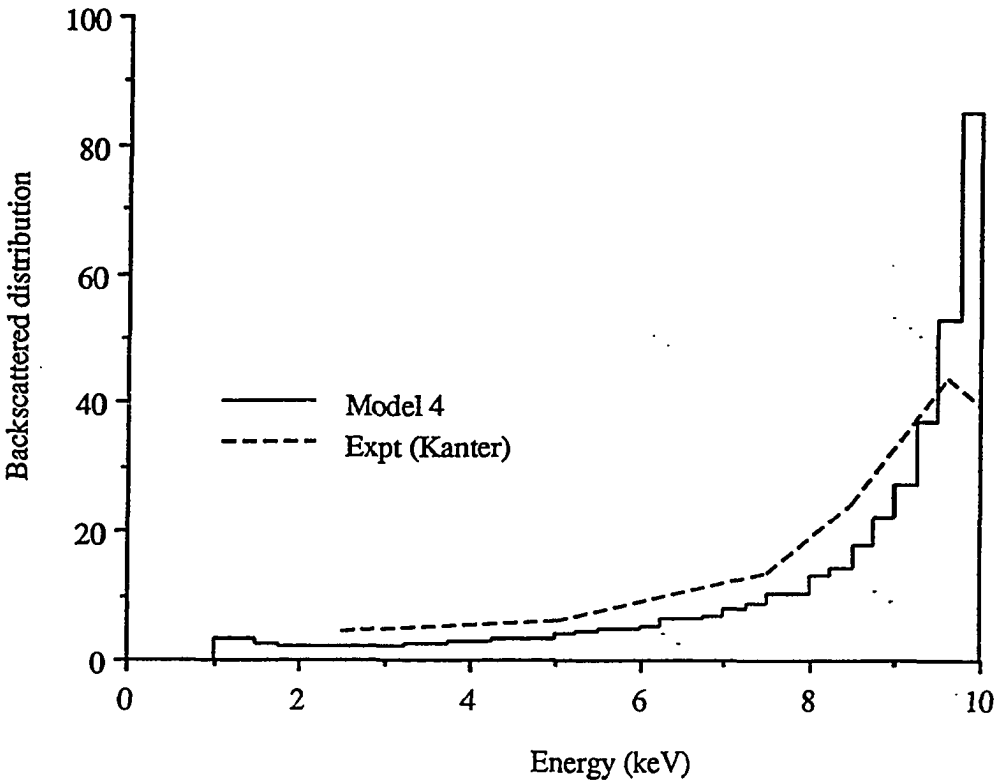

Figure 6.14: Backscattered Electron Energy Distributions for Class I, Model 4 for 10 keV Electrons on Aluminum (80° Incident)

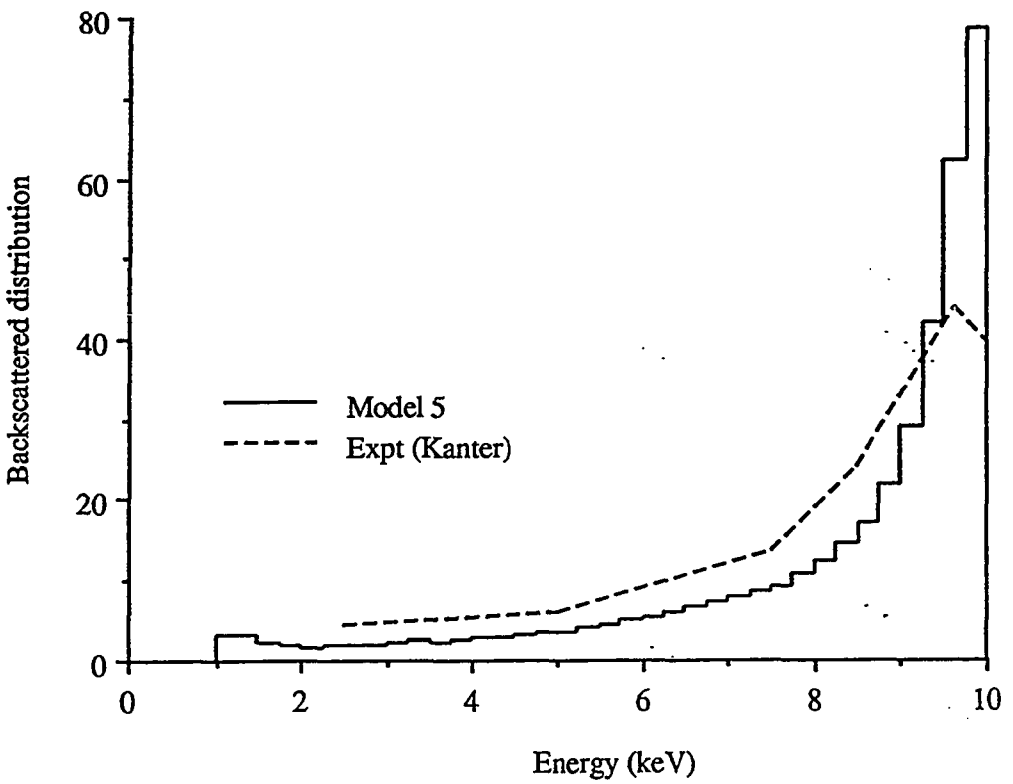

Figure 6.15: Backscattered Electron Energy Distributions for Class I, Model 5 for 10 keV Electrons on Aluminum (80° Incident)

Agreement with experimental results is very good for models 4 and 5 , except for the carbon experiment and the experiments using very obliquely incident electrons. Models 1 and 3 generally perform poorly, tending to underestimate the most probable loss, and to overestimate the intensity at the peaks of the distributions. Model 4 provides a slightly more accurate simulation of the normal incident electrons on aluminum experiment, and Model 5 of the copper and the gold experiments. For obliquely incident electrons, all of the models overestimate the peak intensity and underestimate the most probable loss. This observation suggests that the average energy loss per inelastic collision (which is smallest in model 3), is an important factor in providing extensive details of simulations (although not as influential as the total stopping power), and is not modeled well for any of the experiments. No explanation for the poor performance of all the models in simulating the carbon experiment is obvious, although the problems with other data from the same citation have been noted previously. Further, the shape of the distribution predicted by the model 5 Monte Carlo appears to be more in line with the scale suggested by the other low Z experiments modeled here than the Sternglass experiment.

Computational Comparisons

The number of tracks per incident electron, processing time per track, and total required processing time found in simulating some of these problems with the various schemes are presented in tables 6.8 through 6.9. Results of the chromium photon prediction computations are not included because it is not known how the importance sampling skews the computation time.

These results are at once misleading and enlightening; higher Z materials, even though they have a higher cross section and so would be expected to require more

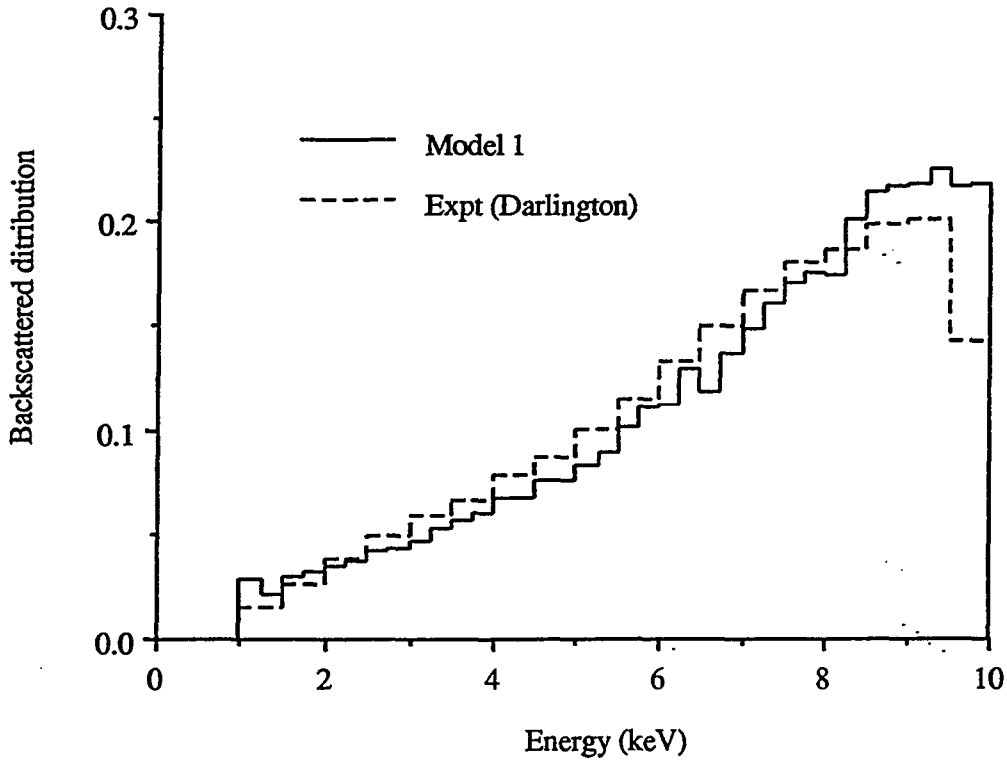

Figure 6.16: Backscattered Electron Energy Distributions for Class I, Model 1 for 10 keV Electrons on Copper (Normally Incident)

Experiment	Model 1	Model 3	Model 4	Model 5
C at 1.92 keV	48	70	45	66
Al at 10 keV	409	603	405	605
Cu at 10 keV	324	358	315	493
Au at 10 keV	245	384	281	439
Al at 10 keV, 80°	212	309	213	321
Au at 10 keV, 80°	126	180	144	222

Table 6.8: Number of Collisions per Incident Particle Predicted by Various Class I Models

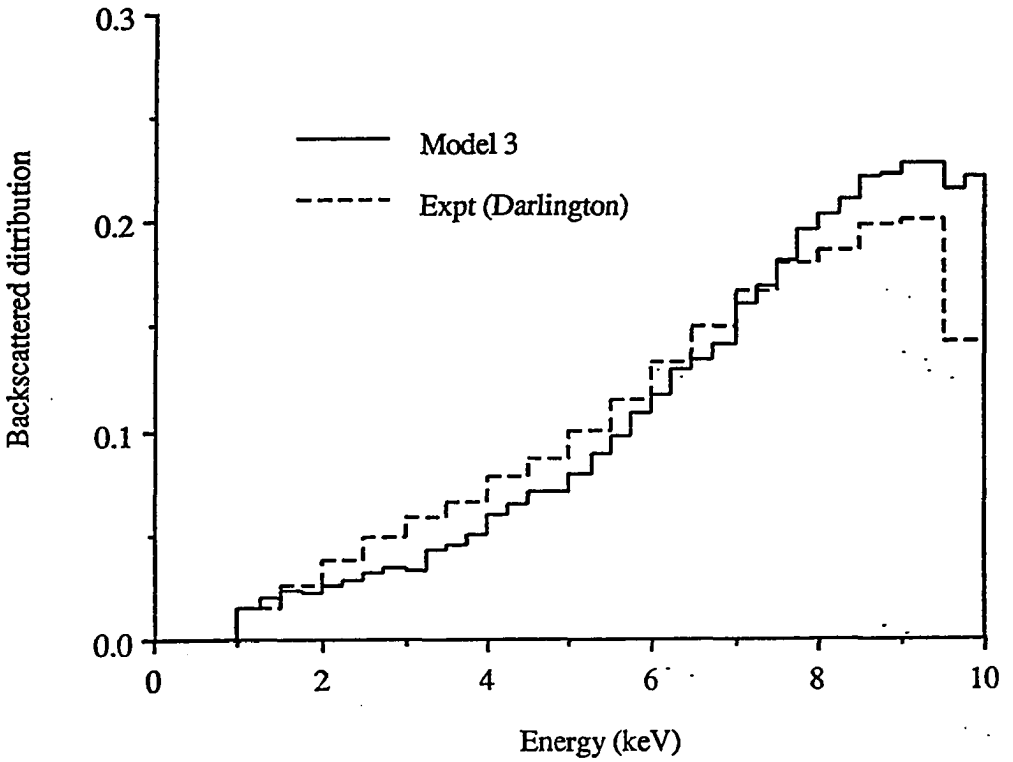

Figure 6.17: Backscattered Electron Energy Distributions for Class I, Model 3 for 10 keV Electrons on Copper (Normally Incident)

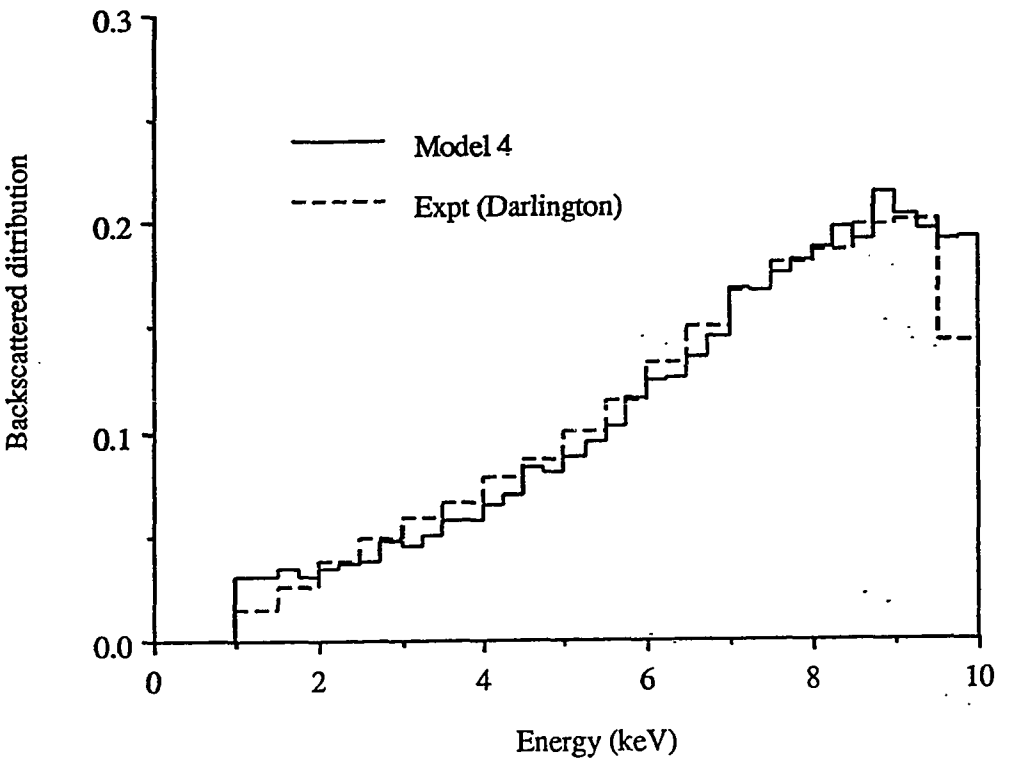

Figure 6.18: Backscattered Electron Energy Distributions for Class I, Model 4 for 10 keV Electrons on Copper (Normally Incident)

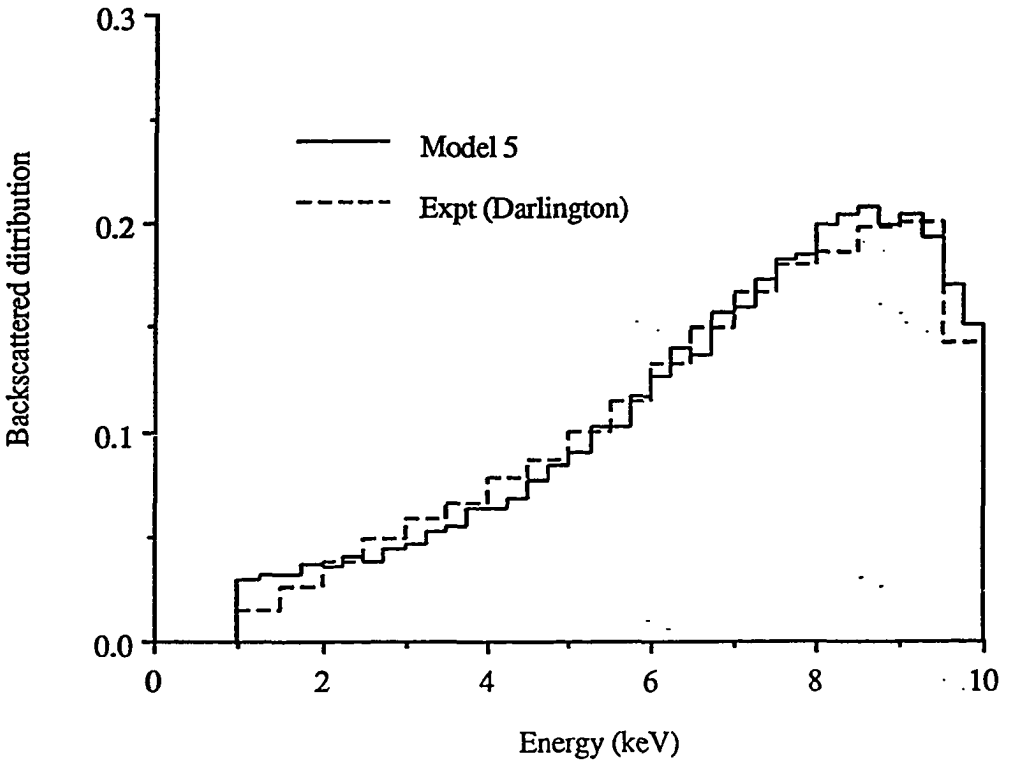

Figure 6.19: Backscattered Electron Energy Distributions for Class I, Model 5 for 10 keV Electrons on Copper (Normally Incident)

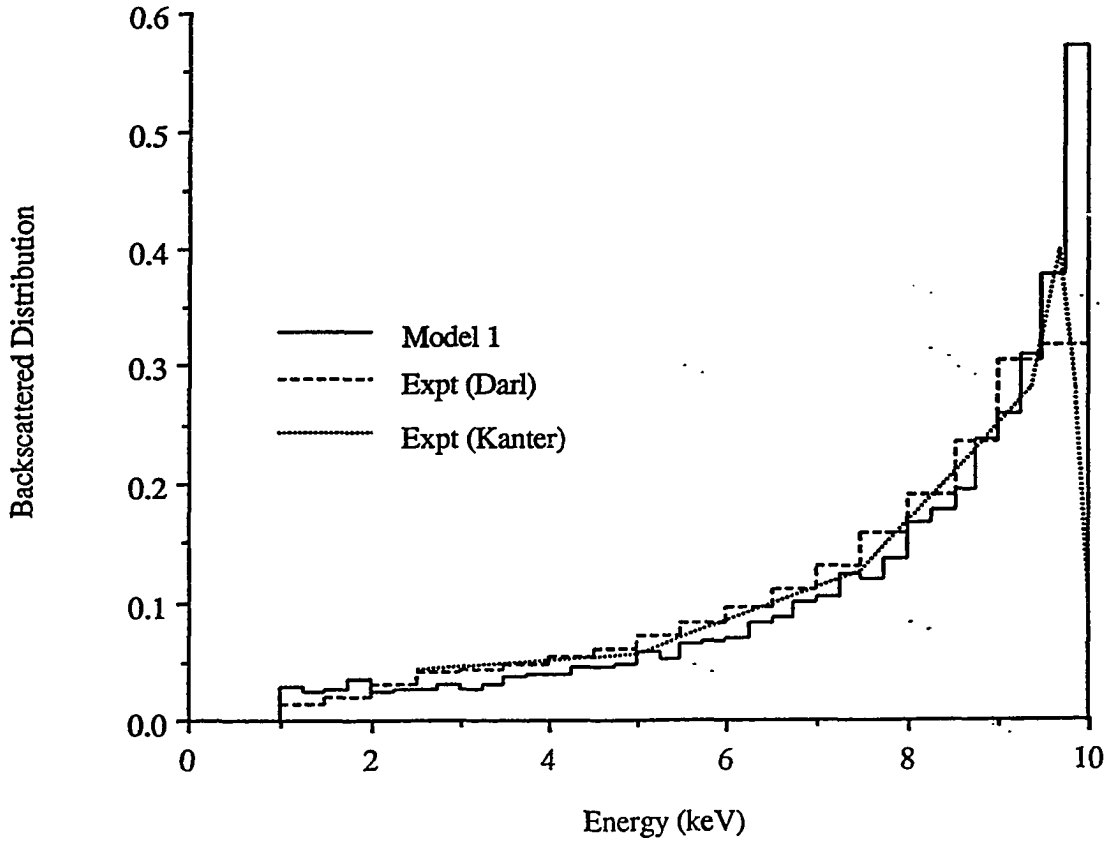

Figure 6.20: Backscattered Electron Energy Distributions for Class I, Model 1 for 10 keV Electrons on Gold (Normally Incident)

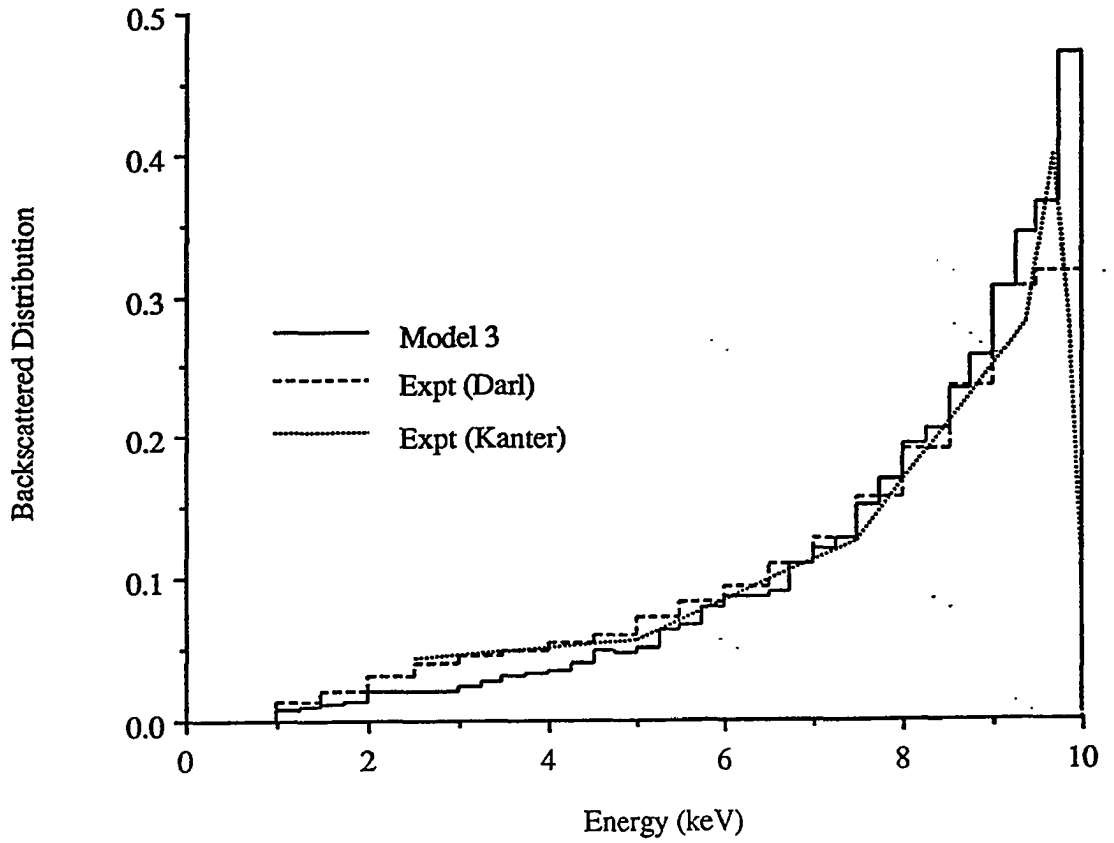

Figure 6.21: Backscattered Electron Energy Distributions for Class I, Model 3 for 10 keV Electrons on Gold (Normally Incident)

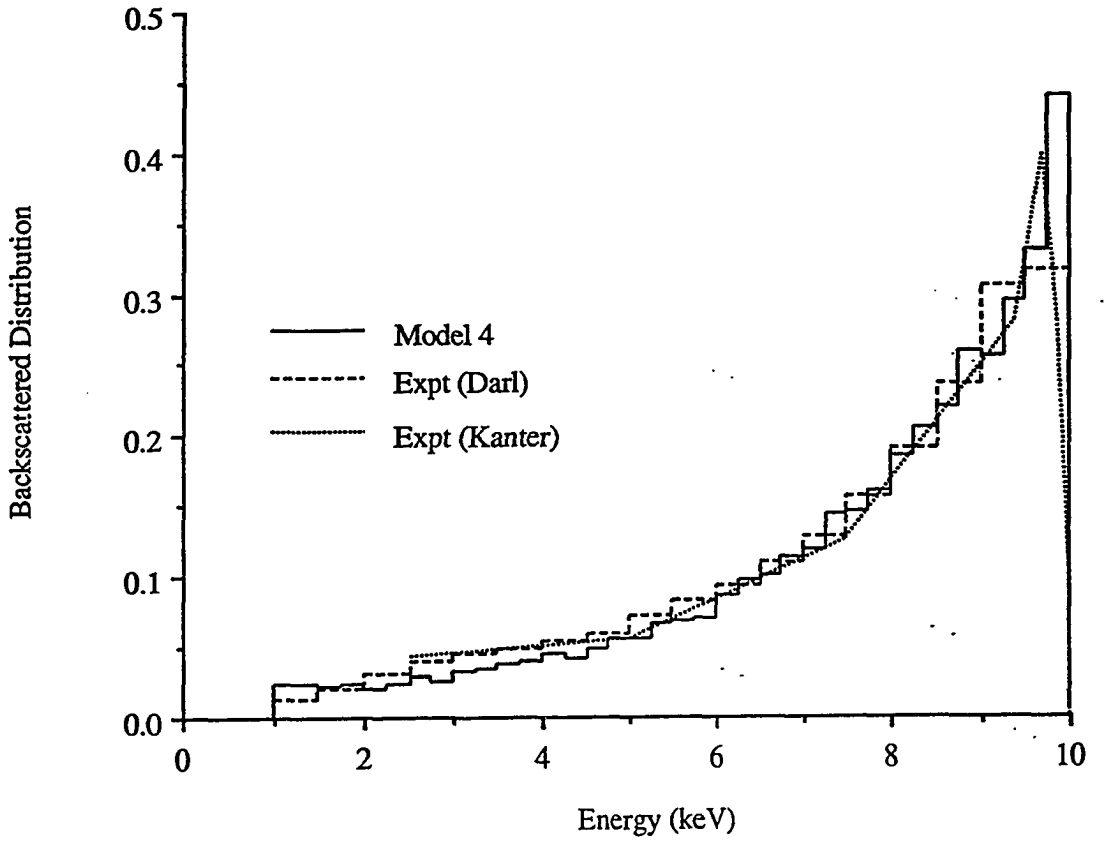

Figure 6.22: Backscattered Electron Energy Distributions for Class I, Model 4 for 10 keV Electrons on Gold (Normally Incident)

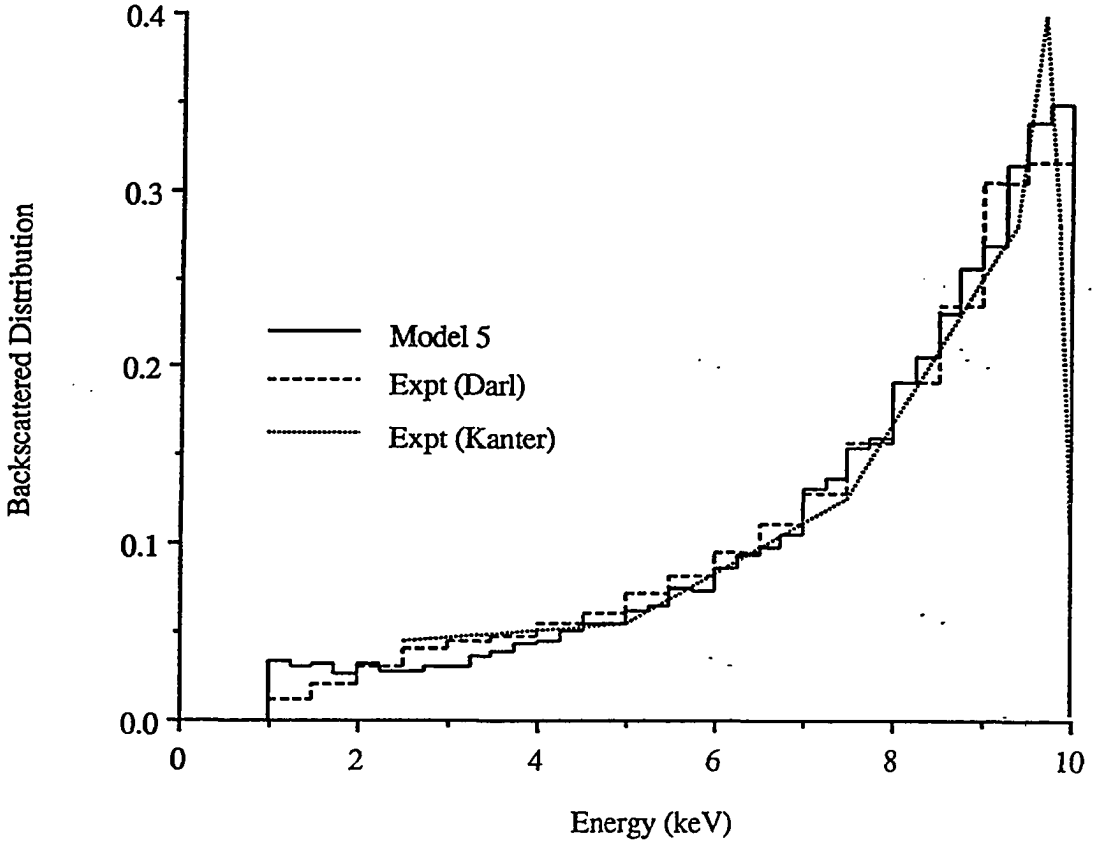

Figure 6.23: Backscattered Electron Energy Distributions for Class I, Model 5 for 10 keV Electrons on Gold (Normally Incident)

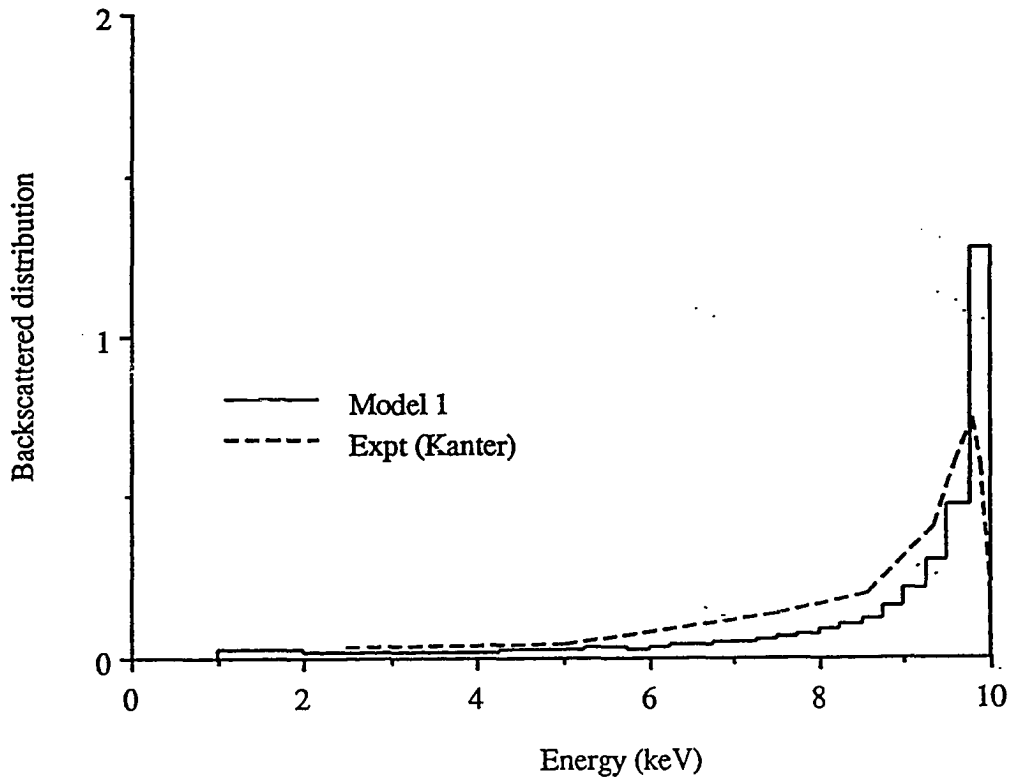

Figure 6.24: Backscattered Electron Energy Distributions for Class I, Model 1 for 10 keV Electrons on Gold (80° Incident)

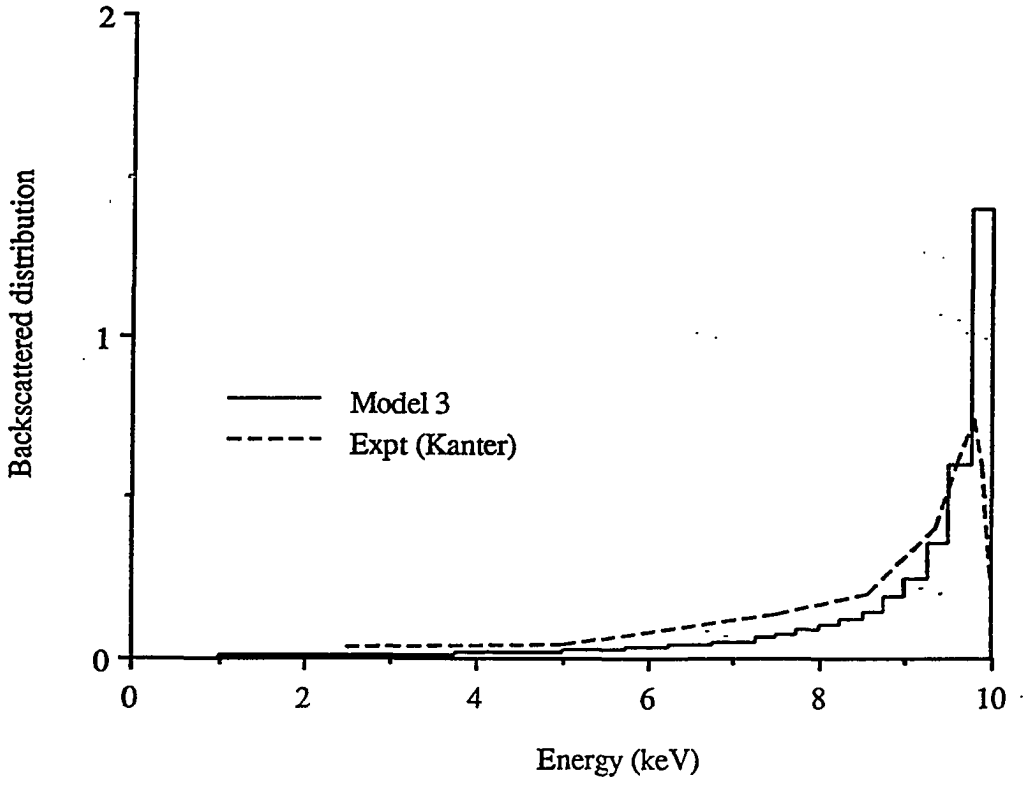

Figure 6.25: Backscattered Electron Energy Distributions for Class I, Model 3 for 10 keV Electrons on Gold (80° Incident)

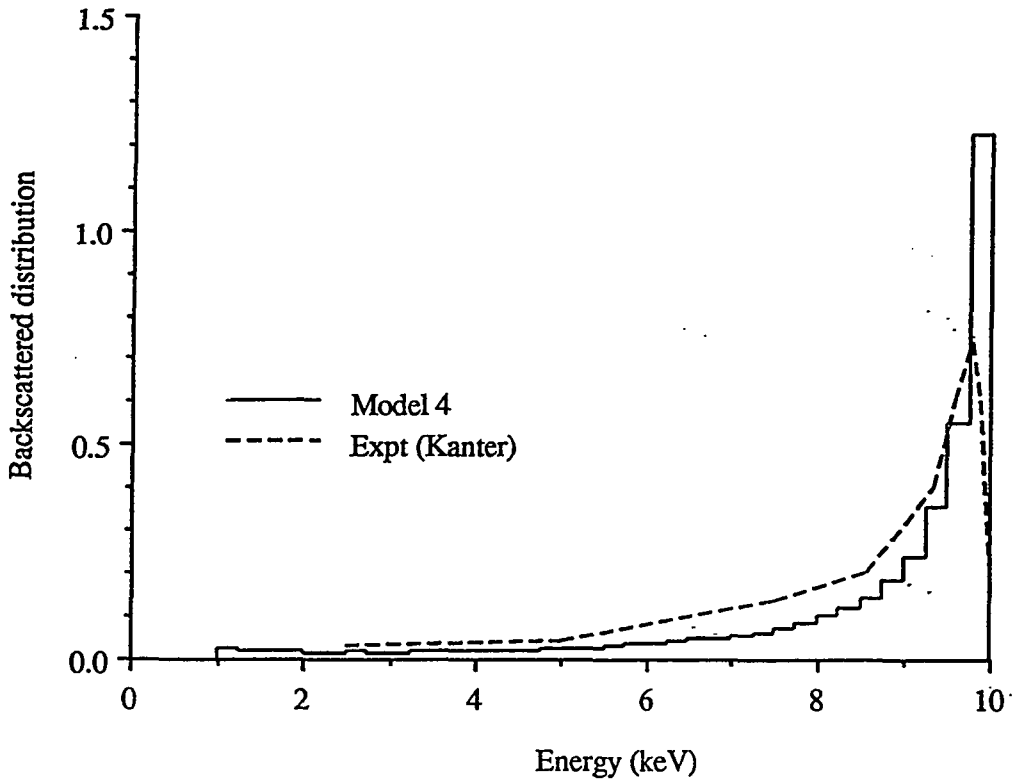

Figure 6.26: Backscattered Electron Energy Distributions for Class I, Model 4 for 10 keV Electrons on Gold (80° Incident)

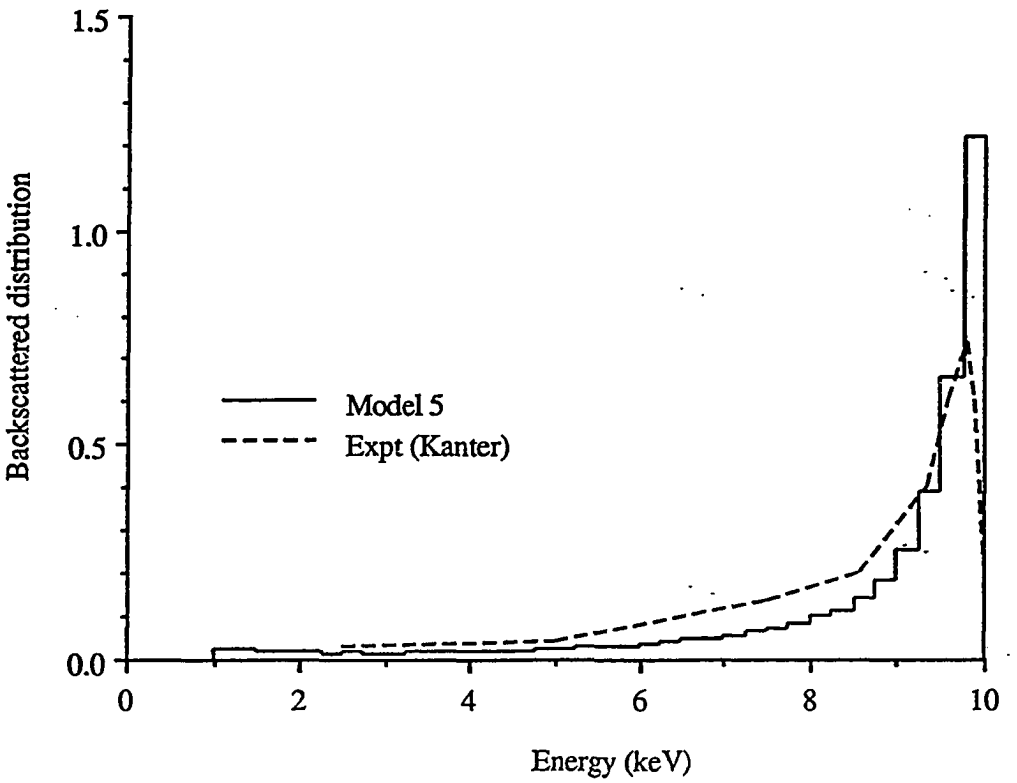

Figure 6.27: Backscattered Electron Energy Distributions for Class I, Model 5 for 10 keV Electrons on Gold (80° Incident)

Experiment	Model 1	Model 3	Model 4	Model 5
C at 1.92 keV	6.43	5.63	6.03	6.13
Al at 10 keV	6.55	5.93	6.27	6.29
Cu at 10 keV	6.87	6.52	6.43	6.48
Au at 10 keV	6.78	6.51	6.36	6.42
Al at 10 keV, 80°	6.68	6.03	6.35	6.37
Au at 10 keV, 80°	6.99	6.68	6.54	6.53

Table 6.9: Computation Speed (μsec/track) for Various Class I Models

collisions to stop, instead are seen to use fewer. This is because these materials have both a higher stopping power (and thus completely stop electrons in a shorter tracklength) and a more preferentially backward scattering distribution, yielding more backscattering and thus fewer collisions per particle *on average* over the course of a full simulation. The interesting result is that this effect is so great that the total problem processing time per particle is *higher* for low Z materials than for heavy elements at comparable energies. Of course, for certain problems in which the backscattered electrons are of no consequence, more particles must be run for high Z materials to limit statistical uncertainty, and so simulations in high Z materials will take longer than in lighter elements.

Model 1 simulations are the slowest in terms of processing time per track because of the large number of secondary particles which this model creates (every inelastic collision, regardless of the energy of the particle created, is modeled as an secondary electron generating ionization in this model) and the mechanism employed by the program to eliminate secondaries born below the problem cutoff. All the models

Experiment	Model 1	Model 3	Model 4	Model 5
C at 1.92 keV	0.312	0.392	.273	.406
Al at 10 keV	2.679	3.577	2.537	3.800
Cu at 10 keV	2.223	2.336	2.024	3.192
Au at 10 keV	1.659	2.500	1.788	2.815
Al at 10 keV, 80°	1.413	1.864	1.345	2.042
Au at 10 keV, 80°	0.883	1.321	0.944	1.453

Table 6.10: Computation Time (msec / particle) Required for Various Class I Models

speed up (in terms of performance per track) at low Z materials because fewer different types of collisions are possible and so the number of trips through loops with short vectors is smaller. In this respect, Models 4 and 5 are very similar in structure, and this is evidenced by their nearly identical processing speed.

Overall simulation time is mainly dependent on the value of the total cross section used by the various models, which, since all models use the same elastic cross section, is determined by the inelastic cross section. Thus models 1 and 4, which have smaller total inelastic cross sections but higher average energy loss per collision, are always faster.

Conclusions

Several conclusions can be drawn from the discussion in the previous sections. The single most important factor in determining the success of a single scattering model is how closely the stopping power which it predicts adheres to experimentally accepted values. No other factor had so great an influence on the results predicted

by all simulations. Second, models which preserve stopping power by using higher total inelastic cross sections with a lower average loss per collision seem to be slightly more accurate in modeling detailed experiments. Overall computation time increases, since more tracks must be processed, but for some types of problems, this appears to be the only way to accurately simulate experiments. In many types of calculations however, faster, less detailed models are suitable. Lastly, Scofield's total ionization cross section is preferred over that of Gryzinski and of Pressa and Newell.

6.1.2 Class II Algorithms

The optimal Class II algorithm is obvious from the results of the class I evaluation. This is true because of the three components of this algorithm class (the elastic cross section, the 'important' inelastic event cross sections, and the continuous loss model), only the choice of the inelastic model is not obvious from the preliminary analysis of chapters II and III, and it is set by the best choice seen in the class I evaluation. As in Class I schemes, the elastic scattering component, partial wave elastic cross sections are mandated. The best choice for continuous slowing down model is Bethe as corrected by Flynn, as noted in chapter III. And from the previous section, it is seen that the optimal discrete inelastic model is one employing Scofield's total cross section. The unsettled portion of the Class I model, the small energy transfer inelastic model, is taken up here in the stopping power. Whether or not this model of low transfer collisions provides adequate detail in Monte Carlo simulations is explored in the next section 2 of this chapter.

6.1.3 Class III Algorithms

Based on the conclusions drawn in chapter III, there can be only slight doubt about the make up of the class III (condensed history) model which is optimal for simulating kilovolt electron transport. The only applicable elastic scattering model is clearly that of Goudsmit and Saunderson with the Riley cross section. Choices for the inelastic scattering model can be limited to two, depending on whether energy loss restricted straggling distributions (which case Vavilov's formalism is superior) or restricted stopping power is used. For the remainder of this section, models employing simply the stopping power will be referred to as scheme 1 models, and models using energy loss fluctuation distributions as scheme 2 models.

The only other facet of these algorithms which is of significance then is the selection of the multiple scattering step size. Recall that it is of paramount importance that the deflection be kept small so that the actual pathlength and the Monte Carlo step size be roughly equivalent, and so that the displacement modeled by the Monte Carlo straight line transport assumption be accurate. It is also important that there be enough collisions over the interval that the distributions functions are valid and numerically determinable.

To evaluate these choices, two primary models were constructed, one using the continuous slowing down formalism of Bethe's model, as corrected by Flynn, and one employing a loss distribution function, the restricted Vavilov. These models included all of the peripheral model (such as the use of pathlength straggling, application of multiple scattering at boundaries and at pre-collision sites, and the inclusion of the no-scatter probability), reasoning that these only enhance the adherence of the Monte Carlo simulation to the physics of electron transport.

Multiple scattering distributions were generated for various fractional energy loss

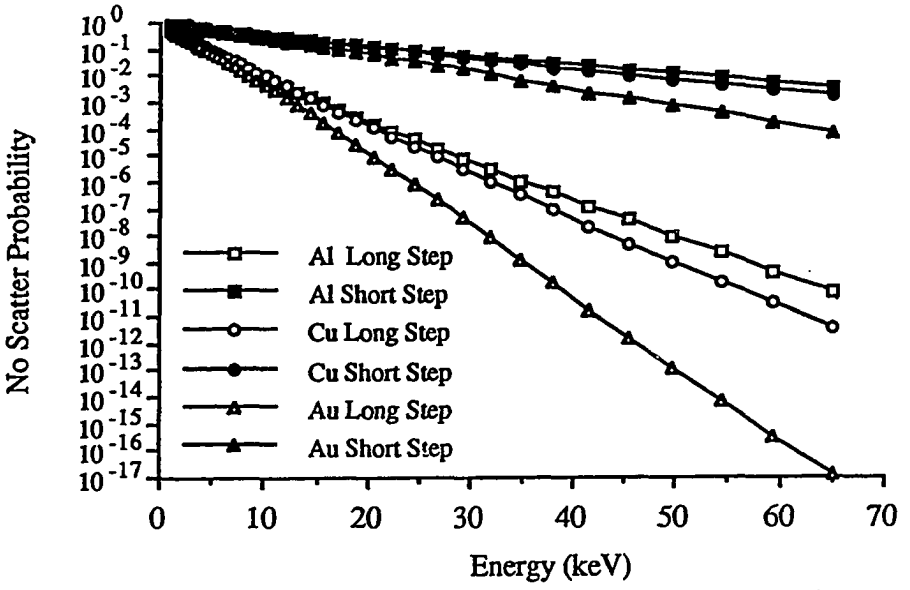

Figure 6.28: No Scattering Probabilities for Various Elements at Various Fractional Energy Loss Steps in Class III Models

steps for both models. The step sizes chosen for the analysis were defined as those which were 1/5, 1/10, 1/15, and 1/20 of the path necessary for an electron to travel a distance so as to lose 8.5% of its energy in a single step. At low energies this distance is often less than one elastic scattering mean free path, and no-scattering probabilities more than 80% are not uncommon. Plots of the no-scattering probability and the average scattering angle (actually, the angle corresponding to the average deflection cosine) as a function of initial step energy for different fractional losses (the longest and shortest tested) are given in figures 6.28 and 6.29.

It is seen that the average cosine increases with atomic number, as expected. Further, the average cosine is constant with energy for steps beginning at higher energies (as by design for condensed history simulations [Be63]) but that the deflections increase dramatically at lower initial energies for all materials. Also noteworthy is the fact that the average deflection for similar energy loss steps is not constant with Z. This suggests that some scheme might be found to generate spacing constants which provide identical average deflections for all elements, at least at high energies.

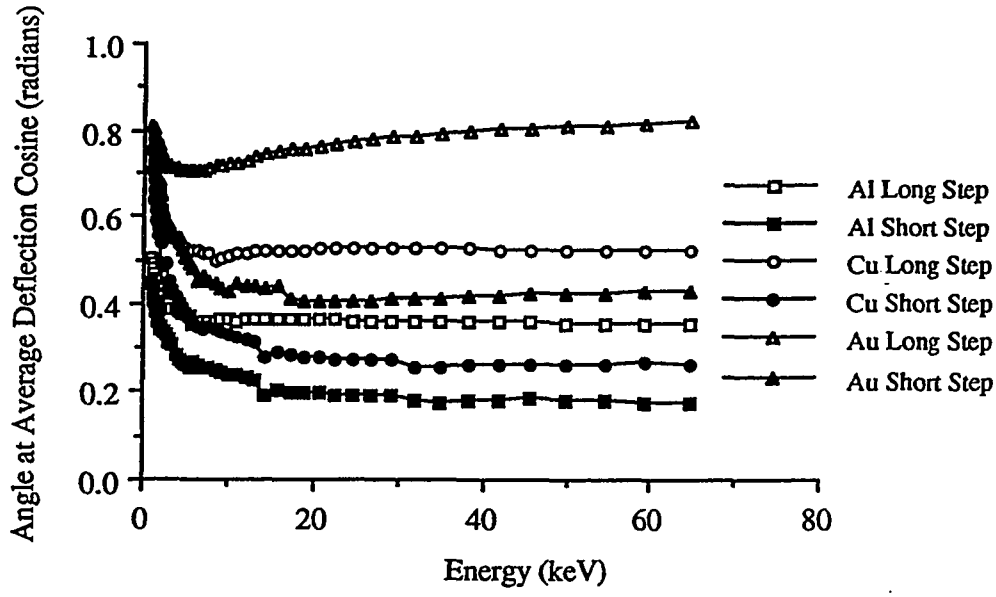

Figure 6.29: Average Scattering Angle in Various Elements for Various Fractional Energy Loss Steps in Class III Models

The results of Monte Carlo runs using the greatest and smallest step sizes for both schemes for this algorithm class (those with and without distributed losses) are discussed below. As with class I models, the evaluation of class III models begins with an comparison of the Monte Carlo and experimental total backscattering coefficients. Results are presented in table 6.11.

A strong dependence on the step size is seen, with long steps repeatedly underestimating the backscattering, except possibly for aluminum. The most interesting result seen here is that only the short step scheme using continuous loss correctly predicts the trend of increasing backscattering for decreasing energy for low Z materials. Two factors seem to be contribute to this, first, an increase in the error in the the shape of the fluctuation distribution at low energy, and second, a potential breakdown in the algorithm at high atomic number beginning around 50 keV. Thus while it appears that it is possible to tailor a calculation to fit a particular backscattering experimental result by a suitable choice of the step size, the physics seems to be subverted, since experiment trends are not correctly portrayed.

Experiment	Expt. Result	Stop. Power Meth. (Scheme 1)		Distributed Loss Meth. Scheme 2	
		Long Step	Short Step	Long Step	Short Step
Al at 30 keV	.137 – .165	.155	.168	.152	.146
Al at 50 keV	.141 – .147	.150	.161	.157	.165
Al at 70 keV	.136 – .145	.155	.145	.158	.153
Cu at 30 keV	.298 – .306	.280	.300	.278	.292
Cu at 50 keV	.295 – .301	.283	.298	.289	.306
Cu at 70 keV	.293 – .298	.304	.299	.294	.315
Au at 30 keV	.490 – .521	.426	.470	.419	.459
Au at 50 keV	.510 – .523	.451	.488	.444	.484
Au at 70 keV	.480 – .525	.461	.501	.452	.495

Table 6.11: Backscattered Fractions from Experiment and Monte Carlo for Class III Simulations

Energy (keV)	Experiment	Scheme 1 Long Step	Scheme 1 Short Steps	Scheme 2 Long Steps	Scheme 2 Short Steps
25	4.29	5.08	5.29	5.51	5.54

(Values in 10^{-4} photons/electron-steradian)

Table 6.12: X-ray Yield for Various Class III Models for 25 keV Electrons on Chromium

The second simulation again involves the prediction of the x-ray yield from chromium at various energies. Based on the results from the analysis of class I schemes, the Scofield total cross section was used to describe the inner ionization process.

This time fairly consistent agreement across models is seen, most likely because the same ionization cross section was used in all cases. Also evident is a gross (20%) overestimation of the x-ray yield. This is somewhat surprising, since all models tended to predict the backscatter of medium Z materials quite well, even at the lowest energies examined so far, and these condensed history models use the same ionization cross section as those single scattering models which performed this calculation quite well.

The final set of experiments simulated were those measuring energy distributions of backscattered electrons. Again, experiments of Kanter are used. Results are shown in table 6.13 (total backscattering fraction) and figures 6.30 through 6.45 (energy distributions).

Agreement is generally good, except for aluminum at 80 degree incident angle. However, Kanter's figure of .73 for the backscattering fraction is considerably larger than the measurements of other investigators, who report a backscatter fraction of

Experiment	Expt	Scheme 1 Long Steps	Scheme 1 Short Steps	Scheme 2 Long Steps	Scheme 2 Short Steps
Al at 70 keV	.14	.156	.149	.157	.155
Al at 70 keV, 80°	.73	.573	.624	.579	.619
Au at 70 keV	.48	.457	.502	.453	.498
Au at 70 keV, 80°	.80	.674	.756	.671	.749

Table 6.13: Backscattered Fractions from Experiment and Monte Carlo

just over .60 [Dr70]. This second number is more in line with the trend of lower backscatter at higher energy (recall that at 10 keV the backscattering fraction was .66) and with the Monte Carlo runs, particularly in the short step situations, which have been seen to model aluminum backscattering fairly well in this energy regime.

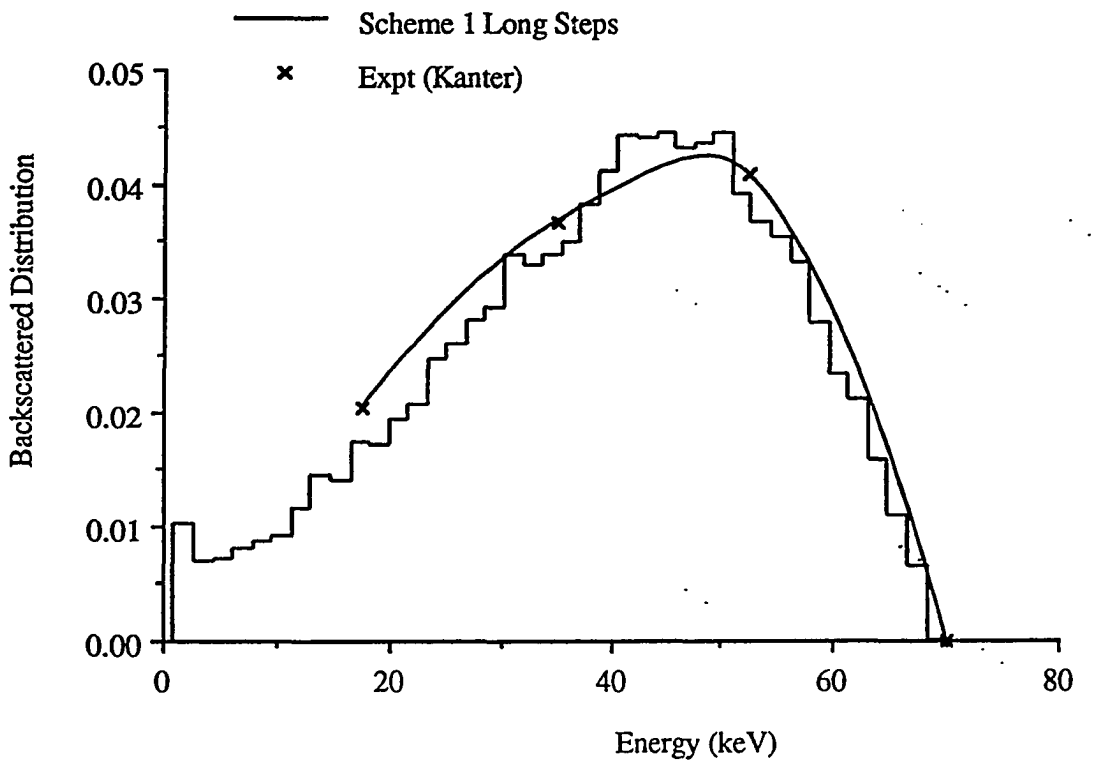

Figure 6.30: Backscattered Electron Energy Distributions for Class III, Scheme 1 (Long Steps) for 70 keV Electrons on Aluminum, Normally Incident

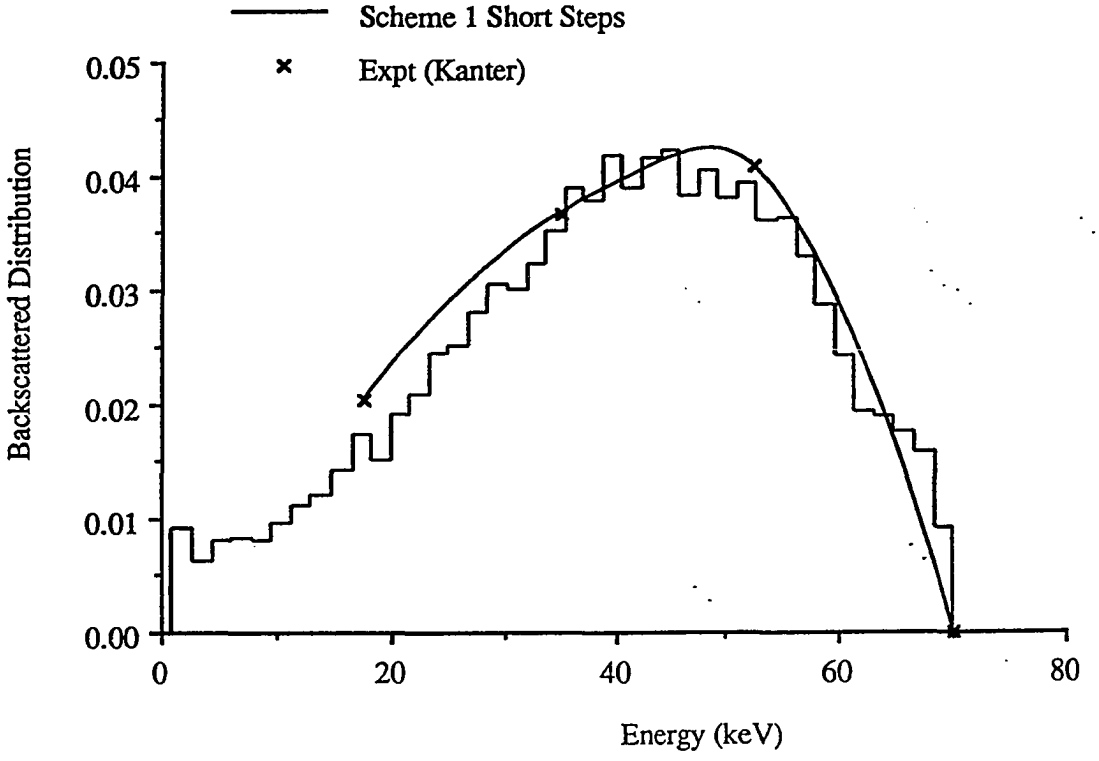

Figure 6.31: Backscattered Electron Energy Distributions for Class III, Scheme 1 (Short Steps) for 70 keV Electrons on Aluminum, Normally Incident

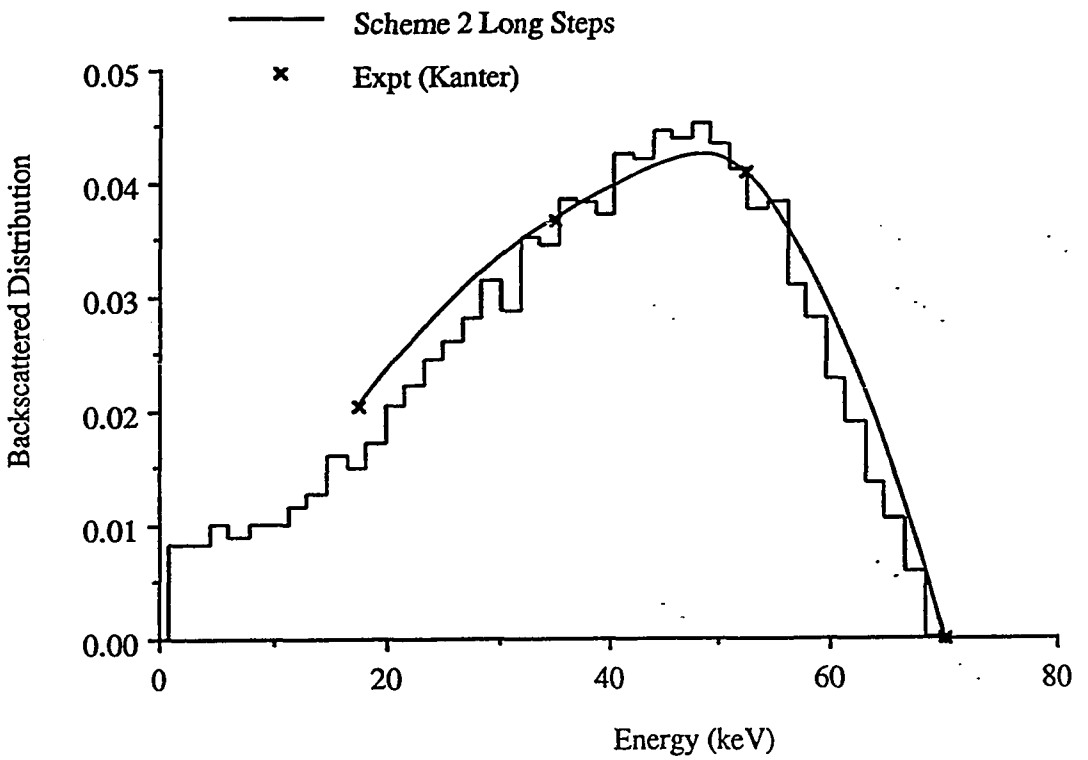

Figure 6.32: Backscattered Electron Energy Distributions for Class III, Scheme 2 (Long Steps) for 70 keV Electrons on Aluminum, Normally Incident

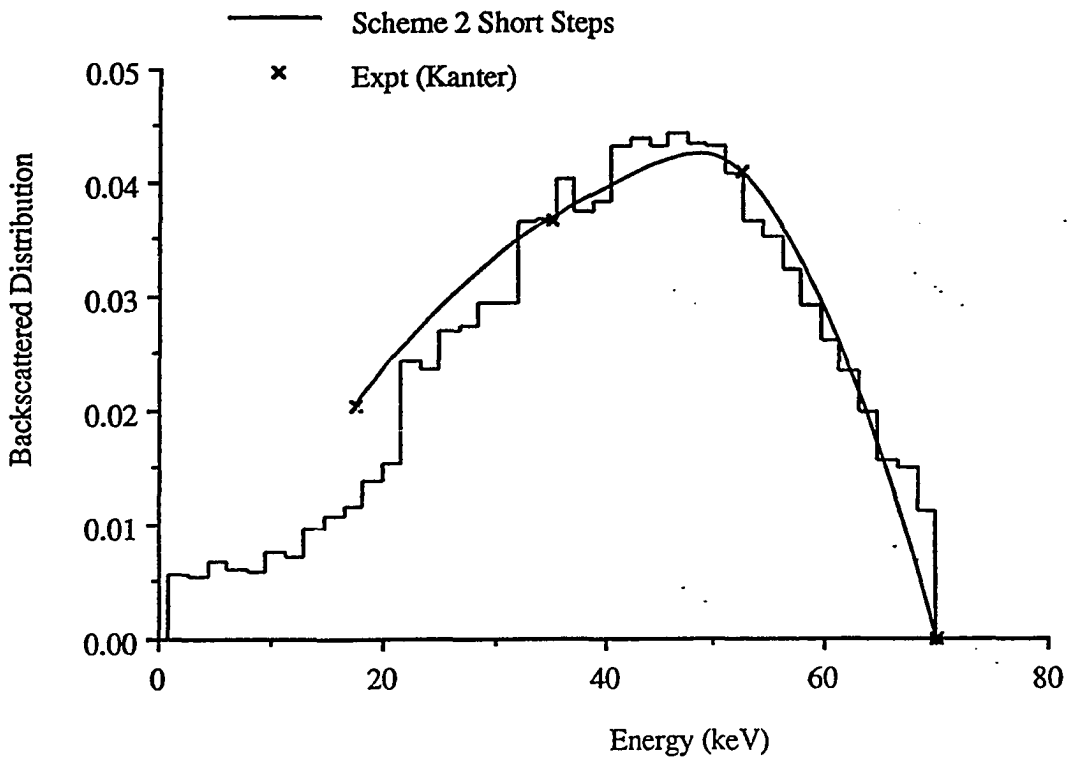

Figure 6.33: Backscattered Electron Energy Distributions for Class III, Scheme 2 (Short Steps) for 70 keV Electrons on Aluminum, Normally Incident

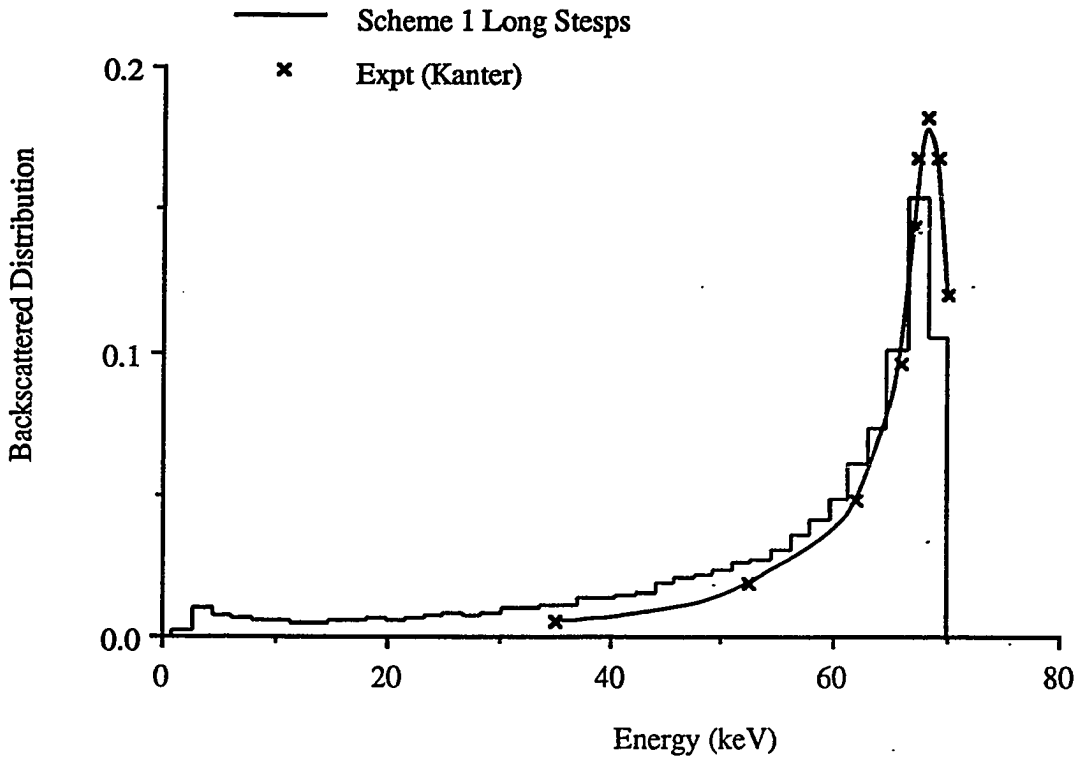

Figure 6.34: Backscattered Electron Energy Distributions for Class III, Scheme 1 (Long Steps) for 70 keV Electrons on Aluminum, 80° Incident

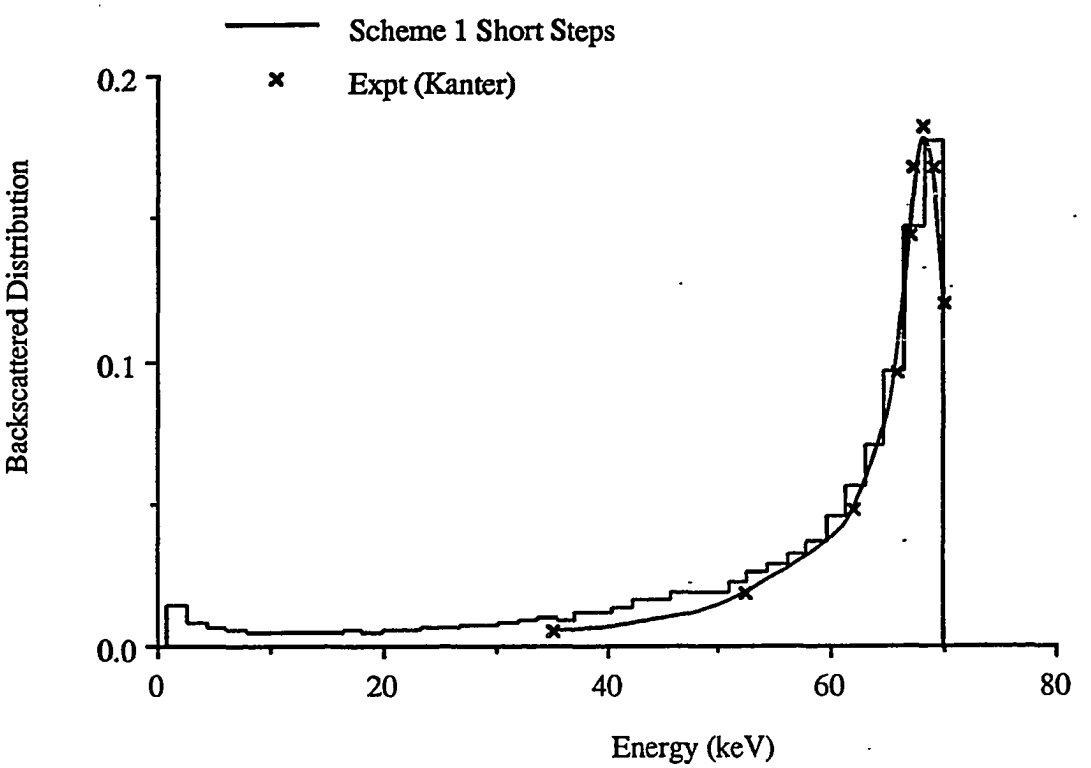

Figure 6.35: Backscattered Electron Energy Distributions for Class III, Scheme 1 (Short Steps) for 70 keV Electrons on Aluminum, 80° Incident

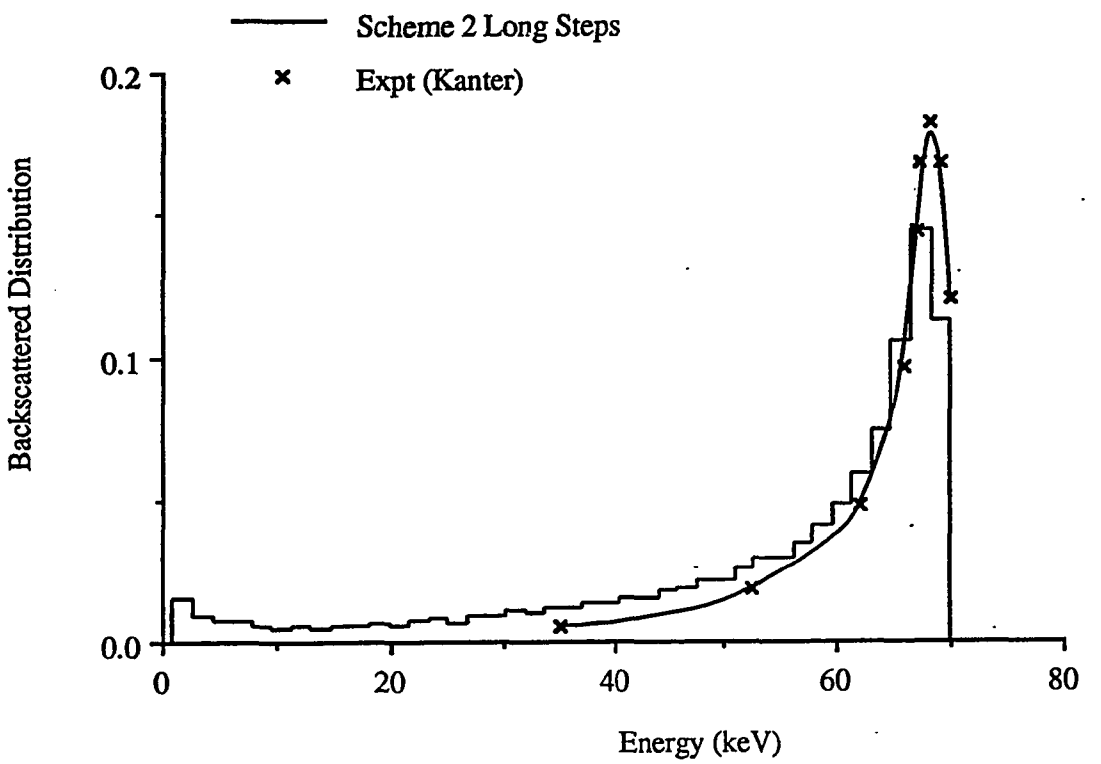

Figure 6.36: Backscattered Electron Energy Distributions for Class III, Scheme 2 (Long Steps) for 70 keV Electrons on Aluminum, 80° Incident

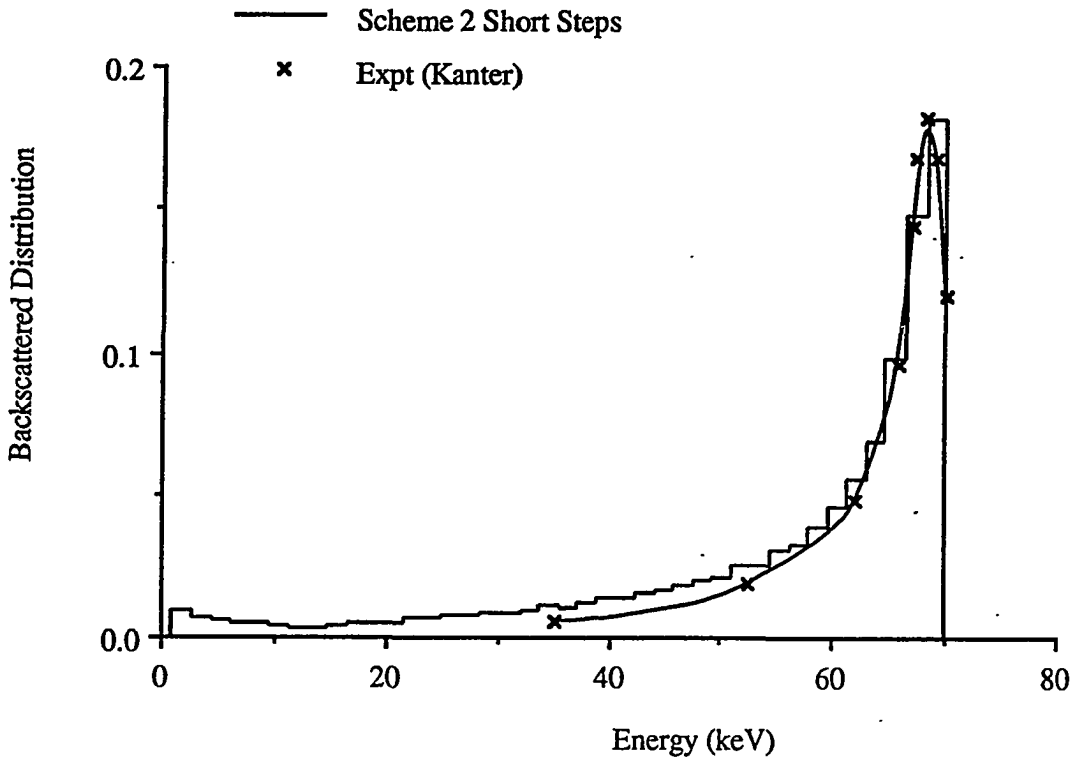

Figure 6.37: Backscattered Electron Energy Distributions for Class III, Scheme 2 (Short Steps) for 70 keV Electrons on Aluminum, 80° Incident

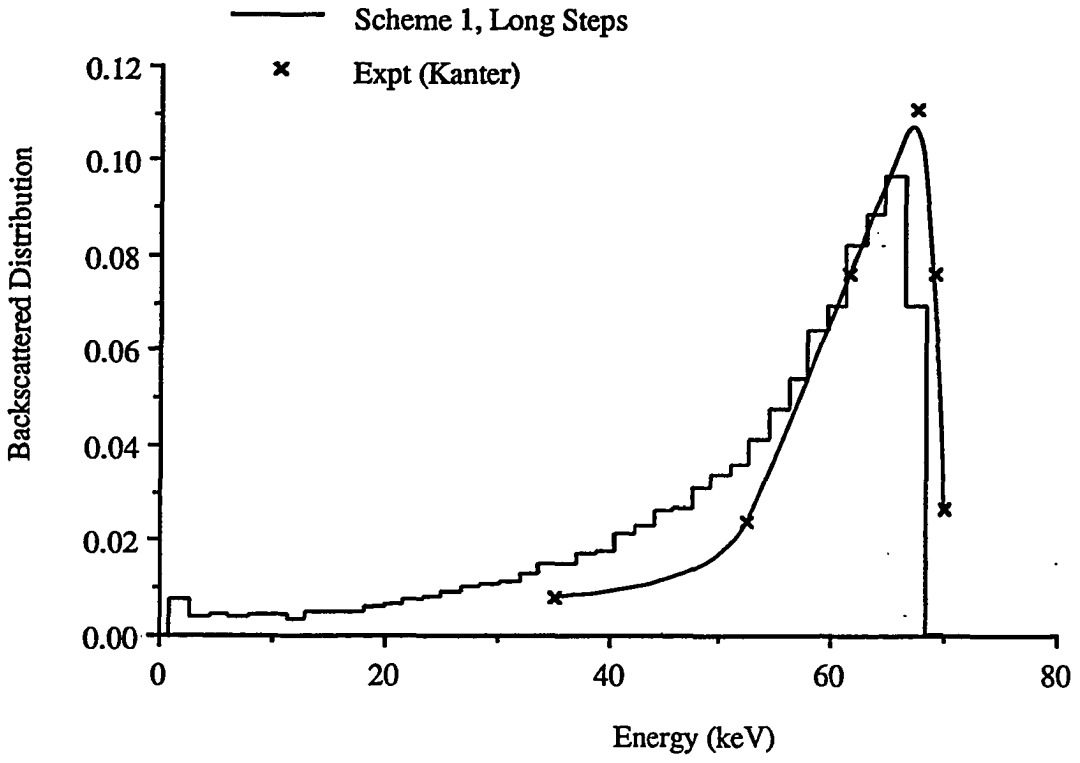

Figure 6.38: Backscattered Electron Energy Distributions for Class III, Scheme 1 (Long Steps) for 70 keV Electrons on Gold, Normally Incident

it is seen in the figures that both scheme 1 and scheme 2 model the distributions extremely accurately, so long as short steps are used. Somewhat surprisingly, the use of short steps even permits correct modeling of the energy spectrum in the region of small energy loss.

Numerical Comparisons

The number of tracks per incident electron, processing time per track, and total required processing time found in simulating some of these problems with the various schemes are presented in tables 6.14 through 6.15.

As expected, the short step simulations, for which the step was one fourth the step of the long step runs, took approximately 4 times as many steps. What is surprising about this data is the far fewer number of steps taken by the scheme 2

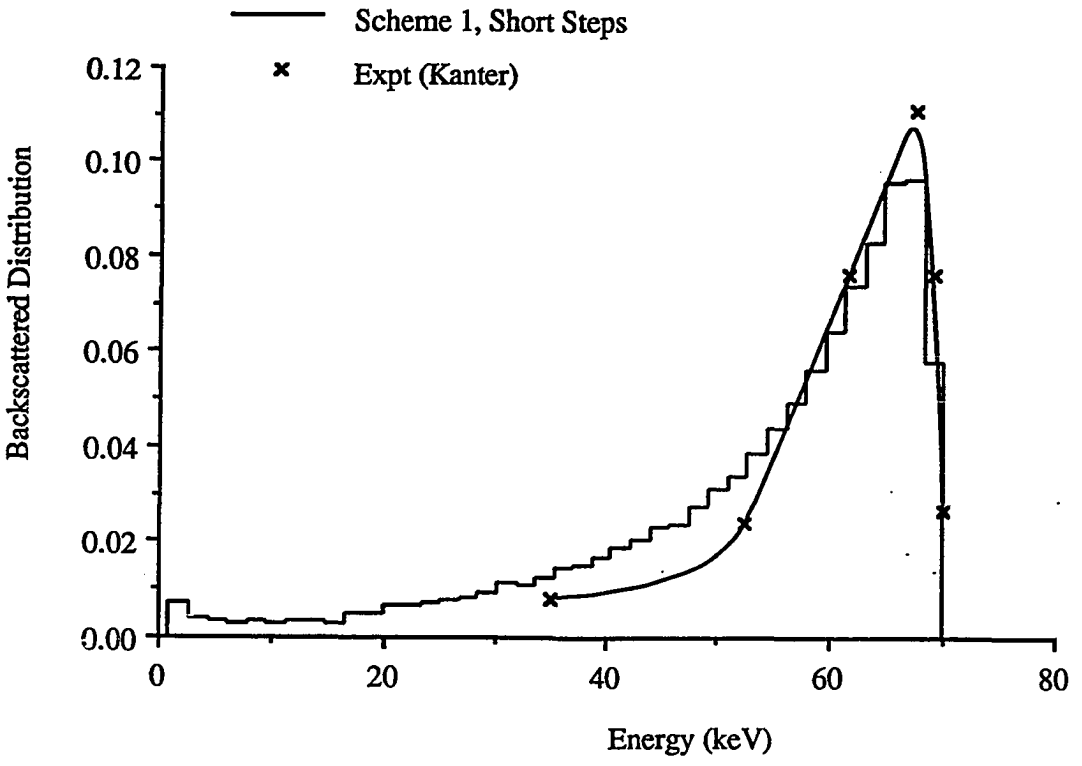

Figure 6.39: Backscattered Electron Energy Distributions for Class III, Scheme 1 (Short Steps) for 70 keV Electrons on Gold, Normally Incident

Experiment	Scheme 1 Long Steps	Scheme 1 Short Steps	Scheme 2 Long Steps	Scheme 2 Short Steps
Al at 70 keV	425	1719	370	1067
Cu at 70 keV	383	1533	304	751
Au at 70 keV	353	1319	225	497

Table 6.14: Number of Tracks per Incident Particle Predicted by Various Class III Models

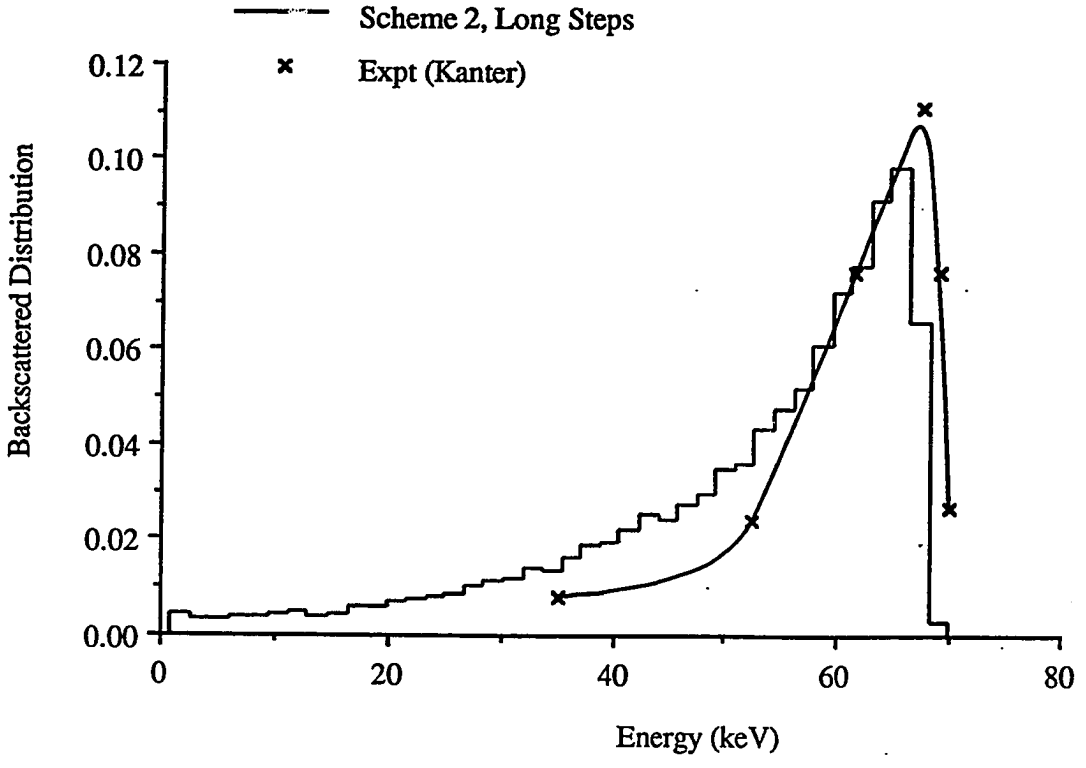

Figure 6.40: Backscattered Electron Energy Distributions for Class III, Scheme 2 (Long Steps) for 70 keV Electrons on Gold, Normally Incident

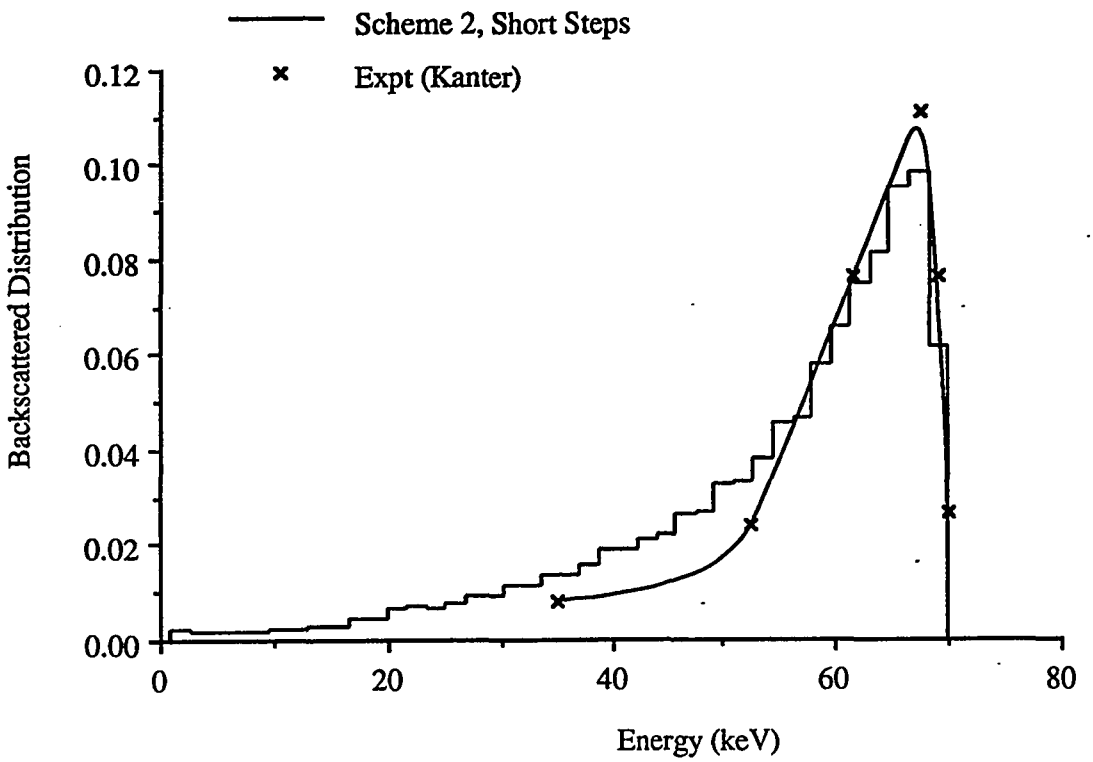

Figure 6.41: Backscattered Electron Energy Distributions for Class III, Scheme 2 (Short Steps) for 70 keV Electrons on Gold, Normally Incident

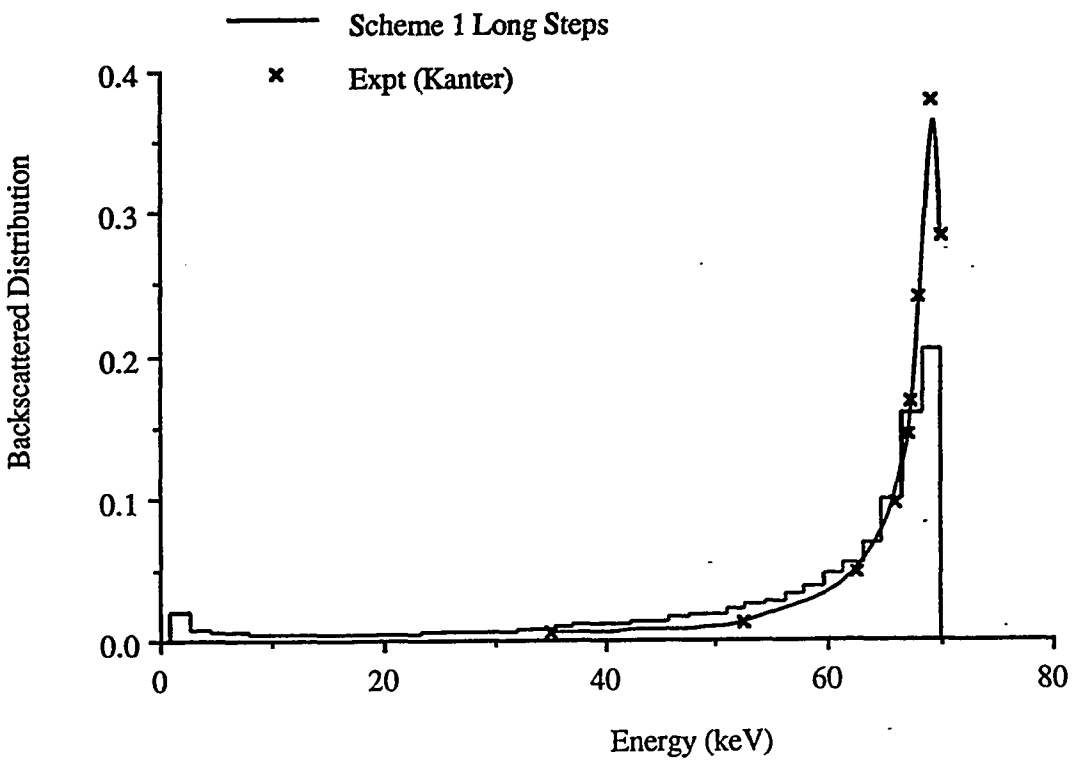

Figure 6.42: Backscattered Electron Energy Distributions for Class III; Scheme 1 (Long Steps) for 70 keV Electrons on Gold, 80° Incident

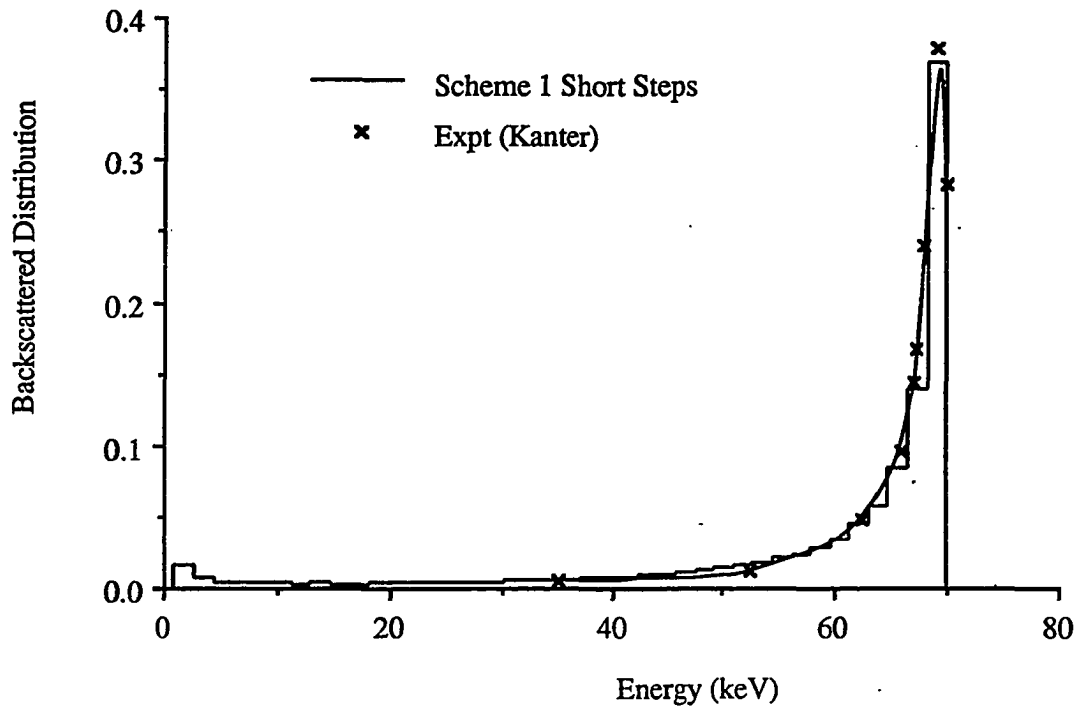

Figure 6.43: Backscattered Electron Energy Distributions for Class III, Scheme 1 (Short Steps) for 70 keV Electrons on Gold, 80° Incident

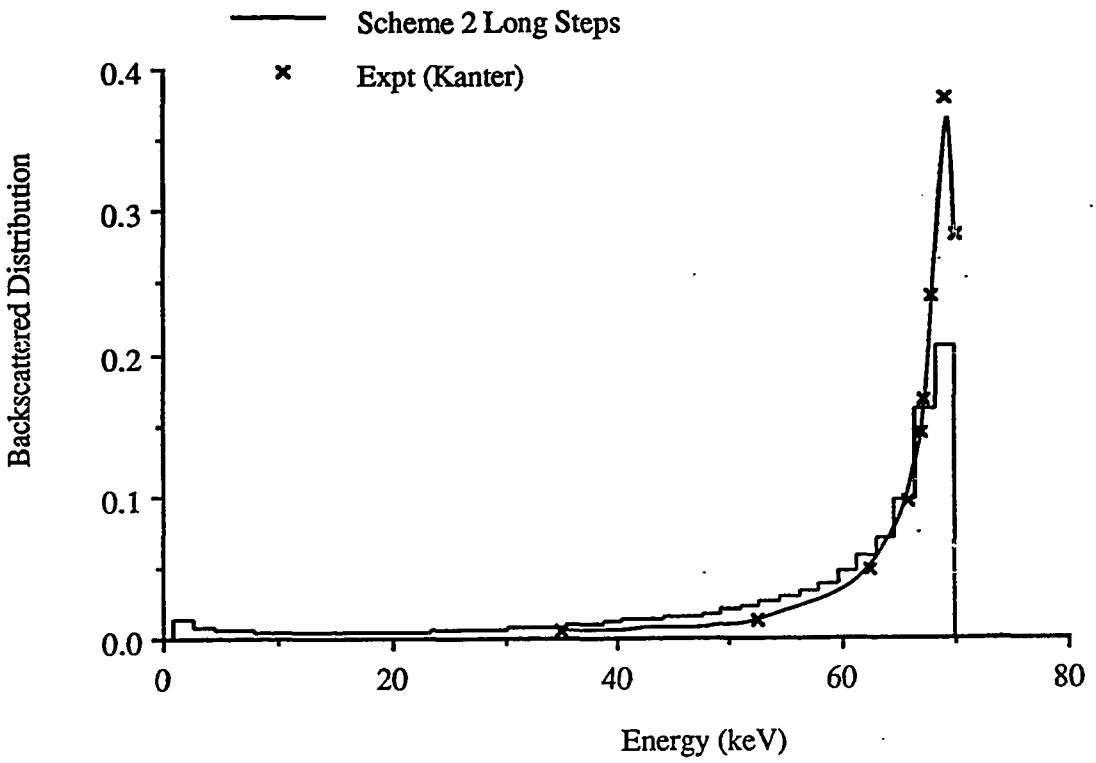

Figure 6.44: Backscattered Electron Energy Distributions for Class III, Scheme 2 (Long Steps) for 70 keV Electrons on Gold, 80° Incident

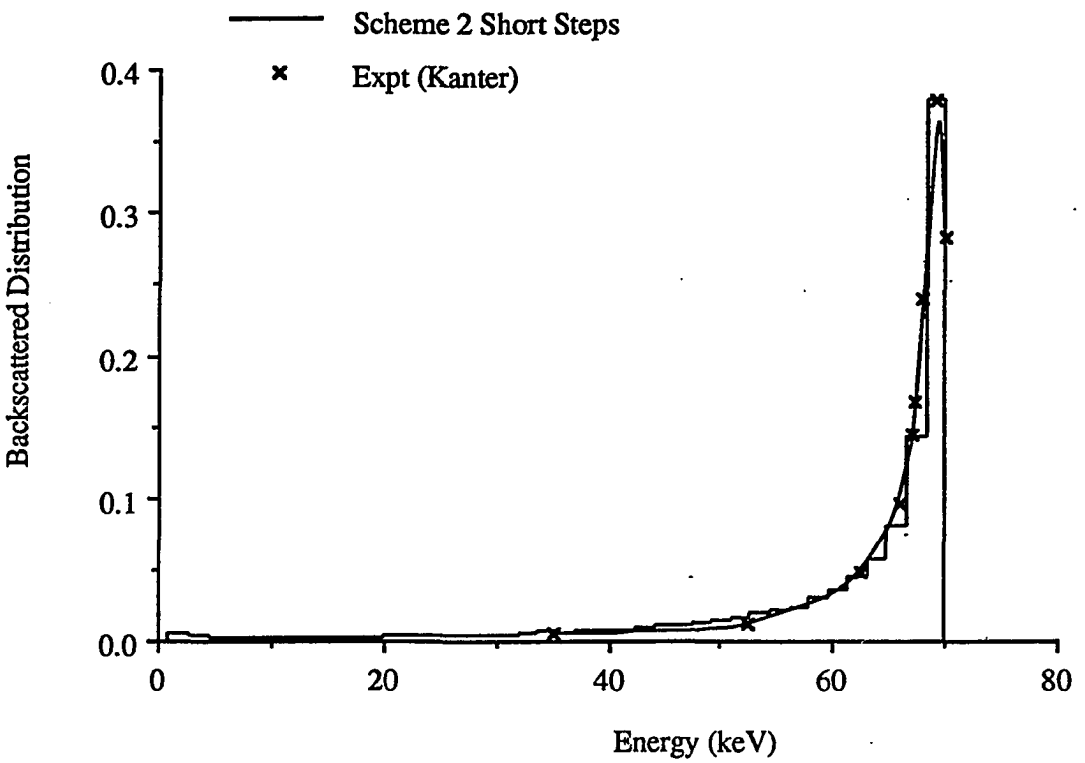

Figure 6.45: Backscattered Electron Energy Distributions for Class III, Scheme 2 (Short Steps) for 70 keV Electrons on Gold, 80° Incident

Experiment	Scheme 1 Long Steps	Scheme 1 Short Steps	Scheme 2 Long Steps	Scheme 2 Short Steps
Al at 70 keV	6.38	5.50	6.88	6.20
Cu at 70 keV	6.37	5.52	6.96	6.43
Au at 70 keV	6.30	5.50	6.98	6.54

Table 6.15: Computation Speed (μsec/track) for Various Class III Models

Experiment	Scheme 1 Long Steps	Scheme 1 Short Steps	Scheme 2 Long Steps	Scheme 2 Short Steps
Al at 70 keV	2.715	9.544	2.545	6.615
Cu at 70 keV	2.437	8.471	2.115	4.833
Au at 70 keV	2.225	7.259	1.571	3.253

Table 6.16: Computation Time (msec/particle) Required for Various Class III Models

models. This can only come about because of a skewing of the distribution toward more high energy losses. The effect is more dramatic for heavier elements.

In keeping with expectations, the use of fluctuations slows the processing time per particle because an extra distribution sampling procedure must be performed. The effect is most dramatic for short steps, for which distribution sampling comprises a greater fraction of the total processing time.

Similar to the results seen for class I algorithm, the high number of backscattered electrons for heavy elements results in shorter processing time for these materials.

Conclusions

Clearly, very small step sizes must be used to accurately simulate transport at low energies. Also, there appears to be a breakdown in scheme 2 caused by inaccuracies in the Vavilov fluctuation distribution at low energies. Additionally, a potential breakdown in the model itself is seen at high Z materials as low as 50 keV. Whether or not this could be alleviated by the use of even smaller steps is uncertain. Indeed, for the short step simulations described above, the average loss in gold is about 100 eV at steps taken around 50 keV and 4 eV for steps at 1 keV.

6.2 Applicability of Algorithm Classes

This section seeks to define the regions in Z and E for which the best models in the different classes of algorithms, as determined in the previous section, are best suited, with respect to both accuracy in reproducing experimental results and computation time. This analysis essentially involved attempting to apply class III models at low velocity and class I schemes at high velocities. Models chosen for this simulation are models 4 and 5 of the class I algorithm, a class II model using the same 'important' cross sections as model 5 of class I, and a class III, scheme 1 model using short steps, as defined in the previous section. The analysis is carried out similar to the analysis of the models within each class, first by generating simple thick target backscattering fractions, and then by examining results of more detailed simulations

Backscattering fractions from simulations and experiment are shown in figures 6.46 through 6.48.

For aluminum, the class I and II schemes consistently overestimate the backscattering fraction for energies above 10 keV. There is a great deal of uncertainty as to the backscatter fraction below 10 keV or so, with recent data suggesting that it is

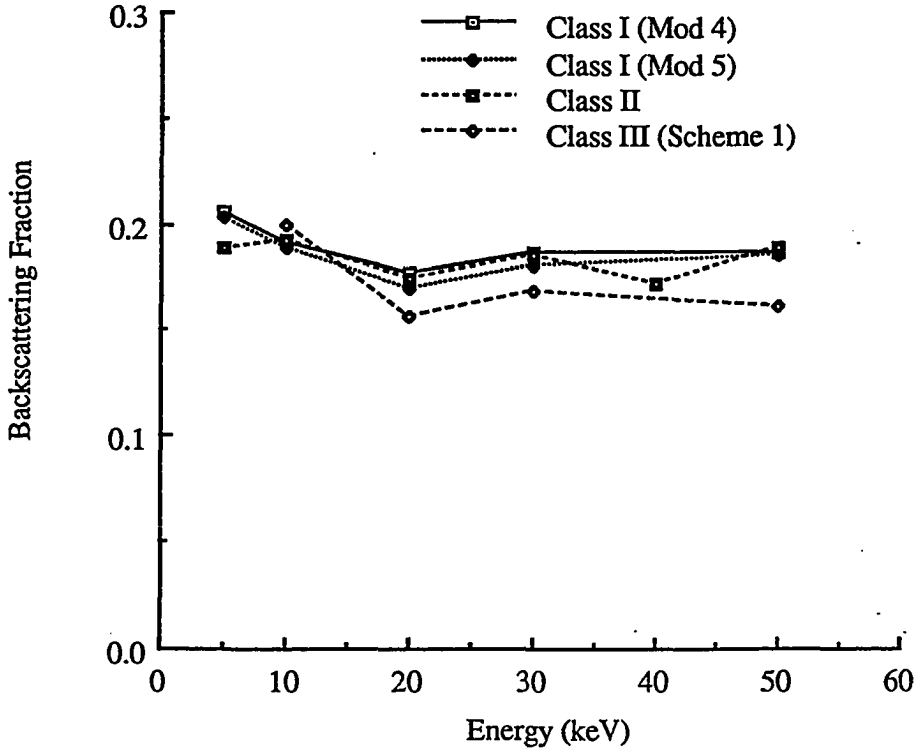

Figure 6.46: Backscattering Fractions at Kilovolt Energies for Aluminum, Experiment and Monte Carlo

around .19, (which agrees well with all three schemes) and older data predicting a somewhat lower value. At energies greater than 110 keV, while there is no general agreement as to the correct value, there is no data which predicts as high a value as the class I and class II schemes. The problem may lie in the extreme difficulty in numerically modeling the Riley elastic cross section for Al, as discussed in a succeeding section.

For copper, all 4 models consistently predict the relatively flat or gently rising backscattering fraction typically encountered in experimental data. All models also lie within the range of experimentally predicted values, with the class II model agreeing very well with the data of Drescher *et al*[Dr70] and of Darlington [Da75], and the class I and II data extremely close to that of Neubert and Rogaschewski [Ne80] and of Bishop (as cited in [Ne80]). No absolute conclusions can be drawn as to validity

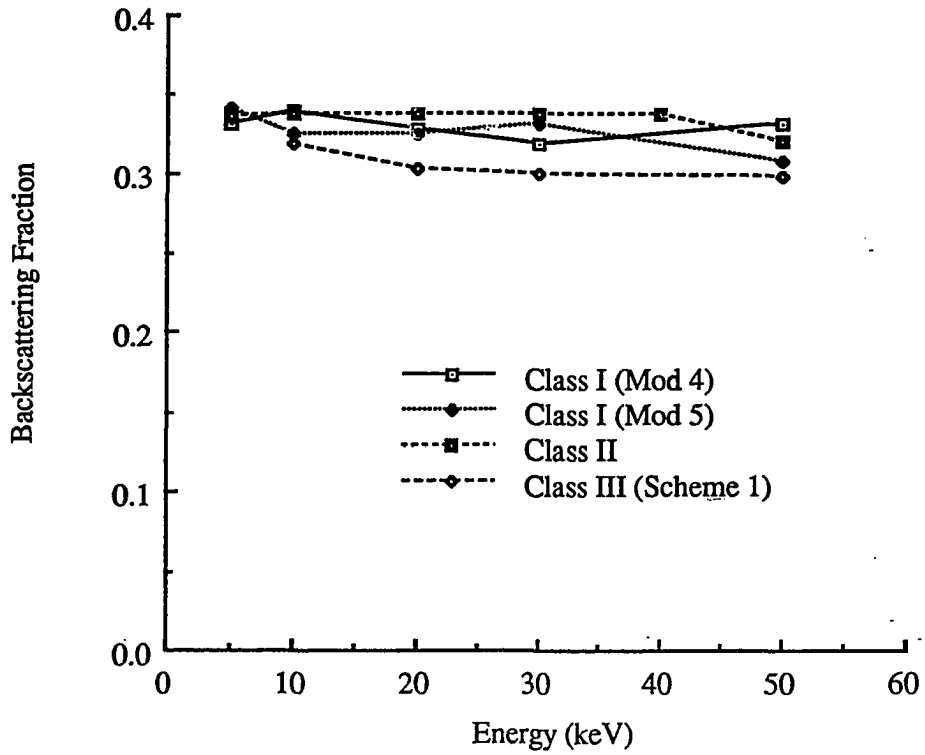

Figure 6.47: Backscattering Fractions at Kilovolt Energies for Copper, Experiment and Monte Carlo

conditions.

The situation for the gold backscattering case is somewhat similar to that in copper, as all models correctly predict the established trend (in this case, softly decreasing backscatter with energy), yet there is a distinct difference in the magnitude predicted by the single scattering and condensed history cases, and all simulated results fall close to one experiment or another. In this instance however, the majority or the data tends validate the single scattering models, which predict slightly higher backscattering fractions.

The number of tracks and total computation time (per particle) required for simulating these backscattering experiment for the 4 models as a function are shown in figures 6.49 through 6.54.

The interesting result from this section is that the number of tracks required to

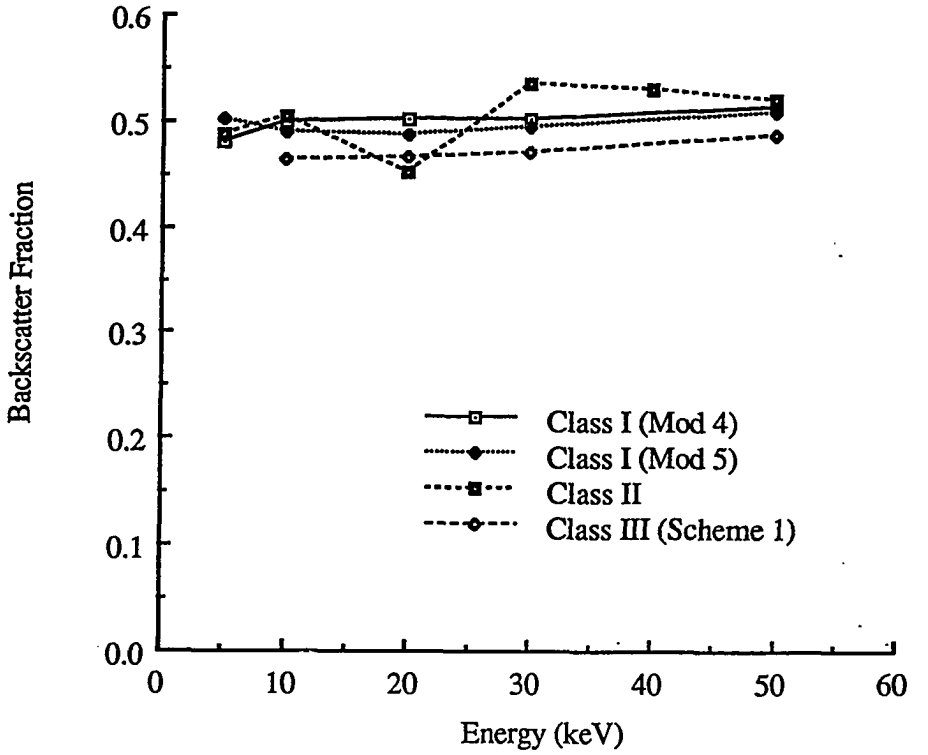

Figure 6.48: Backscattering Fractions at Kilovolt Energies for Gold, Experiment and Monte Carlo

perform a calculation using a condensed history model actually exceeds that required by a class I single scattering model for low energies (below 15 or 20 keV), and is greater than the number of collisions in a class II model at all energies examined here. This is certainly because the very small step sizes required for accurate modeling force a great many transport steps on the class III schemes at low energies.

The time advantage achieved by using class III models at higher energies is apparent from figures 6.52 through 6.54. It is seen that while the single scattering tracking time increase almost linearly with energy, the class III time rises much more slowly, which is as expected since the step sizes are set between logarithmically varying energy points. Note that the the extra vectorization speed attained by the class III schemes yields a fast computation even though more tracks are model, as compared with the class II single scattering model.

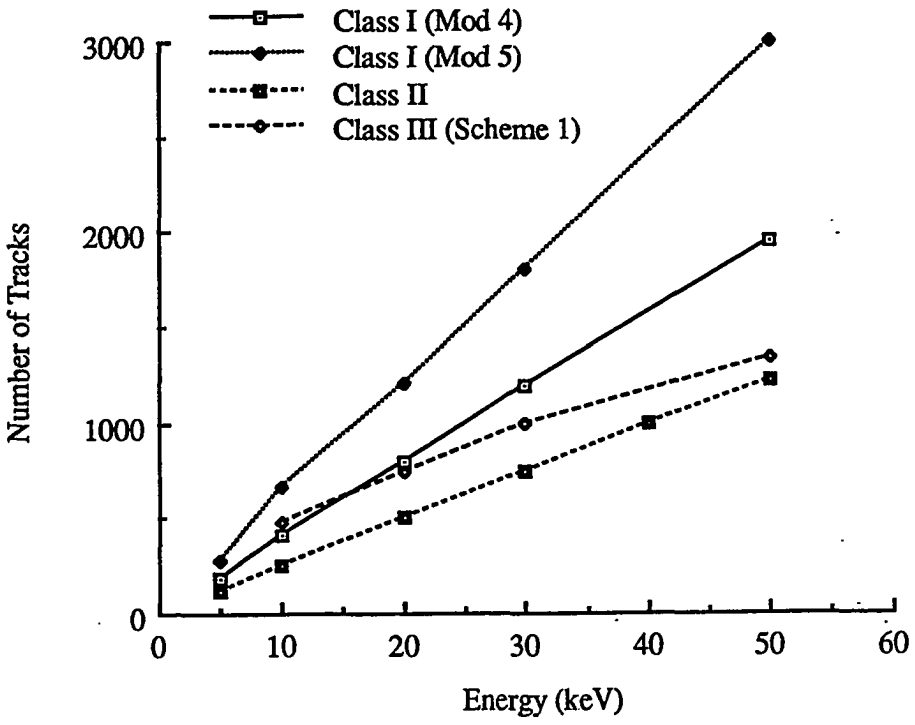

Figure 6.49: Number of Tracks per Incident Particle at Kilovolt Energies for Aluminum

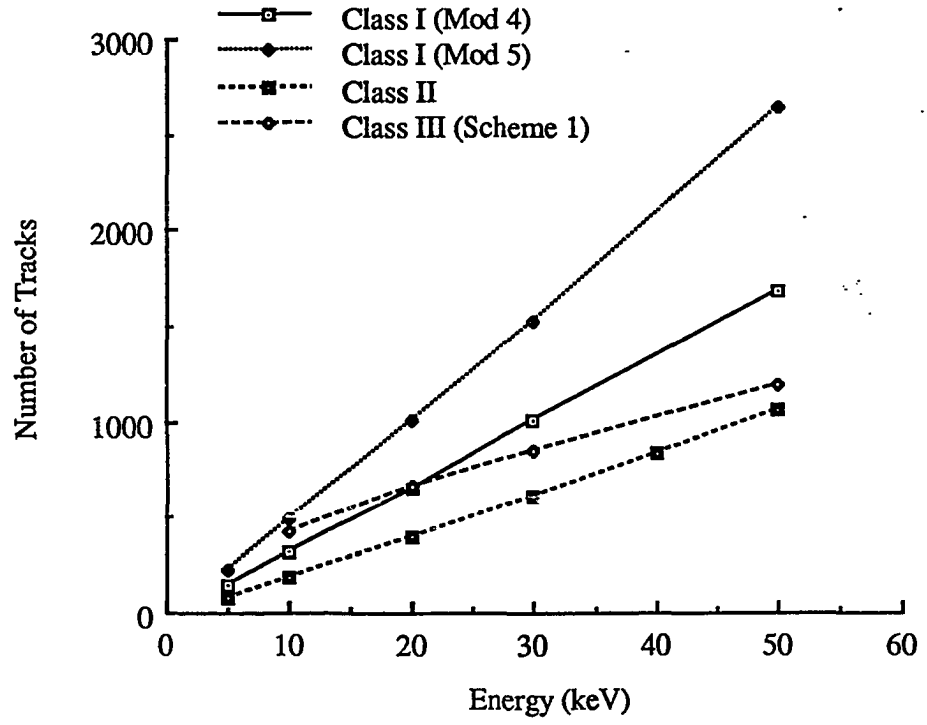

Figure 6.50: Number of Tracks per Incident Particle at Kilovolt Energies for Copper

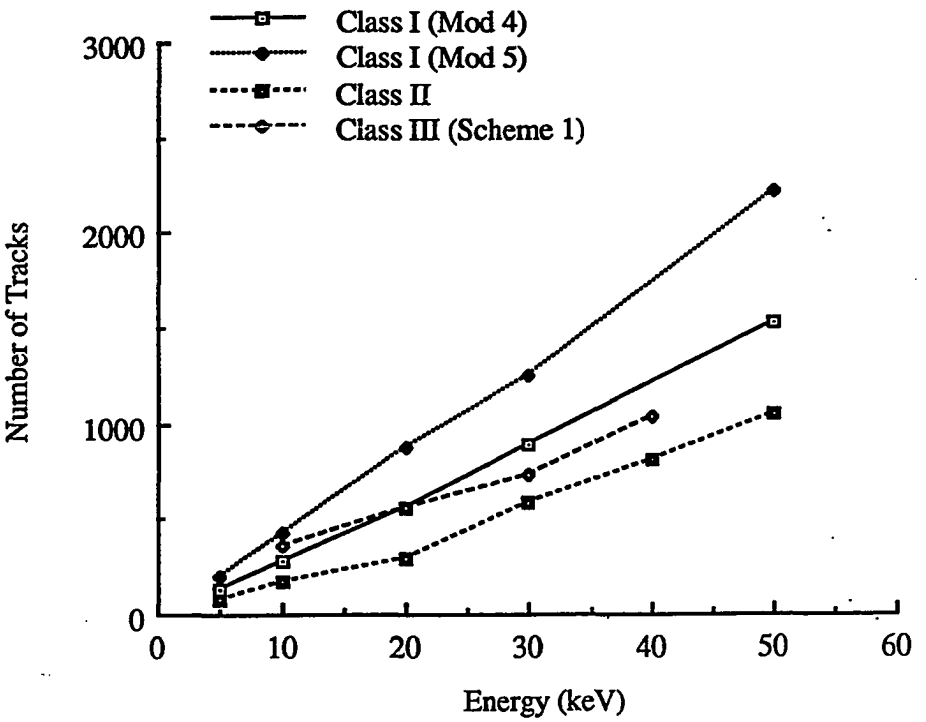

Figure 6.51: Number of Tracks per Incident Particle at Kilovolt Energies for Gold

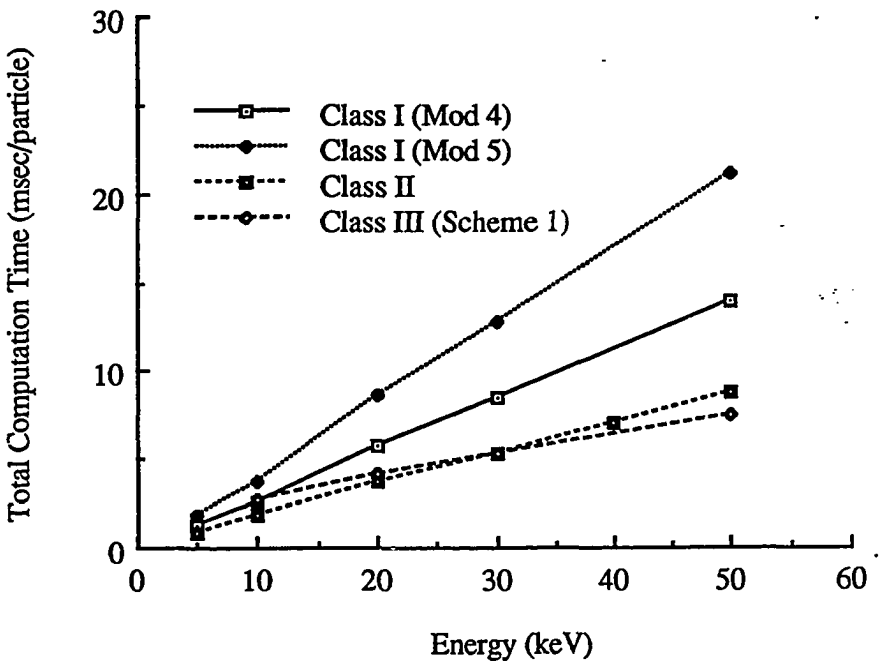

Figure 6.52: Computation Time (msec) per Incident Particle at Kilovolt Energies for Aluminum

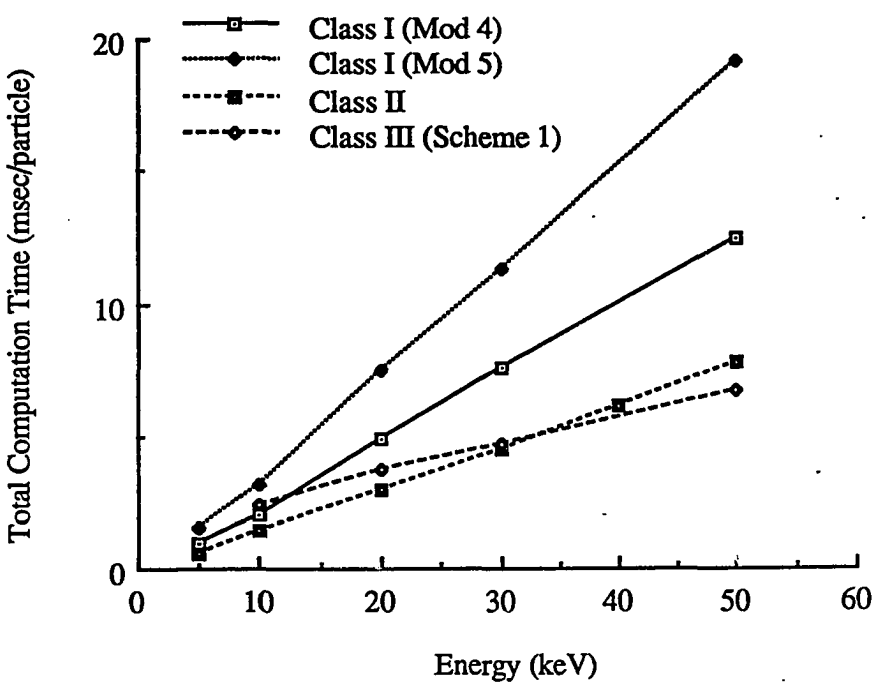

Figure 6.53: Computation Time (msec) per Incident Particle at Kilovolt Energies for Copper

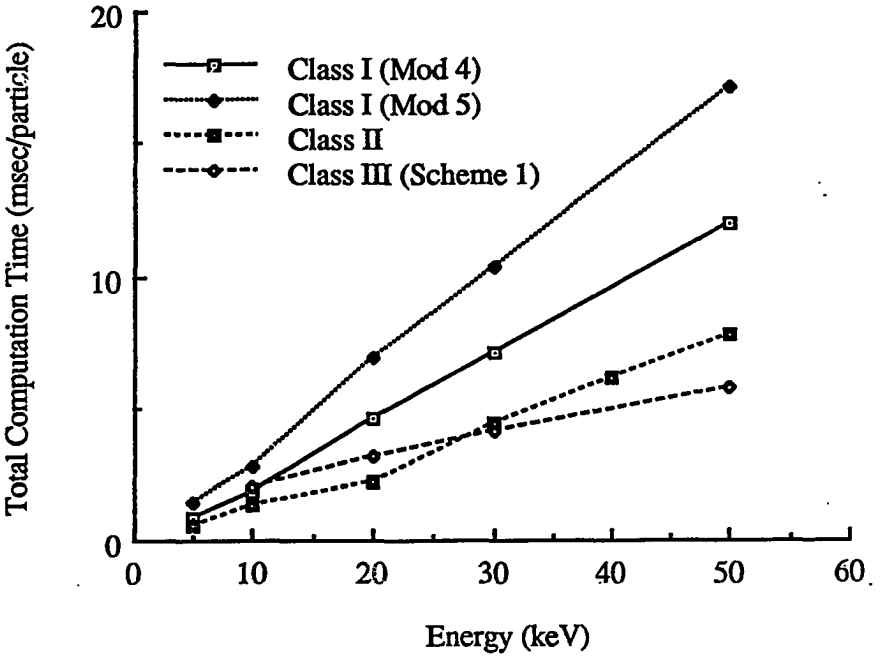

Figure 6.54: Computation Time (msec) per Incident Particle at Kilovolt Energies for Gold

Further experiments used in this analysis are backscattered energy loss distribution experiments of Darlington at 30 keV for aluminum, copper and gold. Plots of results from theses runsa are shown in figures 6.55 through 6.63.

For aluminum, we see that all of the models underestimate the width of the distribution and overestimate the height of the tail, and that the class III scheme best models the low energy loss portion of the distribution. (The class I, model 5 results may be better than the class I, model 4 result. At 10 keV in aluminum, model 5 predicts fewer high energy particles being backscattered, which is where model 4 is deficient. Model 4 was chosen for these runs because it is roughly twice as fast and very time consuming runs were required to achieve good statistics. In retrospect, that may have been a mistake.) It certainly seems as though the condensed history technique is desirable in this regime, as the simulation is accurate and it is much

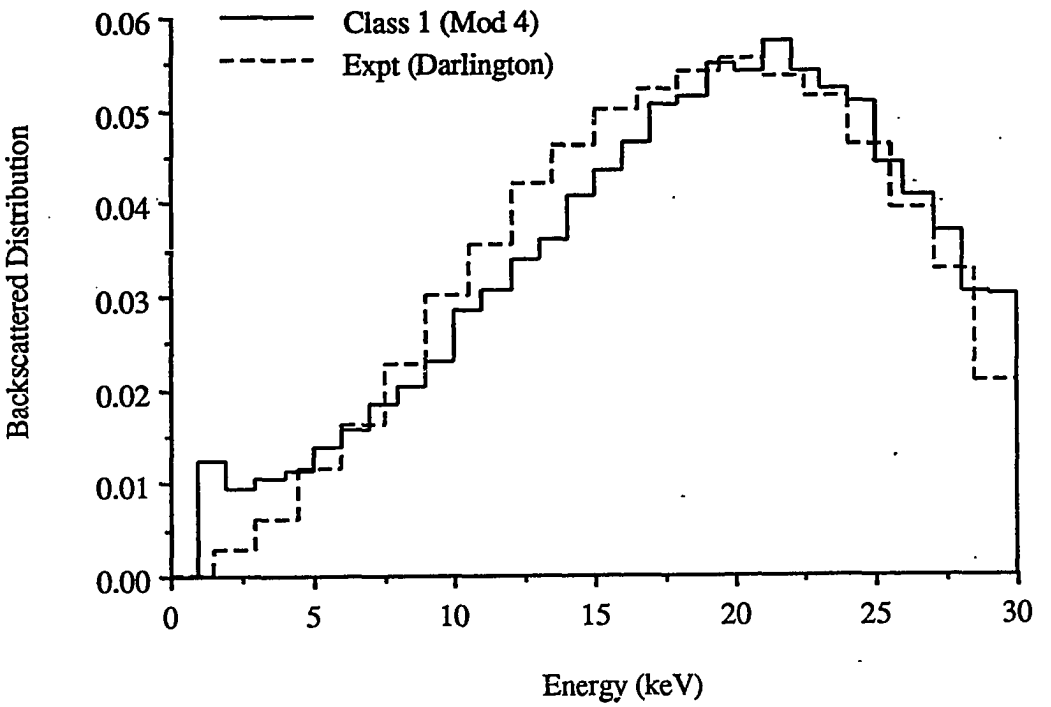

Figure 6.55: Backscattered Energy Distributions for 30 keV Electrons Incident on Aluminum, Experiment vs Class I Model 4

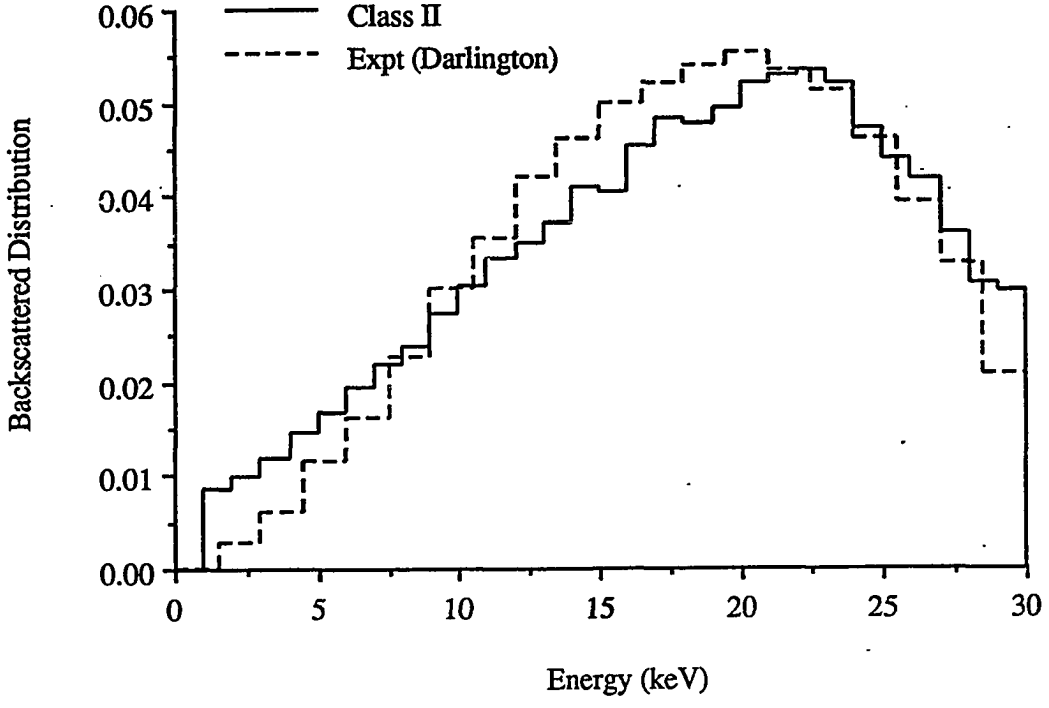

Figure 6.56: Backscattered Energy Distributions for 30 keV Electrons Incident on Aluminum, Experiment vs Class II Model

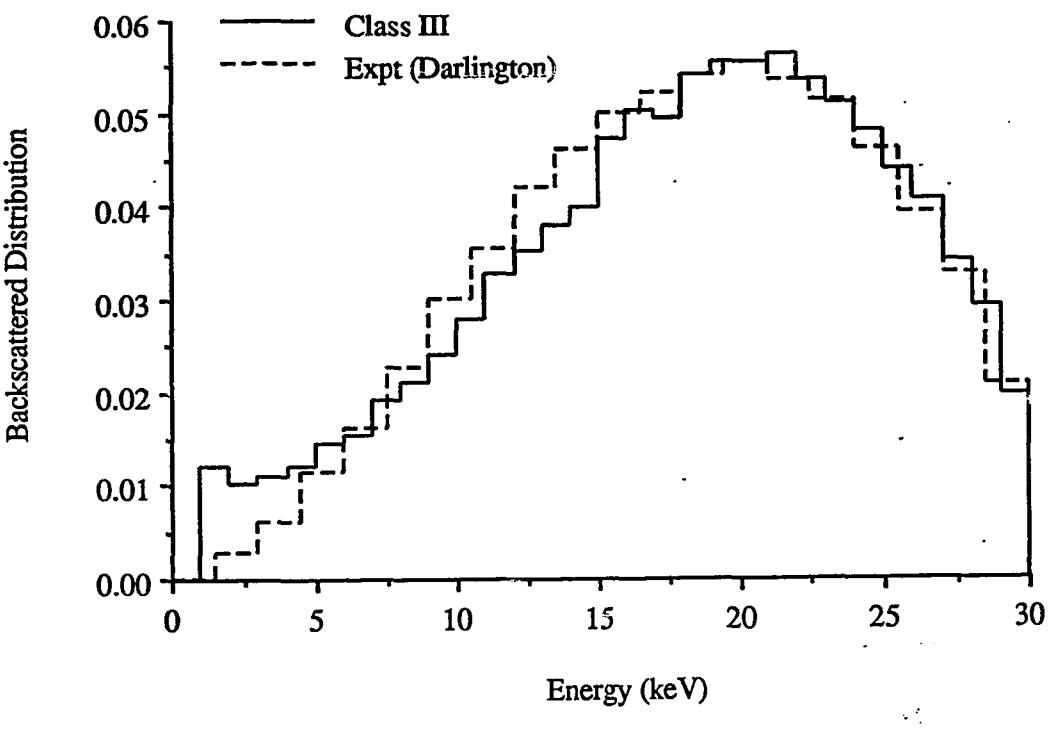

Figure 6.57: Backscattered Energy Distributions for 30 keV Electrons Incident on Aluminum, Experiment vs Class III Model

faster. In general, the condensed history technique does not seem to lose validity in aluminum scattering simulations down to the point below which it becomes slower than single scattering models, roughly 5 to 15 keV. Above 10 keV, it does not suffer from the numerical difficulties incumbent upon single scattering codes, and as it is also faster, it is clearly preferable.

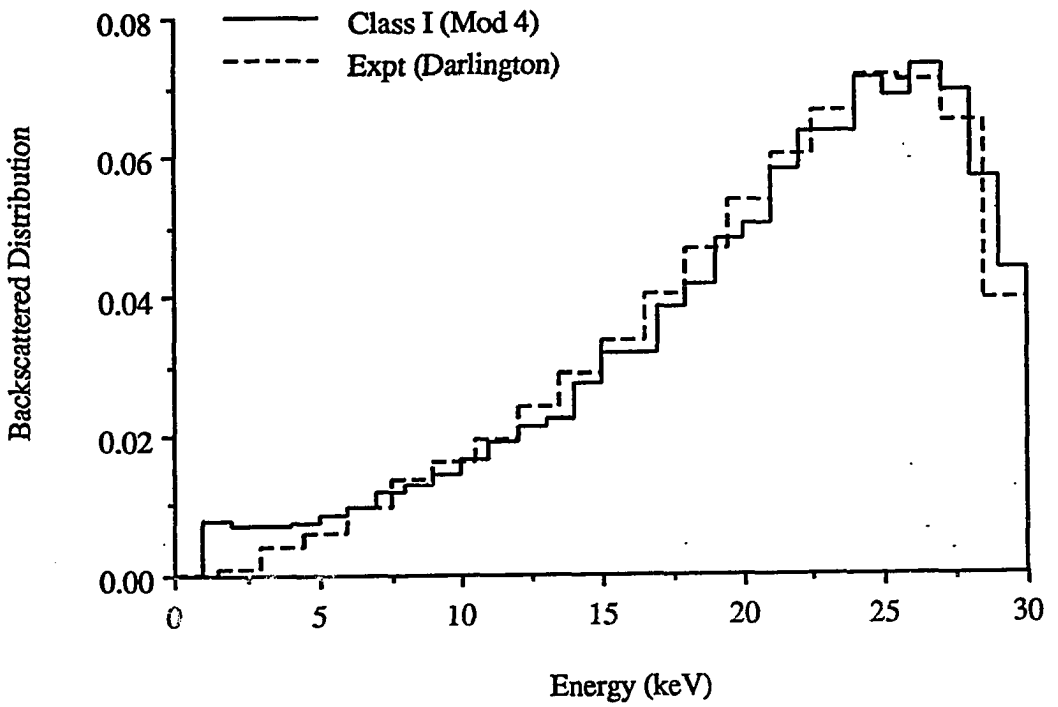

Figure 6.58: Backscattered Energy Distributions for 30 keV Electrons Incident on Copper, Experiment vs Class I Model 4

In the copper simulation, the class II scheme models the low loss region quite well, but the tail very poorly, predicting much too narrow of a spectrum.. The condensed history scheme models the tail extremely well, but underestimates the the low loss portion of the distribution. The class I model does quite well in all regions.

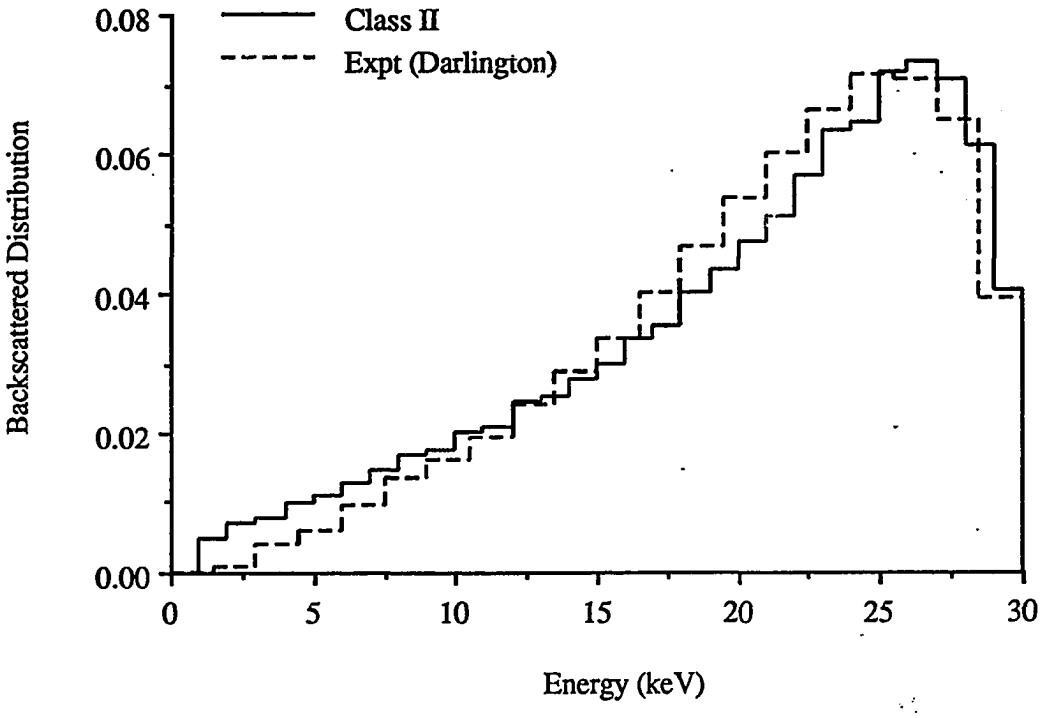

Figure 6.59: Backscattered Energy Distributions for 30 keV Electrons Incident on Copper, Experiment vs Class II Model

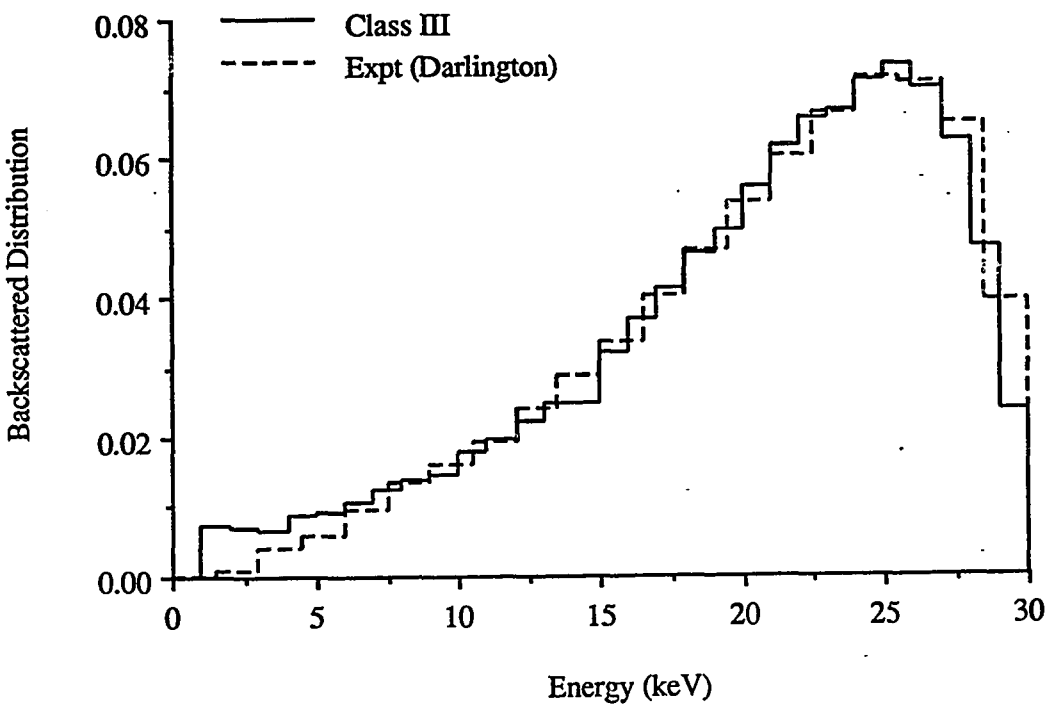

Figure 6.60: Backscattered Energy Distributions for 30 keV Electrons Incident on Copper, Experiment vs Class III Model

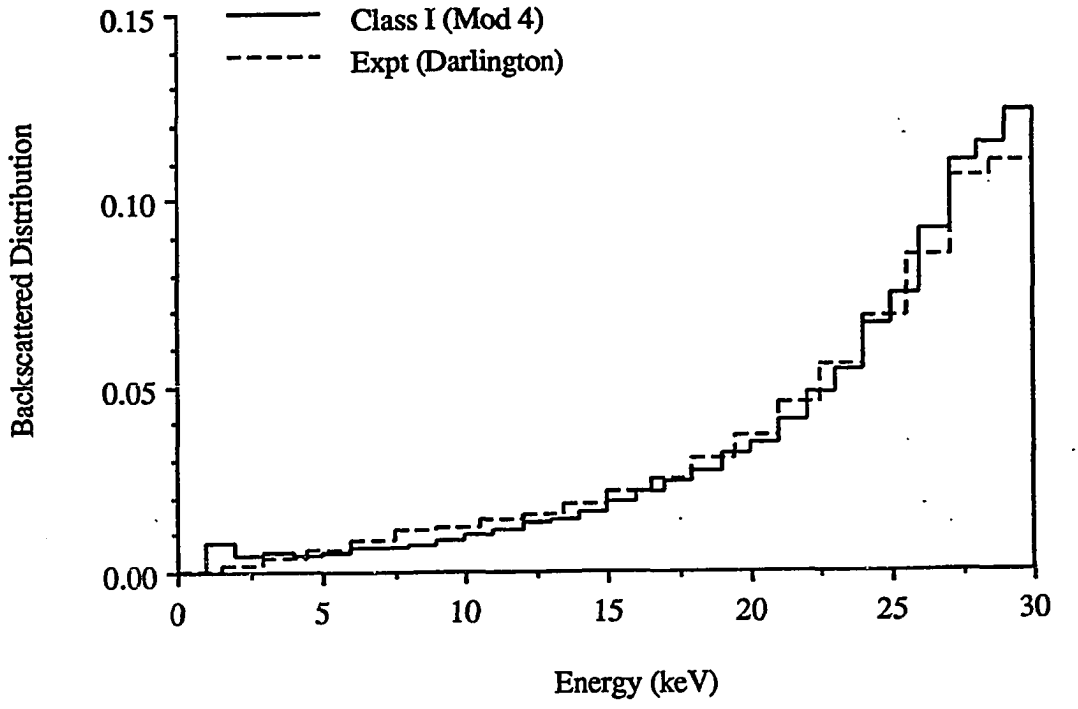

Figure 6.61: Backscattered Energy Distributions for 30 keV Electrons Incident on Gold, Experiment vs Class I Model 4

In gold at 30 keV, the condensed history case performs poorly, shifting the distribution peak toward low energy and overestimating its magnitude. The class II scheme again predicts too narrow of a distribution. The class I scheme underestimates the peak, but locates it correctly and the overestimation is slight.

In summary, condensed history schemes are desirable in low Z materials down to the point at which they become just as time consuming as accurate, class I schemes, from 5 to 15 keV. In high Z materials, they lose accuracy at higher energies (from 20 to perhaps 40 or 50 keV), and a trade-off must be made between the longer run times required by single scattering models and the desire for accuracy which they can provide.

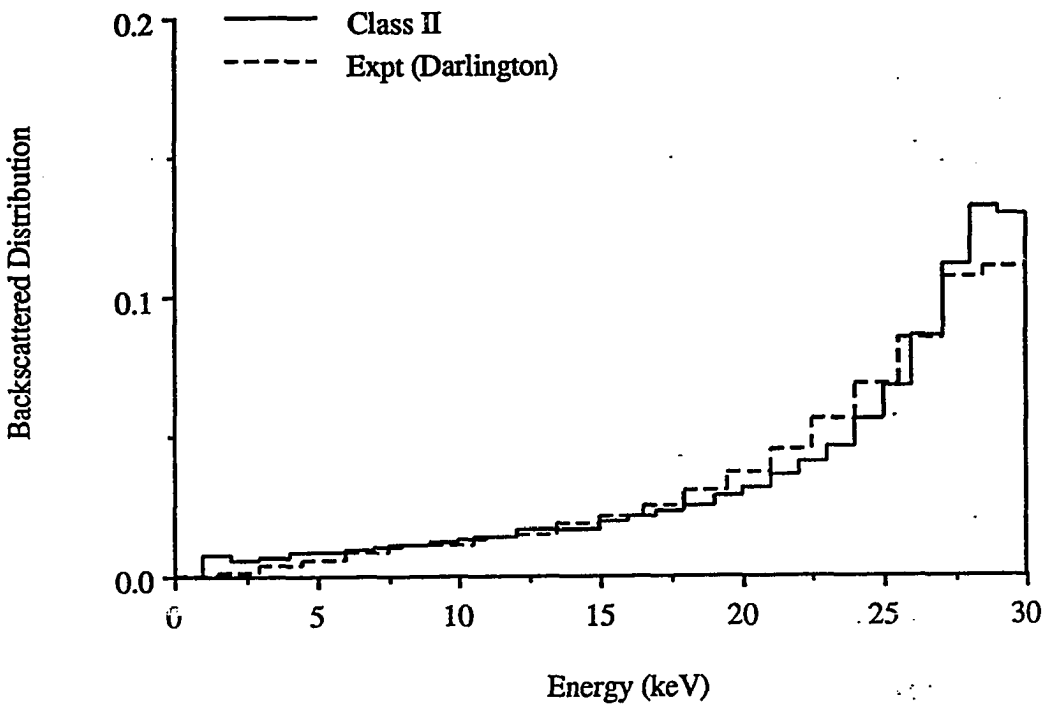

Figure 6.62: Backscattered Energy Distributions for 30 keV Electrons Incident on Gold, Experiment vs Class II Model

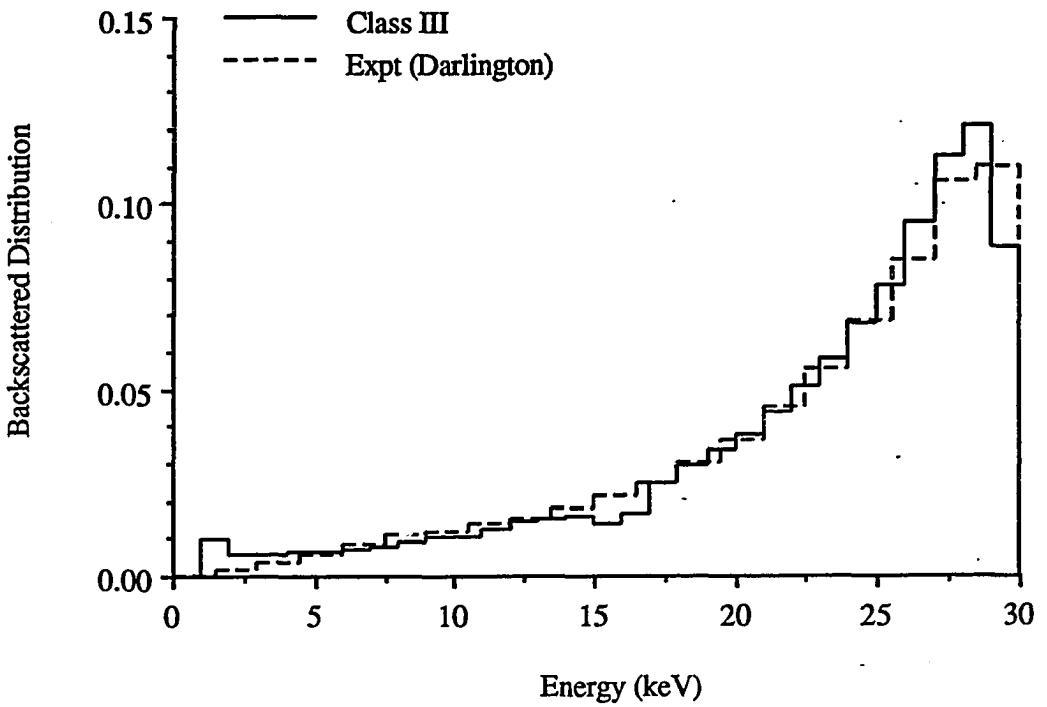

Figure 6.63: Backscattered Energy Distributions for 30 keV Electrons Incident on Gold, Experiment vs Class III Model

Problem	Algorithm (μsec / track)	Scalar Speed (μsec / track)	Vector Speed	Speed Up
Aluminum Backscattering	Class I	37.24	6.03	6.18
	Class II	38.20	6.86	5.56
	Class III	37.45	5.50	6.81
Copper Backscattering	Class I	36.66	6.43	5.70
	Class II	38.38	6.96	5.51
	Class III	36.58	5.52	6.63
Gold Backscattering	Class I	37.71	6.36	5.93
	Class II	38.40	7.02	5.47
	Class III	37.35	5.50	6.79

Table 6.17: Vector Speed ups

Despite the extreme speed relative to the class I single scattering model, the class II scheme never fits a in a niche in which it is the desired technique, as in all situations either a class III scheme would be faster and still be just as accurate, or a class I model would be much more accurate, or both.

6.3 Vectorization Speed-ups

Several examples of each of the three classes of transport algorithms were run in both vector and scalar modes in order to determine the speed up due solely to vectorization. Speed ups are expected to be very similar within each the classes, since much of the same coding was used for each type of algorithm. Three problems were run to check for consistency, and the most accurate models for each class of algorithm were chosen for this comparison. Results are presented in table 6.17.

As anticipated, speed up is consistent within each class, although as explained earlier, class I models run somewhat faster for low Z materials, since the smaller number of rare inner ionizations limits the number of short loops. Between the models there are some differences in speed up, with the speed up is greatest for the class III algorithm, which performs the most long vector operations in all cases.

The vectorization speed up is not particularly impressive, but it is in line with the results for sampling speed ups seen in chapter 5. Also contributing to the small speed enhancement seen is the rather short maximum vector length of 1000, which leads to a good deal of processing with short vectors in some of the secondary particle production modeling loops. Additionally, no optimization, meaning check of vector lengths and designating seldom used loops to be run in scalar, etc.,) was performed. Further, no effort was made to tailor to code (removing test loops, removing conditional checks that apply only to certain models, etc.) to specific models and problems.

6.4 Purely Numerical Artifacts

It was pointed out in chapter V that the discretization most commonly used in Monte Carlo calculations, chosen for the sake of sampling speed, involves dividing distributions or cross section densities into binned sections of equal probability and can introduce substantial discrepancies between the discrete functions and the continuous functions which they attempt to represent. RMS errors often range up to 20%, but are tolerated for the sake of speed and simplicity. The effect that the choice of discretization scheme has on Monte Carlo calculations, with respect to both accuracy and overall computation time, is examined in this section. A single scattering model using Riley's elastic cross section, Gryzinski's classical cross section for inner

shell ionization, and a $1/\Delta E^2$ empirical distribution for excitations (model 5 of the first section of this chapter) was discretized using several schemes and using different errors for the same scheme, and transport results generated from runs using data produced for the different schemes was analyzed. Since it is assumed that the most accurate discretization will result in the most accurate result, no attempt is made to examine the complete range of energies and atomic numbers. Rather, the amount of deviation from the results obtained using the most accurate discretization is studied, in an attempt to discern the magnitude of the effect discretization errors. Also examined is the maximum effect that the slower sampling speed of the more accurate binning schemes can have on total computation time.

6.4.1 Effects of Discretization Errors

The main thrust of the first part of this evaluation is the determination of differences in computational results caused solely by inaccuracy in modeling differential cross section densities and distribution functions. Since the discretization scheme employing arbitrarily spaced spaced bins with linear interpolation between bin endpoints was seen in the previous chapter to be the only scheme permitting highly accurate discretizations of all cross sections, it is used throughout. Requested error tolerances are increased to simulate poor discretization. The discretization errors tested are listed in table 6.18. Note that both the requested error and the obtained error for discretization and energy ladder endpoints and the midpoints between ladders are listed in the table. In most instances, the minimum number of energy basepoint condition, in which the number is automatically set tc 7 (a number arbitrarily set by the ENCHOP routine) if the error in going from one energy to the next does not rise above the requested maximum, was invoked.

Case Number:	Error at Energy Endpts (%)		Error at Energy Midpts (%)	
	Requested	Obtained	Requested	Obtained
1	0.5	0.5	1.0	1.0 – 1.9
2	2.0	2.0	5.0	< 5.0
3	5.0	5.0	10.0	< 10.0
4	10.0	10.0	20.0	< 20.0

Table 6.18: Errors for Discretization Tests

The problem selected was the prediction of the energy distribution of backscattered 10 keV electrons, impingent upon a semi-infinite gold slab. This was chosen since both the energy loss and the angular deflection distributions must be modeled correctly in order to obtain correct results. Test runs used 100,000 incident electrons. Plot of the output histograms for the four tests case are shown in figure 6.64.

Not much difference in the results is in evidence, although the large error case does tend to over estimate the height of the peak of the distribution somewhat more than the small error cases.

A much more dramatic effect was seen when equally probable bins with linear interpolation were used. The data was set so as to use 50 bins regardless of the endpoint error and 40 energy bins. Calculations performed for chapter V show that the error for such discretizations should be in the 2 to 5 percent range for gold, and it was assumed that they would be smaller for lighter Z materials. This assumption was proven glaringly deficient by test results. Table 6.19 shows backscattering fractions predicted by all four class I schemes using 50 by 50 set of equally probable bins and using 1% error arbitrarily probable bins.

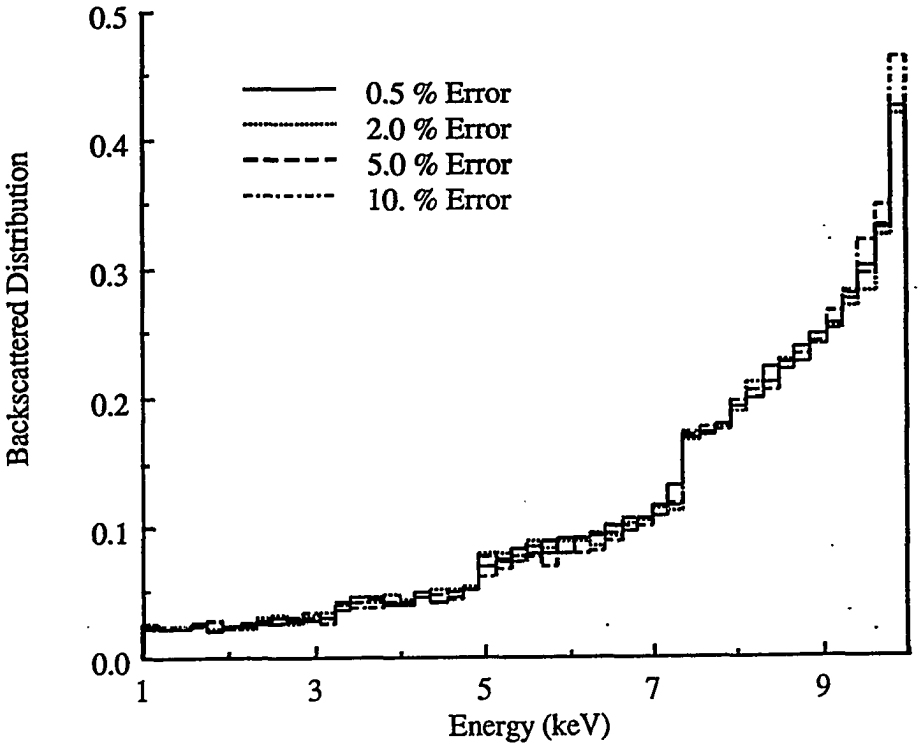

Figure 6.64: Backscattered Electron Energy Distributions for Various Discretization Errors

Monte Carlo	Al at 10 keV	Cr at 25 keV	Au at 10 keV
Model 1, Equal Prob	.298	.430	.486
Model 1, Arb Prob	.213	.330	.505
Model 3, Equal Prob	.289	.468	.446
Model 3, Arb Prob	.215	.326	.465
Model 4, Equal Prob	.264	.443	.473
Model 4, Arb Prob	.191	.295	.487
Model 5, Equal Prob	-	.419	.441
Model 5, Arb Prob	.189	.295	.491

Table 6.19: Backscattered Fractions from Monte Carlo for Class I Simulations, Different Discretizations

It is seen that for both aluminum and chromium, the equally probable bin scheme is inadequate. The discrepancies caused by the discretization errors are enormous. For Gold they are within the limits of statistical fluctuations. It is suggested then that the minimum discretization error, which is usually obtained by a arbitrarily probable scheme, always be employed, particularly at low Z.

6.5 Suggested Future Work

Several comments on the shortcomings of this work and the points which should be examined if the work were to be pursued are included here. Some of these comments are pertinent to all kilovolt electron transport studies, while others refer mainly to the present work.

It is obvious from the discussions of chapter II that the least understood area relevant to kilovolt electron transport is that of inelastic scattering. Further work in this area should start with a somewhat more thorough and comprehensive examination of many of the cross section formulations uncovered during the long course of this study, but not detailed in chapter II. One can envision the end product of such an effort a single program designed to calculate atomic *and* molecular electron wave functions for any input configuration under very little approximation, and produce both a partial wave expansion for accurate elastic cross sections and a complete set of generalized oscillator strengths or differential inverse mean free paths for inelastic process descriptions.

Additionally, as many important physical processes (such as molecular bond dissociation) can be initiated by particles with energies less than 1 keV, the extension of this work to lower energies would be desirable. The main obstacles currently inhibiting this extension are the lack of a good partial wave elastic cross section, as

well as the general uncertainty about

Similarly, as energetic de-excitation products from high Z heterogeneities in mixed media can greatly effect energy asborption characteristics of in surrounding low Z materials, a more accurate and extensive relaxation data base, including more of the possible transitions in the slightly more outer shells (M and N) of high Z materials might be helpful.

Several applications of electron transport in electric and magnetic fields have been noted. The extension of single scattering algorithms to general magnetic field would be simple, and a general prescription applicable to all charge particle transport algorithms has been given by Bielajew [Bi89].

Lastly, the treatment of geometry in this work was trivial. Some sort of surface based or combinatorial geometry algorithm (various geometry packages have previously been applied to other problems in a vectorized format [Br84, Yo89]) should be added.

References

[Be63] M.J. Berger, "Monte Carlo Calculation of the Penetration and Diffusion of Fast Charged Particles," in *Methods in Computational Physics*, vol. 1, B. Adlu, S. Fernbach, M. Rotenberg, eds., Academic Press, New York (1963) 135.

[Bi89] A. F. Bielajew, *Monte Carlo Transport of Electrons and Photons*, T. M. Jenkins, W. R. Nelson and A. Rindi, Eds., Plenum Press, New York (1989) 421.

[Br84] F. B. Brown and W.R. Martin, *Progress in Nuclear Energy* **14**, (1984) 269.

[Da72] E. H. Darlington and V. E. Cosslett, *J. Phys. D* **5**, (1972) 1969..

[Da75] E. H. Darlington, *J. Phys. D* **8**, (1975) 85..

[Dr70] H. Drescher, L. Reimer, and H. Seidel, *Z. Angew. Physik* **29**, (1970) 331.

[Fe79] T. R. Fewell and R. E. Shuping, *Handbook of Mammography X-Ray Spectra*, U.S. HEW Publication (FDA) 79-8071, (1979).

[Ka57] H. Kanter, *Ann. Physik* **20**, (1957) 144.

[Ka82] J. Kalef-Ezra, Y.S. Horowitz and J. M. Mack, *Nucl. Instrum. & Methods* **195**, (1982) 587.

[Li77] E. Lifshin, M.F. Ciccarelli, and R. B. Bolon,"New Measurements of the Voltage Dependence of Absolute X-Ray Yields Using Energy Dispersive Spectrometry", *Proc. 12th MASS Conf.,* (1977) 104A.

[Li79] A. Liuzzi and J. G. Martin, *Trans. Am. Nucl. Soc.* **32**, (1979) 253.

[Ne80] G. Neubert and S. Rogaschewski, *Phys. Stat. Sol.* **59**, (1980) 35.

[St54] E.J. Sternglass, *Phys. Rev.* **95**, (1954) 345.

[Ve77] R.L. Verma, *J. Phys. D* **10**, (1977) 1167.

[Yo89] S. Youssef, W. Martin, T.C. Wan and S. Wilderman, *Comp. Phys. Comm.* **57**, (1989) 251.